

THE UNIVERSITY *of* EDINBURGH

This thesis has been submitted in fulfilment of the requirements for a postgraduate degree (e.g. PhD, MPhil, DClinPsychol) at the University of Edinburgh. Please note the following terms and conditions of use:

- This work is protected by copyright and other intellectual property rights, which are retained by the thesis author, unless otherwise stated.
- A copy can be downloaded for personal non-commercial research or study, without prior permission or charge.
- This thesis cannot be reproduced or quoted extensively from without first obtaining permission in writing from the author.
- The content must not be changed in any way or sold commercially in any format or medium without the formal permission of the author.
- When referring to this work, full bibliographic details including the author, title, awarding institution and date of the thesis must be given.

Transition-Metal-Hydrogen Systems at Extreme Conditions



Thomas Scheler

A thesis submitted in fulfilment of the requirements
for the degree of Doctor of Philosophy
to the
University of Edinburgh

March 2013

Abstract

The application of extreme conditions offers a general route for the synthesis of materials under equilibrium conditions. By finely tuning the thermodynamic variables of pressure and temperature one can manipulate matter on an atomic scale, creating novel compounds or changing the properties of existing materials. In particular, the study of hydrogen and hydrogen compounds has attracted the attention of researchers in the past. Although hydrogen readily reacts with many elements at ambient conditions, there is a significant "hydride gap" covering the *d*-metals between the Cr-group and Cu-group elements. At elevated pressures however, the chemical potential of hydrogen rises steeply. At sufficient pressures, hydrogen overcomes the dissociation barrier at the metal surface and atomic hydrogen diffuses into the metal, usually occupying interstitial sites in the host matrix. These interstitial hydrogen alloys can exhibit interesting physical properties, such as modified crystalline structures, different compressibility, altered microstructure (nanocrystallinity), hydrogen mediated superconductivity or potential hydrogen storage capabilities. Furthermore, theory predicts that hydrogen confined in a host matrix might undergo the elusive transition to a metallic groundstate at considerably lower pressures than pure hydrogen. Most *d*-metals have been found to exhibit hydride phases at extended conditions of pressure and temperature. However, besides rhenium, the 6^{th} row metals between tungsten and gold, as well as silver, have not or only very recently been found to form bulk hydrides. In the course of this PhD-thesis, several of the missing metal-hydrides were successfully synthesized in the diamond anvil cell and characterized by *in-situ* x-ray diffraction using synchrotron radiation.

Declaration

Except where otherwise stated, the research undertaken in this thesis was the unaided work of the author. Where the work was done in collaboration with others, a significant contribution was made by the author.

T. Scheler
March 2013

Acknowledgements

In a way, writing these acknowledgements was the most difficult part of completing this thesis. So many people contributed to this work on various levels and it would be impossible to name you all. First and foremost, I would like to thank my supervisor Eugene Gregoryanz who has been a great mentor over the past few years and was always available when I needed help. Although it is difficult for me now to drink a Radler (Alster) without feeling a tiny amount of guilt. I would like to thank my colleagues Christophe Guillaume, Ross Howie, Phil Simpson and Donna Morton who helped a lot with the preparation of diamond anvil cells and with experiments during beamtimes. The memory of all of us sitting in the Dreyer in Hamburg is still fresh. A big Thank You also goes to everyone who was involved in the hydride projects: Miriam Marqués, who did calculations for the platinum and iridium projects, Yanming Ma and his group for calculations in the tungsten project, Christian Donnerer who took over the copper project and brought it to a nice conclusion, Zuzana Konôpková who spent several nights alone at the beamline at PETRA-III laser-heating our iridium samples, Olga Degtyareva for teaching me the basics of crystallographic data analysis, Thomas Cornelius and Tobias Schülli for giving me a few days of their inhouse beamtime at the ESRF for testing *in-situ* scanning x-ray diffraction microscopy. Additionally, there were so many people in CSEC who contributed with helpful discussions, by looking over data with me or simply during fantastic lunchtime conversations. Thank you Graham, Ingo, John, Emma, Craig, Mungo, Wanaruk, Chris, Rachel, Julian, Michal, Lucy, Alex. Looking back over the past three years, I would have never managed to get anywhere without the help of Jane Patterson. I would also like to extend my thanks to everyone in the CM-DTC, in particular Prof. Andy Mackenzie, Dr. Chris Hooley, Christine Edwards and Dr. Julie Massey and also Prof. Malcolm McMahon, who made it possible for me in the first place to come to Edinburgh. I am grateful to my examiners Prof. Paul Attfield and Dr. Michael Hanfland for their time and for providing constructive criticism which helped to improve this thesis significantly. Finally, the biggest (and I mean that) Thank You goes to Mirjam - for simply everything.

Contents

Abstract i

Declaration ii

Acknowledgements iii

Contents iv

List of figures v

List of tables xiii

1 Introduction 1
1.1 Introduction and Motivation 1
1.2 Thesis Outline 5

2 The Metal-Hydrogen System 9
2.1 Properties of Free Hydrogen 9
2.2 Hydrogen in Host Matrices 13
2.3 Transition Metal-Hydrides: A Review 19

3 Review of High-Pressure Equipment and Techniques 31
3.1 The Diamond Anvil Cell 31
3.2 Pressure Scales 34
3.2.1 The Ruby Pressure Scale 35
3.2.2 Equations of State as Pressure Scales 37
3.2.3 The Diamond Raman Gauge 38
3.2.4 The Hydrogen Vibron Gauge 40
3.3 X-ray Diffraction at High Pressures 41
3.3.1 Basic Diffraction Theory 42
3.3.2 *In-situ* Synchrotron X-ray Diffraction at High Pressure . . 46
3.3.3 Determination of Hydrogen Content with X-rays 48
3.4 Other Techniques 50
3.4.1 Raman Spectroscopy 50

3.4.2 Neutron Diffraction 50
3.4.3 Transmission Electron Microscopy 51
3.4.4 Focused Ion Beams 51

4 Transition Metal-Hydrogen Systems at Extreme Conditions 54
4.1 Platinum 54
4.2 Rhenium 64
4.3 Tungsten 73
4.4 Iridium 90
4.5 Copper 104
4.6 Other metals 106
4.6.1 Gold 106
4.6.2 Silver 109
4.6.3 Osmium 110

5 Conclusions and Future Prospects 112

A Data Tables 116

Bibliography 130

Publications 143

List of Figures

2.1 Raman spectrum of hydrogen at ∼5 GPa (fluid state) in a diamond anvil cell. The peaks denoted D_1 and D_2 are first and second order diamond Raman peaks (see chapter 3.2). The hydrogen rotons are seen at Raman shifts below D_1 ($S_o(1)$ and $S_o(3)$ belong to otho-, $S_o(0)$ and $S_o(2)$ to para-hydrogen), the main hydrogen vibron mode ν_1 at shifts above 4000 cm^{-1}. Data courtesy of R. Howie. 10

2.2 PT-Phase-diagram of hydrogen (see [Howie 12] and references therein (annexed to this thesis)). The thick solid line denotes the proposed melting curve. Coloured dashed lines with open triangles and crosses are theoretical transition boundaries between the molecular and atomic state. Thin solid lines are established phase boundaries between solid phases I, II and III. Thin dashed lines are the recently proposed phase boundaries including phase IV. 13

2.3 The Cr-group to Cu-group elements and their reactions with hydrogen (arrows). α denotes a *bcc* configuration, ϵ an *hcp* and γ an *fcc* configuration. Fully green fields denote the formation of a stoichiometric hydride. Ruthenium is only known to form a substoichiometric hydride with low hydrogen content, while no hydride phases are known for silver and osmium. The existence of a hydride phase in gold is in dispute (see chapter 2.3). The blue frame indicates the scope of the present work, *i.e.* elements investigated during the course of this thesis. For comparison, the state of knowledge prior to this work is included next to the respective symbols. 15

3.1 A) Schematic drawing of a typical DAC. B) Photograph of a closed symmetric DAC ("doughnut" type). C) Close-up schematic of the sample confined between the gasket (drawing) and the two diamond anvils. 32

3.2 Gasket Preparation: A) A sheet of Re is placed between the aligned diamonds. B) The diamonds are pressed into the metal to create an indent. C) A centered hole is drilled into the indent. D) The metal sample is placed with a sharp needle in the hole. E) The cell is closed with one diamond leaving a small gap. F) Air in the cell is replaced with hydrogen gas and the cell is closed. G)-H) Optical micrograph of the sample hole taken through the diamonds. The metal sample and a ruby-sphere can be seen in the 50 μm hole. . 34
3.3 A) Energy levels in the Cr^{3+} ion, taken from [Syassen 08]. B) Fluorescence spectrum from ruby showing the R_1 and R_2 lines. . . 36
3.4 Equations of state for the metals listed in Table 3.1 (see there for references). Inset shows EoS for copper. 38
3.5 Equation of state of hydrogen. Inset shows d-spacings of hydrogen Bragg peaks vs. pressure. The values are derived from the EoS given in [Loubeyre 96]. For practical purposes, the data can be found in Table A.1. 39
3.6 The Akahama pressure scale for the diamond Raman edge [Akahama 07]. Inset shows the observed Raman spectrum at 123 GPa. 40
3.7 The hydrogen vibron frequency plotted against pressure. Data courtesy of R. Howie. 41
3.8 Powder XRD pattern and integrated spectrum (not background corrected) of silicon at ambient conditions. Inset shows enlarged part of the diffraction pattern. Single reflections from individual crystallites that make up the sample are visible. The XRD pattern was recorded at Diamond Light Source using a MAR345 detector. 44
3.9 Schematic layout of a typical high-pressure beamline with characteristic distances of the elements from the source. For more details, see *e.g.* [Liermann 10]. 48
3.10 Left, FIB images of laser drilled gasket holes. For larger holes, the accuracy of the laser is sufficient but the microtexture of the gasket rim is very uneven. Right, FIB-drilled gasket hole (dotted circle indicates diamond culet indent). 52

4.1 Optical micrographs showing a platinum loading. A) Open cell before hydrogen gas loading. B) Closed cell at 10 GPa. Note the significant reduction in volume due to the high compressibility of hydrogen. 56
4.2 Integrated diffraction patterns for platinum and platinum hydride at various pressures below and above synthesis. Tick marks show the peak positions of the according phases. Insets show according 2D diffraction patterns of the mixed phase and the pure hexagonal hydride phase. 57

4.3 Integrated XRD spectrum showing the mixed phase of platinum hydride at 34 GPa. Thin lines are calculated spectra for the individual phases. 58
4.4 3D structural model of PtH-II (left). The unit-cell is indicated by the wireframe. Right, for comparison the unit-cell of PtH-I for which the exact structure remains unknown. 59
4.5 Equation of state of platinum hydride: Left shows pressure range of experiments with data points from various runs. Open circles denote Pt-*fcc*, red diamonds PtH-II, the others PtH-I. Right shows the full pressure range between 0 and 200 GPa. Open squares are data from [Eremets 08], there interpreted as silane (see Table A.7). Solid black lines are fitted EoS for PtH-I, red lines EoS for Pt, green dashed line combined EoS for Pt+$\frac{1}{2}H_2$ (see Table 3.1). 60
4.6 A) Evolution of the volume difference between PtH-II and Pt with pressure. B) Evolution of the c/a-ratio in the same pressure range. See Tables A.3 and A.4 for values. 61
4.7 Micrographs from different loadings (A: Au+H_2 at 50 GPa, B: Ir+H_2 at 110 GPa) showing the extension of the rhenium hydride zone from the sample volume into the gasket. This can be seen as a darkening of the gasket. In A), the zone is indicated by the dashed white line. 64
4.8 Integrated diffraction patterns of ReH before and after heating (see text). Insets show the disappearance of the superstructure reflections upon heating. Green circles indicate *fcc* reflections from the Au coating. 66
4.9 A) Measured volume differences in ReH formed in the gasket during the initial experiment. For a detailed description see text. B) Volume differences and according hydrogen content (x) of the first and second run compared to older data (see [Scheler 11a]). Data is listed in Tables A.8, A.9 and A.10. 67

4.10 *in-situ* Scanning x-ray diffraction microscopy on rhenium hydride at 25 GPa. A) and B) show optical microscopy images of the sample at 17 GPa. C-G) show SXDM scans of the are shown in B) tuned for different signals. The scale bar on the left shows the colour-coding of the measured intensity on a relative scale. C) Rhenium hydride in sample, D) Au-coating (note the comparably bright background intensity), E) rhenium in gasket (only some parts of the gasket are in Bragg condition for the detector), F) diffuse scattering, transmission (note that the broken ruby sphere (see B) is almost invisible compared to rhenium) G) rhenium hydride on the gasket rim. H) compound SXDM image using signals from C,E and G: Green is pure rhenium, yellow rhenium hydride in the gasket, blue rhenium hydride in the sample (which has a different lattice parameter than the hydride in the gasket). . 68

4.11 A) Layered anti-CdI_2 type structure of ϵ_1-Re_2H. The arrows indicate the displacement of the Re-atoms from their equilibrium positions in the *hcp* lattice (not to scale). B) NiAs-type structure of ϵ_2-ReH. The transparent blue sheets depict hydrogen layers with available interstitial sites. In both figures, the unit cell is indicated by the wire frame and circles around atoms belonging to the unit cell. C) c/a-ratios measured for the ϵ_1-phase (upper) and ϵ_2-phase (lower). The single red data point was measured in rhenium hydride formed in the gasket. 70

4.12 Integrated XRD spectrum of tungsten hydride at 44 GPa (inset shows 2D diffraction pattern). The green line denotes the result from a LeBail fit. Tick marks indicate peak positions for cubic W (upper, blue) and hexagonal WH (lower, red). The diffraction spectrum of platinum hydride at 43 GPa is added for comparison (grey dashed line). Note the difference in peak width. 74

4.13 SXDM scans on tungsten hydride. A) Optical micrograph of the loaded cell. B) SXDM scan (low resolution) shows formation of rhenium hydride (green) from rhenium in the gasket (red). The tungsten signal is blue. C) SXDM scan just after passing synthesis conditions. Very weak additional intensity is visible in the tungsten sample. The intensity change below the horizontal line is due to a storage-ring refill and hence a higher photon flux. D) High-resolution SXDM of the sample showing tungsten hydride (blue) forming across the sample. Still strong pure tungsten signal (cyan/white). 76

4.14 2D XRD patterns at various pressures showing pure tungsten (upper), mixed state shortly after surpassing synthesis conditions (second from top), pure tungsten hydride at similar pressure after saturating for several weeks (third from top) and tungsten after decomposition (lower). 77
4.15 XRD pattern of WH at 50 GPa. Note the streaks connecting areas of higher intensity in the incomplete powder rings. 78
4.16 Opical micrographs of the tungsten hydride sample inside the DAC for two different loadings. A) and C) show the hydride before, B) and D) directly after decomposition. 79
4.17 A-F) Preparation process of a TEM sample from recovered material by FIB techniques (see text for details). G) Darkfield image showing an array of elongated tungsten crystallites. H) Brightfield image of crystallites near the surface with preferred orientation perpendicular to the TEM-section. I) Darkfield image of small grains inside the sample. J) Electron diffraction pattern of nanocrystalline tungsten. K) Electron diffraction pattern of a control sample. 80
4.18 Average grainsize of tungsten hydride calculated using the Scherrer formula and the width of the (100) reflection. Data is shown for three independent experiments. The shaded area shows an extrapolation to zero pressure. 82
4.19 PV-data of tungsten hydride (see Tables A.11-A.14). Data were taken in both, compression and decompression. The EoS of tungsten is calculated from literature values (see Table 3.1). For WH, two separate Vinet-type EoS were fitted to the data from fully transformed (black squares and green downward-triangles) and partly transformed (blue triangles and red circles) tungsten hydride. Both EoS were fitted with fixed $B' = 4$ (equivalent to pure tungsten) and yielded 500(12) and 468(20) GPa, respectively. With $B' = 5.1$, the resulting bulk moduli were 476(12) and 410(20) GPa. 85
4.20 Results from the 3rd experimental run (see Table A.14, black squares in Fig. 4.19). A) Equation of state with Vinet fit (green dotted line) and guide to the eye (black line). B) Evolution of volume difference compared to tungsten with pressure. C) c/a ratio and D) lattice parameters vs. pressure. The vertical dashed line indicates synthesis pressure. 86

4.21 Pressure-Volume data of tungsten hydride. The solid line indicates the computational equation of state for WH. Open circles denote calculated PV points for WH_2, open diamonds for a fractional mixture of $\frac{2}{3}$ WH and $\frac{1}{3}$ WH_2. The dashed line is a guide to the eye. Solid symbols are experimental unit-cell volumes fitted with a hexagonal cell. Computational data courtesy F. Peng 88
4.22 Optical micrographs of an open cell with iridium before hydrogen loading (left) and the closed cell at 110 GPa (right). 90
4.23 2D XRD patterns of iridium hydride. The given times are hours after passing 55 GPa. The red arrow indicates the (001) peak of simple cubic iridium hydride, the green arrow in E) and F) indicates the (111) peak of *fcc* iridium. Additional weak rings in this area stem from rhenium hydride. 91
4.24 Ratio of intensities between the (111) peak of iridium and the (001) peak of iridium hydride. The dashed line denotes an exponential fit to the data up to $t = 50$ h. The red solid line indicates the pressure (right scale). Data is listed in Table A.15. 92
4.25 Effect of laser heating. A) Scattering intensity of the strongest *fcc*-Ir peak. B) Relative change of the widths of the observed iridium hydride peaks. The red dashed line denotes the laser out power (right scale). Data is listed in Tables A.16 and A.17. 93
4.26 Integrated spectrum of iridium hydride at 126 GPa, after laser heating. The additional peaks are rhenium hydride. Tick marks show calculated peak positions for spacegroup $Pm\bar{3}m$ with $a = 2.5856$ Å. 94
4.27 Relative Intensity of the (001) peak of iridium hydride compared to Ir-(111) at constant pressure and laser heating (black squares) and at room temperature (red diamonds - see Figure 4.24). Inset shows enlargement of the time-span between 3 and 7 hours after passing synthesis pressure. Data is listed in Table A.18. 96
4.28 Relative Intensity of iridium hydride during decompression (black squares) in run-3. The red diamonds are data from previous run-1. The thin dashed line links pressure to time after decreasing pressure to below synthesis conditions (right scale). The grey vertical line indicates the pressure/time at which a more rapid decrease in scattering intensity was noted. Data is listed in Table A.19. 97
4.29 EoS of iridium hydride (red circles) and pure iridium (black squares) between 6 and 125 GPa. Solid lines are calculated EoS (for Ir see Table 3.1). The EoS parameters for iridum hydride are $V_0 = 23.33$ Å^3, $B_0 = 190$ GPa, $B' = 5.62$. Data is listed in Tables A.20-A.22. 98

4.30 Suggested $Pm\bar{3}m$ structure of iridium hydride, with hydrogen atoms occupying the $3c$ position. 99
4.31 A) Calculated (blue dashed line) compared to measured equation of state. B) Total energy calculations of iridium hydride against decomposition (courtesy Miriam Marqués). 99
4.32 Le Bail fit (green solid line) of the $Pna2_1$ structure to experimental data at 125 GPa (red crosses). The derived lattice parameters are $a = 3.6183$ Å, $b = 3.6834$ Å, $c = 5.1674$ Å, giving a volume of $V_{\mathrm{at}} = 17.2173$ Å^3. Tick marks indicate principal reflections of this space group. However, due to internal symmetry, some reflections have zero intensity. For comparison, a simple cubic lattice ($Pm\bar{3}m$) fitted to the same data yielded a lattice parameter of $a = 2.5823$ Å, giving a nearly identical volume of $V_{\mathrm{at}} = 17.2195$ Å^3. 101
4.33 Atomic positioning in the $Pm\bar{3}m$-structure (left), $Pna2_1$-structure (middle) and $Pnma$-structure (right). Larger red spheres denote iridium atoms, smaller blue spheres hydrogen atoms. 102
4.34 A) Comparison between experimentally derived EoS for iridium hydride and iridium. B) Volume difference between Ir and IrH_3 in comparison to the hydrogen equation of state (here for 3 hydrogen atoms). The red dashed line denotes a guide to the eye for the evolution of ΔV. 103
4.35 Integrated XRD spectrum showing cubic copper (red upper tick marks) and hexagonal copper hydride (blue lower tick marks) at 22 GPa. The blue circle indicates the position of the (001) forbidden reflection. 105
4.36 Experimental equation of state of copper (black squares) and copper hydride (red triangles). The dotted line denotes the equation of state of copper (see Table 3.1), dashed line the EoS of wurtzite CuH [Filipek 07]. The solid line is a Vinet fit to our data, yielding $V_0 = 13.10(1)$ Å^3, $K_0 = 145(5)$ GPa ($K' = 4.8(3)$). The green diamonds are attributed to the formation of cubic copper hydride on repeated compression after decomposition from the hexagonal hydride phase. 106
4.37 Diffraction pattern of a sample provided by V.E. Antonov. Red tick marks indicate *fcc*-Au at ambient pressure ($a = 4.0811$ Å), blue marks are identified reflections not belonging to gold. A refinement of the structure was not possible. Inset shows the same spectrum on linear scale. 108
4.38 EoS of silver measured in a hydrogen atmosphere. The solid red line denotes a Vinet fit to the data: $V_0 = 68.23$ Å^3, $B_0 = 100.5$ GPa, $B' = 5.21$. The dashed line is an EoS taken from literature ([Akahama 04a], see Table 3.1). 109

4.39 Measured EoS of Os under hydrogen atmosphere compared to literature EoS (solid line, see Table 3.1). Inset shows c/a ratio vs. pressure. Grey dashed lines are guides to the eye regarding the difference in EoS and change in c/a ratio. 110

List of Tables

2.1 Important properties of the hydrogen molecule 9
2.2 Important properties of the d-metal hydrides. ϵ-phases denote *hcp* metal host lattices, γ-phases *fcc* metal host lattices. w-CuH denotes the wurtzite-type structure of copper hydride. Lattice parameters are given at ambient conditions, except were stated otherwise. B_0 is the zero-pressure bulk modulus (given where available). Where no temperature is given for synthesis conditions, synthesis takes place at room temperature. 30

3.1 Parameters for the equations of state for the materials investigated in this work. V_0 is given per single atom, in the case of hydrogen per hydrogen molecule. 37

4.1 Results of the Vinet fit to EoS. 98
4.2 Calculated parameters for the $Pna2_1$-structure at 60 GPa 100
4.3 Calculated parameters for the *Pnma*-structure at 120 GPa 102

A.1 Hydrogen EoS (see [Loubeyre 96]), c/a-ratio and observed d-spacings of Bragg reflections up to 120 GPa. 116
A.2 XRD experiments carried out in the course of this thesis. The used DAC's are DC (Symmetric D-type "doughnut"), B (Betsa), GG (Gregoryanz-Guillaume type) and P.C. (long Piston Cylinder). Inhouse beamtimes were conducted in collaboration with the team at the respective beamlines and are not assigned experiment numbers. 117
A.3 Platinum hydride refined unit-cell parameters for phase II (*hcp*), loading 1. 117
A.4 Platinum hydride refined unit-cell parameters for phase II (*hcp*), loading 2. 118
A.5 Platinum hydride refined unit-cell parameters for phase I (complex phase), loading 1. 118
A.6 Platinum hydride refined unit-cell parameters for phase I (complex phase), loading 2. 118
A.7 P-V data extracted from [Eremets 08], there interpreted as silane. 119

A.8 Lattice parameters and volume differences measured for rhenium hydride, initial experiment, pressure increase. Before 16.2 GPa, the sample was heated to 150 °C for 19.5 hours. Waited for 16h between 30.2 and 30.8 GPa. Heated to 200 °C for 4.5h after 45.2 GPa and 300 °C for 8.5h after 46.4GPa. 119
A.9 Lattice parameters and volume differences measured for rhenium hydride, initial experiment, pressure decrease after heating to 300 °C. 119
A.10 Lattice parameters and volume differences measured for rhenium hydride, second experiment, pressure increase. Heated to 200 °C after 18.2 GPa 120
A.11 Lattice parameters and volume differences measured for tungsten hydride, Loading 1 (Feb. 2011). 120
A.12 Lattice parameters and volume differences measured for tungsten hydride, Loading 2 (May 2011). 121
A.13 Lattice parameters and volume differences measured for tungsten hydride, Loading 4 (Nov. 2011). 121
A.14 Lattice parameters and volume differences measured for tungsten hydride, Loading 3 (Oct. 2011). 122
A.15 Synthesis process of iridium hydride. Table shows development of scattering intensities with time and pressure of the (111) peak of *fcc* iridium and the (001) peak if simple cubic iridium hydride. . . 123
A.16 Integrated scattering intensity (arbitrary units) of the (111) peak of iridium during laser heating at 115 GPa. 124
A.17 Widths (FWHM) of the five strongest diffraction peaks of iridium hydride during laser heating at 115 GPa 124
A.18 Laser heating during run-3 of iridium hydride. In addition to the relative scattering intensity, the d-spacing of the (001)-peak (equivalent to lattice parameter a) and the FWHM of this reflection are given. 125
A.19 Decompression process of run-3 for iridium hydride. Shown is the relative intensity of iridium hydride compared to iridium. 126
A.20 Lattice parameters and volume differences measured for iridium hydride, run-1. 127
A.21 Lattice parameters and volume differences measured for iridium hydride, run-2. “0” entries denote values not measured. 128
A.22 Lattice parameters and volume differences measured for iridium hydride, run-3. “0” entries denote values not measured. 129

Chapter 1

Introduction

1.1 Introduction and Motivation

The development of a sustainable and environmentally sound energy source is seen by many as one of the most important present-day challenges with electricity generation in hydrogen fuel-cells being a very promising option, in particular in the e-mobility sector [Züttel 04, Sakintuna 07, Jain 10]. However, although fuel-cell technology is readily available, a suitable hydrogen storage method has yet to be developed. Since pure liquid hydrogen is deemed too dangerous and too difficult to handle for mass-use, research and development concentrates on solid storage materials [Bowman Jr. 02]. The US Department of Energy has published a long-term goal for what is supposed to be a practical and commercially viable storage material (see *e.g.* [Sakintuna 07]): The material in question should exhibit at least 6.5 weight% hydrogen and should make 65g of hydrogen available per liter. Furthermore, decomposition (*i.e.* the emission of pure hydrogen) should take place at accessible temperatures between 60 °C and 120 °C. For commercial use, the hydrogenation process should take place at industrially viable conditions of pressure and temperature (or under otherwise accessible non-equilibrium conditions). Here, the metal hydrides play an important role. Interesting candidates are binary metal-hydrogen alloys based on low-weight metals, such as magnesium [Herranz 10] or titanium [Kalita 08]. Magnesium hydride (MgH_2) exhibits promising properties with a high weight-percentage of 7.6%, double volumetric hydrogen density compared to liquid hydrogen and low-cost base material [Herranz 10]. However, commercial use is yet prohibited by

the very slow hydrogenation-dehydrogenation process and the too high pressures and temperatures under which it occurs [Jain 10]. Hydrides of magnesium-metal alloys have been investigated to the same end but had to conclude that equilibrium synthesis happens at even more extreme conditions reaching pressures of 4 GPa, inaccessible by large industrial-scale processes [Moser 09].

High-pressure techniques play an important role in the development of hydrogen storage materials and in general in research on hydrogen compounds. In fact, it is research on pure hydrogen that has driven the development of techniques and instrumentation in high-pressure research for the past almost 80 years since the original postulate of a metallic groundstate of hydrogen by Wigner and Huntington in 1935 [Wigner 35] (see chapter 2.1). The prospect of metallic hydrogen potentially being a high-temperature superconductor [Ashcroft 68] and the possibility to reach metallization at lower pressures for hydrogen confined in metal host matrices [Ashcroft 04] further fueled research in this area. Thus, the metal hydrides do not only play an important role in the development of hydrogen storage materials but also in the study of the properties of pure hydrogen. Of further interest in this respect are also the alkali metals, in particular lithium as the lightest. In fact it was found that lithium hydride with high hydrogen content might form a metallic hydrogen sublattice at accessible pressures of around 150 GPa [Zurek 09]. Unfortunately, these findings are so far only theoretical and were not yet confirmed experimentally. An experimental review of the alkali-hydrogen systems is given in [George 10]. Meanwhile, the search for metallic hydrogen continues and a recent breakthrough was achieved with the discovery of phase IV of solid hydrogen [Howie 12] at pressures above 220 GPa.

High-pressure research is a broad and interdisciplinary field ranging from industrial applications (such as hydrogen storage materials) to fundamental research (properties of free hydrogen), including research aresas as diverse as geophysics, planetary science, even food science and of course material science. High-pressure synthesis has been used to create a plethora of novel compounds, some with highly interesting properties. Since the early 20^{th} century, the synthesis of ammonia at high pressures and temperatures (Haber-Bosch process) is one of the most important industrial applications of extreme conditions. Diamond is

another example of a very useful material, synthesized under extreme conditions of pressure and temperature, but also cubic boron nitride (c-BN) has become an industrial material of choice for superhard abrasives [McMillan 02]. Platinum nitride further serves as a good example of a material synthesized at very high pressures (above 50 GPa) and temperatures, which can be quenched to ambient conditions [Gregoryanz 04, Solozhenko 05]. A review on this matter is given in [Brazhkin 07], where the superhard materials synthesized at extreme conditions are described as "real treasures of today's industry". One of the main problems with high-pressure synthesis is in many cases the extremely small quantity of substance produced, in particular when pressures above ∼10 GPa (the limit of the large-volume press) are necessary. However, high-pressure synthesis refers to the formation of a material under thermodynamic equilibrium conditions. Once the formation mechanism is understood, non-equilibrium techniques can be developed to synthesize a material in larger quantities. The prime example is artificial diamond formed by chemical vapor deposition (CVD-diamond).

The interest in new materials synthesized at extreme conditions is not only limited to hydrogen storage materials, metallic hydrogen or superhard materials - although nowadays these fields seem to occupy the majority of research groups. Highly interesting fields are the search for novel superconductors or the development of specific nanomaterials (such as graphane, the hydride of graphene [Elias 09]). Many of the superconducting elements undergo the transition only at high pressures, with the latest addition being europium at pressures exceeding 80 GPa [Debessai 09]. An earlier review (not yet including europium) can be found in [Buzea 05]. Apart from the search for superconducting hydrogen, the metal hydrides themselves sometimes show interesting superconducting behaviour. Palladium for example is only superconducting in the milli-Kelvin regime. Palladium hydride on the other side exhibits a hydrogen-content dependent transition temperature of up to 11 K, an effect that led to speculations (and a dispute in the research community) whether over-stoichiometric palladium hydride might be a high-temperature superconductor [Tripodi 04, Baranowski 07, Tripodi 09]. This idea even led to a patent application for high-T_c superconductors [Tripodi 06]. The accuracy of these speculations is questionable. So far, only slightly overstoichiometric palladium hydride has been produced using surface layer ion

implantation which was not sufficient to test this hypothesis. Could palladium incorporate a higher hydrogen content at extreme pressures? Another metal in the same group of elements might show a similar behaviour: We have shown in [Scheler 11b] that superconductivity previously attributed to silane in [Eremets 08] can in fact be attributed to platinum hydride, with a critical temperature even surpassing that of palladium hydride. However, this has not yet been verified experimentally. A review on superconductivity in the metal hydrides is given in [Bashkin 03]. More than 20 years ago, palladium hydride (in fact, palladium deuteride) was, rather interestingly, treated as a candidate for cold fusion under pressure [Baranowski 90], a truly intriguing prospect. Unfortunately (and predictably), this was not confirmed and research quickly moved away.

In summary, research on metal hydrogen systems at extreme pressures targets a variety of different aspects, ranging from potential hydrogen storage materials to the elusive metallic (superconducting) ground state of hydrogen, superhard materials and novel superconductors. Naturally, these prospects led to almost ubiquitous interest in metal hydrides in the past. However, only recent advancements in experimental techniques, such as advances in diamond anvil cell technology, access to 3rd generation synchrotron radiation sources with fast large area detectors or the availability of lab-based fast Raman systems (owing to the development of notch filters, compact laser sources and in particular high-sensitivity CCD detectors), made it possible to explore materials at extended PT-conditions. Due to its significance for geophysics, iron hydride was the first metal hydride studied at very high pressures in the diamond anvil cell in 1991 [Badding 91]. Most of the previous work on metal hydrogen systems was carried out employing the large volume press at pressures below 10 GPa and usually always at high temperatures. Moreover, *in-situ* studies were almost impossible (apart from resistivity measurements) and most information was gained from quenched samples (see *e.g.* the reviews in [Antonov 02] or [Fukai 05]). In the diamond anvil cell, *in-situ* studies of metal hydrides were possible for the first time.

As of 2010 (before this work), the hydrides of iridium, osmium and silver have never been described. Platinum and tungsten hydride were known to exist but

their properties remained unstudied. Rhenium hydride was widely accepted to be fully understood while the equilibrium synthesis of hexagonal copper hydride (despite being known for a very long time) was never demonstrated. The syntheses of cubic copper hydride [Burtovyy 04] and gold hydride [Antonov 82] have never been repeated. This thesis aims at filling these remaining gaps concerning the metal hydrides and to provide a basis on which further research on these systems can build. The hydrides of platinum and tungsten have been studied in detail, new phases of rhenium hydride and copper hydride were discovered and the hydride of iridium was described for the first time. Even at very high pressures, no signs of hydrogenation of osmium, silver and gold were found.

1.2 Thesis Outline

This thesis is divided into three main parts:

Chapter 2 serves as an introduction to free hydrogen (brief), metal-hydrogen systems and in particular as a review of the group-6 to -11 *d*-metal hydrides. The review briefly summarizes the most important properties and characteristics of this group of binary hydrogen alloys. It aims to be a general review that encompasses not only the systems studied in this thesis but also materials not investigated for reasons of completeness and comparison. This is also intended to bring the results of this work, in particular the pressure ranges accessed, into perspective.

Chapter 3 gives general background information on techniques and methods used in this thesis: The high-pressure techniques of the diamond anvil cell, pressure gauges and synchrotron based x-ray diffraction. Supplementary techniques, such as Raman spectroscopy, electron microscopy and focused ion beam techniques are briefly introduced but not discussed in detail since they did not form a major component of this work. Neutron techniques are mentioned for completeness although no neutron experiments were carried out. This is mainly due to the lower accessible pressures by neutron techniques.

Chapter 4 presents the main results of this thesis. The chapter is divided into sections corresponding to the investigated metal-hydrogen system. The sections are ordered chronologically, *i.e.* experiments carried out earlier are presented in the beginning of the chapter. The main results are:

Platinum hydride (chapter 4.1): The formation of PtH was confirmed to take place at 27 GPa and room temperature. The structure was found to be hexagonally closed-packed with hydrogen atoms occupying every octahedral interstitial site. The equation of state was measured up to 55 GPa and a bulk modulus slightly higher than that of pure platinum was found. A second complex phase was found to exist in parallel to the hexagonal phase. However, the synthesis of this phase is not easily reproducible and a more accurate characterization was not possible. This work also shed light on the dispute around the formation of superconducting silane, reported in 2008. This work was published in [Scheler 11b].

Rhenium hydride (chapter 4.2): Rhenium hydride was found to undergo an isomorphous phase transition from the anti-CdI_2- to the NiAs-type structure when heated to temperatures above 150 °C at pressures around 20 GPa. The new phase showed an increase in hydrogen content with increasing pressure. Though no fully stoichiometric ReH was observed in the experiments, its formation can be expected at pressures above 50 GPa. This work was published in [Scheler 11a].

Tungsten hydride (chapter 4.3): Synthesis of tungsten hydride was confirmed at 25 GPa and room temperature, conditions similar to platinum hydride, and decomposition was reproducibly observed below 8 GPa. However, it was found that the formation progresses very slowly and requires several days for the material to fully transform. A TEM study on recovered material revealed a nanocrystalline microstructure with elongated crystallites of ∼20 nm in diameter. The equation of state was measured up to 115 GPa and upon initial analysis yielded a surprisingly high bulk modulus of near 500 GPa. However, additional *ab-initio* calculations revealed that the hydrogen content in tungsten hydride increases to values greater than 1 at pressures above 25 GPa, an effect that can

be mistaken for reduced compressibility. At the time of writing, a publication of these results is submitted for publication and under review.

Iridium hydride (chapter 4.4): Iridium hydride was discovered at pressures above 55 GPa. At room temperature, the formation progresses very slowly and even after 3 weeks at pressures above 100 GPa, the sample was not fully converted. Laser heating facilitates rapid synthesis. The hydride was found to be of non-interstitial nature with a very high hydrogen content of 3 H-atoms per Ir-atom. The equation of state was measured to 125 GPa and revealed a bulk modulus around 50% lower than pure iridium. This is attributed to the hydrogen-metal interaction. Onset of decomposition can be observed at pressures below 16 GPa but the hydride remained visible to 6 GPa. It is speculated that the material can be quenched to ambient pressure at low temperatures. At the time of writing, a publication of these results is submitted for publication and under review.

Copper hydride (chapter 4.5): Although copper hydride can be formed chemically at ambient conditions, no high-pressure synthesis of the hexagonal phase of copper hydride has been reported so far. In high-pressure experiments up to 50 GPa, a novel hexagonal phase of copper hydride was discovered. The new phase appears to have the stoichiometry Cu_2H with hydrogen occupying layers in the metal host matrix, equivalent to the anti-CdI_2 structure which is also seen in several other hydrides. Furthermore, we observed the formation of cubic copper hydride from dehydrogenated copper. At the time of writing, a publication of these results is accepted for publication [Donnerer 13]. The results are only described briefly since they form a major part of the master thesis of C. Donnerer who carried out large parts of the data analysis.

Other metals (chapter 4.6): No hydride phases were found for osmium and silver at pressures up to 87 GPa and gold at pressures up to 115 GPa, extending the experimentally known exclusion zone for hydride formation. Additionally, the application of high temperature (by external or laser heating) at high pressures did not induce the formation of a hydride in these materials.

Chapter 5 summarizes the main results but also puts forward questions arisen

and prospects for further investigations. Most of the systems described in this thesis are not yet fully understood or characterized and require more detailed experiments, in particular targeting the electronic properties.

Chapter 2

The Metal-Hydrogen System

2.1 Properties of Free Hydrogen

Hydrogen is the simplest and most abundant element in the universe and exists in the three isotopes protium, deuterium and tritium. In this thesis, only protium was used, and therefore this introduction will also concentrate on the aspects of this, the lightest isotope. To avoid confusion in nomenclature, any reference to hydrogen in this thesis generally refers to protium, unless otherwise stated. Under ambient conditions of pressure and temperature, hydrogen exists in the molecular state. Table 2.1 gives an overview over the most important properties of molecular hydrogen [Fukai 05]:

Table 2.1: Important properties of the hydrogen molecule

Property	Value
Binding Energy [eV]	4.748
Dissociation Energy [eV]	4.476
Vibrational Energy [eV]	0.516
Rotational Energy [eV]	$7.32 \cdot 10^{-3}$
Bond length [Å]	0.7416
Bohr radius (atom) [Å]	0.529

Due to the large energy of the vibrational movement, most molecules are in the ground state at moderate temperatures below 2000 K [Fukai 05]. For the rotational movement, one has to distinguish between ortho- and para-hydrogen:

The corresponding rotational modes of the two species are of different energy levels which can be clearly seen in a typical Raman spectrum of hydrogen (see Figure 2.1). At room temperature, approximately 75% belong to ortho- and 25% to para-hydrogen species (referred to as "normal hydrogen"). At room temperature, it solidifies in the orientationally disordered phase I (*hcp* structure) at pressures above ∼5 GPa [Hazen 87]. The equation of state of solid hydrogen is shown in Figure 3.5.

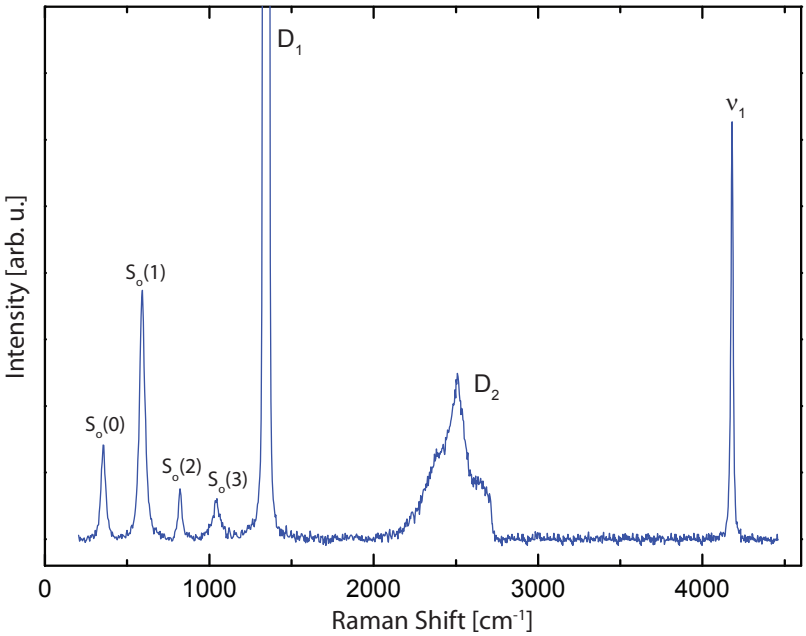


Figure 2.1: Raman spectrum of hydrogen at ∼5 GPa (fluid state) in a diamond anvil cell. The peaks denoted D_1 and D_2 are first and second order diamond Raman peaks (see chapter 3.2). The hydrogen rotons are seen at Raman shifts below D_1 ($S_o(1)$ and $S_o(3)$ belong to otho-, $S_o(0)$ and $S_o(2)$ to para-hydrogen), the main hydrogen vibron mode ν_1 at shifts above 4000 cm^{-1}. Data courtesy of R. Howie.

Hydrogen has always been a playground for advances in Physics, owing in parts to its apparent simplicity and status as a model system. In other parts advances were driven by one of the most intriguing and influencing predictions of the last century. In 1935, Wigner and Huntington speculated on a metallic modification of hydrogen [Wigner 35], which they predicted would emerge in dense solid hydrogen at pressures above 25 GPa. These pressures were out of

the scope of the techniques available at the time, but the prospect of achieving the metallic ground state fueled further development of high-pressure techniques. In 1968, a theoretical study by N.W. Ashcroft further speculated that the metallic ground state might be a high-temperature, maybe even a room-temperature superconductor [Ashcroft 68]. Further theoretical work on the properties of metallic hydrogen followed [Bovman 72a, Bovman 72b]. However, the originally predicted metallization pressures were found to be too low and no transition into a metallic and/or atomic state was observed at pressures up to 109 GPa [Loubeyre 96]. In the same year, 1996, shockwave experiments on fluid molecular hydrogen revealed a metallic behaviour at above 140 Gpa and temperatures of 3000 K [Weir 96]. To date metallic hydrogen at static compression and room temperature remains elusive. More recently, it was proposed that hydrogen confined in a host environment might undergo the insulator-metal transition at considerably lower and experimentally accessible pressures [Ashcroft 04]. In particular, chemical pre-compression of hydrogen in a metallic environment might lower the metallization pressure to pressures easily accessible by diamond anvil cell techniques. At the same time, further modifications of the ground state were suggested and a superconductor to superfluid transition was proposed [Babaev 04, Babaev 05], though these were still out of experimental reach. Therefore, experimentalists turned to Ashcroft's prediction of the possibility to metallize hydrogen as a constituent of a hydrogen-rich alloy. In 2008, Eremets *et al.* produced experimental evidence for apparently superconducting silane (SiH_4) at pressures above 50 GPa [Eremets 08]. They attributed the observed superconductivity to a hexagonal modification of silane with exceptionally high hydrogen density. It quickly became clear however, that silane could not be responsible for the observed behaviour since it readily decomposes at these pressures [Degtyareva 09]. This led to the assumption that a different material formed inside the sample volume, which in turn led to the discovery and characterization of platinum hydride [Scheler 11b] (see chapter 4.1).

Obviously, the search for the elusive metallic state and the quest to reach ever higher static compressions in hydrogen brought with it a plethora of discoveries regarding the properties of free hydrogen. The following paragraph is intended

to give a brief overview of the developments of the past two decades and the current state of knowledge. In 1992 it was established that the Raman shift of the hydrogen vibron exhibited a maximum at approximately 35 GPa and would decrease at higher pressures [Brown 92]. This behaviour is interpreted as a weakening of the molecular bond and hence an indicator for the transition into the atomic state. The dependency of the vibron frequency on pressure can be used as a pressure scale, which is discussed in detail in chapter 3.2. In further experiments, the compressibility of solid hydrogen was measured up to 109 GPa [Loubeyre 96], which has important implications for estimates of the metallization pressure. The equation of state established in this study is still used as a pressure reference during x-ray diffraction experiments (see chapter 3.2). In 2002, hydrogen was compressed to above 300 GPa for the first time, albeit at low temperatures (100 K) [Loubeyre 02]. It was found that the vibron signature (and hence the molecular state) of hydrogen was visible up to the highest pressures. Optical absorption spectroscopy indicated beginning closure of the electronic bandgap. Loubeyre *et al.* extrapolated the observed trend and found bandgap closure and therefore metallization to occur at approximately 450 GPa, yet out of reach of static compression techniques. In 2003 the melting curve was measured up to 140 GPa and a distinct weakening of the molecular bond was found [Gregoryanz 03]. Most recently, the transition into phase IV of solid hydrogen was discovered at pressures above 220 GPa and room temperature [Howie 12]. A number of problems complicate optical measurements at very high pressures and room temperature; first and foremost however, the reactivity of hydrogen with the sample environment (diamond anvils, gasket and pressure calibrant) is the main reason for limiting previous experiments to $\sim$250 GPa [Loubeyre 02]. Figure 2.2 shows the current state of knowledge of the phase diagram of hydrogen. For further details the reader is referred to the PhD thesis by R. Howie (Edinburgh University 2013).

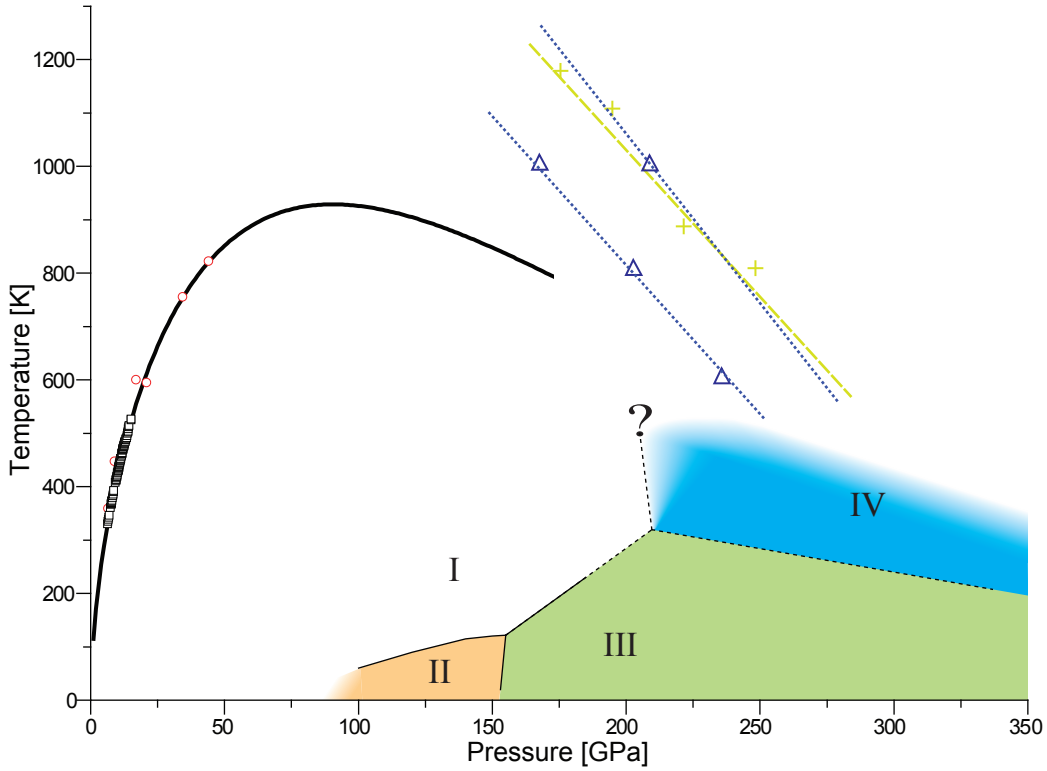


Figure 2.2: PT-Phase-diagram of hydrogen (see [Howie 12] and references therein (annexed to this thesis)). The thick solid line denotes the proposed melting curve. Coloured dashed lines with open triangles and crosses are theoretical transition boundaries between the molecular and atomic state. Thin solid lines are established phase boundaries between solid phases I, II and III. Thin dashed lines are the recently proposed phase boundaries including phase IV.

2.2 Hydrogen in Host Matrices

Hydrogen shows several very interesting reaction properties which are in many cases due to two distinct characteristics: i) Medium electronegativity and ii) small size [Fukai 05]. The small size of the hydrogen atom enables it to occupy small interstitial sites in metallic lattices. In effect, the conduction electrons of the surrounding metal screen the hydrogen nucleus (a single proton) so that it appears as a neutral atom. The medium electronegativity value of 2.2 on the other hand, describing the potential to attract an electron from a neutral atom, means that hydrogen is capable of forming various bonds with other elements [Gao 12]. Thus, hydrogen shows very high reactivity with many elements, even at lower temperatures. Depending on the electronegativity of the other element,

hydrogen may form ionic compounds (smaller electronegativity, *e.g.* with the alkali elements) or hydrogen-bonded compounds (larger electronegativity, *e.g.* the halogens). With the light group I-IV simple metals and the group III-V non-metallic elements showing comparable electronegativity, hydrogen can form covalently bonded crystals. With most heavier simple metals, hydrogen does not react [Fukai 05]. Of particular interest is the remaining group of the *d*-metals, lanthanides and actinides which have comparable electronegativity. Most of the electropositive elements in this group, the lanthanides and actinides as well as the members of the Ti- and Vd-group, readily react with hydrogen at ambient conditions (see *e.g.* [Kalita 08, Fukizawa 83]). However, a significant "hydride gap" is evident covering the row 4-6 elements between the Cr-group (6) and Cu-group (11) metals [Züttel 04]. These elements show a similar electronegativity as hydrogen (*e.g.* 2.2 for ruthenium, palladium, osmium and iridium, 2.28 for platinum and 2.54 for gold) [Gao 12]. Since reaction with hydrogen is chemically unfavourable for the late transition metals (in particular the noble metals), they are not found to form bulk hydrides at ambient conditions. High pressure causes a steep increase of the chemical potential of hydrogen and thus, most of these elements do react with hydrogen at certain conditions [Gao 12]. Nevertheless, there still remain a few metals (notably many of the noble metals) which have not been observed to form a compound with hydrogen. Figure 2.3 shows an overview of group 6-11 *d*-metals and indicates the known reactions with hydrogen.

Hydrogen may form interstitial metallic hydrides with these elements, although in most cases, high pressure and temperature is necessary to facilitate the reaction. Section 2.3 gives a comprehensive review of the *d*-metal hydrides. This section aims at giving a brief introduction to the formation mechanisms and the general properties of interstitial metal hydrides. A more detailed overview can be found in [Fukai 05]. In the following, the term *metal hydride* generally refers to interstitial metallic hydrides, unless otherwise stated.

Most metal hydrides exhibit metallic bonding and exist over a wide range of stoichiometries. The composition, sometimes also referred to as the hydrogen solubility or hydrogen content x, is defined as the hydrogen to metal atomic ratio. In some cases, the metal lattice undergoes a structural phase transition

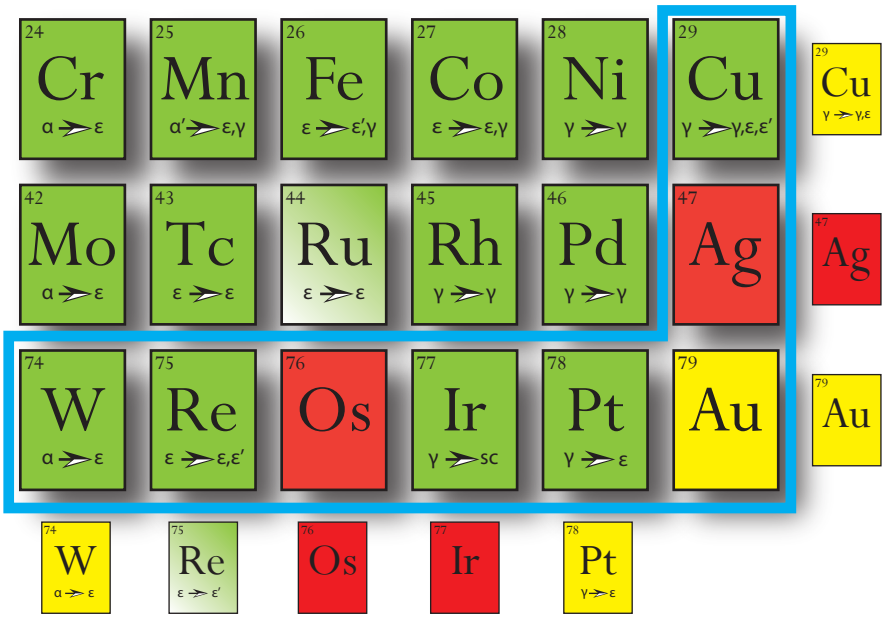


Figure 2.3: The Cr-group to Cu-group elements and their reactions with hydrogen (arrows). α denotes a *bcc* configuration, ϵ an *hcp* and γ an *fcc* configuration. Fully green fields denote the formation of a stoichiometric hydride. Ruthenium is only known to form a substoichiometric hydride with low hydrogen content, while no hydride phases are known for silver and osmium. The existence of a hydride phase in gold is in dispute (see chapter 2.3). The blue frame indicates the scope of the present work, *i.e.* elements investigated during the course of this thesis. For comparison, the state of knowledge prior to this work is included next to the respective symbols.

to accommodate interstitial hydrogen atoms. The resulting hydrides are usually fully stoichiometric (*i.e.* $x = 1$ or $x = 2$). Where the hydrogen atoms are directly incorporated into the metal lattice without the necessity for a structural change, x can be regarded as a variable dependent on the external conditions. For example, in palladium and rhenium, the hydrogen content depends on the applied pressure (see below). Generally, interstitial hydrogen can be regarded as a solid solution confined in a host matrix [Fukai 05]. Most of the metal lattices form closed-packed structures (*fcc* or *hcp*) which offer octahedral and tetrahedral interstitial sites which can be occupied by the hydrogen atoms [Züttel 04]. It was found by neutron diffraction that, in most *d*-metals, hydrogen occupies the octahedral sites [Somenkov 87].

The reaction of a hydrogen molecule with a host metal can be understood in terms of the simplified Lennard-Jones potential [Züttel 04]. At sufficiently small distances from the metal surface the hydrogen molecule feels an attractive force in form of a Van-der-Waals interaction. This leads to the molecule being physisorbed at the metal surface at a distance of approximately the radius of the hydrogen molecule. In experiments on hydride formation in the 1980s, the hydrogen content was often measured using mass-spectroscopic techniques during decomposition (see *e.g.* [Antonov 82, Antonov 83, Antonov 84, Antonov 87]). In some cases, low hydrogen contents were measured (*e.g.* in Ru and Os [Ponyatovsky 84, Antonov 04]) and attributed to low hydrogen solubilities in the metal lattices. It is more likely that comparably large amounts of hydrogen were physisorbed on the metal surface during the experiments (usually at high pressures and high temperatures) and desorbed at ambient conditions. In these instances, no actual metallic hydride was formed. In order to leave the physisorbed state and get closer to the metal, the hydrogen molecule has to overcome the dissociation barrier which in turn depends on the surface elements. Once dissociated, the hydrogen atom shares an electron with one of the host metal atoms and enters the chemisorbed state [Züttel 04]. In this state, the hydrogen atoms show high mobility and form surface compounds at sufficiently high concentrations. In the next step, the atoms can penetrate the bulk material and diffuse deeper into the lattice, occupying interstitial sites. The duration of this diffusion process is governed by prevailing kinetics which may be extremely slow at the experimentally accessible temperatures [Antonov 84]. For that reason, in many early synthesis-attempts the samples were subjected to high pressures and high temperatures for up to 24 hours before quenching to ambient pressure and liquid nitrogen temperatures [Antonov 84]. Due to sharing their valence electron with the metal atoms, the presence of hydrogen influences the band structure of the host lattice. In particular, it has been shown that the filling of the metal d-band increases by 0.5 and it is expected that the s-band filling increases by the same amount [Degtyareva 03]. By comparing the increase in atomic volume along the post-transition elements one derives a volume difference of $\Delta V \sim 4$ Å^3 per s-electron, called the valence electron volume [Degtyareva 03]. If the s-band filling increases by $\sim$0.5, a volume increase of $\sim$2 Å^3 could be expected. Indeed, it was found that the hydrogenation process causes a measurable volume

increase of the metal lattice by 2-3 Å^3 per hydrogen atom [Antonov 02, Fukai 05]. Due to that volume increase, a significant amount of stress is built up at the phase boundary between the hydrogenated and non-hydrogenated parts of the metal lattice. This stress is sometimes released by a decrepitation of microcrystalline host material or the nucleation of very small crystallites. On a larger scale this effect is known as hydrogen embrittlement [Züttel 04], although this term is not commonly used in experiments at extreme conditions due to the small amounts of material involved. However, a similar effect was observed during the formation and decomposition of tungsten hydride (see chapter 4.3). It has been shown that the volume expansion due to hydrogenation is directly proportional to the hydrogen solubility x [Ponyatovsky 84, Fukai 05]. This effect is used as an *in-situ* technique to determine the hydrogen content in x-ray diffraction experiments (see chapter 3.3.3).

One technique to overcome the dissociation barrier at the metal surface is compression to high hydrogen densities[1], where the chemical potential rises steeply [Filipek 07]. Accordingly, most d-metals form hydride phases directly form the elements at varying hydrogen pressures ranging from just under 0.1 MPa in palladium to 27 GPa in platinum and even 55 GPa in iridium (although the structure of iridium hydride is different from any other metal hydride in this group) [Filipek 07, Scheler 11b]. It was also found that, once the hydride is formed, the interstitial hydrogen is almost incompressible in most cases [Fukai 05]. This is evident from measurements of the equations of state which in most cases are equivalent to the parent material, only shifted up in volume by 2-3 Å^3 [Filipek 07]. The first studies on the equilibrium synthesis of metal hydrides at extreme conditions were conducted by Baranowski *et al.* more than 50 years ago (see review in [Baranowski 05]). However, the experimentally accessible pressures were limited to 0.3 GPa. A large amount of experimental work on the high-pressure synthesis of d-metal hydrides was accomplished in the 1980s by a Russian group around V.E. Antonov (for a review see [Antonov 02]). Using a large volume press and an *in-situ* hydrogen source, pressures up to 9 GPa could be reached. Unfortunately, in order to release hydrogen by decomposition of the source material (usually AlH_3, for a review of this material, see *e.g.* [Saitoh 08]), high

[1]The others being non-equilibrium techniques such as plasma sputtering, chemical vapor deposition or electrochemical synthesis. These techniques are not discussed in this thesis.

temperatures were always necessary. Their results form the foundation for the more recent studies on metal hydrogen systems. Diamond anvil cell technology (see chapter 3.1) has been used for the synthesis and study of metal hydrides since the mid 1990s and advances in diagnostic techniques (such as holographic notch filters, fast CCD's and third generation synchrotron radiation sources) made it possible in recent years to study these systems at pressures exceeding 100 GPa. On decompression, most metal hydrides synthesized at high pressures show a significant hysteresis effect, *i.e.* the decomposition pressure can be substantially lower than the synthesis pressure. This leaves it experimentally difficult to determine the equilibrium pressure of a hydride phase. It is an ongoing debate for the past decades whether the equilibrium pressure should be assumed closer to the decomposition pressure, the synthesis pressure or in between [Antonov 04]. In the past few years, experimental evidence points towards the conclusion, that the thermodynamic equilibrium can be found closer to the decomposition pressure. Antonov *et al.* give a phenomenological explanation for the observed hysteresis and the point of equilibrium [Antonov 04]: The large volume expansion during hydrogenation necessitates a macroscopic material flux perpendicular to the hydride phase boundary. This in turn requires elastic forces comparable to the yield strength of the material. In contrast, decomposition usually occurs by precipitation of hydrogen-depleted material of smaller volume. While this process is still considered a theory, our observations of the hydrogenation-dehydrogenation process in tungsten hydride strongly support this idea (see chapter 4.3). Therefore, the assumption of thermodynamic equilibrium close to decomposition conditions is adopted throughout this work.

It is widely accepted that the presence of interstitial hydrogen does not significantly influence the electronic or mechanical properties of the metal host lattice. Small changes to the resistivity are typical (and in fact were used in the large volume press to measure hydride synthesis) [Antonov 84]. However, hydrogen mediated superconductivity is found in several metal hydrides. First and foremost, the palladium-hydrogen system has been under thorough investigation since an increase in the superconducting transition temperature T_c by 4 orders of magnitude upon hydrogenation was found [Bashkin 03]. After the discovery of superconductivity in Pd-H in the 1970s however, no further examples

were found in the *d*-metals at near ambient conditions. In 1985, superconducting phases were discovered in the titanium-hydrogen system at pressures above 4 GPa [Bashkin 03]. In contrast, in rhenium a decrease in T_c dependent on the hydrogen content was discovered, reaching -5K/H-atom. Platinum hydride is another candidate for hydrogen mediated superconductivity at very high pressures, with T_c possibly exceeding that of palladium hydride [Scheler 11b]. More interestingly, in the late 1980s and early 1990s theories about cold fusion reached the metal hydrides and it was speculated that metal deuterides might exhibit direct fusion when compressed in a metal lattice [Baranowski 90]. However, none of these theories were ever successfully proven experimentally. Although hydrogen is usually assumed to be almost incompressible when confined in metal lattices, a few exceptions exist. Hexagonal copper hydride is known to exhibit a reduced bulk modulus and during the course of this thesis it was found that also iridium hydride is much more compressible than the parent metal (see chapter 4.4). This is thought to be caused by the unusual structure: Hydrogen does not occupy the usual interstitial sites since the metal matrix transformed into a distorted simple cubic phase.

2.3 Transition Metal-Hydrides: A Review

The following section reviews the available literature on the metal hydrides of the group 6-11 transition metals (see also Figure 2.3). In the cases of platinum, rhenium, tungsten, iridium and copper, significant progress has been achieved in the course of this thesis and the results are discussed in the corresponding sections in chapter 4. Table 2.2 at the end of this chapter summarizes some of the most important properties of the group 6-11 metal hydrides.

A) Group 6: Chromium, Molybdenum, Tungsten

A-i) Chromium

Chromium exists in the *bcc* configuration and exhibits a small solubility of hydrogen at ambient conditions. Near stoichiometric chromium hydride can be

synthesized either by electrochemical co-deposition of chromium and hydrogen or at high hydrogen pressures [Baranowski 72]. The synthesis pressure depends on the temperature and ranges from <0.2 GPa at room temperature to ∼1.8 GPa at 700 K [Baranowski 72, Ponyatovsky 84]. Upon hydrogenation, the metal undergoes a structural phase transition into the *hcp* phase with hydrogen atoms occupying the octahedral interstitial sites. This is equivalent to the NiAs-type structure which is common amongst the *d*-metal hydrides and is commonly referred to as the ϵ-phase [Antonov 02]. At T $\sim$ 80 K and atmospheric pressure, the lattice parameters of stoichiometric ϵ-CrH were determined as a = 2.717 Å, c = 4.436 Å [Ponyatovsky 84]. Interestingly, a second hydride phase, the *fcc* γ-modification, can be produced electrolytically, but does not form under equilibrium conditions [Antonov 07]. γ-CrH has a lattice parameter of a = 3.854 Å. A strong hysteresis effect between formation and decomposition pressure has been observed. It was speculated that this hysteresis is caused by the elastic stress built up during hydride formation [Ponyatovsky 84]. Thus, the equilibrium pressure separating the hydride phase from the pure metal phase should be close to the decomposition pressure. The bulk modulus of stoichiometric CrH is $B_0 = 240 \pm 7$ GPa ($B' = 5.3$), equivalent to that of pure Cr to within the error of the measurement [Filipek 07].

A-ii) Molybdenum

Molybdenum shows similar behaviour to chromium, although the pressures required for synthesis are significantly higher at 3-4 GPa (almost constant with temperature between 400 and 700 K) [Ponyatovsky 84]. The hydride exhibits near stoichiometric composition and hydride formation is accompanied by a structural phase transition in the metal lattice from the *bcc* to the *hcp* ϵ-phase [Antonov 02]. It also shows a large hysteresis between formation and decomposition. At temperatures below 100 °C, the decomposition pressures can be as low as 0.5 GPa [Antonov 04]. Molybdenum metal at ambient conditions has a lattice parameter of $a = 3.147$ Å. The stoichiometric ϵ-hydride was measured to have $a = 2.937$ Å, $c = 4.758$ Å [Somenkov 87].

A-iii) Tungsten

By means of large-volume-press techniques (i.e pressures below 9 GPa and

high temperatures), no measurable formation of a hydride phase was observed [Ponyatovsky 84, Antonov 02]. However, a drastic change in the diffraction pattern of tungsten in a dense hydrogen medium was observed at pressures above 25 GPa and room temperature [Kawamura 05]. Apart from the metal host structure (*hcp*), no further properties, such as hydrogen content, mechanical or electronic properties were investigated. At the same time as our work was carried out, Zaleski-Ejgierd *et al.* published a thorough theoretical study on tungsten hydride, in particular targeting higher hydrogen concentrations [Zaleski-Ejgierd 12]. Their work was motivated by the observation of the formation of tungsten hydride in experiments on silane at high pressures [Strobel 09]. Several structures with stoichiometries up to WH_8 were predicted but only the hexagonal ϵ modification was experimentally found. Our findings, in particular the change in stoichiometry (fractional synthesis of WH_2) and the formation of a nanomaterial are discussed in detail in chapter 4.3.

B) Group 7: Manganese, Technetium, Rhenium

B-i) Manganese

Manganese exists in various configurations at ambient pressures, amongst others the *fcc* γ-Mn and *bcc* δ-Mn. At high pressures (p>0.4 GPa) it forms a hydride with substoichiometric hydrogen contents ranging from $x = 0.65$ to $x = 0.96$ in the *hcp* ϵ-phase [Antonov 02]. This hydride is stable when quenching to ambient conditions, but decomposes at temperatures exceeding 500 K. At T>700 K, the decomposition pressure approaches the synthesis pressure at close to 1 GPa [Ponyatovsky 84]. At these temperatures and pressures above 1 GPa, it also forms a γ-hydride phase with $x < 0.5$ and at pressures below 1 GPa solid solutions of hydrogen in the α and β modifications of Mn. In the ϵ phase the hydrogen sublattice forms a superstructure similar to the anti-CdI_2 type structure in which hydrogen occupies distinct intermediate layers in the metal host lattice [Antonov 02]. At hydrogen contents of $x > 0.83$, the layered structure breaks up and the hydride undergoes an isomorphic phase transition into a deficient NiAs type structure where the hydrogen atoms are randomly distributed over the available octahedral interstitial sites. At ambient conditions, the lattice

parameters of the near stoichiometric hydride ($x \sim 0.95$) were measured to be $a = 2.70$ Å, $c = 4.37$ Å [Ponyatovsky 84]. Depending on the hydrogen content and structural modification, the hydride phases of Mn show slightly different bulk moduli compared to pure Mn: Pure (α) Mn has $B_0 = 104.1 \pm 12$ GPa and $B' = 13.3 \pm 3.8$. ϵ-Mn-H with $x = 0.84$ was measured to have $B_0 = 92.7 \pm 8.1$ GPa and $B' = 8.77 \pm 1.78$, while for γ-Mn-H with $x = 0.64$ values of $B_0 = 84.1 \pm 9.6$ and $B' = 8.77$ were found [Filipek 07]. However, the large B' are quite unusual and these results should be treated with caution.

B-ii) Technetium

At pressures above 0.2 GPa, technetium forms the first (ϵ_1) of two known hydride phases by undergoing an isomorphous phase transition and incorporating hydrogen atoms into the octahedral interstitial sites of the *hcp* lattice. The hydrogen content reaches $x = 0.5$ by 0.7 GPa. At P$\sim$1 GPa, the $\epsilon_1 \rightarrow \epsilon_2$ transition occurs and hydrogen content increases to $x \sim 0.8$ at 2 GPa [Antonov 02]. Both hydride phases are stable at ambient conditions with slightly reduced hydrogen content. Decomposition occurs when heating to above 350 K [Ponyatovsky 84]. The ϵ_1-phase with $x \sim 0.45$ exhibits the layered anti-CdI_2 structure while the ϵ_2-phase stabilizes with $x \sim 0.7$ in a deficient NiAs-type structure. Technetium is superconducting with $T_c \sim 7.85$ K. In contrast to palladium, increasing hydrogen content caused a decrease in critical temperature to below 1.5 K at $x > 0.2$ [Bashkin 03]. Interestingly, on cooling down, two steps in magnetic susceptibility characteristic for a superconducting phase transition were observed. This was interpreted as the coexistence of two hydride phases with different T_c [Bashkin 03]. The pure *hcp* phase of Tc has lattice parameters of $a = 2.740$ Å, $c = 4.397$ Å. For the compositions $x = 0.69$ and $x = 0.45$, the lattice parameters were measured to be $a = 2.838$ Å, $c = 4.465$ Å and $a = 2.801$ Å, $c = 4.454$ Å, respectively [Somenkov 87].

B-iii) Rhenium

Rhenium hydride was first synthesized in the large volume press which requires high temperatures to release hydrogen from a source material [Antonov 83]. At temperatures above 500 K and pressures above 3 GPa, rhenium incorporates hydrogen into its *hcp* lattice reaching a hydrogen solubility of $x \sim 0.23$ by 9

GPa [Antonov 02]. For this composition, the lattice parameters were determined to be $a = 2.801$ Å, $c = 4.465$ Å, compared to $a = 2.761$ Å, $c = 4.458$ Å for pure Re [Somenkov 87]. At temperatures below 0 °C the hydride appeared to be stable at ambient pressure [Ponyatovsky 84]. It was further found that the critical temperature for superconductivity was reduced from $T_c = 1.7$ K for pure rhenium to ∼0.5 K for the hydride with $x \sim 0.23$ [Antonov 87]. Neutron diffraction data indicated that at this content, the hydrogen atoms are randomly distributed over the octahedral interstitial sites [Shilstein 85]. At room temperature, Re-H can be formed at pressures above 5.3 GPa and exhibits a higher hydrogen content [Atou 95, Besedin 98]. At pressures above 8.6 GPa, the hydrogen content saturates at $x \sim 0.38$ [Atou 95]. This estimate is based on the measured volume expansion of 2.1 Å^3 per hydrogen atom, which was found by neutron diffraction [Shilstein 85]. The interstitial hydrogen was found to be incompressible at pressures up to 123 GPa [Besedin 00]. Similarly to substoichiometric $TcH_{0.45}$ and $CoH_{0.38}$, $ReH_{0.38}$ formed at room temperature was later also found to exhibit a layered superstructure [Kawamura 04]. In the deficient anti-CdI_2-type structure, hydrogen atoms occupy only every second layer of the available octahedral interstitial sites. During the course of this work, it was found that the layered structure breaks down at temperatures above 150 °C and pressures above 20 GPa [Scheler 11a]. After an isomorphous transition into the deficient NiAs-type structure, the hydrogen content was found to increase with pressure up to $x \sim 0.85$ (see chapter 4.2).

C) Group 8: Iron, Ruthenium, Osmium

C-i) Iron

Similar to manganese, iron forms three types of hydrides. The stoichiometric double-*hcp* (*dhcp*) ϵ'-phase forms at room temperature and pressures above ∼3.5 GPa and is stable up to at least 64 GPa [Badding 91]. At pressures above 5 GPa and temperatures exceeding 600 K, the *fcc* γ-phase of iron hydride with as of yet unknown hydrogen content stabilizes [Antonov 02]. In the simple *hcp* ϵ-phase, hydrogen atoms are randomly distributed over the available interstitial sites. This hydride is stable at ambient pressure and temperatures below 150

K [Ponyatovsky 84]. At T=80 K, the lattice parameters were determined to be $a = 2.686$ Å, $c = 4.380$ Å [Ponyatovsky 84]. Although pure iron undergoes a structural phase transition from the *bcc* to the *hcp* phase between 15 and 20 GPa, this does not have any effect on the *dhcp* ϵ'-phase of iron hydride. A Vinet-type fit to the equation of state of iron hydride revealed a bulk modulus of $B_0 = 121 \pm 19$ GPa, $B' = 5.31 \pm 0.9$ and a zero pressure volume of $V_0 = 55.6 \pm 0.5$ Å^3 [Badding 91]. In comparison, pure *hcp* iron has $V_0 = 22.35 \pm 0.03$ Å^3, $B_0 = 160.2 \pm 2.1$ GPa, $B' = 5.82 \pm 0.08$.

C-ii) Ruthenium

It has been found that hydrogen can be incorporated in small quantities into the ruthenium *hcp* lattice, reaching an approximate hydrogen content of $x \sim 0.03$ by 9 GPa and temperatures exceeding 550 K [Antonov 02]. Further information on hydride phases in this element are scarce and it can be assumed that no measurements at higher pressure and/or at room temperature have been carried out. The maximum pressure of 9 GPa in previous experiments was imposed by the limits of the type of large volume press used. In particular, since all measurements of hydrogen contents were carried out at ambient conditions after quenching, it can be expected that the achievable hydrogen content is somewhat higher, although the hydride phase is not stable at ambient conditions. In fact, a recent theoretical study finds that ruthenium hydride forms in the *fcc* configuration and is stable above 10 GPa [Gao 12].

C-iii) Osmium

According to [Ponyatovsky 84] and [Antonov 84], the osmium-hydrogen system is analogous to the ruthenium-hydrogen system with the sole difference of an even lower hydrogen content. The maximum hydrogen content recorded for osmium hydride is $x \sim 0.003$ at pressures up to 9 GPa. Resistivity measurements were used to identify the formation of a hydride phase and a synthesis pressure of $\sim$2 GPa was found [Antonov 84]. In the course of this thesis, osmium was subjected to hydrogen pressures above 80 GPa at room temperature. No significant uptake of hydrogen was discovered (see chapter 4.6). It can be assumed that the finite hydrogen content measured in the large volume press is mainly due to chemisorbed hydrogen on the metal surface.

D) Group 9: Cobalt, Rhodium, Iridium

D-i) Cobalt

At pressures below 7 GPa, hydrogen is directly incorporated into the hexagonally closed packed metal lattice without it undergoing a structural transition. The hydrogen content rises monotonically with pressure and reaches a maximum of $x \sim 0.6$ at 7 GPa [Antonov 02]. At higher pressures and temperatures between 500 and 600 K, the metal lattice transforms into the *fcc* γ-structure and a stoichiometric hydride is formed [Ponyatovsky 84]. At hydrogen contents $x < 0.26$, the hydrogen atoms are randomly distributed over the host lattice. Interestingly however, at higher concentrations, the hydrogen atoms form layered sublattices and with that create a superstructure. At $x = 0.34$, they occupy every third layer and at $x > 0.38$ every second layer. As in rhenium, this ordered arrangement causes the intermediate layers of metal atoms to deviate from their equilibrium positions. Layers of Co atoms without a hydrogen layer in between them move closer together while those with a (deficient) hydrogen layer separating them are pushed apart [Antonov 02]. X-ray diffraction experiments on recovered Co-H with $x \sim 0.6$ revealed a volume increase of ~ 1.8 Å^3 per atom extrapolated to full stoichiometry [Ponyatovsky 84].

D-ii) Rhodium

At pressures above 3.5 GPa at room temperature, hydrogen atoms are incorporated into the *fcc* lattice of rhodium and form a near stoichiometric hydride [Antonov 02]. The transition pressure depends on temperature and increases monotonically to 5 GPa near 700 K. The hydrogenation process takes place instantaneously [Antonov 84] and causes a lattice expansion from $a = 3.803$ Å to $a = 4.010$ Å [Somenkov 87]. Decomposition at ambient pressure begins at temperatures above 170 K [Ponyatovsky 84]. Very recently, a second phase of rhodium hydride with high hydrogen content was discovered [Li 11]: At pressures above 8 GPa, the metal undergoes another transition and forms the fluorite-type *fcc* RhH_2. This is the first di-hydride discovered in the platinum-group metals. Here, hydrogen atoms move from the octahedral interstitial sites to the

tetrahedral sites. This phase was quenchable to ambient pressure at very low temperatures (6.1 K) and a third order Birch-Murnaghan fit to the equation of state revealed a zero-pressure volume of $V_0 = 81.7 \pm 0.2$ Å^3 and a bulk modulus of $B_0 = 194 \pm 3$ GPa [Li 11].

D-iii) Iridium

Iridium (as well as platinum) was subjected to pressures reaching 9 GPa and temperatures above 500 K without measuring any significant uptake of hydrogen [Ponyatovsky 84]. A small release of hydrogen from a sample subjected to these conditions after quenching was interpreted as hydrogen adsorption on macroscopic defects and the sample surface [Antonov 84]. According to theoretical calculations, iridium hydride should form in the *fcc* configuration [Gao 12]. However, no pressure of formation is given in this study. The hydride is supposedly stable at 100 GPa. In the course of this thesis it was found that iridium forms a hydride at pressures above 55 GPa (see chapter 4.4). This novel hydride phase exhibits an unusual crystal structure that was indexed in the $Pm\bar{3}m$ spacegroup (simple cubic) with hydrogen atoms occupying the 3c Wyckoff positions in the unit cell. Therefore, iridium hydride reaches an unrivalled hydrogen content of $x = 3$ although it can not be regarded as an interstitial hydride.

E) Group 10: Nickel, Palladium, Platinum

E-i) Nickel

Nickel hydride exhibits the same metal host lattice structure (*fcc*) as pure Nickel. The hydride can be synthesized electrolytically or under equilibrium from the elements at high pressures at p<0.5 GPa and room temperature [Baranowski 05]. The review article [Baranowski 05] gives comprehensive background information not only on the history of nickel hydride, but also the development of high-pressure techniques and applications. Hydride formation is characterized by a sudden increase in hydrogen content from very low values ($x = 0.01$) to $x \sim 1$. Decomposition takes place at ∼0.2 GPa below synthesis pressure [Baranowski 05]. Compared to pure Ni, the stoichiometric hydride shows an increase in lattice

parameter from $a = 3.524$ Å to $a = 3.740$ Å [Somenkov 87]. The hydride is unstable at ambient conditions and decays over the period of a few days [Ponyatovsky 84]. The bulk modulus of stoichiometric NiH is with $B_0 = 195 \pm 5$ GPa and $B' = 5.3$ slightly higher than that of pure Ni ($B_0 = 187 \pm 5$ GPa) [Filipek 07]. It is stable up to at least 123 GPa [Besedin 98, Besedin 00].

E-ii) Palladium

Palladium is exceptional in the group 6-11 elements. It was discovered in 1866 and hydrogen pressures of just 0.007 atmospheres are sufficient to form the *fcc* γ_2 hydride with a hydrogen content $x \sim 0.61$ [Baranowski 72, Ponyatovsky 84, Wolf 93, Baranowski 05]. This is usually referred to as the β-phase of palladium hydride. Despite the rapid increase of hydrogen solubility at low pressures, significant pressures p>1 GPa are necessary to reach $x \sim 1$ [Antonov 02]. No other transformation has been observed at pressures up to 9 GPa and temperatures above 500 K [Antonov 84]. Stoichiometric PdH has lattice parameter $a = 4.090$ Å [Schirber 75]. Palladium is also the only known element in the group 6-11 transition metals that undergoes a paramagnetic-to-superconducting transition upon hydrogenation. With a hydrogen content of $x \sim 1$, the critical temperature reached 9 K for PdH and 11 K for PdD, an increase by nearly 5 orders of magnitude ($T_c < 4 \cdot 10^{-4}$ K for pure Pd) [Hemmes 89, Bashkin 03]. Interestingly, T_c depends directly on the hydrogen content with $T_c \sim 1$K at $x \sim 0.8$. The bulk modulus of palladium hydride ($x \sim 0.8$) was measured as $B_0 = 130 \pm 5$ GPa and $B' = 4.8$ [Tkacz 90], equivalent to that of pure palladium to within the error of the measurement. This strong dependence of T_c on the hydrogen content led to the assumption that PdH_x with $x > 1$ could be a high-temperature superconductor [Tripodi 04]. However, this idea is heavily disputed [Baranowski 07, Tripodi 09].

E-iii) Platinum

In the first major reviews on the transition metal hydrides [Ponyatovsky 84] and also in more recent articles and books [Antonov 02, Fukai 05], platinum was regarded incapable of forming a hydride phase. In fact, it requires pressures above 27 GPa to synthesize stoichiometric PtH from the elements [Hirao 08, Scheler 11b]. Of particular interest are the potential superconducting

properties of PtH. While platinum is superconducting in the low mK regime [König 99], observations in experiments involving silane indicate that PtH might be superconducting at temperatures up to 17 K [Degtyareva 09, Eremets 08]. Our own calculations as well as other theoretical studies targeting this material also found superconductivity emerging at very high pressures [Kim 11, Zhou 11]. However, this idea is not altogether new as the possibility of PtH being a high-temperature superconductor has been discussed before [Papaconstantopoulos 80]. A recent theoretical study finds several stable structures for Pt-H, amongst others our experimentally observed $P6_3/mmc$ (*hcp*) which was predicted to stabilize at pressures above 42.9 GPa [Gao 12]. These findings are discussed in detail in chapter 4.1.

F) Group 11: Copper, Silver, Gold

F-i) Copper

Some confusion about copper hydride seems to exist in the literature. In 2007, it was reported that CuH has never been synthesized from the elements [Filipek 07] although this was achieved in 2004 in the diamond anvil cell at pressures above 14 GPa [Burtovyy 04]. Traditionally, CuH is synthesized in the hexagonal wurtzite form (corresponding spacegroup $P6_3mc$ [Goedkoop 55]) as the result of a reaction between hypophosphorous acid and copper sulphate [Filipek 07]. It is unstable at ambient conditions but can be stored permanently at -5 °C [Fitzsimons 92]. In contrast to other hydrides in the group 6-11 transition metals, the bonding between Cu and H is described as being partly covalent and/or ionic [Filipek 07]. The hydride synthesized by Burtovyy and Tkacz [Burtovyy 04] however shows an *fcc* crystalline structure in which hydrogen is directly incorporated into the metal matrix. This has since then not been observed by anyone else[2]. High-pressure studies on chemically synthesized copper hydride revealed a drastic change in the elastic properties [Filipek 07]. While pure copper has a bulk modulus of $B_0 = 137.4$ GPa, $B' = 5.52$ ($V_0 = 11.81$ Å^3), CuH was found to exhibit $B_0 = 72.5$

[2]Private communication with M. Tkacz (Institute of Solid State Physics, Chernogolovka, Russia): The copper sample used in their experiments was dehydrogenated Cu in order to obtain pure samples. He speculates that the history of the sample plays a role whether an *fcc* or *hcp* hydride is formed.

GPa, $B' = 2.7$ ($V_0 = 16.75$ Å^3, fitted with a simple Murnaghan equation of state). This difference can be explained by the different bonding of the hydrogen in the metal. Our results on the copper-hydrogen system are presented in chapter 4.5.

F-ii) Silver

Silver is the only row-4 metal in the considered group of elements for which a bulk hydride phase has never been reported. A recent theoretical study predicts the formation of Ag-H in the *fcc* configuration with hydrogen occupying octahedral sites [Gao 12]; however, no pressure of formation is given. Our experiments on silver up to 87 GPa did not reveal any signs of hydrogenation.

F-iii) Gold

The synthesis of gold hydride was first reported in 1982 [Antonov 82]: Synthesis was observed after the sample was subjected to pressures of 5 GPa and temperatures of $\sim$ 700 K for 1 hour. X-ray analysis of the recovered material showed a complex crystal structure and the optical appearance of the sample changed to a grey-white colour with a brittle surface. Although the exact crystal structure was not solved, an orthorombic unit cell with dimensions $a = 6.80$ Å, $b = 9.61$ Å and $c = 7.85$ Å was fitted to the data [Antonov 82]. However, to date, the existence of gold hydride is in dispute in the material science and high-pressure community. A recent theoretical study found no evidence that gold can form a hydride at pressures accessible by current diamond anvil cell techniques (*i.e.* up to $\sim$350 GPa) [Gao 12]. Apart from the study from 1982, no further experimental evidence for the synthesis of gold hydride is known[3]. It is speculated that this is mainly due to the large electronegativity of Au (2.54) and the accordingly high dissociation barrier for H_2 at the metal surface.

[3]Private communication with T. Strobel (Carnegie Inst., Washington, USA): A reaction between gold and hydrogen was apparently observed at pressures above 60 GPa. However, no more details are known. We were not able to replicate these results and found no reaction up to 115 GPa.

Table 2.2: Important properties of the *d*-metal hydrides. ϵ-phases denote *hcp* metal host lattices, γ-phases *fcc* metal host lattices. *w*-CuH denotes the wurtzite-type structure of copper hydride. Lattice parameters are given at ambient conditions, except were stated otherwise. B_0 is the zero-pressure bulk modulus (given where available). Where no temperature is given for synthesis conditions, synthesis takes place at room temperature.

	Hydride	x	lattice parameter [Å]	Synthesis	B_0 [GPa]
Cr	ϵ-CrH	1	$a = 2.717$ $c = 4.436$	0.2 GPa	240 ± 7
	γ-CrH	1	$a = 3.854$	n.a.	
Mo	ϵ-MoH	1.05	$a = 2.937$ $c = 4.758$	> 3 GPa	
W	ϵ-WH	1	$a = 2.886$ (25.5 GPa) $c = 4.604$	25 GPa	
Mn	ϵ-MnH	0.83	$a = 2.692$ $c = 4.355$	>0.4 GPa	92.7 ± 8.1
	ϵ-MnH	0.95	$a = 2.70$ $c = 4.37$		
Tc	ϵ-TcH	0.69	$a = 2.838$ $c = 4.465$	0.2 GPa	
	ϵ-TcH	0.45	$a = 2.801$ $c = 4.454$		
Re	ϵ_1-ReH	0.23	$a = 2.801$ $c = 4.465$	5.2 GPa	
Fe	ϵ'-FeH	1	$a = 2.679$ $c = 8.77$	3.5 GPa	121 ± 19
Ru	ϵ-RuH	0.03	$a = 2.705$ $c = 4.278$	9 GPa, 620 K	
Co	ϵ-CoH	0.26	$a = 2.544$ $c = 4.116$		
	γ-CoH	1		6 GPa, > 500 K	
Rh	γ_1-RhH	1	$a = 4.010$	3.5 GPa	
	γ_2-RhH_2	2	$a = 4.339$	8 GPa	194 ± 3
Ir	IrH_3	3	$a = 2.691$ (55.8 GPa)	55 GPa	190 ± 3
Ni	γ-NiH	1.05	$a = 3.740$	0.5 GPa	195 ± 5
Pd	γ-PdH	1	$a = 4.090$	> 1 GPa	
	γ-PdH	0.8		> 0.007 GPa	130 ± 5
Pt	ϵ-PtH	1	$a = 2.783$ (27.5 GPa) $c = 4.742$	27 GPa	310 ± 10
Cu	*w*-CuH	1	$a = 2.81$ $c = 4.61$	n.a.	72.5
	ϵ-CuH	0.5	$a = 2.532$ (21.1 GPa) $c = 4.214$	18.6 GPa	140 ± 5
	γ-CuH	?		14 GPa	

Chapter 3

Review of High-Pressure Equipment and Techniques

This chapter reviews the high-pressure techniques that were employed in this work to study metal-hydrogen systems at extreme conditions. In particular, the diamond anvil cell, pressure calibration techniques and aspects of *in-situ* x-ray diffraction are discussed. Supporting techniques, such as Raman spectroscopy, electron microscopy and focused ion beam applications, are briefly introduced. This chapter is *not* intended to give a comprehensive overview of high-pressure techniques.

3.1 The Diamond Anvil Cell

The diamond anvil cell (DAC) has been the tool of choice for experiments at very high pressures for the past 50 years. A review of its history and applications is given in [Bassett 09] and in [Feng 10] for low-temperature applications. The principle is based on the fundamental definition of pressure as force per area. Diamonds are shaped (usually mechanically polished) into pointed anvils with top culets ranging in diameter from a few hundred to just over 10 μm. Figure 3.1A shows a schematic drawing of the working principle of a DAC. The two pointed anvils are aligned opposing each other. With a sample confined between them, very high pressures can be generated by externally exerting a force on the diamonds. The maximum pressure achievable is determined by several factors,

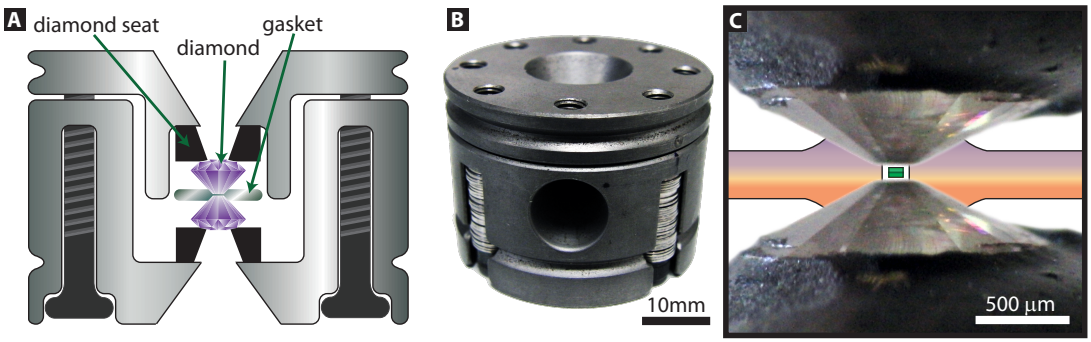


Figure 3.1: A) Schematic drawing of a typical DAC. B) Photograph of a closed symmetric DAC ("doughnut" type). C) Close-up schematic of the sample confined between the gasket (drawing) and the two diamond anvils.

such as overall geometry of the pressure-cell, the size and shape of the diamonds and the sample itself. The sample is sealed from the environment by a metal gasket. In this thesis, only rhenium gaskets were used, although tungsten and stainless steel gaskets are widely used as well. The symmetric "doughnut"-type cell (see Figure 3.1B) has been used almost exclusively throughout this thesis (for list of experiments see Table A.2). The Betsa-type and modified Gregoryanz-Guillaume (GG)-type cell have been used occasionally. The long piston-cylinder cell is well suited to reach the highest static pressures and was extensively used in the experiments described in [Howie 12]. Other purpose-built cell types have emerged over the years but are not discussed in further detail here (see *e.g.* [Kamenev 07, Gavriliuk 09]).

The DAC owes its popularity mainly to the properties of diamond which make this a highly versatile tool [Bassett 09]: Diamond is not only the hardest known material, it is also transparent to infrared and visible radiation as well as x-rays. In particular, single crystal diamonds that are aligned properly in a monochromatic x-ray beam only show minimal absorption as long as no, or only a few, crystal planes are in Bragg condition. Furthermore, because of diamond's electrical and thermal properties, it is possible to conduct *in-situ* measurements of specific heat, resistivity and susceptibility inside a DAC (see *e.g.* [Gao 05]). Infrared laser heating can be used as well as external resistive heating in order to study samples at very high temperatures [Bassett 09]. A full description of the available high-pressure techniques involving the DAC is out of the scope of this

introductory chapter.

One of the main limiting factors for the achievable pressures are size and in particular shape of the used anvils. Typically, with flat-culet 250 μm diamonds, pressures between 50 and 80 GPa are possible, with a maximum pressure of $\sim$100 GPa for 150 μm culets. For higher pressures, single or double beveled diamonds are used. These geometries can be polished mechanically and are widely used. More recently, laser shaped diamonds with arbitrary geometry[1] became available [Okuchi 09]. In this thesis, both flat-culet and beveled diamonds were used.

Rhenium foil of 200 or 250 μm thickness was used exclusively as a gasket material throughout this work. Although rhenium reacts with hydrogen at considerably lower pressure than iridium or tungsten, it possesses ideal properties as a gasket material. It has a very high bulk modulus (370 GPa) but is at the same time more ductile than tungsten or iridium. For gasket preparation, the Re-foil is thinned between the two anvils to form a tight indent with 20-30 μm thickness. The gasket hole which will contain the sample during the experiment is subsequently either drilled using an infrared-YAG laser or, on smaller length scales, using focused ion beams (see chapter 3.4.4 and [Orloff 00]). Figure 3.2 shows the gasket preparation process.

A metal sample is subsequently placed inside the sample volume (see Figure 3.2). In order to guarantee hydrostatic conditions, the excess volume is filled by a pressure transmitting medium (PTM). Throughout this thesis, gaseous hydrogen was loaded at an initial pressure of 1000-2000 bar into the sample volume. This facilitated direct reactions between the metals and hydrogen while excess hydrogen surrounding the sample acted as the PTM. Other PTM are *e.g.* methanol-ethanol mixtures, silicone oil or inert gases such as helium or argon [Klotz 09]. A description of a gas-loading system is given in [Machida 10]. The DAC is placed in a high-pressure cylinder, connected to a two-stage gas compressor[2]. The remaining air inside the cylinder is replaced with hydrogen compressed to the desired pressure (maximum 2000 bar). The initially open cell

[1] See for example the novel laser shaped concave diamonds offered by Almax Industries: www.almax-easylab.com

[2] Nova Swiss diaphragm compressor, see www.novaswiss.ch

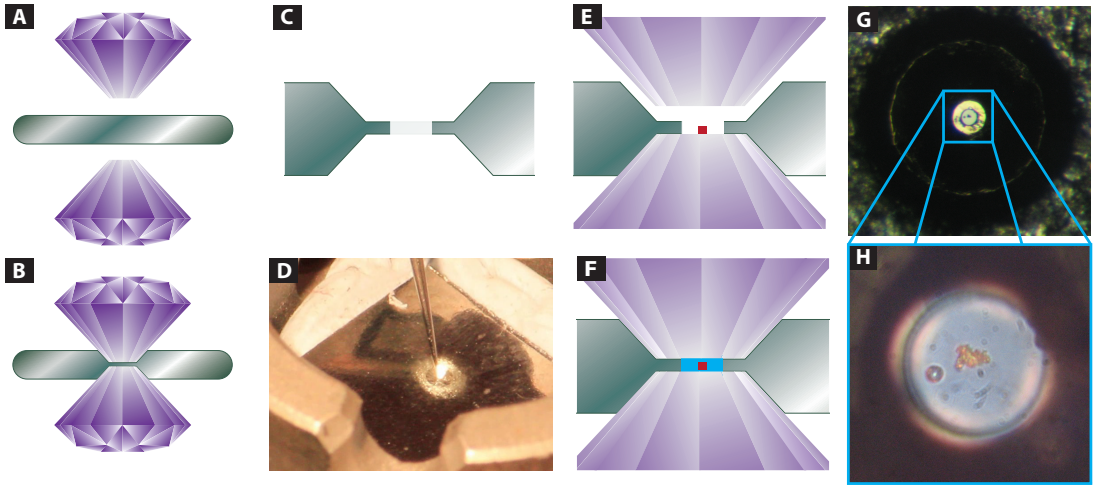


Figure 3.2: Gasket Preparation: A) A sheet of Re is placed between the aligned diamonds. B) The diamonds are pressed into the metal to create an indent. C) A centered hole is drilled into the indent. D) The metal sample is placed with a sharp needle in the hole. E) The cell is closed with one diamond leaving a small gap. F) Air in the cell is replaced with hydrogen gas and the cell is closed. G)-H) Optical micrograph of the sample hole taken through the diamonds. The metal sample and a ruby-sphere can be seen in the 50 μm hole.

is then closed through an external mechanical system and the hydrogen inside the sample volume further compressed to >1 GPa to ensure secure sealing (see Figure 3.2F). In earlier experiments (see *e.g.* the review article [Antonov 02]), *in-situ* hydrogen sources such as AlH_3 or $LiAlH_4$ were used. These release hydrogen in a decomposition process at high temperatures. The disadvantages include the necessity for separating the sample from the hydrogen source and low available amounts of hydrogen. The properties of these materials and other hydrogen sources are reviewed in [Chen 02, Chellappa 06, Saitoh 08, Ares 09].

3.2 Pressure Scales

Of fundamental importance is accurate determination of the applied pressure within the sample volume. Several techniques have been developed over the years which are applicable to varying pressure ranges and accuracies. The ubiquitous ruby pressure scale can be used up to pressures of ~80 GPa at room temperature, above which the fluorescence signal usually becomes too weak. The Raman shifts

of diamond and hydrogen have been developed into pressure scales in the past few years and are used up to the highest pressures. In x-ray diffraction experiments, the equation of states for known materials is used to reliably determine pressure. All of these techniques have been used in this work. It should be noted that this section is intended to give an overview and the necessary practical details in order to use the introduced pressure standards. For full reviews, the reader is referred to referenced literature.

3.2.1 The Ruby Pressure Scale

A comprehensive review of ruby under pressure can be found in [Syassen 08]. Ruby, a chromium doped variety of corundum (aluminium oxide Al_2O_3:Cr^{3+}), exhibits distinct fluorescent emission lines, called the R1 and R2 lines. The two lines correspond to the ^{2}E excited state of the Cr^{3+} ion. The energy level is split due to spin-orbit coupling, leading to a separation of the two lines by $\Delta R_{12} = 29\text{cm}^{-1}$ [Syassen 08] (see Figure 3.3A). The broad absorption lines of the $^4T_2$ (U) and $^4T_1$ (Y) states (which cause the red, pink appearance of ruby) decay into the ^{2}E state which has a relatively long lifetime of $\sim$4 ms. At ambient conditions, these lines are observed at $\lambda_{R1} = 694.25$ nm and $\lambda_{R2} = 692.86$ nm. A ruby fluorescence spectrum is shown in Figure 3.3B.

The relatively small shift of the R-lines with pressure of only 0.365 nm/GPa at pressures below 10 GPa, the ease of use and the relative inertness of ruby make the ruby pressure scale (RPS) the most widely used [Datchi 07]. Since the intermediate U and Y absorption bands shift to higher energies with increasing pressures, it becomes inefficient to populate the R-lines with green lasers. As a consequence it can be more efficient to use a red laser at higher pressures to excite the $^2T_1$ state which also decays into the ^{2}E states [Syassen 08]. Furthermore, at higher pressures, the frequency shift deviates from linearity. There is up to now no fundamental theory describing and calibrating the RPS at higher pressures. The most widely used method to calibrate the RPS experimentally is by measuring the R-line shift and the volume of a known compound simultaneously by x-ray diffraction (see also method described in the following section). The known equation of state of the calibration material is used to determine the pressure

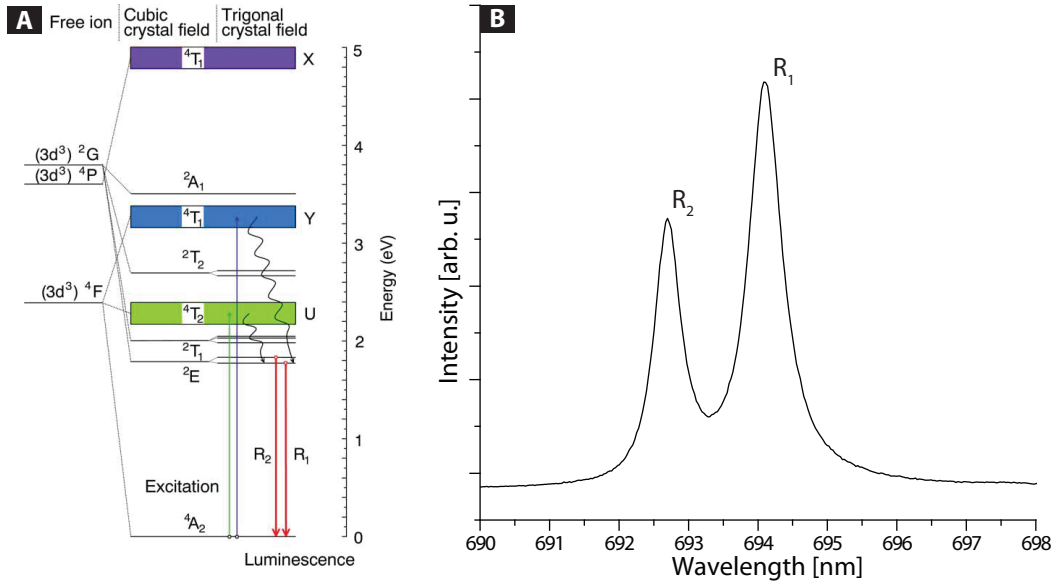


Figure 3.3: A) Energy levels in the Cr^{3+} ion, taken from [Syassen 08]. B) Fluorescence spectrum from ruby showing the R_1 and R_2 lines.

accurately for a given shift of the R-lines. However, since the equation of state of any material can also only be known to a certain accuracy, this calibration method becomes unreliable at very high pressures. Several approaches to reliably determine the equation of state are discussed in [Syassen 08]. A more detailed introduction at this point is out of the scope of this work.

The two calibrations developed independently by Holzapfel [Holzapfel 05] and Dorogokupets *et al.* [Dorogokupets 07b] offer to date the best consistency with other pressure scales and in particular with equations of state of various materials at higher pressures [Datchi 07].
The calibration proposed in [Holzapfel 05] relates pressure and wavelength as

$$P = \frac{A}{B+C}\left[\exp\left[\frac{B}{B+C}\left(1-\left(\frac{\lambda}{\lambda_0}\right)^C\right)-1\right]\right] \tag{3.1}$$

with $A = 1845$ GPa, $B = 14.7$ and $C = 7.5$.
The relation in [Dorogokupets 07b] has the simpler form

$$P = 1884\left(\frac{\Delta\lambda}{\lambda_0}\right)\left[1+5.5\left(\frac{\Delta\lambda}{\lambda_0}\right)\right] \tag{3.2}$$

3.2.2 Equations of State as Pressure Scales

The measurement of the equations of state (EoS) has only been used as a secondary pressure scale in this thesis. In most cases, the equation of state of the parent metal was used to establish a first estimate of the pressure during XRD experiments or to derive the hydrogen content by deviation from the known EoS (see chapter 3.3.3). In this section, the EoS for various metals are given that were investigated in the course of this thesis. Furthermore, the EoS of hydrogen is given. Despite the extremely small scattering cross section, the hydrogen Bragg peaks can be seen in high-resolution XRD patterns if there is no other reflection in the vicinity. The Vinet EoS [Vinet 87] is nowadays the most widely used:

$$P = 3B_0 \left(\frac{V}{V_0}\right)^{-2/3} \left[1 - \left(\frac{V}{V_0}\right)^{1/3}\right] \exp\left(\frac{3}{2}(B' - 1) \cdot \left[1 - \left(\frac{V}{V_0}\right)^{1/3}\right]\right) \tag{3.3}$$

Table 3.1: Parameters for the equations of state for the materials investigated in this work. V_0 is given per single atom, in the case of hydrogen per hydrogen molecule.

Element	V_0 [Å^3]	B_0 [GPa]	B'	Reference
W	15.862	298.3(3.6)	3.81(10)	[Dewaele 04]
Re	14.713	372	4.05	[Cynn 02]
Os	13.978	462(12)	2.4(5)	[Cynn 02]
		421(3)	4	[Armentrout 10]
Ir	14.145	383(14)	3.1(8)	[Cynn 02]
Pt	15.095	275.3(2.0)	4.78(8)	[Dewaele 04]
		277.3	5.12	[Dorogokupets 07a]
Cu	11.810	135.1(1.1)	4.91(5)	[Dewaele 04]
		137(4)	5.5(3)	[Wang 09]
Ag	17.021	103.9(1.4)	5.78(9)	[Dewaele 08]
	17.057	89.8(1.3)	5.92(7)	[Akahama 04a]
Au	16.962	172.5(1.4)	5.40(8)	[Dewaele 04]
		167.0	5.90	[Dorogokupets 07a]
H_2	42.231	0.162	6.813	[Loubeyre 96]

Table 3.1 lists the parameters for the EoS of the metals tungsten, rhenium, osmium, iridium, platinum, copper, silver and gold as well as molecular hydrogen. Figure 3.4 shows the corresponding P-V relations in the metals up to a pressure of 200 GPa while Figure 3.5 shows the P-V relation for hydrogen and the according development of the observable d-spacings.

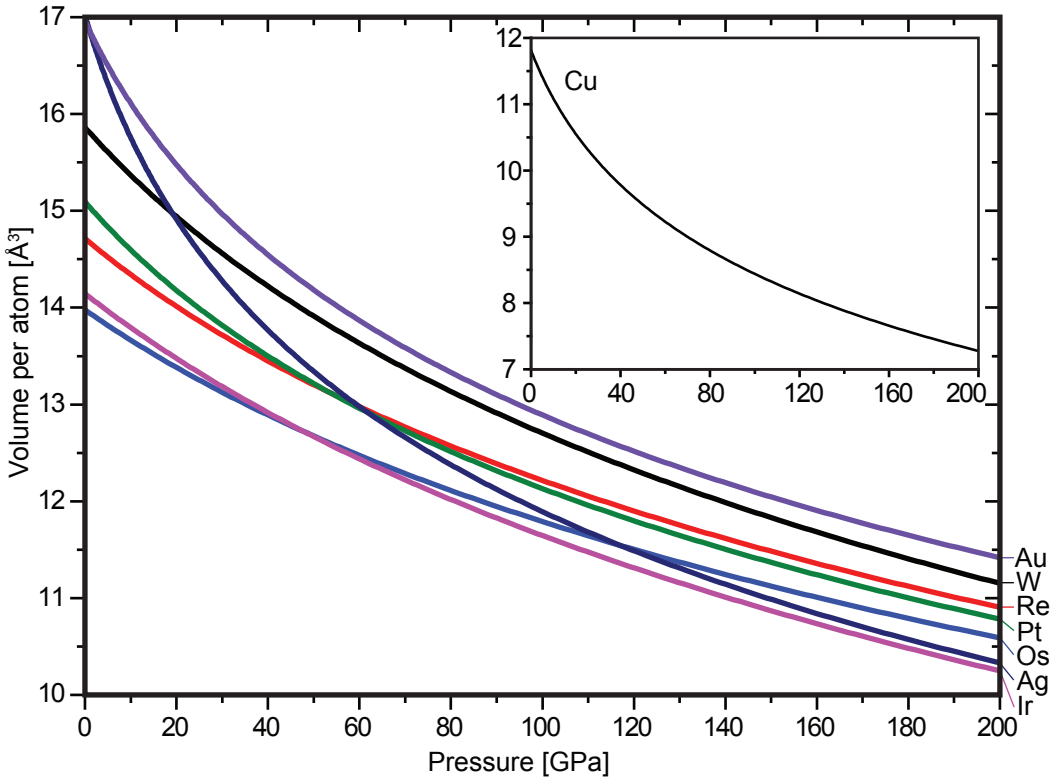


Figure 3.4: Equations of state for the metals listed in Table 3.1 (see there for references). Inset shows EoS for copper.

3.2.3 The Diamond Raman Gauge

The possibility of using the signal from the fundamental Raman mode of diamond as a pressure gauge has been first proposed in [Hanfland 85] and was calibrated against the ruby gauge at pressures up to 40 GPa. At zero pressure, the first order Raman peak of diamond can be observed at 1333±0.5 cm^{-1} and shifts nearly linearly to higher frequencies with increasing pressure. In recent years, the diamond gauge has been further developed and allows pressure measurements in the multi-megabar pressure range where ruby fluorescence is too difficult to excite and hence too weak. At such pressures, only the measurement of the unit-cell volume of pressure calibrants with known EoS in the sample volume could be used to determine the pressure. However, this technique

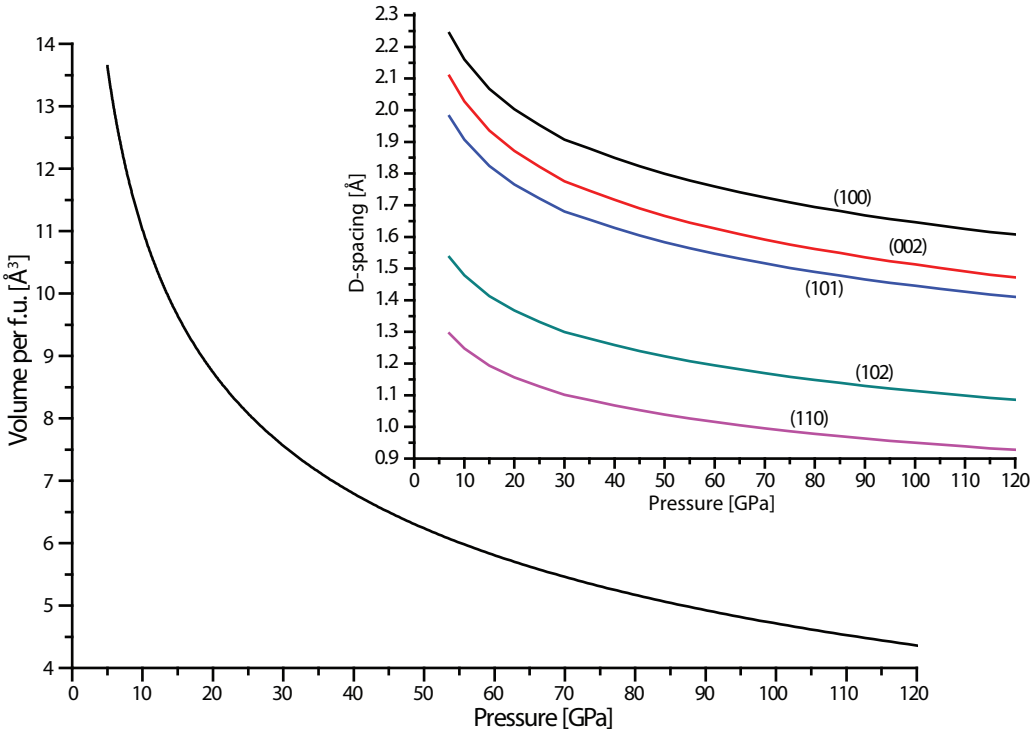


Figure 3.5: Equation of state of hydrogen. Inset shows d-spacings of hydrogen Bragg peaks vs. pressure. The values are derived from the EoS given in [Loubeyre 96]. For practical purposes, the data can be found in Table A.1.

requires access to microfocused synchrotron radiation due to the extremely small samples [Akahama 04b]. The diamond gauge facilitates lab-based optical pressure measurements without the need of an additional pressure calibrant in the sample volume. The most recent calibration of this pressure gauge can be found in [Akahama 07] where the data is fitted to the following quadratic equation:

$$P = A\frac{\Delta\omega}{\omega_0}\left[1 + \frac{1}{2}(B-1)\frac{\Delta\omega}{\omega_0}\right] \tag{3.4}$$

With A and B being the fitting parameters, $\omega_0 = 1333\text{cm}^{-1}$ the zero-pressure Raman frequency of diamond and $\Delta\omega$ the observed frequency shift. The results of the fit up to ∼300 GPa were $A = 547(11)$ GPa and $B = 3.75(20)$. For practical purposes the relation can now be written as:

$$P[\text{GPa}] = 0.410\Delta\omega + 4.233 \cdot 10^{-4}\Delta\omega^2 \tag{3.5}$$

However, it was found that due to the presence of uniaxial strain in the diamond anvils during compression, the exact frequency shift depends on the culet size and anvil geometry [Baer 08]. This leads to a certain inaccuracy in the pressure measurement when measuring using the diamond Raman gauge on the pressure-anvils. Figure 3.6 shows the pressure according to [Akahama 07] for the measured diamond edge. The inset shows the observed Raman spectrum at 123 GPa.

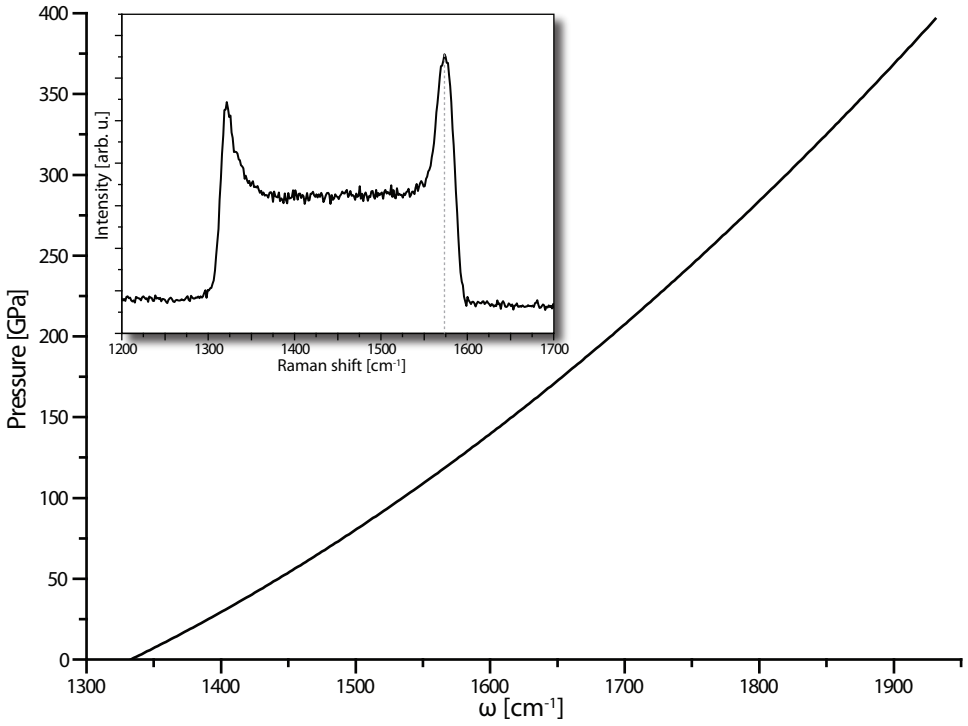


Figure 3.6: The Akahama pressure scale for the diamond Raman edge [Akahama 07]. Inset shows the observed Raman spectrum at 123 GPa.

3.2.4 The Hydrogen Vibron Gauge

The hydrogen Raman spectrum exhibits a distinct peak at frequencies between 3800 and 4250 cm^{-1} in the pressure range of 0-200 GPa. This mode corresponds to the vibrational motion of the hydrogen molecule and its frequency is very sensitive to pressure changes. Figure 3.7 shows the development of the hydrogen

vibron with pressure[3]. A clear maximum can be seen at pressures between 30 and 40 GPa which limits the use of the hydrogen vibron as a pressure gauge to pressures above 50 GPa [Baer 08]. Although the hydrogen vibron has not been properly calibrated to absolute pressures, it allows direct comparability with other experiments (see *e.g.* [Howie 12]). In this thesis, the hydrogen gauge has been used in addition to the ruby and the diamond pressure scales as a secondary pressure indicator.

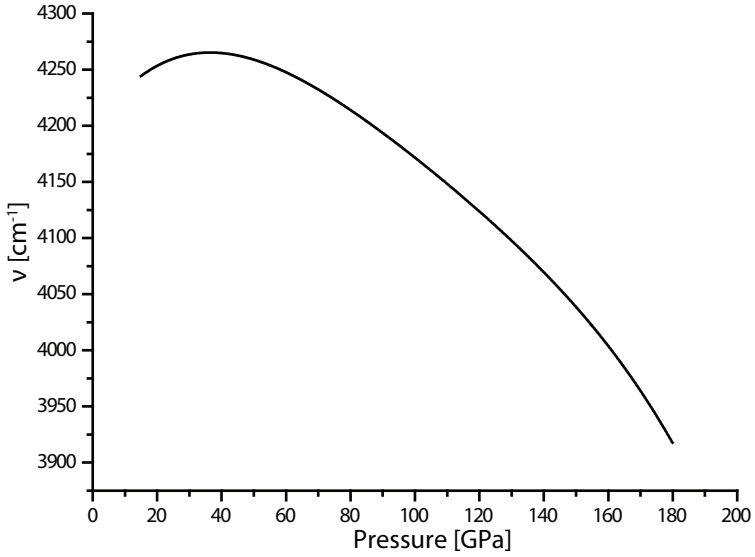


Figure 3.7: The hydrogen vibron frequency plotted against pressure. Data courtesy of R. Howie.

3.3 X-ray Diffraction at High Pressures

The main diagnostic method used in this work was synchrotron based *in-situ* x-ray diffraction (XRD). This chapter aims at giving a brief introduction to XRD, synchrotron radiation and the specific aspects of XRD at high pressures. Comprehensive introductions to synchrotron radiation and related applications

[3]The data shown here has been produced in an internal study at CSEC, The University of Edinburgh, mostly by R. Howie and C. Guillaume. At the time of writing an according publication was in preparation.

are given in [Baruchel 93] and [Hippert 05].

3.3.1 Basic Diffraction Theory

In all experiments related to this work, monochromatic synchrotron radiation with energies between 30 and 45 keV (corresponding to wavelengths λ between $\sim$0.3 and $\sim$0.4 Å) was used for angle-dispersive XRD. Therefore, white-beam applications and scanning-energy techniques such as x-ray absorption spectroscopy (XAS) are not discussed here. A monochromatic beam, described by the wavevector $\mathbf{k}$ with $k = 2\pi/\lambda$, can react with a solid sample in three different ways: Absorption, Refraction and Scattering. In an absorption process, the incident photon transmits its energy to an (inner-shell) electron of the target atom, leaving the atom in an excited or ionized state. Subsequent filling of the vacant state from lower-energy shells causes characteristic fluorescent radiation. The transmitted intensity through a material of thickness z is then given by

$$I(z) = I_0 e^{-\mu z} \tag{3.6}$$

where μ is the material- and energy specific absorption coefficient. When the energy of the incident photon is increased and exceeds the threshold for exciting a lower lying shell (absorption edge), the absorption coefficient is increased significantly. This can be seen in characteristic steps in the absorption cross section and is exploited in XAS and extended x-ray absorption fine structure (EXAFS) techniques.

An x-ray beam is refracted in a similar way in a sample as visible light in a lens or a prism. However, the refractive index n is negative for x-rays and of the order 10^{-5}. Therefore, the development of refractive x-ray optics is challenging and has only been made possible with the advent of third generation synchrotron radiation sources. Compound refractive lenses (CRL), made from beryllium, are nowadays commonly used to focus x-ray beams to spot sizes in the order of 1 μm (see *e.g.* [Scheler 09]). However, their effectiveness is reduced at higher photon energies and other types of optics (such as reflective Kirkpatrick-Baez (KB) mirrors or diffractive Fresnel zone plate setups) are used for focusing.

Elastic Bragg scattering (*i.e.* scattering without energy loss from an object with

internal structure) occurs when the scattering vector $\mathbf{K} = \mathbf{k} - \mathbf{k}'$ coincides with a reciprocal lattice vector $\mathbf{G}_{hkl}$ (known as the Laue condition). This is equivalent to the Bragg condition:

$$n\lambda = 2d_{hkl}\sin\Theta \tag{3.7}$$

where d_{hkl} denotes the lattice spacing of the crystallographic plane corresponding to the reciprocal lattice vector $\mathbf{G}_{hkl}$. Θ is the corresponding scattering angle, 2Θ accordingly the angle between **k** and **k'**. The scattering cross section for x-rays depends exponentially on the atomic number of the sample which makes x-ray diffraction on hydrogen challenging, in particular when heavier elements are involved. The scattering intensity of a Bragg reflection corresponding to the lattice vector $\mathbf{G}_{hkl}$ is determined by the structure factor $F(\mathbf{G}_{hkl})$ defined as:

$$F(\mathbf{G}_{hkl}) = \sum_j f_j(\mathbf{G}_{hkl}) e^{i\mathbf{G}\mathbf{r}_j} \tag{3.8}$$

where the sum is over all atoms in the unit cell and f_j and $\mathbf{r}_j$ their corresponding atomic form factor (scattering power) and fractional atomic coordinates respectively. The scalar product $\mathbf{G}\mathbf{r}_j$ can thus be written as $hx + ky + lz$. This leads to the following form of the structure factor:

$$F(\mathbf{G}_{hkl}) = \sum_j f_j(\mathbf{G}_{hkl}) e^{2\pi i(hx+ky+lz)} \tag{3.9}$$

The observed integrated intensity of a Bragg peak is given by:

$$I = \Phi_0 r_0 P |F(\mathbf{G}_{hkl})|^2 N \frac{\lambda^3}{V\sin(2\Theta)} \tag{3.10}$$

Here, Φ_0 denotes the incident photon flux, $r_0 P$ the contribution of polarization, N the number of unit cells of volume V per cell, λ the wavelength and 2Θ the scattering angle.

In the case of powder diffraction, the sample volume illuminated by the incident x-ray beam consists of a large number of individual crystallites (in contrast to single crystal diffraction) of random orientation. Accordingly, the sum of the Bragg spots from single crystallites forms a diffraction cone with opening angle $4\Theta_{hkl}$. Figure 3.8 shows the powder diffraction pattern of silicon

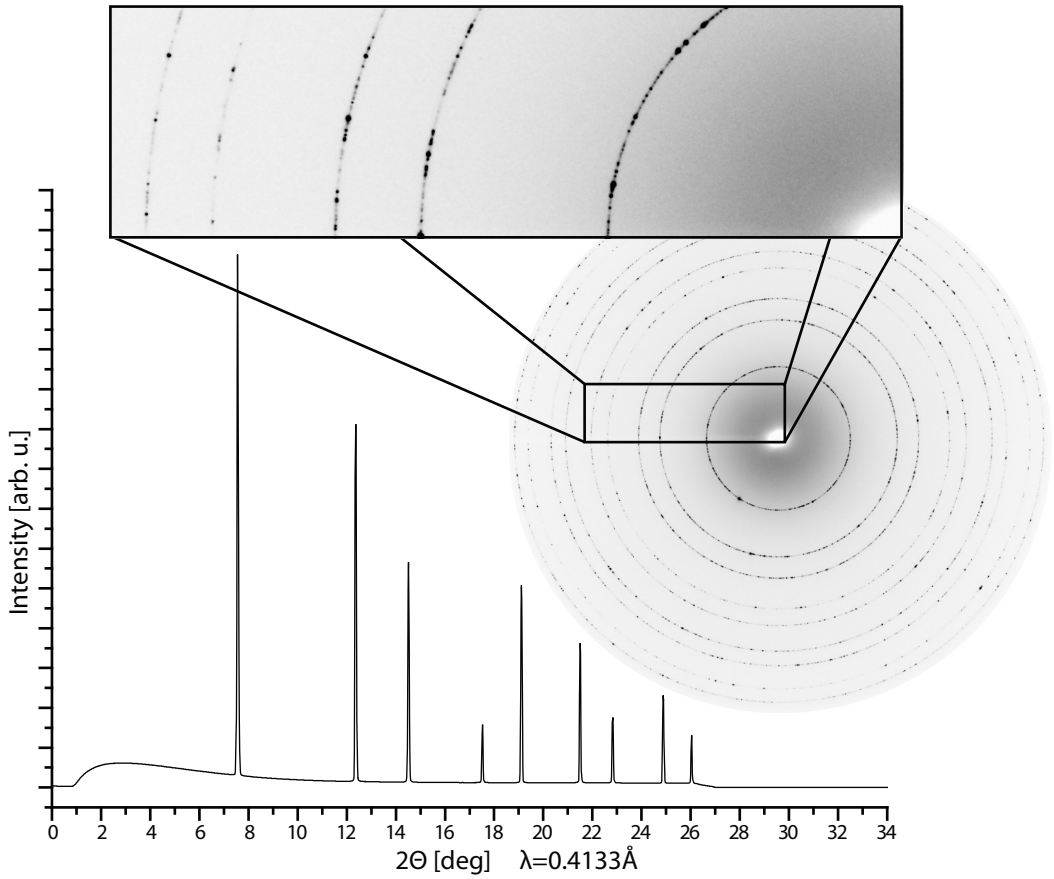


Figure 3.8: Powder XRD pattern and integrated spectrum (not background corrected) of silicon at ambient conditions. Inset shows enlarged part of the diffraction pattern. Single reflections from individual crystallites that make up the sample are visible. The XRD pattern was recorded at Diamond Light Source using a MAR345 detector.

and the corresponding integrated spectrum. The peak shape is best described by a Voigt function, which is a convolution of the Gauss and Lorentz functions. Since there is no analytical solution for the convolution integral, the pseudo-Voigt function approximation is used for peak fitting:

$$V_p(x) = \eta L(x) + (1-\eta)G(x) \tag{3.11}$$

$$G(x) = e^{-ln(2)\left(\frac{x-x_0}{\omega}\right)^2} \tag{3.12}$$

$$L(x) = \frac{1}{1+\left(\frac{x-x_0}{\omega}\right)^2} \tag{3.13}$$

with $0 < \eta < 1$. 2ω is the full width at half maximum (FWHM) of the curve and x_0 the center position.
Several factors influence the peak width 2ω: i) Instrument broadening, ii) strain broadening and iii) size broadening. Instrument broadening depends on the experimental setup and in particular on the source. Taking into account the geometry of experiments undertaken for this work, instrument broadening can be neglected. Strain broadening arises from varying d_{hkl} within the illuminated sample volume due to a strain gradient across the sample. Local compression of crystallites causes a shift in lattice spacing of Δd and accordingly a shift in diffraction angle of $\Delta 2\Theta$. Averaging across the strained sample therefore causes broadening. The amount of observed broadening depends on the diffraction angle:

$$2\omega = \Delta 2\Theta = (\Delta d/d) \cdot \tan\,\Theta \tag{3.14}$$

Size broadening is caused as a finite-size effect in the Fourier transform of extremely small crystallites. The smaller the individual particles, the broader the observed Bragg peaks. A simple approximation to this relation is given by the Scherrer formula:

$$L = \frac{K\lambda}{2\omega\cos\Theta} \tag{3.15}$$

where L is the average crystallite size, derived from the width 2ω observed for a reflection at a diffraction angle Θ. K is the empirical Scherrer constant which is usually 1.
In a real experiment, both size and strain influence the observed peak width and can be separated by a Williamson-Hall analysis (see *e.g.* [Cullity 83]). The analysis is done by plotting $2\omega\cos\Theta/\lambda$ against $\sin\Theta/\lambda$, where 2ω is the observed peak width, for all observable Bragg peaks. If size broadening is the only contribution to peak broadening, then the resulting plot shows a horizontal line. If strain contributes significantly, $2\omega\cos\Theta$ is a linear function of $\sin\Theta$. However, in order to achieve a reasonable quality, the obtained diffraction patterns have to be of exceptional quality. In most *in-situ* experiments at high pressure, conditions are not good enough (*e.g.* too few diffraction peaks visible, too weak) to allow a separation of strain and size effects. Significant peak broadening was observed in one case during this work (tungsten hydride, see chapter 4.3) and the attempts and strategies to separate the two effects are discussed in more detail there.

3.3.2 *In-situ* Synchrotron X-ray Diffraction at High Pressure

The advances in high-pressure techniques in the past have been largely possible thanks to the development of novel synchrotron radiation techniques [Hemley 05]. Third generation synchrotron radiation sources produce electromagnetic radiation as Bremsstrahlung from relativistic electrons. A description of this technology can be found *e.g.* in [Baruchel 93]. During the course of this thesis, experiments were carried out at the synchrotron radiation sources ESRF (Grenoble, France), PETRA-III (Hamburg, Germany) and Diamond Light Source DLS (Didcot, UK). These facilities operate electron storage rings (positrons in the case of PETRA-III) with beam energies ranging from 3 GeV (DLS) to 6 GeV (ESRF, PETRA-III). The dedicated high-pressure beamlines ID09a (ESRF) and P02.2 (PETRA-III) use undulator insertion devices for maximum photon flux in a narrow energy range. Beamline I15 at DLS is equipped with a wiggler source producing a white beam similar to a bending magnet. It is therefore capable of a wider range of experiments, albeit at the cost a significantly lower photon flux. Both, undulator and wiggler sources are based on the same principle: They consist of alternating magnets which force electrons along their path to follow an undulating path and thus emit Bremsstrahlung as they are accelerated laterally. The first order emission wavelength and corresponding photon energy from an undulator source are given as:

$$\lambda = \frac{\lambda_U}{2\gamma^2}\left(1 + \frac{K^2}{2} + \gamma^2\Theta^2\right) \tag{3.16}$$

$$E[\mathrm{keV}] = \frac{0.9496 E_e^2}{\lambda_U\left(1 + \frac{K^2}{2} + \gamma^2\Theta^2\right)} \tag{3.17}$$

λ_U is the undulator period in cm, E_e the energy of the storage ring particles in GeV and γ the relativistic Lorentz factor

$$\gamma = \frac{1}{\sqrt{1 - \frac{v^2}{c^2}}} = \frac{E_e}{mc} \approx 1957 E_e[\mathrm{GeV}] \tag{3.18}$$

It is $\Theta \approx 1/2\gamma$. The factor K characterizes the undulator and is given as

$$K = \frac{eB_0\lambda_U}{2\pi mc} \approx 0.9337 B_0 \lambda_U \tag{3.19}$$

with B_0 being the magnetic field produced by the undulator in T. The energy resolution of an undulator source is determined by the number of periods N:

$$\frac{\Delta\lambda}{\lambda} = \frac{1}{N} \tag{3.20}$$

Since electrons are stored as packages in the synchrotron, the monochromatic radiation emitted by an undulator is not unlike a pulsed laser source. In fact, fourth generation light sources (free electron lasers) basically consist of undulators with a large number of periods.

The vacuum of the storage ring is separated from the experimental endstations (beamlines) by the frontend shutter which is capable of withstanding the heat load of the incident radiation. Between the frontend and the sample station, the beam is shaped (both spatially and spectrally) by the x-ray optics. Polished single crystals of silicon are used to produce monochromatic radiation based on Bragg diffraction. Also reflected higher order radiation can be attenuated using a double crystal monochromator where the second crystal can be detuned (tilted) with respect to the first crystal. For high-energy applications, mostly KB mirror systems are used to focus the resulting beam to a few μm in diameter. KB mirrors are achromatic devices and thus work at any wavelength while CRLs and Fresnel zone plates depend on the photon energy.

The general layout of a beamline for high-resolution powder XRD is shown in Figure 3.9. For experiments at high pressures, the sample stage is designed to house pressure cells of various geometry. A high-resolution 2D large area detector (such as MAR345 or Perkin Elmer) is used to collect the diffraction patterns. Most dedicated high-pressure beamlines offer the possibility for online optical spectroscopy (*i.e.* without removing the cell from the stage) for ruby fluorescence measurements. Additionally, some beamlines (*e.g.* ID27, ESRF and P02, PETRA-III) offer *in-situ* laser heating facilities. These usually consist of YAG-lasers emitting at 1064 nm which can be focused onto the sample through

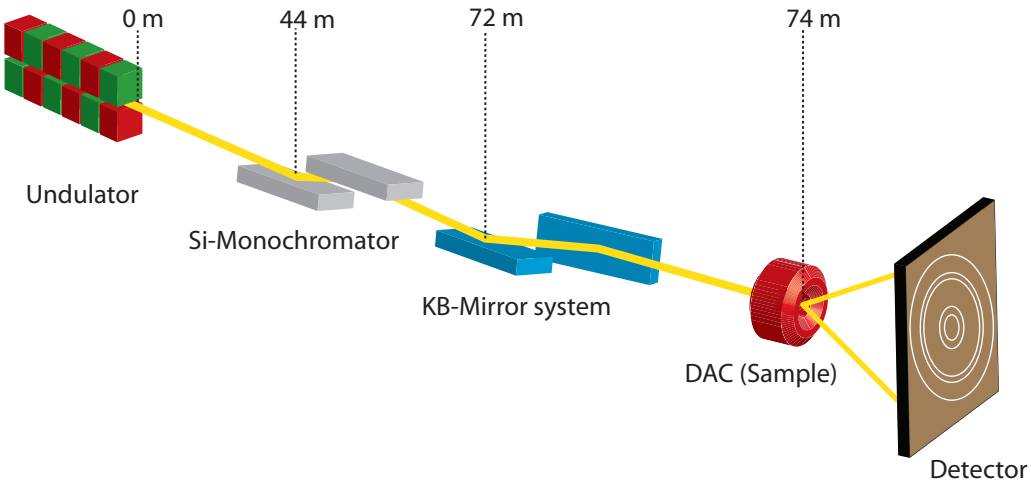


Figure 3.9: Schematic layout of a typical high-pressure beamline with characteristic distances of the elements from the source. For more details, see *e.g.* [Liermann 10].

the diamonds and at a slight angle from the x-ray beam so that parallel heating and XRD experiments are possible (see *e.g.* [Liermann 10]).

In order to calibrate the experimental setup (*i.e.* the exact photon wavelength, distance between detector and sample and detector tilt), a calibration sample is measured at the beginning of each experimental run. The most widely used calibration materials are powder samples of silicon or cerium oxide. Figure 3.8 shows the calibration pattern of a silicon sample.

3.3.3 Determination of Hydrogen Content with X-rays

The most important aspects of a novel metal hydride to be addressed are the crystal structure, its hydrogen content and the equation of state. All three properties are difficult to quantify in a diamond anvil cell, mainly due to the nature of hydrogen as an extremely weak scatterer of x-rays. For all intents and purposes, hydrogen can be regarded invisible in the surroundings of heavy elements such as most of the *d*-metals investigated in this work. Therefore, the influence of hydrogen can only be derived indirectly from the behaviour of the metal matrix.

The crystal structure of the metal lattice can be determined from XRD measurements. The position of the hydrogen atoms within the metal lattice is a priori unknown and can only be estimated from comparison with other hydrides with similar metal structure and known hydrogen orientation. In chapter 2.2 it was discussed that in most closed packed structures, hydrogen occupies the octahedral interstitial sites which is therefore also assumed for novel hydrides exhibiting this kind of host structure. However, it was also shown that not every hydride is stoichiometric although the underlying crystal structure would indicate this. Some of the available interstitial sites remain vacant. Therefore, the actual hydrogen content is a very important characteristic of a metal hydride. The volume expansion of the metal lattice due to absorption of hydrogen is proportional to the hydrogen content [Baranowski 71], which allows for the *in-situ* determination of the hydrogen content, provided two quantities are known: The exact volume of the parent metal at the given pressure and the equation of state of the hydride. In most cases, the hydride exhibits the same compressibility as the parent metal and thus the measured hydride volume can be directly compared to the volume of the parent metal at any given pressure. However, in some cases (*e.g.* copper, iridium), the compressibility changes upon hydrogenation. Then, the volume comparison is only feasible at zero pressure.

The measurement of the compressibility (*i.e.* the bulk modulus) is usually facilitated by constructing the P-V EoS for the metal hydride. However, volume expansion due to hydrogen uptake and volume contraction due to compression are competing mechanisms and not always separable in XRD experiments. In order to construct the EoS, a constant hydrogen content has to be implied, which is not always possible.

In summary, the hydrogen content of a novel metal hydride under pressure is estimated in the following way: If the compressibilities of hydride and parent metal are identical (to within the errors of the measurements), the hydrogen content can be derived by measuring the volume difference between metal and hydride. The volume difference is then compared to other hydrides with a similar structure. In the absence of comparable values, an average volume expansion of 2.1 $Å^3$ per atom is used. If the bulk moduli are different, the zero pressure

volumes can be compared in the same way. This is only valid if it can be assumed that the hydrogen content is constant.

3.4 Other Techniques

In this section, various supporting techniques are briefly introduced. They are listed here for reasons of completeness.

3.4.1 Raman Spectroscopy

Raman spectroscopy was used in this thesis alongside fluorescence spectroscopy for the main purpose of measuring pressure, employing the hydrogen vibron and diamond edge pressure scales (see chapter 3.2). Although the *hcp* lattice generally exhibits a Raman active mode at low Raman shifts (typically below 100 cm^{-1}, [Olijnyk 02]), this was not observed in our experiments.

3.4.2 Neutron Diffraction

This technique was not used in this work. However, neutron diffraction is a widely used technique and complimentary to XRD. Due to the different scattering cross sections of the elements for neutrons compared to x-rays, the hydrogen isotope deuterium can be resolved very well and a refinement of the deuterium positions within the unit-cell is possible (see *e.g.* [Antonov 02, Fukai 05]). Hydrogen (protium) has a significantly higher incoherent scattering cross section compared to deuterium leading to an intense diffuse background signal. Unfortunately, high-pressure techniques for neutron diffraction are generally limited to <20 GPa (within practical considerations, techniques for higher pressures exist but not yet routinely applied), while most of the effects investigated in this work take place at higher pressures. However, based on comparison with results from previous neutron diffraction experiments at lower pressures, structural models of hydrides investigated by x-ray diffraction can be established.

3.4.3 Transmission Electron Microscopy

The investigation of very small samples by transmission electron microscopy (TEM) has been a standard technique for the past decades and is well established. In this thesis, TEM was used for the characterization of recovered samples of dehydrogenated tungsten (see chapter 4.3). Similar applications have been demonstrated in [Irifune 03, Irifune 05]. In particular the microstructure is addressed in TEM experiments.

3.4.4 Focused Ion Beams

Focused Ion Beams (FIB) have become more widely available since the late 1990's and are approaching a state where they are comparable and in fact complimentary to scanning electron microscopes (SEM) and essential for sample preparation for TEM. Overviews and introductions to modern aspects of FIB-techniques can be found in [Reyntjens 01, Volkert 07, Gierak 09]. FIB-systems work in the same way as SEM's but instead of using accelerated electrons, they use ions from a liquid metal ion source (LMIS). The ions are extracted by field emission from a droplet of supercooled metal in the LMIS (usually gallium) and accelerated to several 10 keV before being shaped by electrostatic lenses. The applications of FIB-systems range from simple imaging (with different contrast and depth-sensitivity compared to electrons) over local sputtering and engraving to the deposition of metallic films from injected precursor gases [Gierak 09]. A very distinct property of micro-imaging using ions is channeling contrast which allows for an analysis of the microstructure of the sample [Phaneuf 99].

The sputtering capability of FIB-systems can be used to drill very small gasket holes which are necessary for ultra-high-pressure experiments (see [Howie 12]). Figure 3.10 shows a secondary electron FIB image of a gasket hole drilled into rhenium. The technique is described in [Orloff 00]. Laser drilling which is normally used for gasket preparation produces insufficiently clean holes on length scales of <10 μm. A FIB-milled gasket hole was used for experiments on the iridium-hydrogen system (see chapter 4.4). Unassisted milling of rhenium metal using Ga ions at an energy of 50 keV achieves a depth rate of ~ 0.15 μm/nC ion

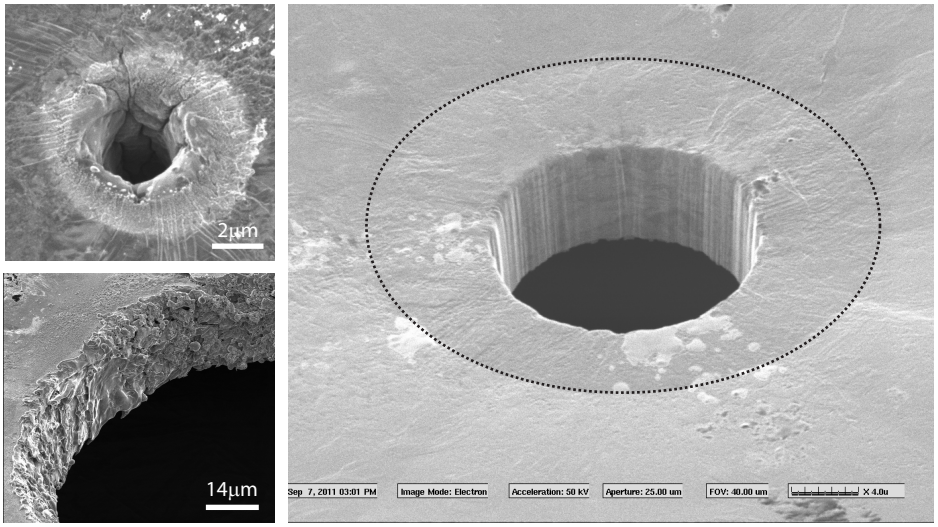


Figure 3.10: Left, FIB images of laser drilled gasket holes. For larger holes, the accuracy of the laser is sufficient but the microtexture of the gasket rim is very uneven. Right, FIB-drilled gasket hole (dotted circle indicates diamond culet indent).

dose[4]. Unassisted FIB-milling is further used in the preparation of TEM-samples (see *e.g.* [Miyahara 08]) and was used for that purpose during the investigation of the tungsten-hydrogen system (chapter 4.3). The injection of a suitable precursor gas also allows for the deposition of specific materials onto the sample surface and thus patterning and the creation of micro-circuits [Langfischer 02, Sadki 04].
Gas-assisted milling (*e.g.* H_2O vapor) can enhance the sputtering rate by up to a factor of 10 which is of particular interest for micro-machining diamond [Adams 03]. With the emergence of ultra-hard nano-polycrystalline diamond (NPD) [Irifune 03], non-mechanical shaping techniques for diamond gained importance, since NPD is extremely difficult to polish. Up to now, the tool of choice was laser ablation [Wang 00, Zhang 07, Sudheer 08, Okuchi 09] which is capable of achieving astonishing results. However, due to surface damage to the diamonds during thermal ablation, diamond anvils shaped with a laser lack the mechanical stability of their single crystal counter parts despite being made from a harder material. FIB-milled double-stage diamond anvil cells similar to the setup proposed in [Dubrovinsky 12] could push the boundary of static compression to

[4]This was measured in a series of test millings on an unprepared Re surface on the Micrion/FEI 2500 system at CSEC, University of Edinburgh.

beyond the metallization pressure of hydrogen.

Chapter 4

Transition Metal-Hydrogen Systems at Extreme Conditions

In this chapter the results of work on the various metal-hydrogen systems is discussed. The order in which these are presented reflects the chronological order of the experiments.

4.1 Platinum

The noble metal platinum plays an important role in several industrial applications, *e.g.* as a catalyst in automobile exhaust systems or specific gas sensors (such as oxygen) and of course jewelery [Loferski 10]. Platinum also acts as a chemical hydrogenation catalyst but was long thought to be incapable of forming a bulk hydride (see chapter 2.3). In high-pressure research, platinum is widely used as a heat absorber in laser heating experiments, internal pressure standard for XRD experiments and electrical leads for resistivity measurement. The formation of platinum nitride [Gregoryanz 04] and platinum carbide [Ono 05] has been observed at high pressures and temperatures. Under inert atmosphere, the *fcc* phase of pure platinum is stable to very high pressures (measured up to 660 GPa in shock-compression experiments) [Holmes 89, Dewaele 04]. It was found that platinum powder is superconducting in the low mK regime [König 99].

The formation of platinum hydride directly from the elements was first

observed by Hirao *et al.* in 2008 [Hirao 08] at pressures above 27 GPa and room temperature, although important properties such as hydrogen content, equation of state or stability range remained unknown. This discovery, presented on the 2008 AIRAPT conference, went largely unnoticed by the high-pressure community. Also in 2008, a different study caught the attention of a wider audience: Eremets *et al.* observed superconductivity in silane at pressures above 50 GPa [Eremets 08]. The XRD study showed the appearance of a new phase at this pressure with drastically reduced volume. This new phase was indexed in the $P6_3/mmc$ spacegroup, corresponding to the hexagonally closed packed structure. According to the silane stoichiometry of SiH_4, the unit-cell of this new phase would contain 8 hydrogen atoms, a density corresponding to free hydrogen at pressures close to 500 GPa. The emergence of superconductivity was thus interpreted as the formation of the superconducting ground state of hydrogen, as predicted by Ashcroft [Ashcroft 04].

It was found shortly thereafter by a group at Edinburgh University that silane decomposes at pressures above 50 GPa [Degtyareva 09]. Therefore, the structure observed by Eremets *et al.* could not have been a densely packed phase of silane. In order to measure apparent superconductivity in silane, electrical leads had to be present in the sample volume in the experiment of Eremets *et al.*. As it turned out, these leads consisted of platinum and it was speculated in [Degtyareva 09] that the release of hydrogen due to decomposition of silane would lead to the formation of platinum hydride from the electrodes. However, this was not proven in the paper from 2009.

Therefore, a series of experiments on a platinum-hydrogen mixture were conducted in order to verify the formation of platinum hydride and characterize this material. This work was published in [Scheler 11b] and constitutes to date the only experimental study of this material at pressures up to 50 GPa. However, the dispute between Eremets *et al.* and Degtyareva *et al.* prompted several theoretical studies, which were published in parallel to our experimental work [Zhou 11, Kim 11]. More recently, further theoretical work on the noble-metal hydrides was published [Gao 12]. Here, the authors used the by then well-characterized PtH system to test the predictive stability of their approach.

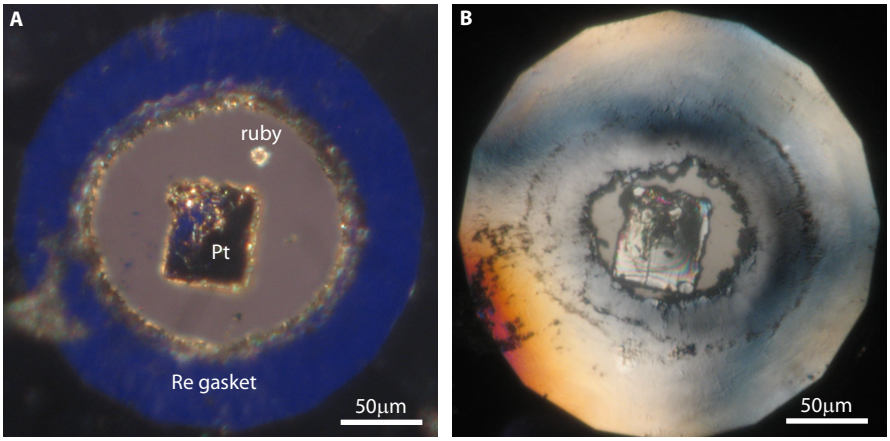


Figure 4.1: Optical micrographs showing a platinum loading. A) Open cell before hydrogen gas loading. B) Closed cell at 10 GPa. Note the significant reduction in volume due to the high compressibility of hydrogen.

In three experimental runs, platinum thin foil or powder (Alfa Aesar, 99.95% purity) was loaded into a symmetric DAC (DC-type) with flat diamond culets of 250 μm diameter[1]. The gasket was made from rhenium foil, originally 250 μm thick and thinned to $\sim$30 μm at the position of the gasket hole. A gasket hole of 100-130 μm diameter was subsequently drilled using a YAG-NIR laser. Hydrogen was gas-loaded to a pressure of $\sim$1800 bar into the sample volume before the cell was closed. XRD measurements were conducted at beamline ID09 at the ESRF (see Table A.2). Pressure was measured using the ruby scale (see chapter 3.2). During these experiments, the pressure range between 10 and 55 GPa was covered. Figure 4.1 shows optical micrographs of a typical loading with thin foil before closure of the cell (A) and at $\sim$10 GPa (B).

XRD patterns were collected using a large area MAR555 flat panel detector[2] and processed using FIT2D [Hammersley 96]. Figure 4.2 shows XRD patterns and integrated spectra of platinum and platinum hydride at various pressures. At pressures below 27(1) GPa and room temperature, the *fcc* structure of pure

[1]cell preparation and data acquisition was mainly carried out by other members of the Gregoryanz-group at CSEC, namely C. Guillaume and J. Proctor

[2]See www.marresearch.com

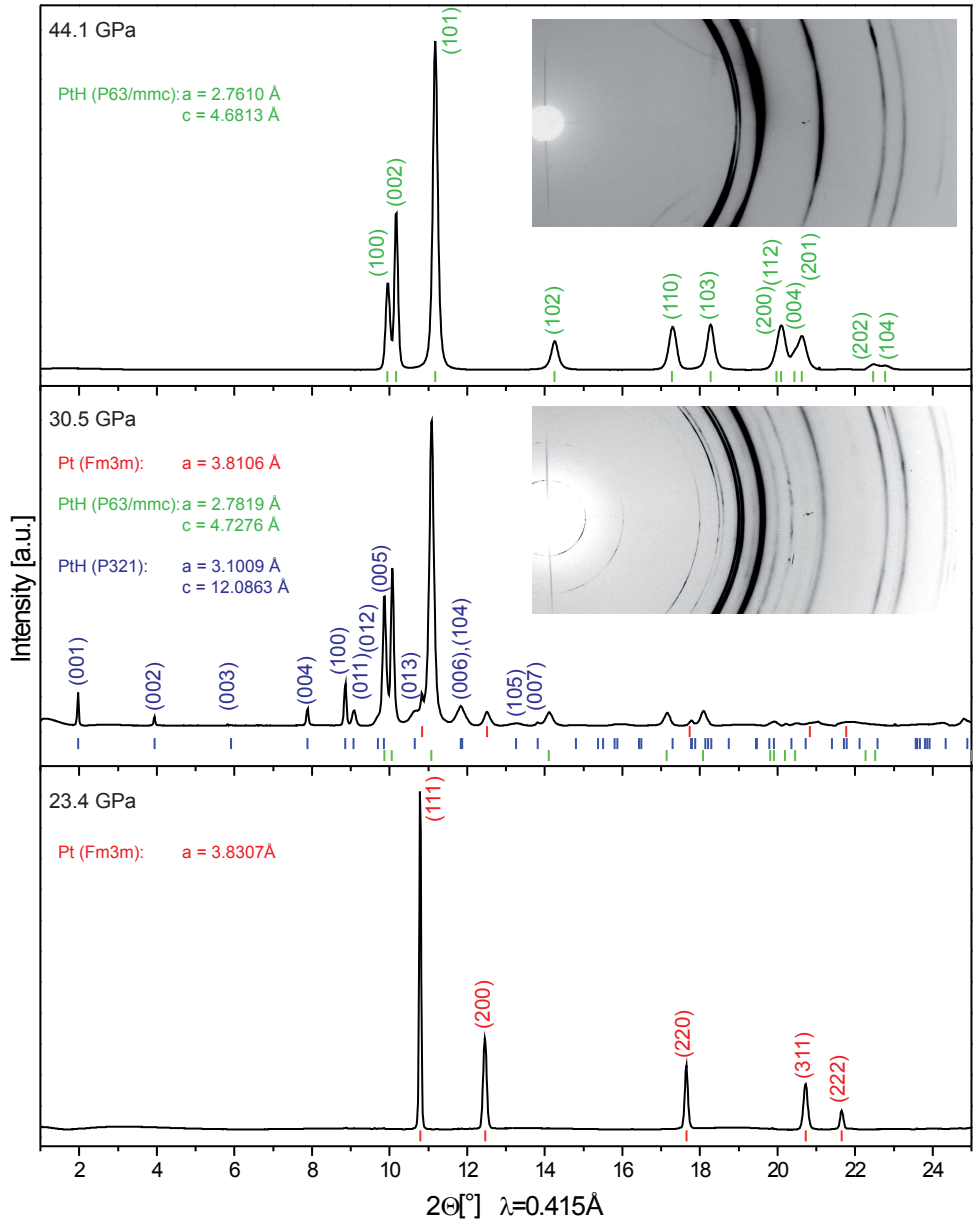


Figure 4.2: Integrated diffraction patterns for platinum and platinum hydride at various pressures below and above synthesis. Tick marks show the peak positions of the according phases. Insets show according 2D diffraction patterns of the mixed phase and the pure hexagonal hydride phase.

platinum is well resolved and stable (lower panel in Figure 4.2). In one of the runs the platinum sample was embedded in solid hydrogen for the duration of several days at 25 GPa but no reaction was observed. When pressure was increased to above 27 GPa the diffraction pattern changed instantaneously (middle panel in Figure 4.2). The new complex pattern contains signatures belonging to three distinct phases: *fcc* platinum and two different phases of platinum hydride which we named PtH-I and PtH-II [Scheler 11b]. Both phases can be indexed in hexagonal settings, PtH-I in the $P321$ spacegroup, PtH-II in the $P6_3/mmc$ spacegroup. Figure 4.3 shows a diffraction pattern taken at 34 GPa, showing all three phases including calculated spectra for each individual phase.

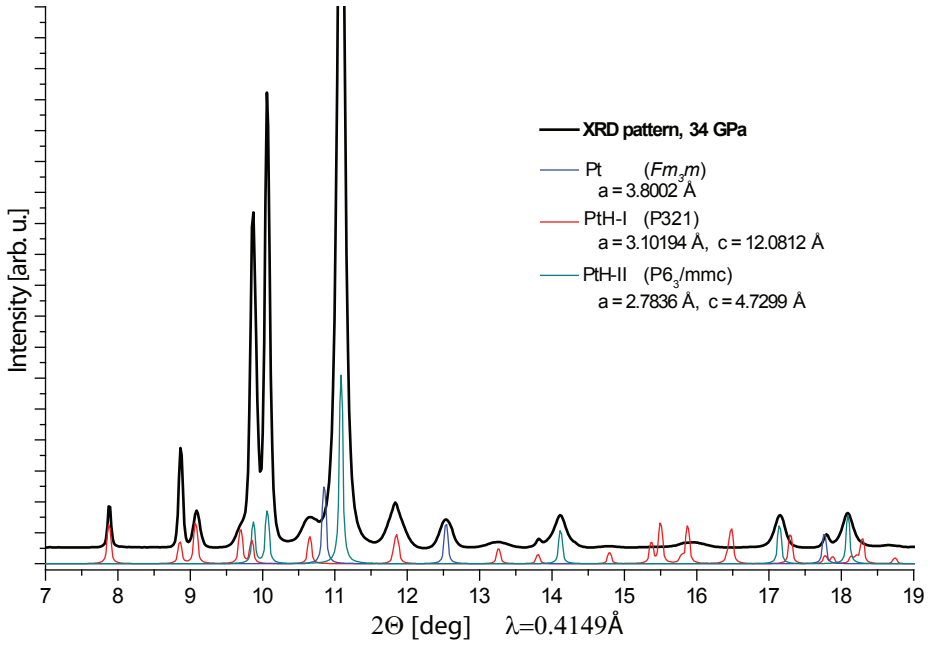


Figure 4.3: Integrated XRD spectrum showing the mixed phase of platinum hydride at 34 GPa. Thin lines are calculated spectra for the individual phases.

In one of our experimental runs, the PtH-I phase was visible up to 42 GPa. At higher pressures, only PtH-II can be identified (upper panel Figure 4.2) and remained stable up to 55 GPa, the highest pressure reached in our experiments. Upon pressure decrease, PtH-II remained the stable phase down to ∼20 GPa. At lower pressures, PtH-I appeared briefly in an unmixed state, *i.e.* no PtH-II was present, before decomposing into *fcc*-Pt below 18 GPa. However, the

observation of PtH-I was not easily reproducible as its formation seems to be dependent on specific (and not further known) experimental circumstances. In one experimental run, PtH-I was only observed up to 34 GPa and in a different experiment this phase was not observed at all when increasing pressure directly to 30 GPa from below 25 GPa. The irreproducibility of this phase rendered characterization extremely difficult. Hence, there is no complete structural model for this phase yet. Interestingly, none of the recent theoretical studies predicted a phase similar to PtH-I or discussed its existence in any further detail.

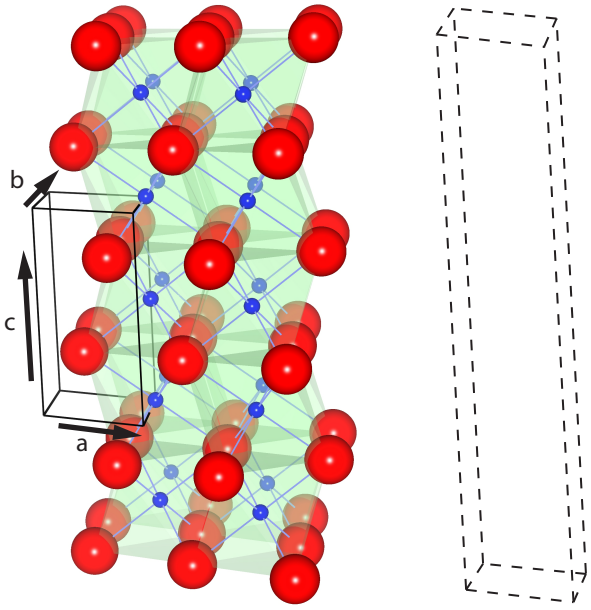


Figure 4.4: 3D structural model of PtH-II (left). The unit-cell is indicated by the wireframe. Right, for comparison the unit-cell of PtH-I for which the exact structure remains unknown.

According to other metal hydrides where the metal host matrix forms an *hcp* lattice (*e.g.* rhenium hydride, see chapter 4.2), we assume that hydrogen atoms occupy the octahedral interstitial sites in phase II of PtH (see chapter 2.3). The resulting structure is shown in Figure 4.4. The rather complex phase PtH-I is not known from other hydrides and comparison is difficult. If a constant stoichiometry is assumed for the transition between PtH-I and PtH-II, volume considerations suggest 6 platinum atoms in the unit-cell of PtH-I and a tetrahedral occupation of hydrogen in this structure, in analogy to the observed structure in niobium

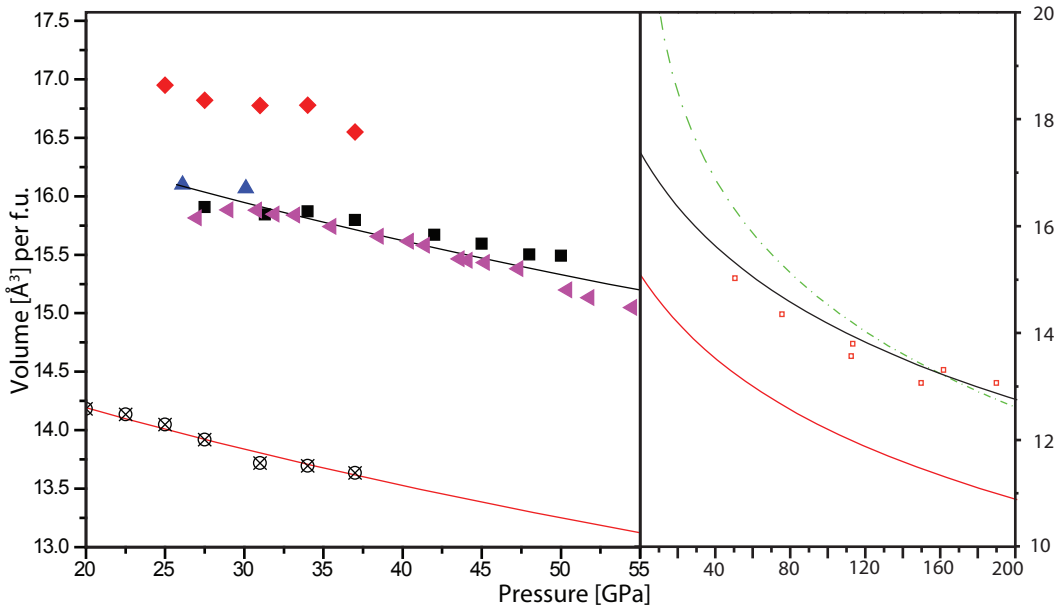


Figure 4.5: Equation of state of platinum hydride: Left shows pressure range of experiments with data points from various runs. Open circles denote Pt-*fcc*, red diamonds PtH-II, the others PtH-I. Right shows the full pressure range between 0 and 200 GPa. Open squares are data from [Eremets 08], there interpreted as silane (see Table A.7). Solid black lines are fitted EoS for PtH-I, red lines EoS for Pt, green dashed line combined EoS for Pt+$\frac{1}{2}$H$_2$ (see Table 3.1).

hydride [Fukizawa 83].

Fitting these unit-cells to the diffraction patterns allowed for the construction of the equation of state in the observed pressure range. Results for PtH-II are given in Tables A.3 and A.4, results for PtH-I in Tables A.5 and A.6. The observed p-V relation for PtH-II was fitted with a Vinet EoS (see chapter 3.2) and extrapolated to ambient conditions yielding a zero-pressure bulk modulus of B_0=310(10) GPa (B_0' fixed to 5.08) and V_0=17.33 Å^3 (see Figure 4.5). Platinum hydride thus appears to have a slightly increased bulk modulus compared to its parent material (B_0=277 GPa). However, due to the fairly large extrapolation from 20 GPa to zero pressure, the bulk modulus could be regarded as identical to pure platinum. Nevertheless, a marginal decrease in compressibility could be expected from the structural transition into the hexagonally closed packed structure.

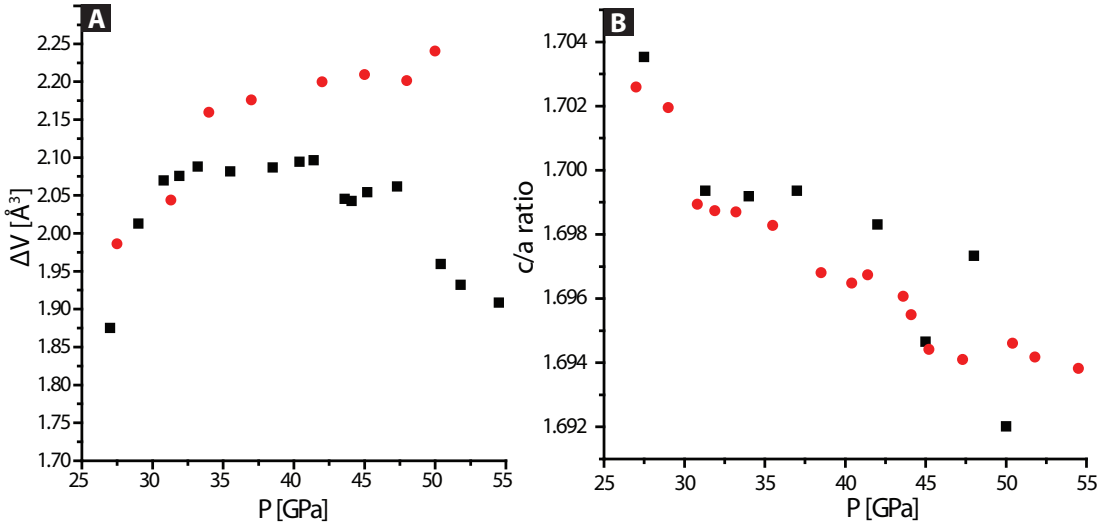


Figure 4.6: A) Evolution of the volume difference between PtH-II and Pt with pressure. B) Evolution of the c/a-ratio in the same pressure range. See Tables A.3 and A.4 for values.

Within the stability range of PtH-II the volume difference ΔV between PtH and Pt varied between 1.90 and 2.25 Å^3 with an average value of 2.1 Å^3 (Figure 4.6A). This corresponds very well to the average volume expansion observed in other metal hydrides with octahedral hydrogen orientation (see chapter 2.2). Furthermore, it has been observed in substoichiometric hydrides such as rhenium, that the hydrogen content depends on pressure and that phase transitions do not happen instantaneously. Therefore we conclude that PtH-II is a stoichiometric monohydride. The volume difference measured in PtH-I, assuming 6 atoms in the unit-cell, is in average ΔV=2.9 Å^3, again in good agreement with tetrahedral occupancy of the hydrogen atoms. The c/a ratio was found to be larger than the ideal value of 1.633 but to slightly decrease with pressure (Figure 4.6B). This suggests that the *hcp* lattice is not perfectly isotropic due to the uptake of hydrogen. The lattice seems to relax with increasing pressure. However, since interstitial hydrogen is mostly incompressible, this happens very slowly. It can further be argued, that at pressures between 160 and 200 GPa, PtH-I becomes unstable when the volume of interstitial hydrogen becomes larger than that of free hydrogen.

The synthesis and characterization of PtH, in particular the novel, and

apparently metastable, complex phase as well as the synthesis conditions extended the understanding of synthesis conditions of metal hydrides in two ways: i) Synthesis does not need to involve high temperatures and ii) considerably higher pressures than previously accessed can facilitate the formation of hydrides from parent materials which are highly inert under ambient conditions. For the nitrides of platinum, iridium and osmium this was shown a few years ago [Gregoryanz 04, Young 06], as well as for platinum carbide [Ono 05]. In those cases, synthesis took place at pressures above 50 GPa and involved laser heating to temperatures exceeding 2000 K. It was believed that kinetic barriers would hinder the formation of any binary phase at room temperature and these pressures. In the case of platinum hydride however, synthesis was observed at room temperature and the thermodynamic equilibrium pressure can be assumed to be slightly above 20 GPa. Another interesting difference is that in the case of the metal nitrides, although the metals were significantly heated, only the thin surface layer reacted to form nitrides [Young 06]. It was estimated (from the relative intensity of the x-ray diffraction peaks of the nitride with respect to its parent metal) that different nitrides were synthesized in very different quantities but the amount of nitride was always less than the remaining parent metal [Young 06]. In platinum however, the whole sample readily transforms into the hydride phase. In our studies the Pt samples occupied from 15% to 75% of the available volume above the solidification pressure of hydrogen (5.5 GPa). Even in the latter case the whole platinum sample completely transformed into PtH and no detectable platinum diffraction signal was visible.

The present characterization also revealed that it was indeed platinum hydride that was observed by Eremets *et al.*. The data from [Eremets 08] is included in Figure 4.5 (see Table A.7) and shows that the hydride formed from decomposed silane is apparently not fully stoichiometric. This can be explained by a lack of available hydrogen. Therefore it might be argued, that the presence of hydrogen in the platinum host matrix mediates superconductivity. Theoretical calculations have indeed revealed that PtH-II is superconducting with T_c comparable to those observed by Eremets *et al.* [Scheler 11b]. Unfortunately, this has not yet been confirmed experimentally.

4.2 Rhenium

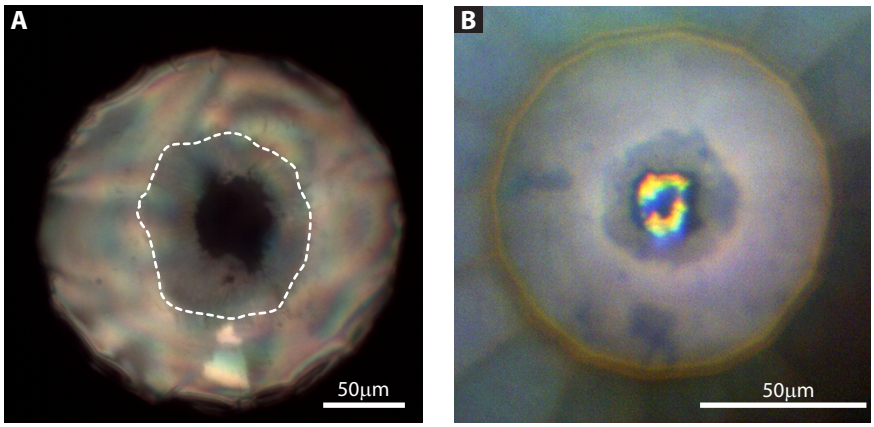


Figure 4.7: Micrographs from different loadings (A: Au+H_2 at 50 GPa, B: Ir+H_2 at 110 GPa) showing the extension of the rhenium hydride zone from the sample volume into the gasket. This can be seen as a darkening of the gasket. In A), the zone is indicated by the dashed white line.

A detailed study of rhenium hydride was not at the forefront of interest of this work. Rhenium is widely used as a gasket material in high-pressure experiments and rhenium hydride forms already at moderate pressures above 5 GPa at room temperature. The formation of rhenium hydride in the gasket is therefore often observed (see Figure 4.7) and is accordingly well studied (see chapter 2.3). However, over the years, different approaches to synthesis and characterization revealed first a higher hydrogen content [Atou 95] and later a different crystalline structure from what was previously accepted [Kawamura 04]. Before the present work, it was widely believed that rhenium hydride exists in the deficient anti CdI_2-type structure with a hydrogen content between $0.36 < x < 0.4$ and remains in this state even at pressures exceeding 100 GPa. Most data on rhenium hydride in the past was collected from the hydride formation in a rhenium gasket when pure hydrogen filled the sample volume. In similar circumstances, we studied the behaviour of gold under hydrogen atmosphere at pressures up to 45 GPa and external heating up to 300 °C in order to reproduce the synthesis reported by Antonov in 1982 [Antonov 82]. As a side effect we noticed a temperature-

and time-dependence of the hydrogen solubility in rhenium and subsequently undertook dedicated measurements in the rhenium-hydrogen system. The results of this work have been published in [Scheler 11a].

In the first of two independent experiments, the formation of rhenium hydride from the gasket material in a DAC was observed. In the second run, pristine Re powder (Alfa Aesar, 99.99% purity) was loaded into a DAC. In both runs, symmetric DACs were used and hydrogen was gas-loaded to a pressure of 1500 bar. The solid hydrogen also acted as the pressure transmitting medium. The ruby pressure scale was used to measure the pressure inside the sample volume. In the second run, the Re-gasket was sputter coated with gold in an attempt to prevent the formation of rhenium hydride in the gasket. In order to allow full hydrogenation, the sample was loaded and compressed to 15 GPa more than one month prior to carrying out the x-ray measurements. The cells were heated in an oven to temperatures between 150 °C and 300 °C for durations between 8 hours and 20 hours. X-ray diffraction experiments were conducted at beamline I15 at DLS. Synchrotron radiation at a wavelength of 0.4133 Å (30keV) was collimated by a stack of tungsten pinholes to obtain a beam diameter of approximately 20 μm. Angular dispersive powder diffraction patterns were recorded using a MAR345 image plate detector. All data after heating were taken after the cells cooled down to room temperature.

In both runs, before and after heating, the integrated diffraction patterns clearly show the *hcp*-like structure of rhenium hydride up to 46 GPa (Figure 4.8). Also in both runs, a difference in unit-cell volume between pure rhenium and our sample was found, indicating the formation of rhenium hydride.

Before the first heating cycle, the weak superstructure reflections of the anti-CdI_2 structure were visible at $2\Theta \sim 5.4°$ and $2\Theta \sim 16.2°$ (see insets Figure 4.8). These are the (001) and (003) forbidden reflections of the *hcp* lattice, first reported for rhenium hydride in [Kawamura 04]. Figure 4.9A shows the development of the first heating experiment[3]. In a first step (I), the sample was heated at 16 GPa in an oven for 19 hours at 150 °C. Prior heating to 100 °C did not entail any changes.

[3]Note that the rhenium signal stems from the gasket and a strong pressure gradient is present

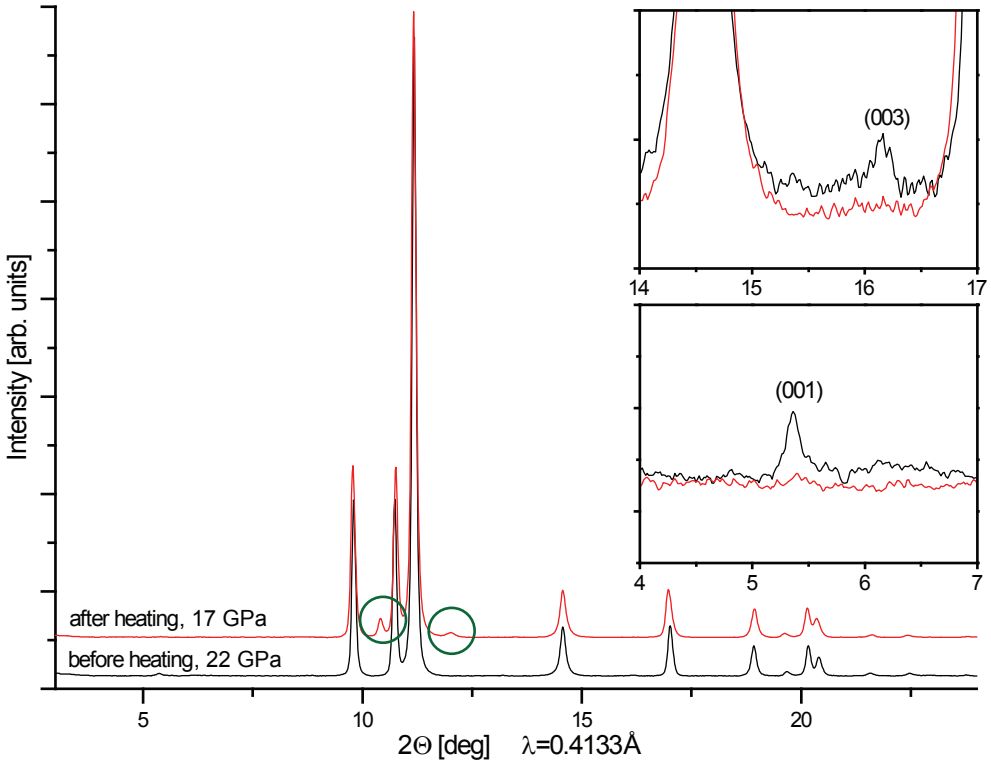


Figure 4.8: Integrated diffraction patterns of ReH before and after heating (see text). Insets show the disappearance of the superstructure reflections upon heating. Green circles indicate *fcc* reflections from the Au coating.

A clear volume increase compared to rhenium hydride is observed (see Table A.8), equivalent to a hydrogen content of $x > 0.7$. Upon pressure increase however, the hydrogen content dropped significantly and reached $x \sim 0.4$ by 30 GPa. After waiting at constant pressure and room temperature for 16h (II), the hydrogen content recovered again to $x > 0.7$ and from there on stayed at this high level (III). The two smaller values measured at intermediate pressures were derived from data taken further into the gasket. When heating the sample to even higher temperatures (300 °C, 8.5h (IV)), the volume difference dropped to the usual level and remained there on pressure decrease (V) (Table A.9). During the final heating cycle, the gasket hole had collapsed completely. The non-hydrostatic ruby signal did not indicate a significant pressure drop and we were able to detect the rhenium hydride signal from the gasket. In the second run, a similar behaviour was observed in the hydrostatic sample. After heating the sample for several hours at 200 °C, an increase in unit-cell volume was measured (see Table

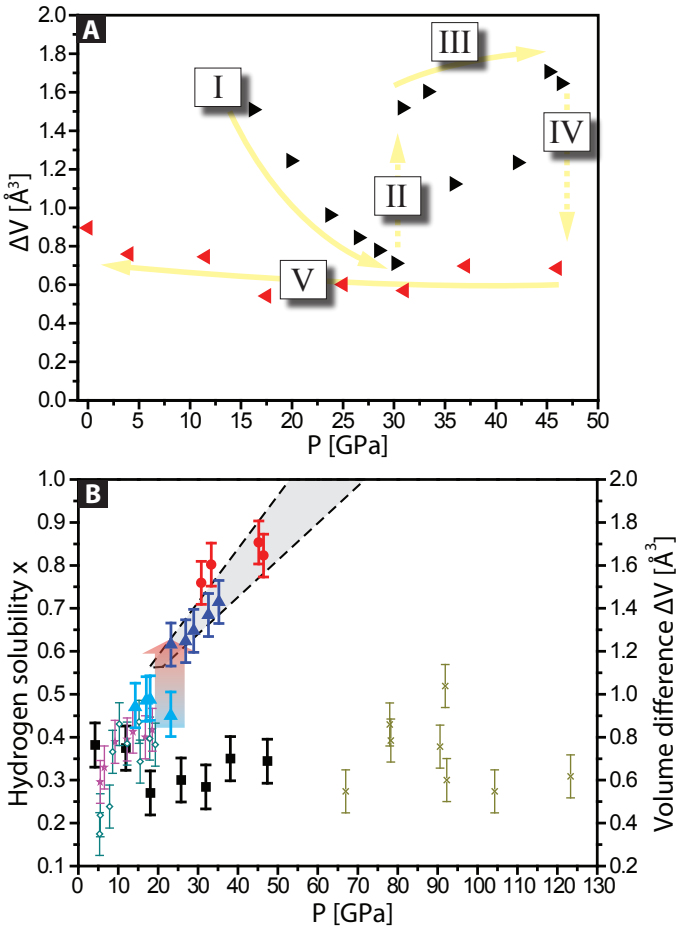


Figure 4.9: A) Measured volume differences in ReH formed in the gasket during the initial experiment. For a detailed description see text. B) Volume differences and according hydrogen content (x) of the first and second run compared to older data (see [Scheler 11a]). Data is listed in Tables A.8, A.9 and A.10.

A.10). Upon further pressure increase, the volume difference to pure Re increased monotonously. The highest pressure reached in the second run was 35 GPa due to diamond failure at this point. During the first heating cycles to 200 °C in both cases it was found that the superstructure reflections disappeared (see Figure 4.8). Interestingly, the weak reflections appeared again after hole collapse in the first run. The general effect of heating on rhenium hydride is shown in Figure 4.9B: Heating causes a hydrogen uptake beyond the hitherto known limitation of $x \sim 0.4$, with a pressure dependent increase of hydrogen content.

In a third experiment, scanning x-ray diffraction microscopy (SXDM) was

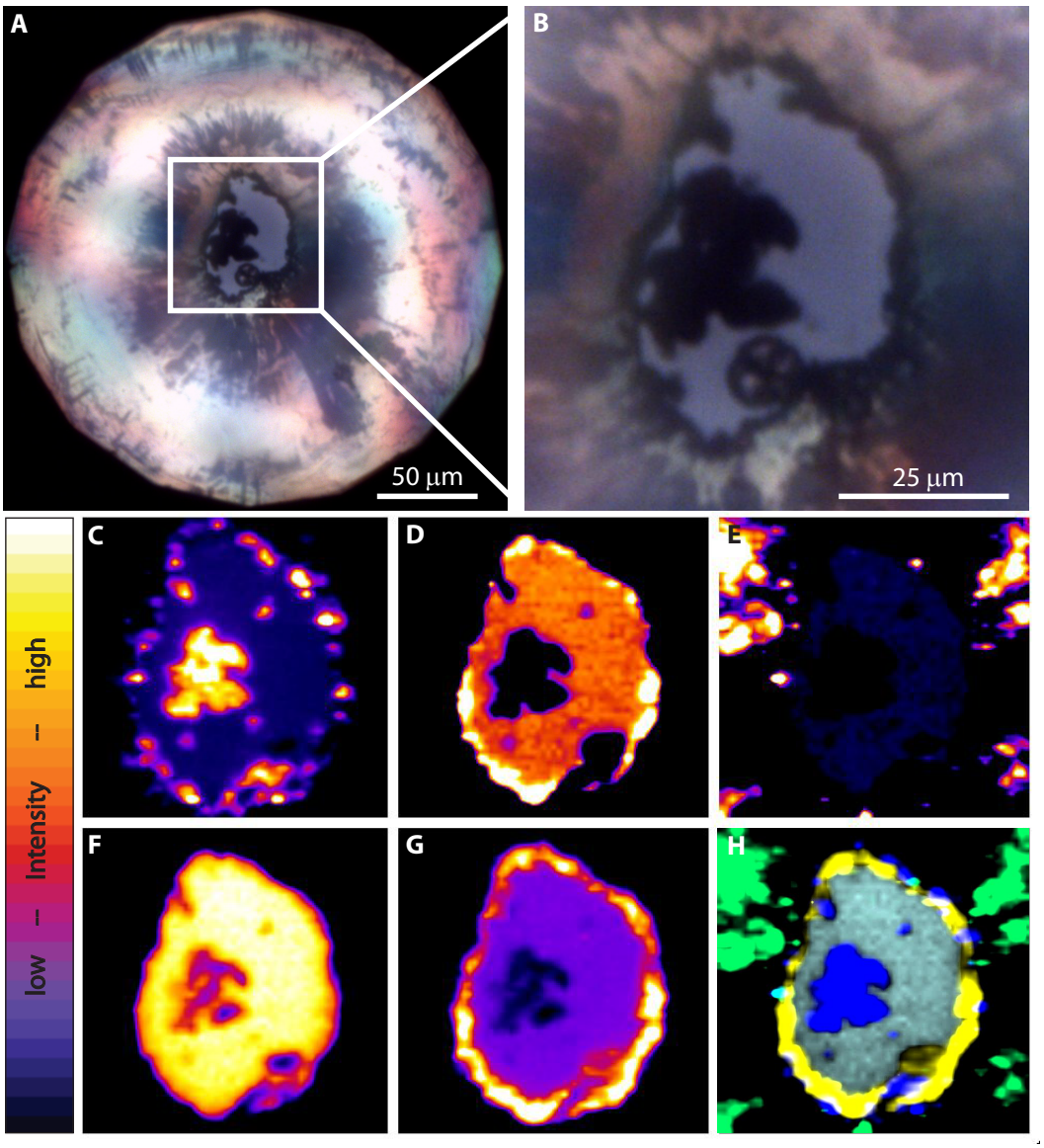


Figure 4.10: *in-situ* Scanning x-ray diffraction microscopy on rhenium hydride at 25 GPa. A) and B) show optical microscopy images of the sample at 17 GPa. C-G) show SXDM scans of the are shown in B) tuned for different signals. The scale bar on the left shows the colour-coding of the measured intensity on a relative scale. C) Rhenium hydride in sample, D) Au-coating (note the comparably bright background intensity), E) rhenium in gasket (only some parts of the gasket are in Bragg condition for the detector), F) diffuse scattering, transmission (note that the broken ruby sphere (see B) is almost invisible compared to rhenium) G) rhenium hydride on the gasket rim. H) compound SXDM image using signals from C,E and G: Green is pure rhenium, yellow rhenium hydride in the gasket, blue rhenium hydride in the sample (which has a different lattice parameter than the hydride in the gasket).

performed on the hydrostatic sample at beamline ID01, ESRF. To the best of our knowledge, this is the first time, this technique has been used with a high-pressure cell. SXDM has been recently developed after microfocused x-ray beams, fast noise-free detectors and reliable sample positioning became routinely available at synchrotron radiation sources ([Scheler 09] and references therein). By scanning the x-ray beam across the sample and tuning a fast noise-free detector to a certain scattering angle, the occurrence of a specific signal in the sample can be mapped. This way, a 2D real-space map of the distribution of certain materials or phases can be constructed. In this experiment, beryllium CRL's were used to focus a monochromatic beam of 15 keV to a diameter of $\sim$1 μm. The fast noise-free direct-illumination Maxi-Pix detector[4] was used for pattern recording. Figure 4.10 shows the result of the SXDM scan on rhenium hydride. Panels A) and B) optical microscopy images of the sample. Panels C)-G) show SXDM scans corresponding to the signal intensity at various diffraction angles during SXDM scans. The angles were selected to detect the presence of the different phases in the scan range. Interestingly, the Bragg peaks for the hydrostatic sample were found at slightly lower angles than the hydride peaks from the gasket rim (see difference between panels C) and G)). This clearly shows that a different form of rhenium hydride is formed in the immersed sample. In fact, the diffraction signal from the sample corresponds to a higher hydrogen content of $x \sim 0.5$.

Thus far, two key observations can be made: i) Heating at pressures above 15 GPa (possibly lower) causes a significant uptake of hydrogen to $x > 0.5$ and ii) long immersion of a rhenium sample at room temperature and sufficient pressure in hydrogen causes the hydrogen content to saturate at $x = 0.5$.

$ReH_{0.36}$ exhibits a layered structure where hydrogen atoms occupy only every second layer in the *hcp* lattice [Kawamura 04]. This irregularity causes a slight deviation of the rhenium atoms from their equilibrium position entailing the emergence of the forbidden reflections. In accordance with the notation for other metal hydrides, this anti-CdI_2-type structure of rhenium hydride is referred to as the the ϵ_1-phase here. The presence of the (001) and (003) superstructure reflections in our data confirm that before heating our sample was indeed in the ϵ_1-

[4]http://www.esrf.eu/Instrumentation/DetectorsAndElectronics/maxipix

phase (residing at pressure for more than one month). At this point we measured a volume difference of 1.98 Å^3 per unit-cell or $\sim$ 0.99 Å^3 per metal atom (see Table A.10 at 18.2 GPa), indicating a hydrogen solubility of $x \sim 0.5$. This is already larger than the previously reported maximum solubility of hydrogen in rhenium of $x < 0.4$. The increased hydrogen solubility in our sample can be explained by the long hydrogenation time. Most previous experiments were presumably performed on a time scale of a few hours between initial hydrogenation and reaching the highest pressure. If slow kinetics hinder the immediate hydrogen saturation, this would not be seen in those experiments. A hydrogen solubility of $x \sim 0.5$ would also be the stoichiometric composition of ϵ_1-Re_2H.

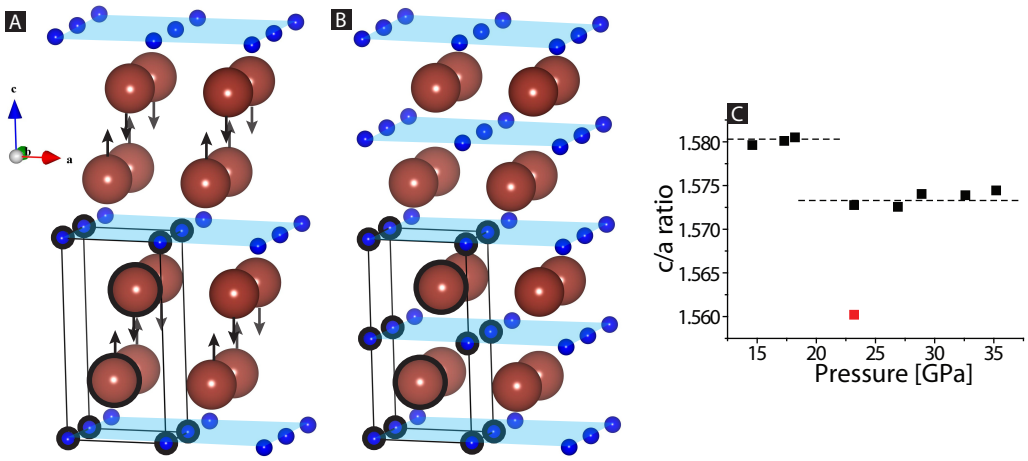


Figure 4.11: A) Layered anti-CdI_2 type structure of ϵ_1-Re_2H. The arrows indicate the displacement of the Re-atoms from their equilibrium positions in the *hcp* lattice (not to scale). B) NiAs-type structure of ϵ_2-ReH. The transparent blue sheets depict hydrogen layers with available interstitial sites. In both figures, the unit cell is indicated by the wire frame and circles around atoms belonging to the unit cell. C) c/a-ratios measured for the ϵ_1-phase (upper) and ϵ_2-phase (lower). The single red data point was measured in rhenium hydride formed in the gasket.

After heating the sample to 200 °C at a pressure of 23 GPa, an increase in volume difference to $\Delta V = 2.46$ Å^3 was measured, which is interpreted as an increase in hydrogen solubility to $x \sim 0.6$. At this point the superstructure reflections were not observable anymore, indicating an isomorphous phase-transition into a structure where the hydrogen atoms randomly occupy all vacant octahedral interstitial sites. This corresponds to a deficient NiAs-type structure

and is denoted as the ϵ_2 phase here. For a comparison of the two structures, see Figure 4.11. The ϵ_2-phase with $x = 1$ would be the equivalent structure to PtH-II. The $\epsilon_1 \rightarrow \epsilon_2$ phase transition is also evident in a change of the c/a ratio of the hydride lattice parameters (Figure 4.11C). Pure rhenium has a $c/a = 1.613$ (close to the ideal value of 1.633) while ϵ_1-$ReH_{\sim 0.4}$ has a pressure independent $c/a = 1.583$ [Atou 95]. We measured $c/a = 1.582(2)$ for the ϵ_1-phase and a lower $c/a = 1.573(2)$ for the ϵ_2-phase, both constant with pressure.

Upon pressure increase, the difference in unit-cell volumes between pure rhenium and rhenium hydride and thus the hydrogen solubility increased further to reach a level of $x \sim 0.7$ at 35 GPa in the second run. Data from the first run up to 46 GPa showed a further increase to $x \sim 0.85$, the highest value reached in this study and more than twice as high than the previously found saturation limit (see Figure 4.9B). Linear extrapolation of x leads to the estimate of full stoichiometry at pressures between 50 and 70 GPa. A continuous increase in hydrogen solubility with pressure is not uncommon and can also be observed in rhenium upon initial hydrogenation in the ϵ_1-phase. At room temperature, the hydrogenation process in rhenium starts at 5 GPa and leads to saturation at 10 GPa with $x \sim 0.4$. Further increase of the hydrogen solubility to 0.5 might be hindered by slow kinetics and is only observable with time.

The observation that the ϵ_2 phase in Re-H is stable after cooling down to room temperature suggests the presence of a large energy barrier preventing the phase transition at lower temperatures. Heating to 300 °C for 8.5h at 46 GPa decreased the hydrogen solubility to $x < 0.4$. At the same point the (001) and (003) superstructure peaks appeared again, *i.e.* rhenium hydride transformed back into the ϵ_1-phase (see Figure 4.9A). Upon pressure decrease, x remained constant within the error of the experiment (non-hydrostatic conditions). One explanation for the transformation from the ϵ_2- back into the ϵ_1-phase could be pressure and temperature driven hydrogen diffusion further into the gasket. At the point where the gasket hole collapsed completely due to hydrogen loss, the central hydrogen supply was depleted and the hydrogen solubility would drop. Below a certain limit (presumably $x \sim 0.5$) the hydride would then transform back into the ϵ_1-phase. The drop in hydrogen content with pressure upon initial

formation of the ϵ_2-phase at 16 GPa however, does not indicate a phase-transition. It can be assumed that in this case, because excess hydrogen was still available, the hydride remained in the ϵ_2 phase even at low hydrogen contents. The decrease can be explained by an extension of the hydride phase in the lattice due to pressure increase. A larger volume of rhenium metal becomes available to the hydrogen atoms and as along as the hydrogen content at the gasket rim is higher than the saturation limit of the ϵ_1-phase no additional hydrogen diffuses into the metal, causing the overall drop in hydrogen content.

This study shows, that kinetic effects can have substantial influence on the formation of metal hydrides. In most cases, emphasis in experiments is given to direct thermodynamic effects, *i.e.* that reactions occur immediately once the equilibrium conditions for synthesis are reached (as *e.g.* in PtH, see previous section). It should be noted here, that the increase in hydrogen content after the transition into the ϵ_2 phase was interpreted as a pressure-driven effect. This is not necessarily the case, as will be discussed in chapter 4.4. The time scale on which the pressure increase took place could also be the intrinsic timescale on which the transition happens. This theory is strengthened by a comparison of the time scales in this experiment: Heating to 150 °C at 16 GPa for almost 20 hours caused a solubility increase of > 0.3. Heating at 23 GPa and 200 °C for 8 hours increased the hydrogen content by ~ 0.15 and a further increase of 0.2 is measured during compression over a comparable time span. On this basis, it can be argued that, once the conditions for the $\epsilon_1 \rightarrow \epsilon_2$ transition have been reached, the hydrogen uptake progresses as long as the conditions are favourable, independent of pressure, reaching full stoichiometry after a given time (from the current data probably within 30 hours).

4.3 Tungsten

Tungsten is a widely used material in both industry and science. In high-pressure applications it is particularly valued as a pressure calibrant and gasket material. In the past, it was widely accepted that tungsten does not react with hydrogen, even at very high pressures, and therefore was frequently used as a sealing material in high-pressure experiments. However, it has been reported that the formation of binary tungsten hydride can be observed when compressing pure tungsten to above 25 GPa at room temperature in a dense hydrogen medium [Kawamura 05]. No further properties apart from the *hcp* metal host structure are given. We therefore started our investigation with the aim of establishing the stability range, hydrogen content, exact structure and equation of state of tungsten hydride. Several experimental runs at synchrotron radiation sources were carried out at pressures up to 115 GPa. TEM measurements on recovered samples were performed in order to study the microstructure. Tungsten hydride turned out to be a highly interesting material with a large synthesis-decomposition hysteresis and a nanocrystalline microstructure. However, the equation of state was difficult to address experimentally which led to a collaboration with the theoretical group of Prof. Yanming Ma[5]. What experimentally appeared to be a very high bulk modulus (see discussion below) was found to be the transition from a pure monohydride into a mixed state with a fractional composition of $(1-y)$WH $+ (y)$WH$_2$ with $y \sim \frac{1}{3}$. Although the implications of the computational work are discussed here, for further reading and details on methods the reader is referred to the accompanying manuscript[6].

In four experimental runs, we loaded pristine tungsten powder consisting of single crystalline grains, several microns in size (Alfa Aesar -325 mesh powder, 99.9% purity), together with hydrogen compressed to 2000 bar into symmetric DACs. Even at the highest pressures reached in these experiments, the tungsten sample was always surrounded by excess hydrogen. In three out of four runs we used diamonds with 250 μm culets, in the fourth run we used 90 μm beveled diamonds to achieve pressures above 1 Mbar. Pressure was determined using the

[5]The main computational work was carried out by Feng Peng and Yanming Ma, State Key Lab of Superhard Materials, Jilin University, 130012 Changchun, P.R. China.

[6]See annex to this thesis. At the time of writing, the manuscript was submitted for publication

ruby scale up to 70 GPa and the calibrated hydrogen vibron shift above. As a complimentary technique, pressure was also controlled by the diamond Raman shift. Rhenium foil of 250 μm was used as a gasket material. Gasket holes of around 50% of the culet diameter were drilled using a YAG infrared laser. The final thickness of the gasket was measured to be 25 μm in the case of the larger culets and $\sim$15 μm for the beveled culets. Angle-dispersive x-ray diffraction patterns using microfocused monochromatic synchrotron radiation were collected at beamlines I15 (DLS) and ID09a (ESRF). MAR345, MAR555 and PerkinElmer flat panel[7] detectors were used for data collection. TEM-samples were prepared by focused ion beam milling and subsequent lift-out and transfer to a copper TEM-grid. The finished samples had a thickness of 80-100 nm. TEM data was collected at the Leeds Electron Microscopy And Spectroscopy centre, UK.

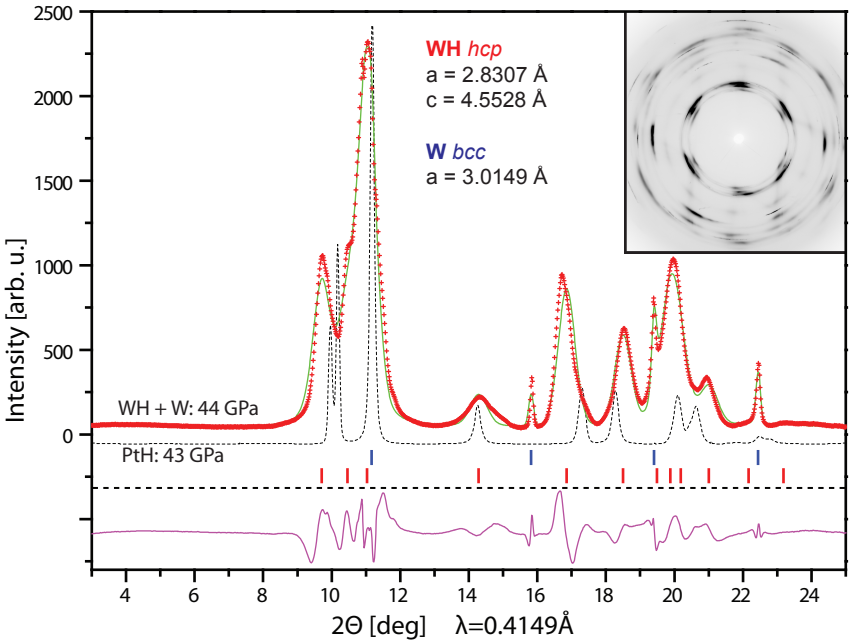


Figure 4.12: Integrated XRD spectrum of tungsten hydride at 44 GPa (inset shows 2D diffraction pattern). The green line denotes the result from a LeBail fit. Tick marks indicate peak positions for cubic W (upper, blue) and hexagonal WH (lower, red). The diffraction spectrum of platinum hydride at 43 GPa is added for comparison (grey dashed line). Note the difference in peak width.

[7]See http://www.perkinelmer.com/pages/050/flat-panel-detectors/xrd-16-inch-field-of-view-detectors.xhtml

At pressures below 24 GPa, the diffraction patterns clearly show the *bcc* structure of pure tungsten. After increasing pressure to above 25 GPa, additional peaks with significantly larger widths compared to the tungsten peaks appear. These are extremely weak in the beginning and only increase in intensity with time and pressure. Once strong enough, the peaks can be indexed in the $P6_3/mmc$ spacegroup confirming the observations by Kawamura *et al.* [Kawamura 05] and Strobel *et al.* described in [Zaleski-Ejgierd 12]. Figure 4.12 shows a diffraction pattern of tungsten hydride after only partial conversion of the sample, with the Bragg peaks of *bcc* tungsten still clearly visible. From volume considerations, a hydrogen occupation of the octahedral sites and content of $x \leq 1$ can be assumed, equivalent to the NiAs-type structure. Synthesis conditions and structure of tungsten hydride are reminiscent of platinum hydride (see chapter 4.1), which forms at pressures above 27 GPa and room temperature and exhibits the same hydrogen ordering.

However, in contrast to PtH, the hydride formation in tungsten progresses very slowly over time and the diffraction pattern of WH exhibits broadened Bragg peaks (for a comparison see Figure 4.12). In one of our experimental runs, we reached pressures of ∼45 GPa within hours of surpassing synthesis conditions. At this time, the sample has not been completely converted to tungsten hydride and the sharp Bragg peaks of *bcc*-tungsten are still clearly visible. It is evident that the diffraction peaks of tungsten hydride are considerably broadened compared to both its parent metal and another hydride synthesized under nearly identical conditions. While increasing pressure seems to accelerate the hydrogenation process, with time the whole sample fully transforms into the hydride also at constant pressures. In one of the experimental runs the sample was left at a pressure of 38 GPa for one month. Afterwards, the whole sample was hydrogenated and no sign of *bcc*-tungsten was detected. Zaleski-Ejgierd *et al.* [Zaleski-Ejgierd 12] report a similar effect and were able to observe the *bcc*-phase of tungsten up to 80 GPa. Apparently, laser heating accelerates the transition into the hydride phase.

In an SXDM experiment (see chapter 4.2), the transition can be clearly seen (see figure 4.13). In particular, it can be seen, that only parts of the tungsten

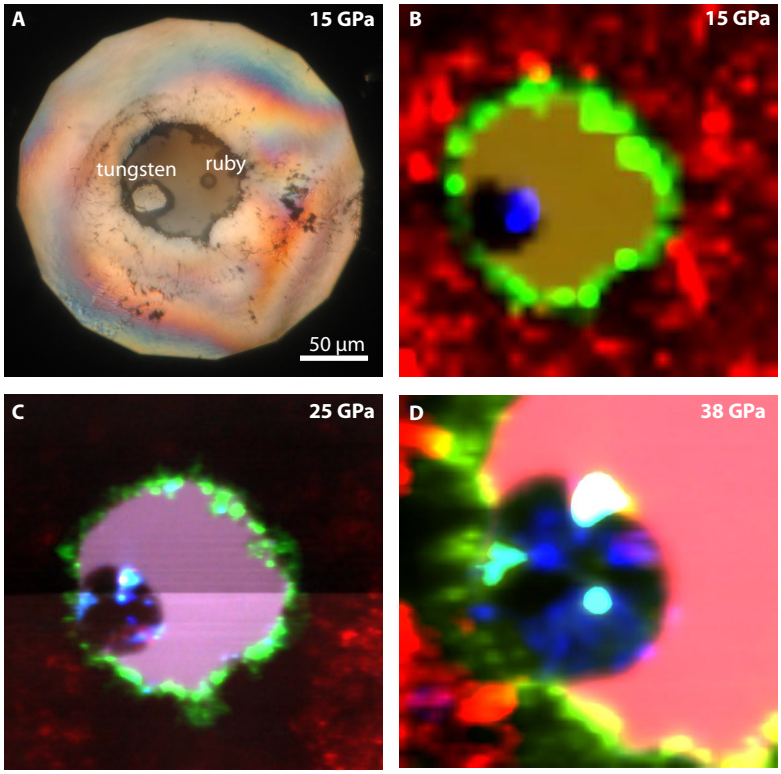


Figure 4.13: SXDM scans on tungsten hydride. A) Optical micrograph of the loaded cell. B) SXDM scan (low resolution) shows formation of rhenium hydride (green) from rhenium in the gasket (red). The tungsten signal is blue. C) SXDM scan just after passing synthesis conditions. Very weak additional intensity is visible in the tungsten sample. The intensity change below the horizontal line is due to a storage-ring refill and hence a higher photon flux. D) High-resolution SXDM of the sample showing tungsten hydride (blue) forming across the sample. Still strong pure tungsten signal (cyan/white).

sample are in Bragg condition with respect to the incident x-ray beam. The hydride on the other hand, although weak, can be seen everywhere in the sample, indicating a more powder-like distribution of the crystallites.

On decompression, tungsten hydride was found to be stable to pressures far below synthesis conditions. We observed decomposition reproducibly at pressures between 8 and 9 GPa. The slow progression of the hydrogenation process, its acceleration upon heating and the large hysteresis effect in decomposition suggest the presence of a kinetic energy barrier preventing the formation at lower pressures and faster hydrogenation. This would also corroborate the lower

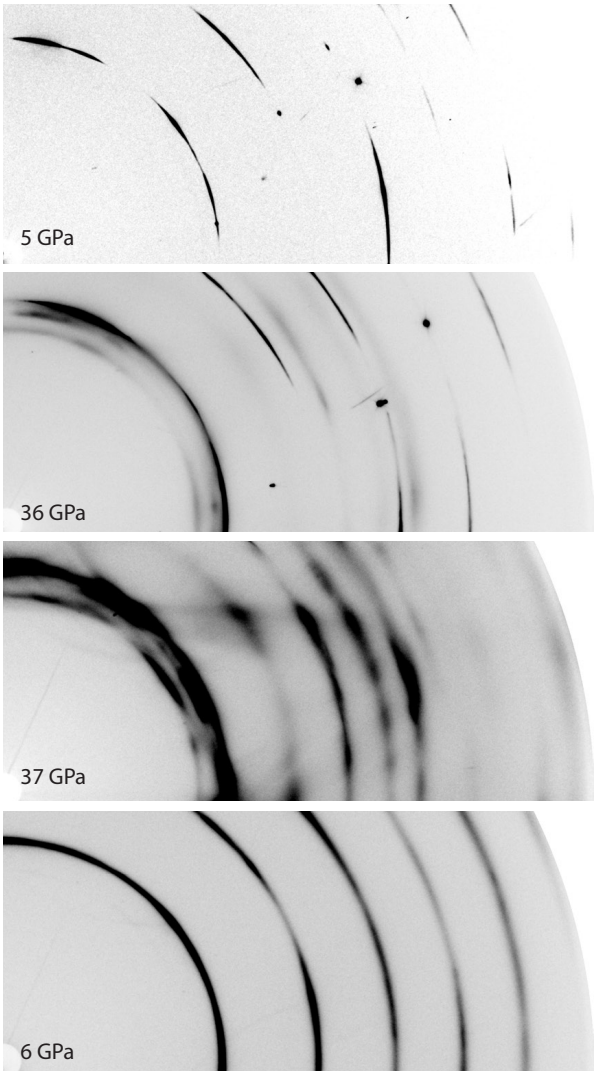


Figure 4.14: 2D XRD patterns at various pressures showing pure tungsten (upper), mixed state shortly after surpassing synthesis conditions (second from top), pure tungsten hydride at similar pressure after saturating for several weeks (third from top) and tungsten after decomposition (lower).

predicted pressure of formation for WH of only 15 GPa [Zaleski-Ejgierd 12]. We found that dehydrogenated tungsten still exhibits broadened Bragg peaks compared to its original state. A comparison of diffraction patterns at various pressures is shown in Figure 4.14. A very intriguing phenomenon can be seen in

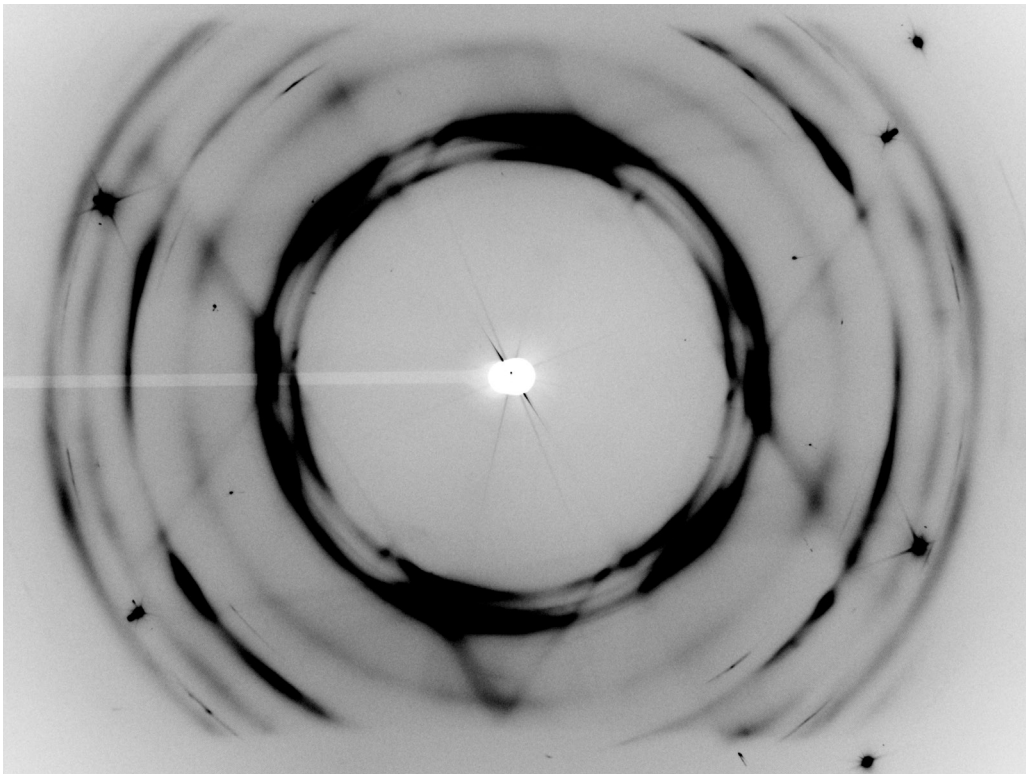


Figure 4.15: XRD pattern of WH at 50 GPa. Note the streaks connecting areas of higher intensity in the incomplete powder rings.

the diffraction patterns of tungsten hydride: Some of the high-intensity areas of the diffraction rings seem to be connected by diffuse scattering streaks. Figure 4.15 shows an XRD pattern of WH at 50 GPa. Several streaks can be seen connecting the diffraction rings. Various effects could be responsible for the appearance of these streaks, but the most likely seems to be thermal diffuse scatteing (TDS): While diffuse scattering in general is caused by any form of disorder in an otherwise periodic crystals (such as atomic displacement, atomic substitution or incommensurate structures [Baruchel 93]), TDS is caused by the lattice vibrations of the crystal. Although often regarded as nuisance, when the experiment aims at observing Bragg-reflections, it was suggested that TDS can

be used to extract phonon-dispersion relations [Xu 05] and to visualize the Fermi surface of the material [Bosak 09]. This in turn could allow direct access to various properties of the material, such as the elastic modulus. However, in all reported cases, single-crystal diffraction is crucial and the technique is not yet established and stable enough. It was therefore concluded that further investigation in this direction regarding tungsten hydride would most likely be unsuccessful[8].

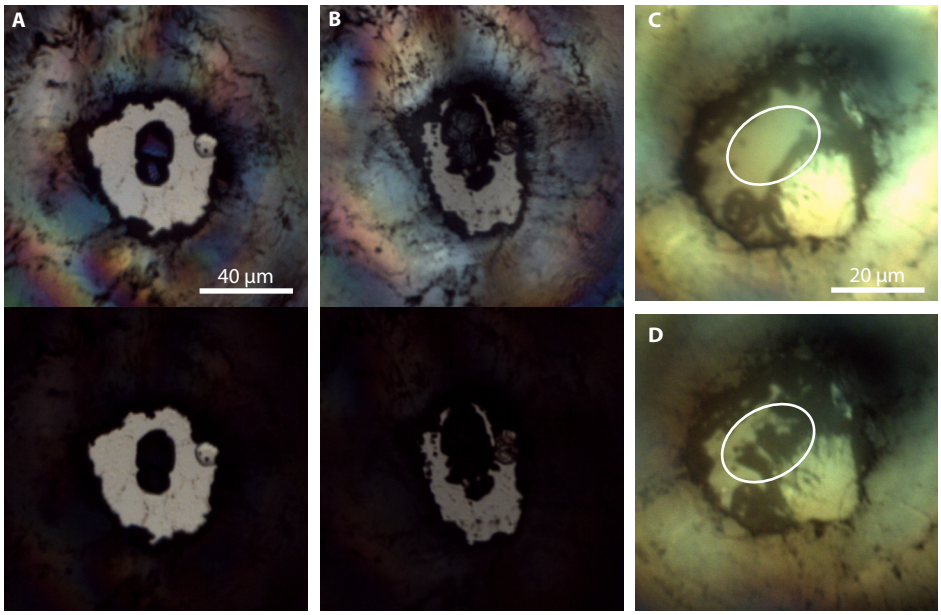


Figure 4.16: Opical micrographs of the tungsten hydride sample inside the DAC for two different loadings. A) and C) show the hydride before, B) and D) directly after decomposition.

Another interesting observation was made during the decomposition process (Figure 4.16): A macroscopic movement of sample material can be clearly seen in the sample volume. This is interpreted as the precipitation of dehydrogenated tungsten during the decomposition process, direct evidence for hydrogen embrittlement even on such a small scale and has its origin most probably in the modified microstructure of tungsten hydride which is discussed below.

[8]The appearance of the TDS streaks has been discussed with several experienced researchers both at the ESRF and CSEC and the consensus was that the data does not allow further treatment or interpretation of the TDS signal.

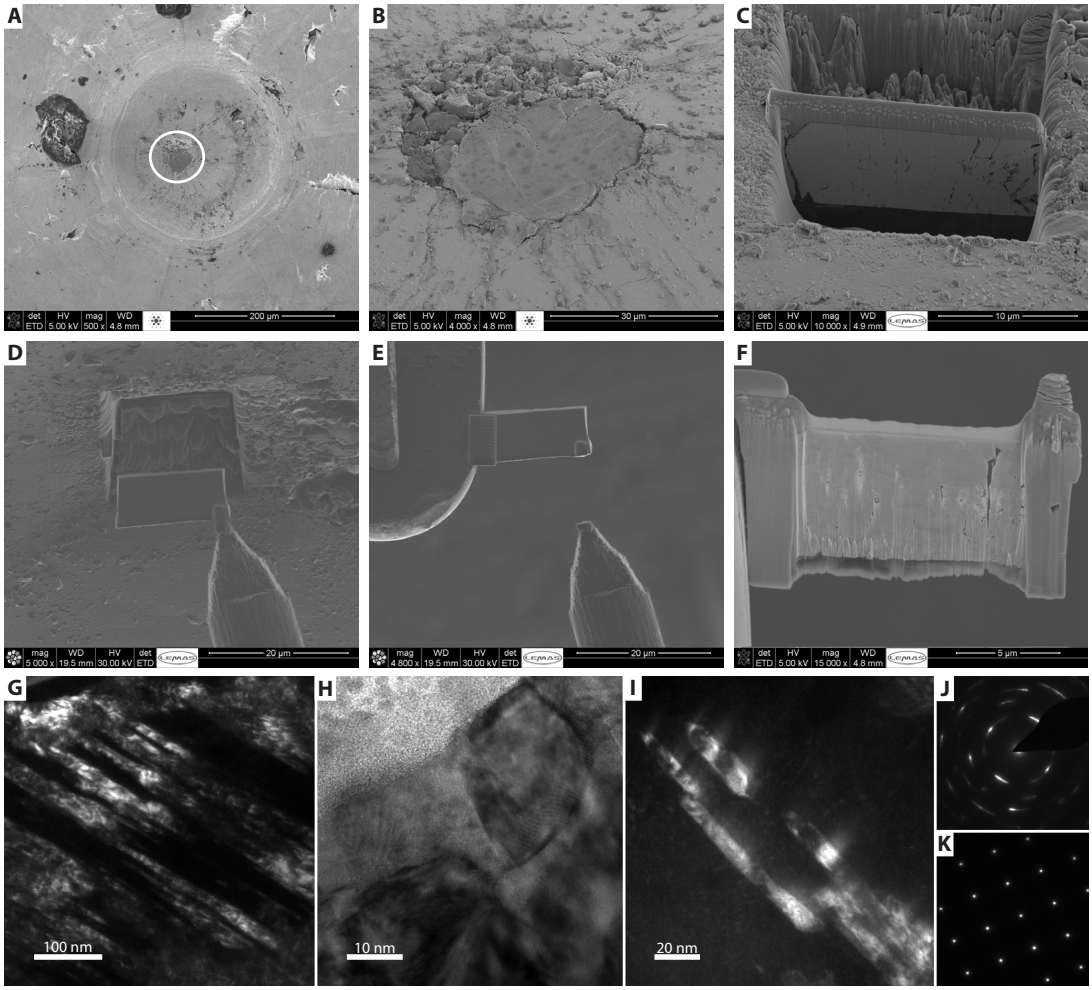


Figure 4.17: A-F) Preparation process of a TEM sample from recovered material by FIB techniques (see text for details). G) Darkfield image showing an array of elongated tungsten crystallites. H) Brightfield image of crystallites near the surface with preferred orientation perpendicular to the TEM-section. I) Darkfield image of small grains inside the sample. J) Electron diffraction pattern of nanocrystalline tungsten. K) Electron diffraction pattern of a control sample.

We recovered such dehydrogenated tungsten samples from the diamond anvil cells and used focused ion beam techniques to prepare TEM samples[9]. Figure 4.17A shows a SEM micrograph of the recovered gasket. The circle indicates the position of the tungsten inside the rhenium, magnified view under 45° shown in Figure 4.17B. The tungsten is subsequently excavated by FIB-milling, leaving a vertical section (Figure 4.17C). The dark line on the left side of the sample is the boundary between tungsten and rhenium. The section is then attached to a micromanipulator needle using FIB-assisted deposition (*in-situ* soldering) (Figure 4.17D) and transferred to a copper TEM sample holder (Figure 4.17E). At this stage, the sample is ∼500 nm thick. The final thinning to 80-100 nm thickness is achieved by low-energy FIB milling. The finalilzed TEM-sample is shown in Figure 4.17F. TEM brightfield and darkfield imaging revealed elongated crystallites with shortest dimensions of below 20 nm (see Figure 4.17G-I). The observed structure is similar to that of nanopolycrystalline diamond (NPD) which also exhibits elongated crystallites with diameters of 10-20 nm and lengths of up to a few 100 nm [Irifune 03]. This new form of artificial diamond was reported to be harder than natural single crystalline diamond [Irifune 03, Okuchi 09]. Electron diffraction measurements on dehydrogenated tungsten further show that the crystallites are not randomly oriented but follow a preferred orientation which explains the observed texture in the x-ray diffraction patterns. In a control experiment we prepared TEM samples from untreated tungsten. Both, TEM micrographs and electron diffraction patterns (Figure 4.17K) indicate perfect single crystallinity.

This microstructure can be related to the observed broadening of the diffraction peaks. As explained in chapter 3.3, peak broadening in x-ray diffraction patterns during synchrotron-based high-pressure experiments can be attributed to a mixture of strain broadening and size broadening. Due to insufficient quality of the XRD spectra, a Williamson-Hall analysis did not yield usable information. Therefore, we used the simple Scherrer formula (equation 3.15) to estimate the grain size observed in the x-ray experiments. The results for tungsten hydride are shown in Figure 4.18. It is evident that strain plays a significant role at higher pressures (indicated by the decreasing calculated grain

[9]Carried out at the LEMAS facility, Leeds, with M. Ward as local contact.

size).

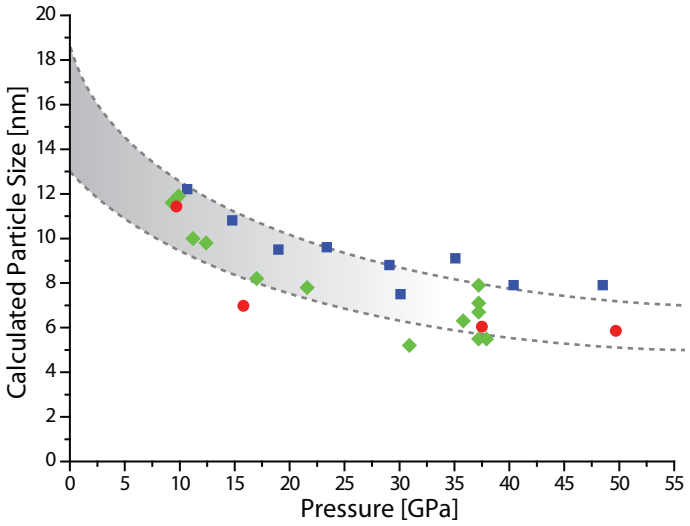


Figure 4.18: Average grainsize of tungsten hydride calculated using the Scherrer formula and the width of the (100) reflection. Data is shown for three independent experiments. The shaded area shows an extrapolation to zero pressure.

At zero pressure, strain effects due to non-hydrostatic compression in the DAC should vanish and the calculated grain size should be close to the actual grain size. Indeed, when simply extrapolating the trends seen in Figure 4.18 to zero pressure, a grain size comparable to what is found in the TEM images can be derived. It should be emphasized here, that the calculated values at high pressures do not correspond to actual grain sizes. Since the results of the Scherrer approximation for pressure increase as well as decrease are identical within the error of the method, it can be assumed that the microstructure does not change with pressure and that the observed microstructure in the recovered material is the same that is present at high pressures, and therefore also in the hydride phase. From the emergence of the broad diffraction peaks upon synthesis it can be concluded that it is, in fact, the hydrogenation process that leads to the formation of a nanomaterial.

On the basis of the presented data, the following hypothesis for the formation mechanism of a nanostructured material during the hydrogenation process is formed: The unusually slow progression of hydride formation (hindered by a

large energy barrier), accompanied by a structural phase transition, and the volume expansion during hydrogenation, creates significant stress between the hydrogenated and non-hydrogenated parts of the tungsten sample. Starting from the sample surface, hydrogenation slowly progresses into the material with only a very small volume near the hydride boundary undergoing the transition at any given time. With the release of local boundary strain, this leads to the formation of nanometer sized crystallites. The long dimension of the crystal grains found in our TEM studies is probably oriented along the hydride boundary during synthesis. The decomposition pressure usually lies close to the thermodynamic equilibrium of the system while the formation pressure lies higher due to the dissociation barrier encountered by the hydrogen molecule at the metal surface. Thus, once pressure is lowered below the equilibrium conditions, rapid dehydrogenation occurs leaving the microstructure intact. The rapid, and for a nanomaterial possibly rather violent decomposition could cause the observed precipitates. As a consequence, dehydrogenated tungsten exhibits the same microstructure as its binary hydride. It can be expected, that annealing at high temperatures would lead to a realignment of the nanometer sized grains and the formation of larger crystallites. Indeed, Zaleski-Ejgierd *et al.* seem to have observed this exact effect when laser heating tungsten hydride to above 1000 K [Zaleski-Ejgierd 12]. Room temperature however does not appear to have immediate or short term effect on the crystallite size. One of the samples studied by transmission electron microscopy was residing at ambient conditions for several months before TEM-sample preparation, while a different sample was recovered from high pressure only a few days prior to TEM measurements. There were no detectable differences in the microstructure between the two specimens.

Decreasing the grain size in materials down to a few tens of nanometers often entails significantly altered material properties, and it is known that, as the grain size decreases, the influence of interface and confinement effects on the properties of a material increases [Uchic 04, Janssen 07]. As a result, a nanostructured material might exhibit increased resistance to plastic deformation [Veprek 10] or different chemical stabilities compared to macroscopic systems [Fichtner 09]. In the case of metal hydrides, the grain size has profound impact on (de)hydrogenation processes, the overall hydrogen content and the volume

expansion of the metallic host lattice [Fichtner 09] due to interface stress between the grains. It was found for example in ball milled nanoparticles of vanadium hydride that the hydrogen content depends on the particle size [Orimo 01]. These possible nanometric effects make it difficult to compare tungsten hydride to other transition metal hydrides, *e.g.* in terms of volume expansion as a measure for hydrogen content, or to compare experimental with computational results. The phenomenon of increased resistance to plastic deformation is often summarized in the phrase "smaller is stronger" [Uchic 04] and can lead to an increase in a material's hardness by up to a factor of two [Veprek 10]. At the particular length scale of ∼20 nm (the "strongest size") the macroscopic hardness of a material is maximized [Veprek 10]. In contrast to the *intrinsic* hardness, being governed by the bulk material's elastic moduli, the *extrinsic* hardness is mainly influenced by the microstructure, *i.e.* crystallite shape and size. The ideal grain size arises from two competing mechanisms; the strengthening due to inhibited mobility of dislocations along crystallite interfaces (Hall-Petch effect [Petch 53]) and weakening caused by increased grain boundary shear [Veprek 10]. While the overall hardness of a material is usually tested using micro-indentation techniques, it has been shown in the past that high hardness is in many cases accompanied by high values of bulk and shear moduli [Fichtner 09, Berube 07, Veprek 10, Solozhenko 05]. However, at high pressures, where indentation techniques can not be applied, the hardness of a material is extremely difficult to address, with the bulk modulus - as a parameter in the material's equation of state - being the only easily accessible indicator.

A Vinet-type equation of state was therefore fitted to the x-ray diffraction data (see Figure 4.19). The EoS-data is listed in Tables A.11-A.14. Two cases had to be distinguished: While in some of the experimental runs the hydrogenation time was long enough and the whole sample was transformed, in others the measurements were conducted directly after passing synthesis conditions resulting in not fully transformed samples. In the data this is reflected in a slight unit-cell volume difference. Since WH does not exist below 8 GPa, the equation of state can only be established to this pressure. The resulting bulk moduli are 536 GPa (fully transformed samples) and 480 GPa (not fully transformed samples), respectively. However, in order to compare with other materials, extrapolation to 0 GPa is

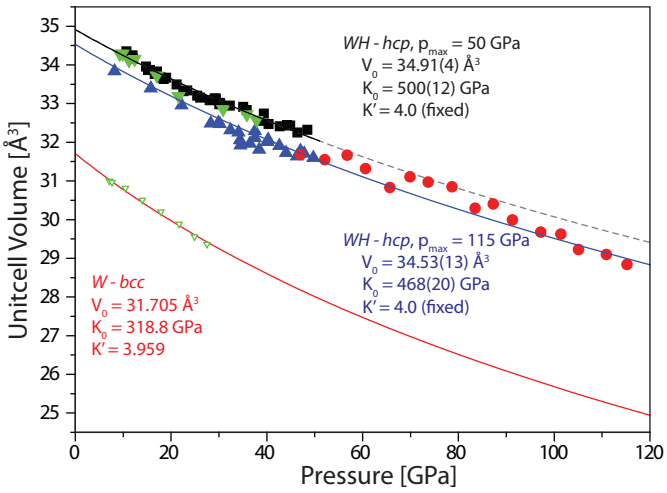


Figure 4.19: PV-data of tungsten hydride (see Tables A.11-A.14). Data were taken in both, compression and decompression. The EoS of tungsten is calculated from literature values (see Table 3.1). For WH, two separate Vinet-type EoS were fitted to the data from fully transformed (black squares and green downward-triangles) and partly transformed (blue triangles and red circles) tungsten hydride. Both EoS were fitted with fixed $B' = 4$ (equivalent to pure tungsten) and yielded 500(12) and 468(20) GPa, respectively. With $B' = 5.1$, the resulting bulk moduli were 476(12) and 410(20) GPa.

necessary. The zero-pressure bulk modulus of the fully transformed samples was found to be 500(12) GPa, while for the not fully transformed samples, the resulting equation of state yielded a zero-pressure bulk modulus of 468(20) GPa. In the former case, the maximum pressure was 50 GPa, reaching a compression of only ∼10%. This compression range is not sufficient to confidently constrain the bulk modulus. Nevertheless, given the results from the not fully transformed samples, for which the EoS was measured up to a pressure of 115 GPa, the bulk modulus can be constrained to above ∼460 GPa, surpassing all known compounds synthesized at high pressure and even diamond.

The finding of such a high bulk modulus in WH, more than 150 GPa higher than pure tungsten (see Table 3.1), is a very unusual result. Therefore, its validity has to be discussed in detail. The construction of the equation of state depends on the assumption of constant stoichiometry with increasing pressure. As discussed in chapter 3.3, the determination of the hydrogen content at any given pressure depends on the assumption that the compressibility of the hydride is identical to

that of the parent material. In other words, the two properties compressibility and hydrogen content, both measured as a function of the unit-cell volume, are not independent parameters. It is thus not possible to validate the equation of state as long as the hydrogen content is not known. Vice versa, it becomes difficult to make any statements about the hydrogen content at higher pressures. Furthermore, the empirical method of determining the hydrogen content has only been proven valid for macroscopic bulk material. In nanocrystalline materials, interface stress between the grains has an influence on the volume as well which poses an additional difficulty in addressing the hydrogen content.

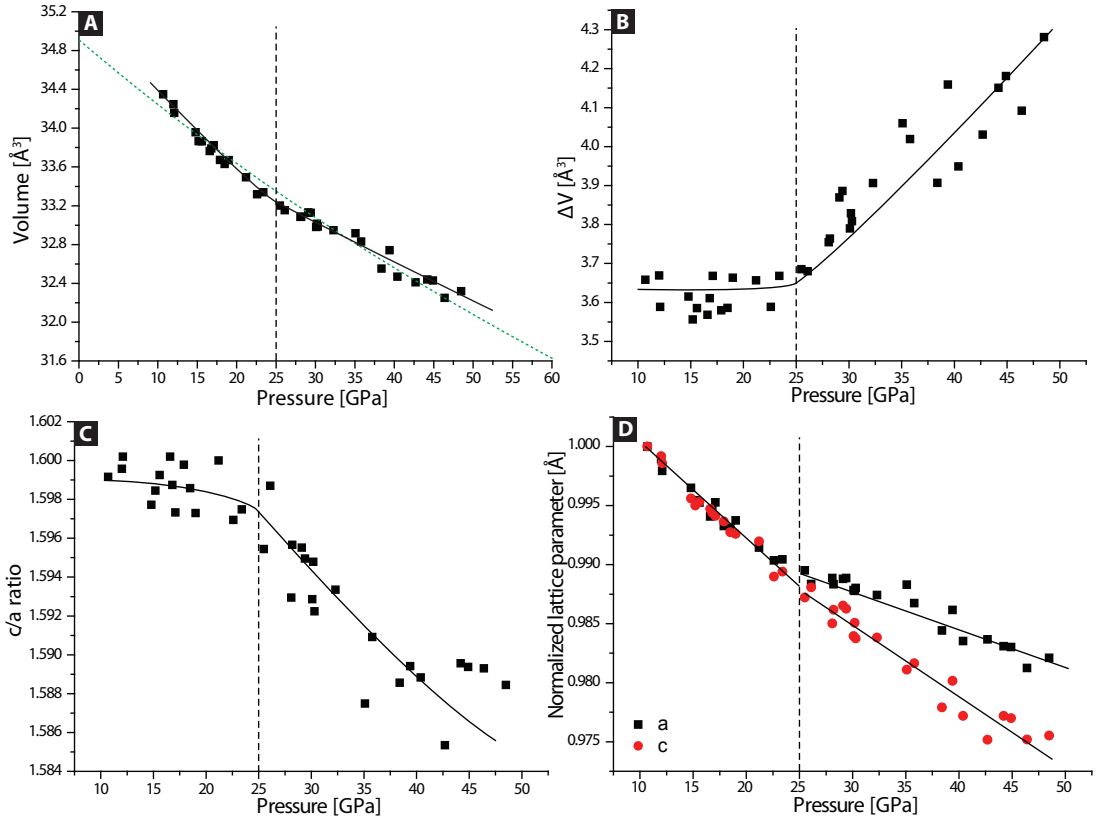


Figure 4.20: Results from the 3rd experimental run (see Table A.14, black squares in Fig. 4.19). A) Equation of state with Vinet fit (green dotted line) and guide to the eye (black line). B) Evolution of volume difference compared to tungsten with pressure. C) c/a ratio and D) lattice parameters vs. pressure. The vertical dashed line indicates synthesis pressure.

The extremely low compressibility *could* be attributed to a size-effect of the

nanocrystalline microstructure. However, the quality of fit is not convincing, showing deviations at lower and very high pressures. The best-quality data was collected during an experiment in October 2011 (see Table A.14). Although only a maximum pressure of 50 GPa was reached, it was possible to decompress from there to 16 GPa, then increase pressure again to 32 GPa and finally decompress to below the decomposition pressure. It was therefore possible to cross synthesis conditions in the hydride phase in both compression and decompression. The results of this single experiment are shown in figure 4.20. The data show a clear change in behaviour above synthesis conditions, independent of whether this point is crossed in compression or decompression. Below 25 GPa, both ΔV and c/a-ratio are constant, but change at higher pressures. Figure 4.20A) in particular shows a comparison of the result of a Vinet-fit to the data and a guide to the eye, indicating the clear change in behaviour above 25 GPa. Due to the insufficient quality of other experimental data this observation could not be reproduced. In particular, the results from the experimental run reaching 115 GPa are less reliable due to the fact that the sample was not fully transformed below at least 80 GPa.

Therefore, *ab-initio* calculations were employed to target crystalline structure, hydrogen content and equation of state. Similarly to [Zaleski-Ejgierd 12] the *hcp* structure of WH was found to emerge as thermodynamically stable at pressures above 20 GPa. Furthermore, WH_2 appears as stable against decomposition into $W+\frac{1}{2}H_2$. At pressures below 50 GPa, WH_2 would assume the $P6_3/mc$ structure, above the *Pnma* structure. Interestingly, the *Pnma* phase also appears to be metastable, *i.e.* stable against decomposition into $WH+\frac{1}{2}H_2$. Both phases are very similar to the *hcp* structure of WH where hydrogen atoms occupy the octahedral interstitial sites. In the $P6_3/mc$ arrangement of WH_2, tungsten atoms occupy the same hexagonal lattice points as for *hcp*-WH, but in addition to the octahedral sites, hydrogen atoms also occupy half of the available tetrahedral sites (2 per W-atom). The predicted *Pnma* structure is that of a slightly distorted hexagonal arrangement of the tungsten atoms. A transition between these phases therefore does not require a major rearrangement of the metal host lattice and thus, WH_2 might form in addition to WH at higher pressures.

Figure 4.21 shows the predicted equation of state for WH and PV-points for a mixed phase $(1-y)$WH + (y)WH$_2$ ($y = \frac{1}{3}$) in addition to experimental data. The computational EoS does not show a significant change in compressibility from pure tungsten. Comparison indicates that at pressures below 25 GPa (synthesis conditions), the sample seems to be purely tungsten monohydride. At pressures between 25 and 50 GPa, the volume deviates from the ideal equation of state, prompting an additional uptake of hydrogen and beginning occupation of the tetrahedral interstitial sites in the $P6_3/mc$ lattice. This can be described as a mixture of WH and WH$_2$ where all octahedral sites but only few tetrahedral sites are occupied. At pressures above 50 GPa, tetrahedral occupation seems to saturate at ~17% ($= y/2$). Even with time (some of our samples resided in this pressure region for several weeks), no higher hydrogen content seems to be reached. The lower volume in not fully transformed samples can be explained by a lower hydrogen content, probably due to a deficient filling of the octahedral sites.

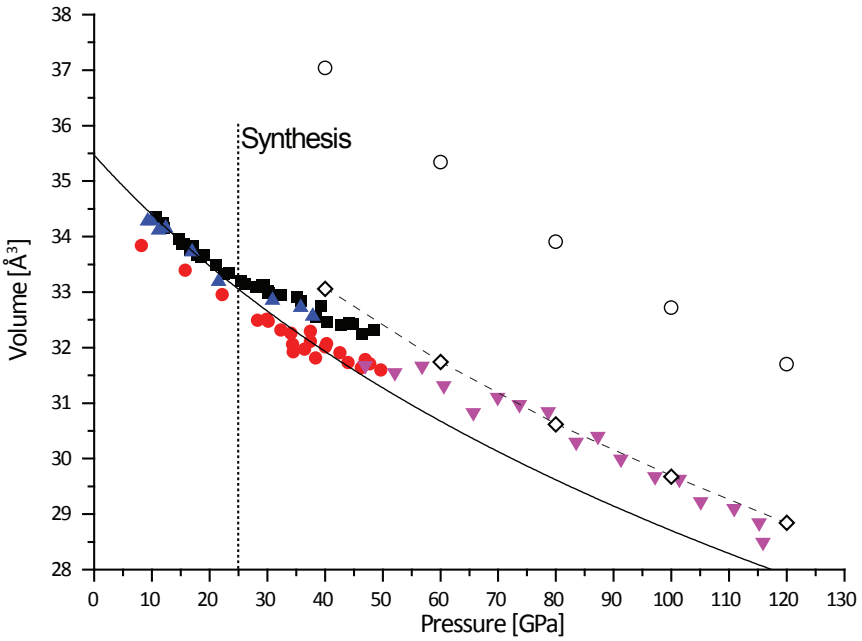


Figure 4.21: Pressure-Volume data of tungsten hydride. The solid line indicates the computational equation of state for WH. Open circles denote calculated PV points for WH$_2$, open diamonds for a fractional mixture of $\frac{2}{3}$ WH and $\frac{1}{3}$ WH$_2$. The dashed line is a guide to the eye. Solid symbols are experimental unit-cell volumes fitted with a hexagonal cell. Computational data courtesy F. Peng

From the computational results it can therefore be concluded that nanocrystalline tungsten hydride does *not* have a higher bulk modulus (as initially indicated by a simple Vinet fit to the data). It seems that in an intermediate pressure range, hydrogen atoms can occupy tetrahedral sites to a certain extent, depending on the applied pressure. This mechanism is hysteresis-free since atomic hydrogen can readily move from octahedral to tetrahedral sites and the dissociation barrier is overcome at above 25 GPa. At lower pressures, only octahedral sites are occupied because no additional hydrogen can be incorporated due to the dissociation barrier.

After platinum hydride, tungsten hydride exhibits the highest pressure of formation (25 GPa) for any interstitial transition-metal hydrides between the Cr-group and Cu-group elements. In contrast to PtH, tungsten hydride does not form instantly. A kinetic energy barrier hinders the transition and it requires at least several days for the whole sample to transform into the hydride phase at room temperature. The slow progression of hydride synthesis is suggested to be responsible for the transition from a coarsly grained or even single crystalline parent material into a nanomaterial. The change in microstructure as well as variable pressure-dependent hydrogen uptake could have potentially significant consequences for high-pressure experiments where tungsten is employed as a sealing material in experiments involving hydrogen.

4.4 Iridium

Iridium belongs to the group of elements for which no hydride phase was known. Resistivity measurements suggested that very small amounts of hydrogen might be absorbed ($x \sim 0.005$) at pressures around 9 GPa and a temperature of 150 °C [Verbetsky 00]. However, this is not commonly accepted as the formation of a bulk hydride. From the formation of the nitrides of iridium and osmium at conditions similar to the formation of platinum nitride [Young 06], it might be expected that an equivalent behaviour could be observed for hydrogen. However, although platinum hydride forms at pressures above 27 GPa, no formation of iridium hydride was observed in initial experiments at room temperature and pressures up to 50 GPa.

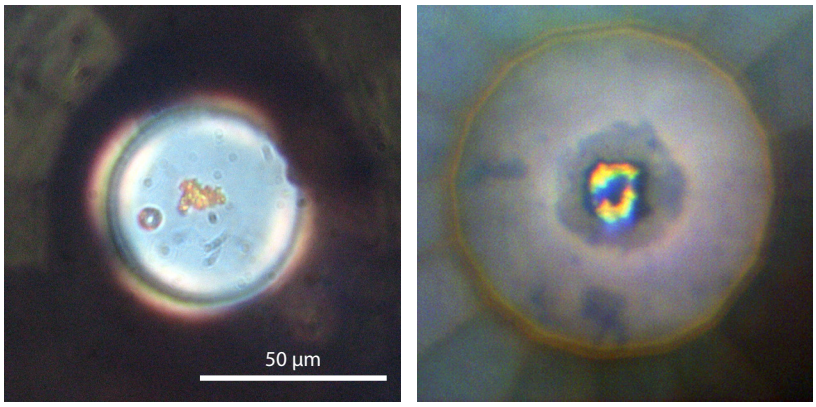


Figure 4.22: Optical micrographs of an open cell with iridium before hydrogen loading (left) and the closed cell at 110 GPa (right).

In a series of experiments reaching pressures of up to 125 GPa the formation of a novel phase in iridium surrounded by hydrogen was observed at pressures above 55 GPa. The new phase can initially be indexed in the $Pm\bar{3}m$ spacegroup (simple cubic) and exhibits a drastically reduced bulk modulus compared to pure iridium. Volumetric considerations combined with *ab-initio* calculations[10] identify the new phase as IrH_3 with hydrogen atoms occupying the $3c$ positions in the cubic metal

[10]Calculations were performed by Miriam Marqués, MALTA-Consolider Team, Spain, and University of Edinburgh and CSEC, UK. Here, only the implications of these calculations are discussed. For further details the reader is referred to the annexed manuscript (presubmission state at time of writing).

host lattice, a structure that has not yet been observed in this group of elements. This also makes iridium hydride the material with the highest hydrogen content of all known noble-metal hydrides, and the one with the highest synthesis pressure yet. Both, formation and decomposition were observed to be extremely slow, happening over a time period of several days. On decompression, the hydride phase was observed at pressures as low as 6 GPa. High temperature accelerates the formation which indicates the presence of a high kinetic energy barrier. The low decomposition pressure and slow kinetics of the reaction suggest that the material can be quenched to ambient pressure at low temperatures.

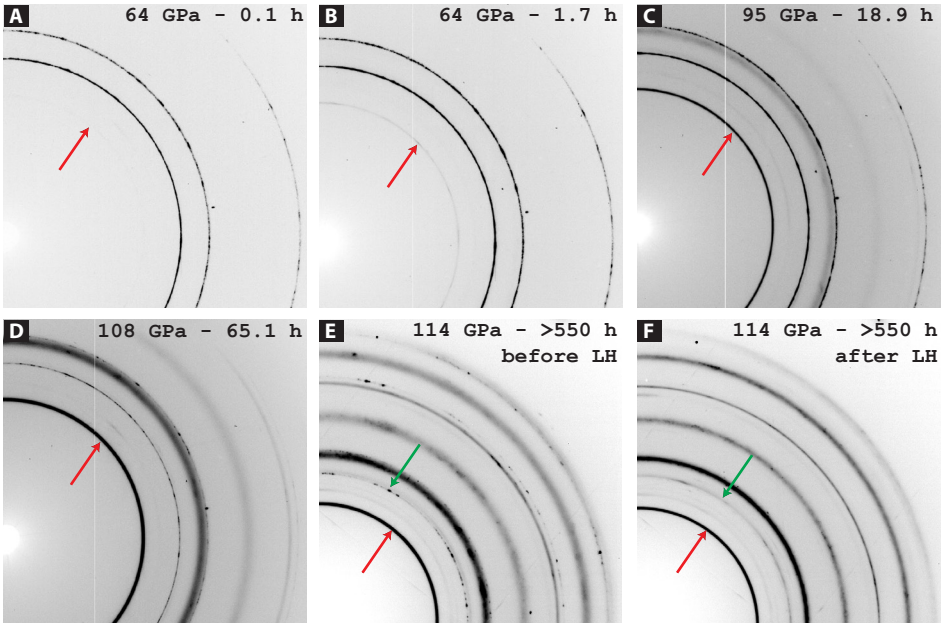


Figure 4.23: 2D XRD patterns of iridium hydride. The given times are hours after passing 55 GPa. The red arrow indicates the (001) peak of simple cubic iridium hydride, the green arrow in E) and F) indicates the (111) peak of *fcc* iridium. Additional weak rings in this area stem from rhenium hydride.

In three experimental runs, we loaded symmetric diamond anvil cells with pristine iridium powder (Alfa Aesar, 99.9% purity) and hydrogen precompressed to 2000 bar. In two cases, flat diamond culets of 200 μm diameter, in the third case beveled diamonds with a top culet diameter of 90 μm were used. The gasket material was rhenium. Gasket holes were laser drilled and in the case of the beveled diamond run FIB-techniques were employed. The FIB-drilled

gasket hole shows superior shape-stability up to very high pressures and allowed high-quality XRD-measurements to be carried out even at pressures reaching 125 GPa. Figure 4.22 shows the development of the gasket hole with pressure. The ruby fluorescence scale was used at pressures below 70 GPa. Above, the calibrated hydrogen vibron scale was used in conjunction with the diamond Raman scale. Single-sided laser heating was used to study the reaction kinetics. XRD-measurements were carried out at I15 (DLS), ID09a (ESRF) and P02.2 (PETRA-III).

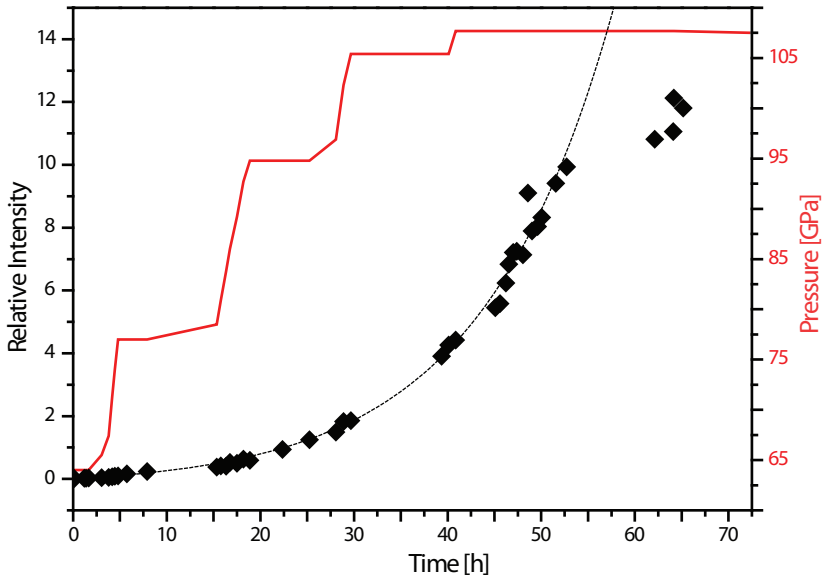


Figure 4.24: Ratio of intensities between the (111) peak of iridium and the (001) peak of iridium hydride. The dashed line denotes an exponential fit to the data up to $t = 50$ h. The red solid line indicates the pressure (right scale). Data is listed in Table A.15.

The three experimental runs had three complimentary goals: Run-1 used flat 200 μm diamonds which allowed to reach pressures between 60 and 70 GPa. Despite experimental difficulties at beamline P02.2 (PETRA-III)[11], we were able to reach 60 GPa and observed the appearance of extremely weak new reflections. The new peaks gained intensity with time but remained extremely weak (comparable to Figure 4.23B - from the second run). After the experiment, the cell was kept at pressure and measurements were continued two months later

[11]The beamline only became operational a few weeks prior to our experiments

at beamline I15 (DLS). However, pressure had dropped over time to $\sim$ 50 GPa. The new phase was clearly visible but still weaker than the parent *fcc*-phase of pure iridium. On decompression, the phase remained stable and did not show any signs of decomposition down to 23 GPa at which point diamond failure occurred and the sample was quenched to ambient conditions. Although the diamond culet was still intact (ring crack around the culet), the sample hole had collapsed entirely and it was not possible to detect any signal besides rhenium and traces of pure iridium.

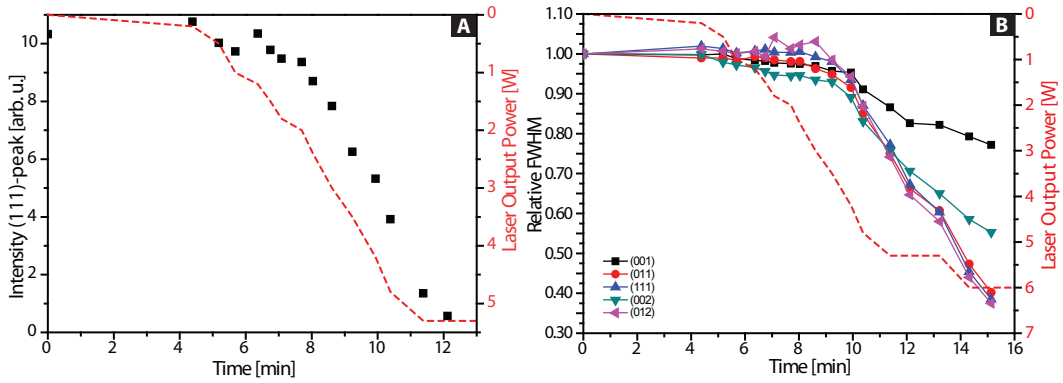


Figure 4.25: Effect of laser heating. A) Scattering intensity of the strongest *fcc*-Ir peak. B) Relative change of the widths of the observed iridium hydride peaks. The red dashed line denotes the laser out power (right scale). Data is listed in Tables A.16 and A.17.

Run-2 employed beveled diamonds and a gasket specifically prepared by focused ion beam milling in order to reach the highest possible pressures. Synthesis conditions were confirmed by XRD at beamline ID09a and the first weak signature of the new phase was detected at 60 GPa. Over the period of three days, pressure was increased in steps up to 108 GPa with times of constant pressure between increases (Figures 4.23A-D). The process of formation was monitored over time by comparing the scattering intensity of the (111) peak of *fcc*-Ir and the strongest peak of the new phase (red arrows in Figure 4.23) . The result is displayed in Figure 4.24. It can be clearly seen that the transformation of the sample accelerates exponentially during the first 50 hours of the transition process, independent of pressure. Afterwards, the transition slows down. Run-2 was continued 3 weeks later at beamline P02.2. Even after that time, the sample was not completely converted and small portions of iridium remained

(a ratio of 13-15 was measured). We therefore applied gentle single-sided laser heating to the sample. The higher temperatures should allow the sample to overcome kinetic barriers and complete the formation. This was indeed observed as can be seen in Figure 4.23E-F. Comparably low laser power of below 6 W was sufficient to reduce the scattering intensity of the remaining Ir signal resulting in a complete conversion within 12 minutes (Figure 4.25A). The sample was not

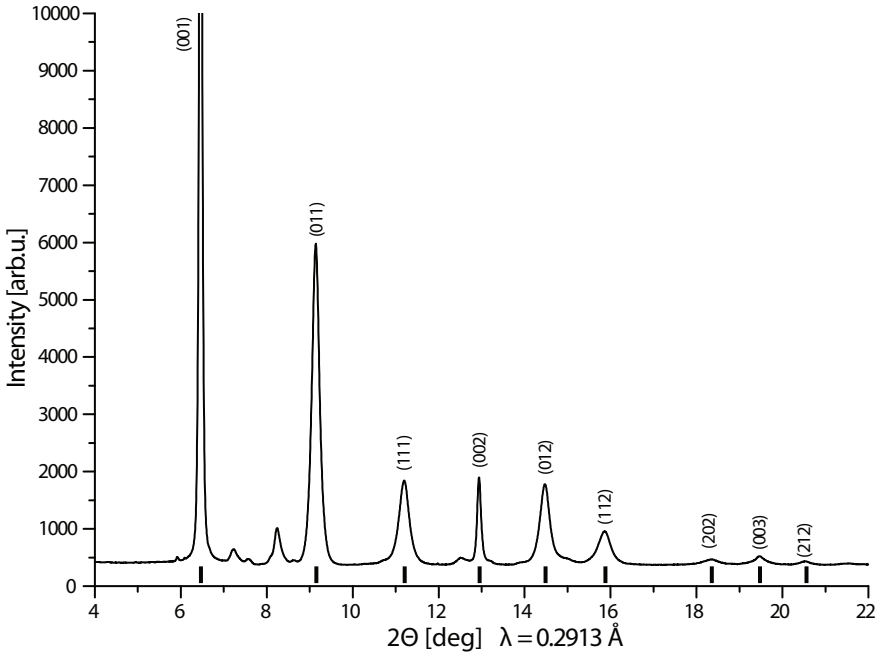


Figure 4.26: Integrated spectrum of iridium hydride at 126 GPa, after laser heating. The additional peaks are rhenium hydride. Tick marks show calculated peak positions for spacegroup $Pm\bar{3}m$ with $a = 2.5856$ Å.

observed to glow and thus temperature measurements were not possible. It can only be assumed that the temperatures were below 1000 K. It was also observed that the widths of the diffraction peaks were reduced at laser powers above 3 W (Figure 4.25B). This suggests that, above a certain temperature, internal strain or disorder in the new phase is released or a possible microstructure is annealed, forming larger crystallites (analogue to the process observed in tungsten - see chapter 4.3).

Pressure was increased to 125 GPa and no *fcc*-Ir signal could be detected at this point. The resulting spectrum was used to identify the host structure as $Pm\bar{3}m$ (simple cubic) - see Figure 4.26. Earlier XRD experiments at I15 and

ID09a were carried out at lower photon energies and did not resolve any peak above the (112) reflection. Thus, the structure was at first mistaken for a *bcc*-phase. It should be noted here that the peaks show different widths, which was difficult to interpret at this point. This is discussed in further detail below.

Run-3 was intended to study two aspects of this material: i) Formation kinetics and ii) equation of state and stability. For this reason, flat diamonds of 200 μm culet size were used again in order to reach synthesis conditions but also facilitate decompression. Pressure was increased to 50 GPa and kept there for two weeks. No signs of synthesis were detected. At 55 GPa, a weak signal was measured and at this point single-sided laser heating[12] was employed at constant pressure to accelerate the formation process (see Figure 4.27). Due to insufficient coupling between the laser and the sample no direct effect was observed for the first few hours and it can be seen that the transformation process is almost identical to what is observed at room temperature and variable pressure. Once good coupling of the laser to the sample was established, fast transformation was observed and within less than 30 min, the sample had almost completely converted (see inset in Figure 4.27). The d-spacing of the (001)-peak remained almost constant during the heating process, which indicates that no significant change in stoichiometry or pressure took place. Unfortunately, only incomplete transformation was achieved because the sample moved during the heating process and was afterwards in contact with the rhenium gasket which acted as a heat dump. On decompression, the simple cubic phase remained visible to pressures as low as 6 GPa although the relative scattering intensity decreased throughout the decompression process (Figure 4.28). From the data it is not conclusive whether the decrease in scattering intensity is due to pressure or a kinetic effect with time. However, a more rapid decomposition can be observed below $\sim$16 GPa indicating that this marks the decomposition pressure. Interestingly, no decrease in scattering intensity was noted in the previous run-1 (diamond failure at 23 GPa), where the relative composition was always below the level of what was reached in run-3. It can be argued that a fully converted sample might not show any signs of decomposition at pressures above 16 GPa. If it is assumed that the speed of decomposition below 16 GPa is governed by kinetic

[12]Laser heating experiments were carried out by Zuzana Konôpková, beamline P02.2 (PETRA-III)

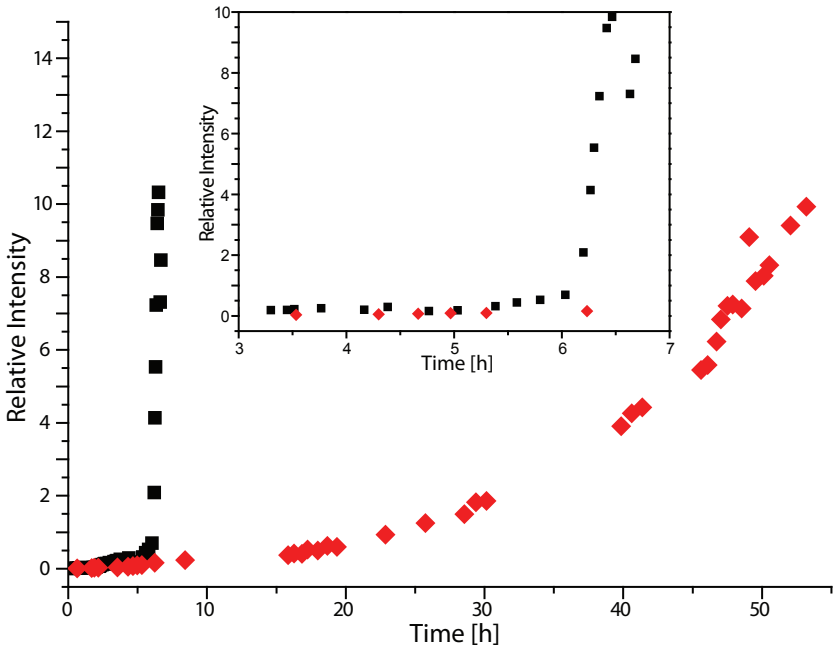


Figure 4.27: Relative Intensity of the (001) peak of iridium hydride compared to Ir-(111) at constant pressure and laser heating (black squares) and at room temperature (red diamonds - see Figure 4.24). Inset shows enlargement of the time-span between 3 and 7 hours after passing synthesis pressure. Data is listed in Table A.18.

effects, then i) decomposition is a slightly faster process than formation and ii) the sample might be recovered to ambient pressure during a fast decompression process. Furthermore, if higher temperature accelerates the formation process, low temperature might hinder decomposition below 16 GPa.

The combined data from all three runs allowed for the construction of the equation of state in the pressure range from 6 to 125 GPa. The EoS was fitted to a Vinet function resulting in a zero pressure volume of $V_0 = 23.33$ Å^3. The bulk modulus varied between 190 and 230 GPa, depending on the choice of B'. Table 4.1 shows the detailed results and Figure 4.29 displays the equations of state of iridium and the simple cubic hydride phase.

As can be seen from the equation of state, the new phase has a significantly increased atomic volume compared to the parent metal but at the same time a

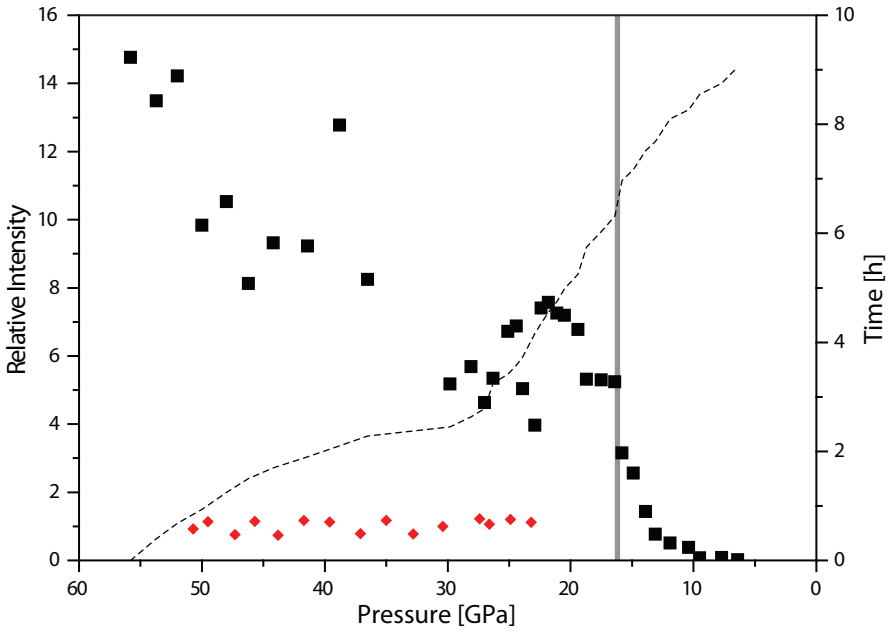


Figure 4.28: Relative Intensity of iridium hydride during decompression (black squares) in run-3. The red diamonds are data from previous run-1. The thin dashed line links pressure to time after decreasing pressure to below synthesis conditions (right scale). The grey vertical line indicates the pressure/time at which a more rapid decrease in scattering intensity was noted. Data is listed in Table A.19.

drastically reduced bulk modulus, almost half of that of pure iridium (383 GPa [Cynn 02]). No other hydride is known to exhibit a simple cubic metal host lattice. Comparison with other metals is therefore not applicable. The simple cubic lattice only offers one interstitial site, the $1b$ position, corresponding to the body-centered location in the unit-cell. However, the volume of this interstitial site is much larger than for the octahedral and tetrahedral sites in closed-packed structures. For hydrogen atoms occupying this location the interaction with the metal host lattice would be weaker and a correspondingly smaller lattice expansion should be measured. In the present case however, $\Delta V > 9$ Å^3 was found at zero pressure. Such a large volume expansion can not be explained by single site occupation of the 1b position, even if a hydrogen molecule is considered. Simple volumetric considerations thus suggest a hydrogen content of $x = 3$ and lead to the initial assumption of hydrogen atoms occupying the $3c$ sites (see Figure 4.30), corresponding to face-centered positioning of hydrogen atoms.

Table 4.1: Results of the Vinet fit to EoS.

Refined parameters	B_0 [GPa]	B'
B_0 and B'	190(3)	5.62(11)
B_0 only	205(1)	5 (fixed)
B_0 only	231(1)	4 (fixed)

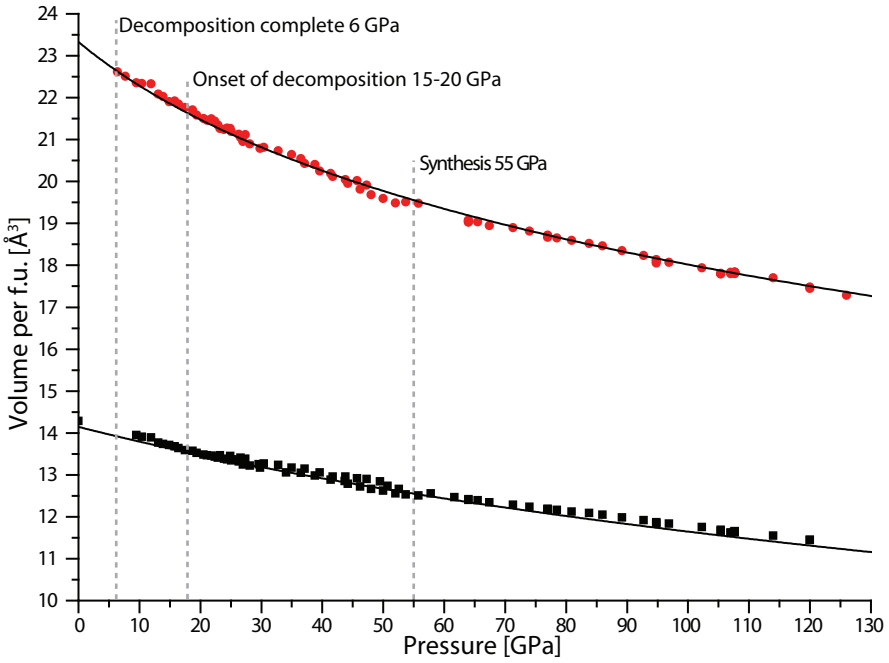


Figure 4.29: EoS of iridium hydride (red circles) and pure iridium (black squares) between 6 and 125 GPa. Solid lines are calculated EoS (for Ir see Table 3.1). The EoS parameters for iridum hydride are $V_0 = 23.33$ Å^3, $B_0 = 190$ GPa, $B' = 5.62$. Data is listed in Tables A.20-A.22.

However, there is no experimental proof for this assumption. For this reason, *ab-initio* calculations were carried out on this material. The results of these calculations confirm IrH_3 as the most likely stoichiometry. Assuming the $Pm\bar{3}m$ spacegroup (Ir atoms located on the 1*a* sites), the according pressures for varying hydrogen occupations were calculated. From simple volume-pressure considerations the structures with H-atoms located on 1*b* and 3*d* sites can be disregarded: Taking the experimentally measured volume per atom at 81 GPa (V = 18.59 Å^3), the calculated pressures for both structures are too low or too high at -0.5 GPa and 324.6 GPa, respectively. Good agreement (98.5 GPa) is found

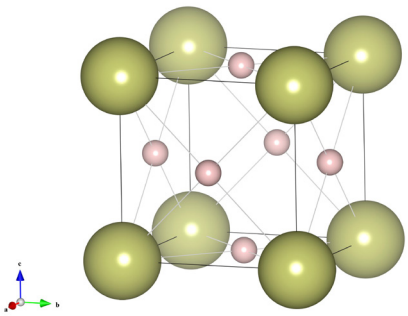


Figure 4.30: Suggested $Pm\bar{3}m$ structure of iridium hydride, with hydrogen atoms occupying the $3c$ position.

for the structure with hydrogen atoms occupying the $3c$ sites (equivalent to the initial assumption). For this structure, the calculated parameters for the equation of state are, V_0=23.291 Å^3, B_0=249.9 GPa, B_0'=4.32. The calculated EoS thus lies above the experimentally observed (see Figure 4.31A). When constraining $B' = 4$ in fitting the equation of state to our experimental data, a bulk modulus of $B_0 = 231$ GPa is found, closer to the computational result. However, the quality of fit deteriorates drastically, rendering this value significantly less plausible. It is possible that the synthesized hydride is not fully stoichiometric which would result in a lower volume. Although a deviation from ideal stoichiometry at higher pressures can not be excluded, it does not seem likely. Even if site vacancies exist in the synthesized material, the H:M ratio would still be very close to 3.

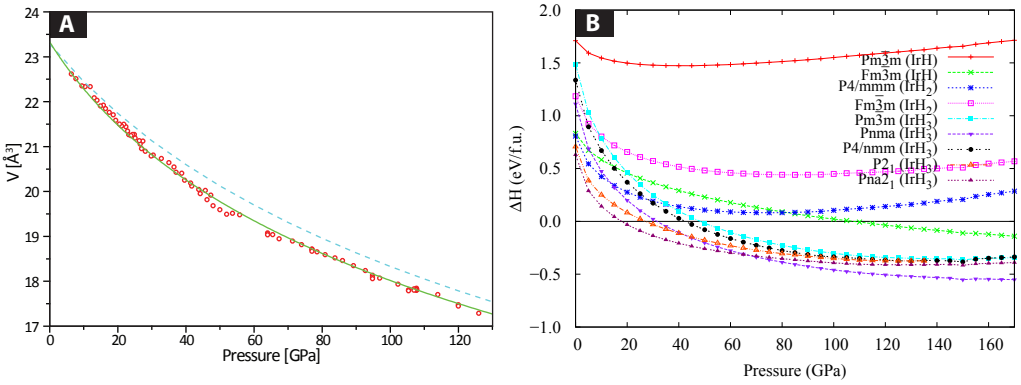


Figure 4.31: A) Calculated (blue dashed line) compared to measured equation of state. B) Total energy calculations of iridium hydride against decomposition (courtesy Miriam Marqués).

Interestingly, the $Pm\bar{3}m$ structure appears to be neither energetically favourable nor dynamically stable. Figure 4.31B shows the enthalpy difference of various possible hydride structures against decomposition. It can be seen that, at pressures below 65 GPa, the $Pna2_1$ structure with 4 metal atoms per unit-cell is energetically favourable and, as it turned out, also dynamically stable. It becomes unstable against decomposition into iridium and molecular hydrogen at pressures below 20 GPa, in good agreement with the onset of decomposition observed experimentally. This structure can be seen as a slightly distorted simple cubic lattice in which the positions of the iridium atoms deviate from their equilibrium positions in a simple cubic cell. This leads to a splitting of Bragg peaks into doublets or triplets in the diffraction pattern, which offers a possible explanation for the observed difference in peak width (see Figure 4.26). A Le Bail fit of the $Pna2_1$ spacegroup is in good agreement with experimental data at 125 GPa and also agrees with the initial indexing in a simple cubic phase (see Figure 4.32). Additional visible reflections not accounted for in the $Pna2_1$ structure can be identified as rhenium hydride.

Table 4.2: Calculated parameters for the $Pna2_1$-structure at 60 GPa

Parameter	Value	
a	3.78707 Å	
b	3.98280 Å	
c	5.47426 Å	
α,β,γ	90°	
Atom	Site	Fractional coordinates (x,y,z)
Ir	4a	0.46417, 0.50267, 0.22593
H	4a	0.30900, 0.69722, -0.03158
H	4a	0.75778, 0.78019, 0.54176
H	4a	0.01244, 0.57245, 0.26057

Table 4.2 shows the calculated parameters and atomic positions for the $Pna2_1$ structure at 60 GPa. The actual distortion of the lattice might be smaller than predicted computationally due to kinetic effects. At pressures above 65 GPa, a different structure ($Pnma$ spacegroup) emerges as dynamically stable and energetically favourable. This structure, which still exhibits a H:M ratio of 3, can not be treated as a distortion of the simple cubic lattice. For a comparison of atomic positions in the $Pm\bar{3}m$, $Pna2_1$ and $Pnma$ structures, see Figure 4.33.

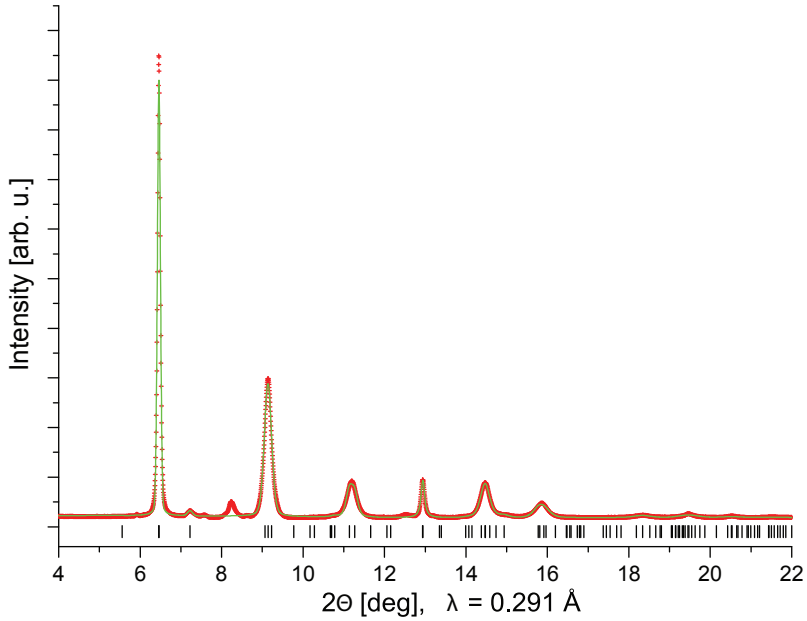


Figure 4.32: Le Bail fit (green solid line) of the $Pna2_1$ structure to experimental data at 125 GPa (red crosses). The derived lattice parameters are $a = 3.6183$ Å, $b = 3.6834$ Å, $c = 5.1674$ Å, giving a volume of $V_{\mathrm{at}} = 17.2173$ Å^3. Tick marks indicate principal reflections of this space group. However, due to internal symmetry, some reflections have zero intensity. For comparison, a simple cubic lattice ($Pm\bar{3}m$) fitted to the same data yielded a lattice parameter of $a = 2.5823$ Å, giving a nearly identical volume of $V_{\mathrm{at}} = 17.2195$ Å^3.

Details of the *Pnma* phase are given in Table 4.3.

No experimental evidence is found for this phase in our data up to 125 GPa. It can be assumed that, similarly to other hydride phases, the formation is hindered by an energy barrier, which also accounts for the large hysteresis between synthesis and decomposition pressure in the cubic phase. The observed change in compressibility between the hydride and the parent material can be explained on the basis that the hydrogen atoms are positioned directly on the crystalline planes of the metal lattice and thus influence its mechanical properties. Figure 4.34A shows a comparison of the equations of state of pure iridium and iridium hydride to very high pressures. It can be seen that the volume difference stabilizes at ~ 4.725 Å^3, corresponding to ~ 1.575 Å^3 per hydrogen atom. Applying the hydrogen equation of state (see chapter 3.2) one finds this to correspond to free hydrogen at ~ 250 GPa.

Table 4.3: Calculated parameters for the *Pnma*-structure at 120 GPa

Parameter	Value	
a	3.46685 Å	
b	3.46582 Å	
c	5.95841 Å	
α,β,γ	90°	
Atom	Site	Fractional coordinates (x,y,z)
Ir	4c	0.24575, 0.25, 0.08289
H	4c	0.12279, 0.25, 0.60209
H	8d	0.62608, 0.03759, 0.68183

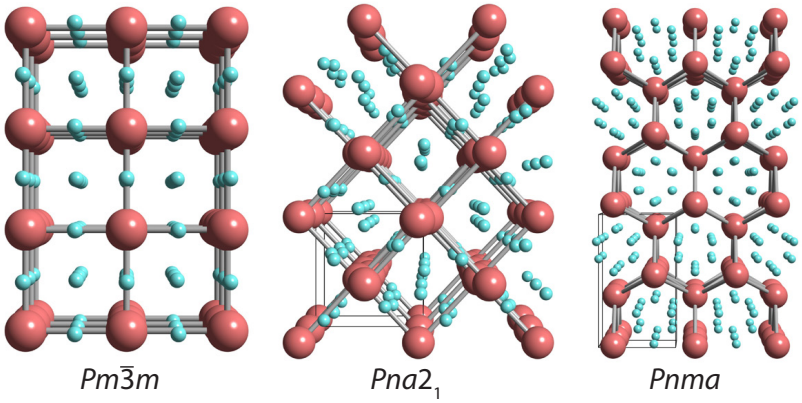


Figure 4.33: Atomic positioning in the $Pm\bar{3}m$-structure (left), $Pna2_1$-structure (middle) and *Pnma*-structure (right). Larger red spheres denote iridium atoms, smaller blue spheres hydrogen atoms.

Therefore, hydrogen atoms are not as incompressible in this structure as they are in interstitial hydrides. Although hydrogen appears to be precompressed at lower pressures, the equivalent hydrogen pressure never surpasses 250 GPa. This finding is interesting regarding the prediction that chemically precompressed hydrogen might undergo metallization at experimentally accessible pressures [Ashcroft 04]. Figure 4.34B shows ΔV for IrH_3 compared to the hydrogen equation of state for 3 hydrogen atoms. The evolution of ΔV with pressure can be interpreted as the equation of state of the confined hydrogen. It can be seen that the observed curve approaches the equation of state of free hydrogen and crosses it at ~250 GPa. It can be expected that the structure will decompose once the volume of the confined hydrogen becomes larger than that of free hydrogen at

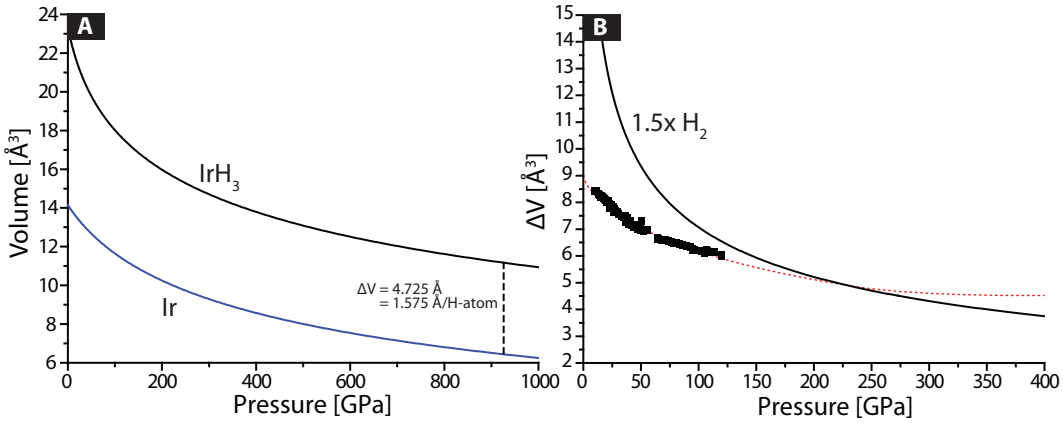


Figure 4.34: A) Comparison between experimentally derived EoS for iridium hydride and iridium. B) Volume difference between Ir and IrH_3 in comparison to the hydrogen equation of state (here for 3 hydrogen atoms). The red dashed line denotes a guide to the eye for the evolution of ΔV.

this point.

IrH_3 has the highest hydrogen content of all noble-metal hydrides, the highest synthesis pressure and a structure unknown for any other hydride. Formation and decomposition are governed by slow kinetics which may stabilize the material at ambient pressure and low temperatures. It has a drastically reduced bulk modulus compared to pure iridium due to the confined hydrogen being non-interstitial and as such being able to influence the metal lattice. Theoretical calculations show iridium hydride as a metal, although this is not proven experimentally.

4.5 Copper

The following section contains a brief summary of our findings on copper hydride. For a more detailed report, the reader is referred to the master thesis by Christian Donnerer and the accompanying publication (see annex to this thesis). The primary goal was to replicate the cubic phase of copper hydride reported in [Burtovyy 04]. There seemed to be a dispute in the community as to whether this form of copper hydride exists or not. In preliminary experiments, we found pure copper to react with hydrogen at pressures between 18 and 20 GPa to form a hexagonal phase of copper hydride, not the cubic phase observed in [Burtovyy 04]. However, from private communications with M. Tkacz, co-author of the paper from 2004, it appeared as if copper showed some kind of memory effect in hydrogenation: If the metal had been in the hydride phase and subsequently dehydrogenated, it would form under equilibrium conditions not the hexagonal but the cubic phase.

In two experimental runs, we loaded copper thin foil (Alfa Aesar, 99.8% purity) into symmetric diamond anvil cells with 300 μm culets and gas-loaded hydrogen to a pressure of 1800 bar. Rhenium was used as gasket material and ruby for pressure measurements. In two independent runs, pressure was increased to 50 GPa, released to below 10 GPa (when the decomposition of the hexagonal phase was observed) and increased again to 20 GPa.

A closer analysis of the hexagonal phase showed that the structure formed under equilibrium conditions in the DAC was not the wurtzite structure of chemically synthesized copper hydride: Weak superstructure reflections of the *hcp* lattice were found indicating a structure similar to rhenium hydride (see Figure 4.35). Volumetric considerations suggest fully stoichiometric anti-CdI_2-type Cu_2H. The phase transition was found to occur between 18 and 20 GPa in both experimental runs. However, in the first run, only incomplete transformation was observed with *fcc*-Cu visible even at 50 GPa. In the second run, immediate and complete transformation was observed at 18.5 GPa with no *fcc*-Cu evident. The equation of state did not show any significant change in compressibility (see Figure 4.36). Fitting a Vinet equation of state to the data yielded $V_0 = 13.10(1)$ Å^3, $K_0 = 145(5)$ GPa ($K' = 4.8(3)$), apart from the volume expansion no significant

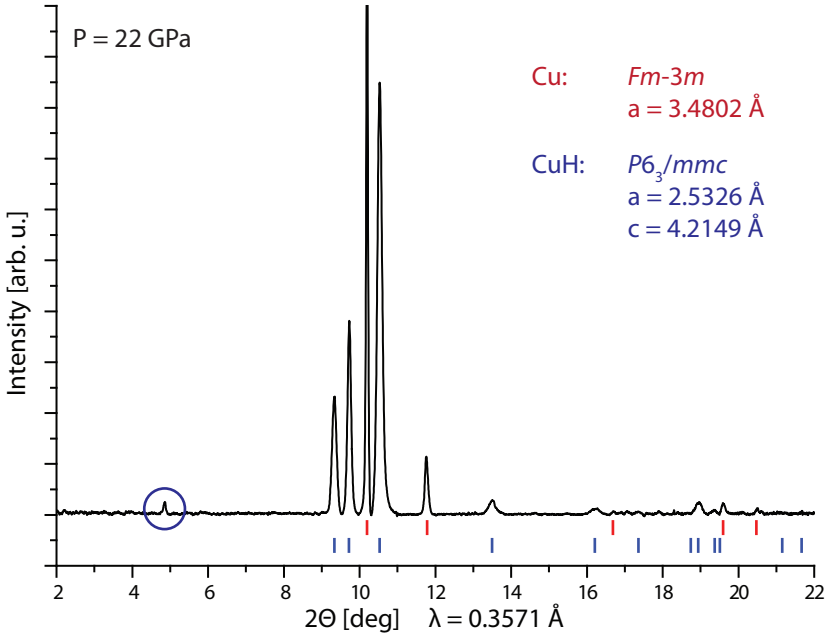


Figure 4.35: Integrated XRD spectrum showing cubic copper (red upper tick marks) and hexagonal copper hydride (blue lower tick marks) at 22 GPa. The blue circle indicates the position of the (001) forbidden reflection.

difference to pure copper. Decomposition was observed on decompression below 10 GPa.

In the second run, pressure was increased again after decomposition and a slight volume increase in *fcc*-Cu was observed, indicating possible formation of the cubic phase of copper hydride. However, the measured volume difference was considerably smaller than reported in [Burtovyy 04]. This is assumed to be due to either different previous hydrogenation states or longer hydrogenation times in the study from 2004.

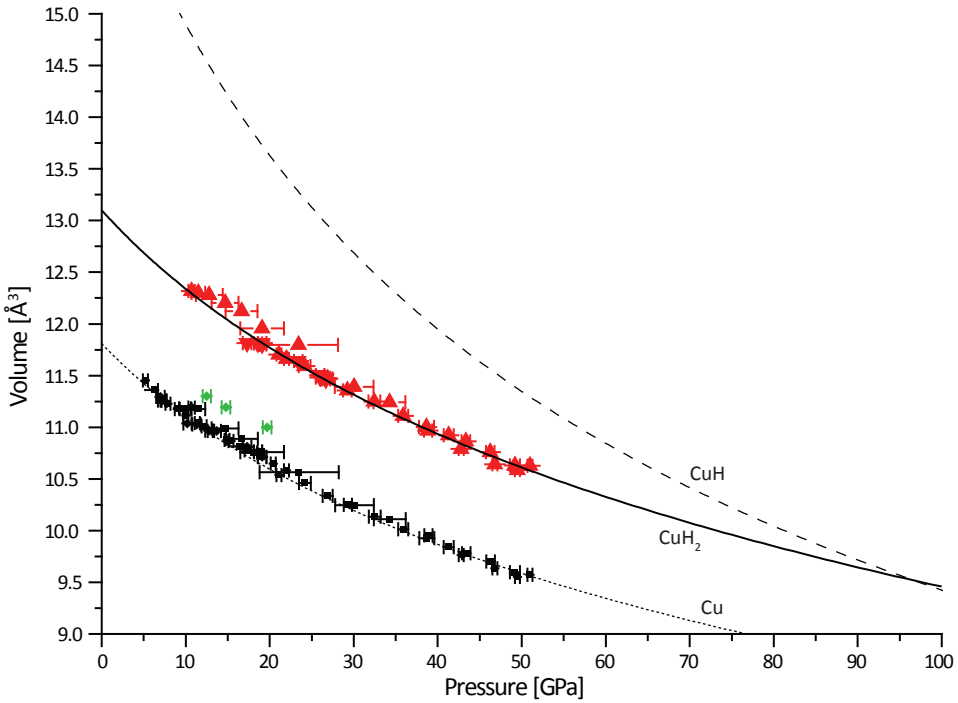


Figure 4.36: Experimental equation of state of copper (black squares) and copper hydride (red triangles). The dotted line denotes the equation of state of copper (see Table 3.1), dashed line the EoS of wurtzite CuH [Filipek 07]. The solid line is a Vinet fit to our data, yielding $V_0 = 13.10(1)$ Å^3, $K_0 = 145(5)$ GPa ($K' = 4.8(3)$). The green diamonds are attributed to the formation of cubic copper hydride on repeated compression after decomposition from the hexagonal hydride phase.

4.6 Other metals

In this section, the attempts to synthesize the hydrides of gold, silver and osmium are described. Considerable effort was put in the synthesis of Au-H but no hydride phase was observed. All three metals were compressed to very high pressures (87 GPa for Ag and Os, 115 GPa for Au) without showing any signs of hydrogenation.

4.6.1 Gold

There is considerable dispute in the high-pressure community whether the hydride phase of gold exists or not. In 1982, a report by V.E. Antonov claimed the synthesis of gold hydride at moderate pressures of only 2.8 GPa and temperatures

above 600 K with time [Antonov 82]. Upon hydride formation, the sample (a gold wire of 0.2mm diameter) increased notably in volume and the surface became uneven and of grey colour. The hydride was apparently kinetically unstable at ambient conditions and decomposed into Au and H_2 within several weeks. X-ray diffraction on the sample showed a very complex structure which could be indexed in an orthorombic unit-cell with $a = 6.8$ Å, $b = 9.61$ Å and $c = 7.85$ Å. V.E. Antonov kindly provided us with a sample from the original synthesis from almost 30 years ago. An x-ray diffraction pattern of that sample, taken in 2011 at Diamond Light Source is shown in Figure 4.37. The pattern clearly shows a strong presence of gold with the lattice parameter expected for ambient conditions. More than 40 additional weak reflections can be identified. However, they can not be indexed using an orthorombic unit-cell and the cell parameters given by Antonov. Due to severe overlap with the gold peaks in some areas, a clear identification of the additional phase was not possible. In particular since it is not clear if there is only one underlying phase. It is therefore questionable whether the complex phase seen in Figure 4.37 is indeed a hydride phase of gold, stable after 30 years at ambient conditions, or an artifact from synthesis conditions such as contamination or surface reaction with sealing material.

In the past three decades, the results described in [Antonov 82] were not observed again. It is therefore widely accepted nowadays that gold does not form a hydride phase, at least not at commonly accessible pressures which is also backed up by theoretical studies (*e.g.* [Gao 12]). Gold is sometimes used as a sealing material in experiments involving hydrogen. A layer or coating of gold between the sample volume and a rhenium gasket should prevent the formation of rhenium hydride and thus the loss of hydrogen. However, there are indications that gold hydride might form at certain pressures and room temperature[13]. In a study from 2007, it was found that gold (there called "the noblest of all metals") undergoes a structural phase transition from the *fcc* to the *hcp* phase at pressures above 250 GPa [Dubrovinsky 07]. The formation of a hydride at this pressure is a possibility. Furthermore, it can be argued that, once hydrogen is at least in a partly atomic state, hydrogen atoms do not have to overcome the dissociation

[13]Private communications with T. Strobel (Carnegie Inst. Washington, USA): A reaction that might be attributed to the formation of gold hydride was observed at pressures above 60 GPa and room temperature. However, this was not confirmed and no detailed study exists.

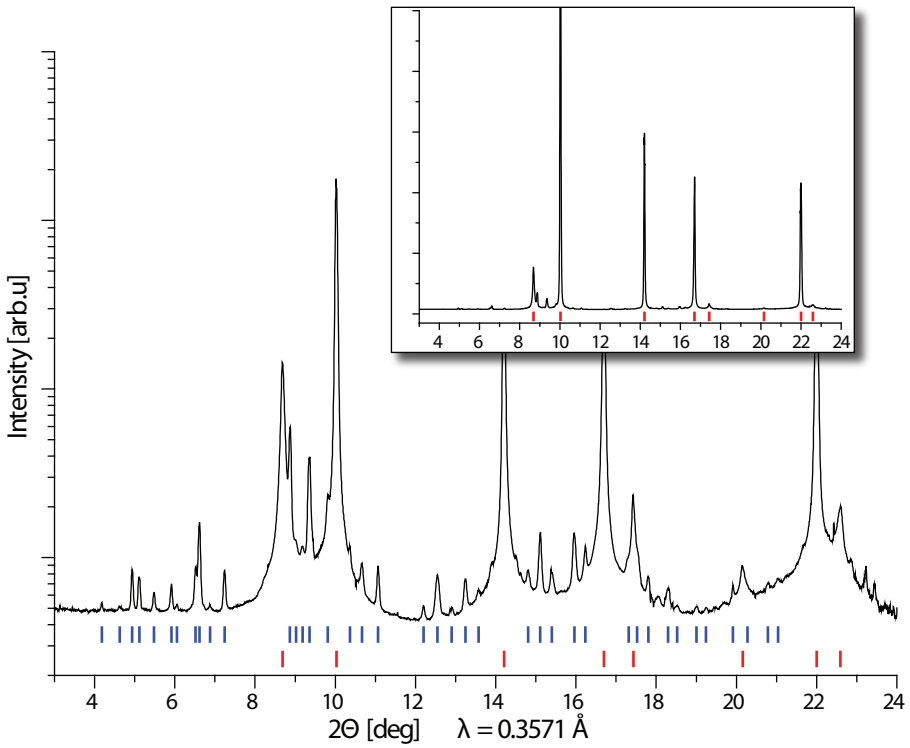


Figure 4.37: Diffraction pattern of a sample provided by V.E. Antonov. Red tick marks indicate *fcc*-Au at ambient pressure (a = 4.0811 Å), blue marks are identified reflections not belonging to gold. A refinement of the structure was not possible. Inset shows the same spectrum on linear scale.

barrier at the metal surface and any metal will undergo hydrogenation. The structure of phase IV of hydrogen, reported in [Howie 12], is partly atomic and thus the formation of a hydride might be expected at pressures above 220 GPa.

In the work presented in this thesis, attempts were made to replicate the original synthesis conditions of gold hydride as well as synthesis at high pressure and room temperature. In several experiments, diamond anvil cells were prepared with a rhenium gasket, hydrogen gas-loaded to ∼2000 bar and gold powder (Alfa Aesar, 99.96+% purity). No reaction was detected up to 115 GPa at ambient temperatures. In experiments up to 50 GPa the cells were heated using both external resistive heaters and ovens without any reactions occurring. The experiments involving heating in an oven led to the discovery of ϵ_2-ReH (see chapter 4.2).

4.6.2 Silver

There is no report of a bulk hydride phase of silver (see chapter 2.3). However, recent theoretical studies speculate that silver hydride might form at very high pressures. In [Kim 11], AgH appears dynamically stable at pressures above 50 GPa, while [Gao 12] gives a formation pressure for AgH of more than 180 GPa. In a series of experiments we studied silver (thin foil, Alfa Aesar, 99.97% purity) under a hydrogen atmosphere up to a pressure of 80 GPa and room temperature without observing any signs of hydride formation. Laser heating to above 1000 K (no controlled temperature measurement was possible) at pressures around 40 GPa also had no effect on the structure of the sample.

Figure 4.38 shows the measured equation of state of silver in a hydrogen

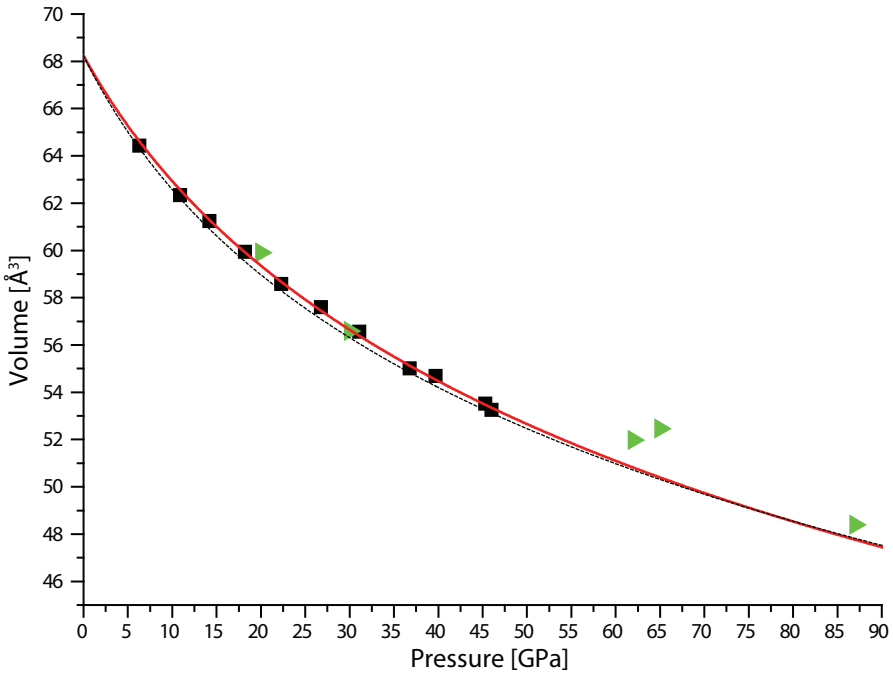


Figure 4.38: EoS of silver measured in a hydrogen atmosphere. The solid red line denotes a Vinet fit to the data: $V_0 = 68.23$ Å^3, $B_0 = 100.5$ GPa, $B' = 5.21$. The dashed line is an EoS taken from literature ([Akahama 04a], see Table 3.1).

medium compared to the EoS from literature. The two data points at ∼65 GPa suggest a volume increase of $\sim$ 1.5 Å^3 compared to pure silver. However, this difference is not seen in subsequent measurements at higher pressures. In this particular experimental run, pressure calibration was difficult: No ruby was used and pressure was derived using the diamond and hydrogen Raman scales which

are unreliable at this pressure (see chapter 3.2). The observed volume difference could therefore be explained by erroneous pressure measurement.

4.6.3 Osmium

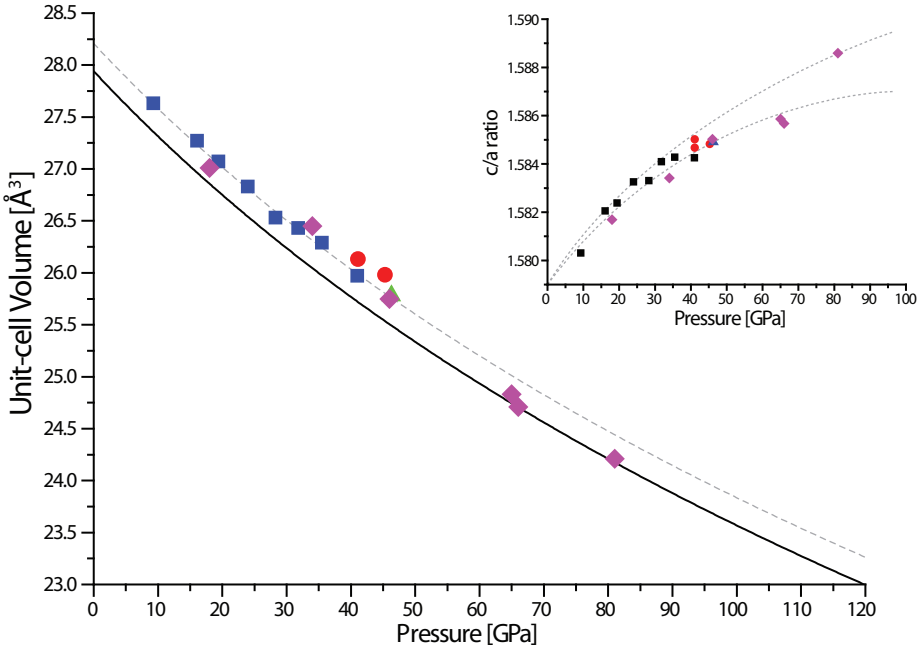


Figure 4.39: Measured EoS of Os under hydrogen atmosphere compared to literature EoS (solid line, see Table 3.1). Inset shows c/a ratio vs. pressure. Grey dashed lines are guides to the eye regarding the difference in EoS and change in c/a ratio.

In [Antonov 84], a hydrogen content of 0.03% was reported for osmium under hydrogen atmosphere. It has been discussed (see chapter 2.3) that such a low hydrogen content might indicate the adsorption of hydrogen on a surface layer of the metal sample and not the formation of a bulk hydride. We conducted a series of experiments with osmium (Alfa Aesar, -200 mesh powder, 99.8% purity) in a hydrogen medium reaching pressures of 80 GPa. Laser heating at lower pressures had - similarly to silver - no effect on the structure or unit-cell volume of the sample. Interestingly however, a very small constant volume difference of $\sim$0.25 Å^3 was measured (see Figure 4.39), equivalent to $\sim$6% hydrogen content. This was measured at different synchrotron radiation sources and independently

also in various samples. However, at higher pressures above 50 GPa, the volume expansion could not be seen any more. The observed trend of increasing c/a ratio (see inset in Figure 4.39) with pressure was also mentioned in literature [Armentrout 10]. It is therefore difficult to conclude whether a reaction between hydrogen and osmium took place or not. Several data points presented in Figure 4.39 were collected from the same sample over a period of 6 months during which the sample remained at pressure. No change in volume was detected. If the measured volume difference is attributed to an uptake of hydrogen it also has to be concluded that the uptake happens almost immediately and does not increase with time. Also, laser heating did not have any effect, excluding kinetic barriers as reasons for hindered hydrogen uptake (as observed *e.g.* in rhenium and iridium).

Chapter 5

Conclusions and Future Prospects

The aim of this thesis was to study the synthesis of the remaining unknown hydrides of the transition metals. Three new phases were discovered (ϵ_2-ReH, ϵ-Cu_2H and IrH_3) while the known hydrides of tungsten and platinum were characterized experimentally for the first time. Despite considerable experimental effort, the hydrides of silver, gold and osmium remain elusive.

The study of platinum hydride was motivated primarily by the findings of superconducting silane in [Eremets 08]. It was shown that through the decomposition of silane at 50 GPa [Degtyareva 09], hydrogen is released and reacts with the platinum probes present in the study by Eremets *et al.*. We characterized the hydride of platinum in terms of mechanical properties, crystalline structure and stability regarding decomposition. In theoretical calculations it was found that PtH might be superconducting [Scheler 11b] and as such might be responsible for the superconductivity observed in [Eremets 08]. However, to date, this was not observed experimentally which provides a very interesting prospect for future experiments. In fact, in [Kim 11], the critical temperature for superconductivity in PtH was estimated to be in the range of 25 K, significantly higher than palladium hydride which up to now holds the record for the highest T_c in the d-metal hydrides. Furthermore, the elusive intermediate phase I of PtH has not been fully characterized yet. This is the only known instance in the d-metals where such a phase forms. Can this phase be stabilized

at temperatures different from room temperature? What is its interaction with PtH-II?

Tungsten hydride was, similarly to PtH, known but its existence went largely unnoticed by the research community due to a lack of available information. Our primary goal was to replicate the synthesis conditions described in [Kawamura 05] and establish a thorough characterization of tungsten hydride. In the process we found that tungsten hydride exhibits a very unusual behaviour: It does not form instantaneously when crossing the synthesis conditions but only converts with time. Our data suggest that this very slow hydrogenation process might be responsible for the formation of a nanocrystalline microstructure, reminiscent of nanopolycrystalline diamond [Irifune 03]. What at first appeared to be very low compressibility was, with the help of computational methods, found to be the fractional formation of tungsten dihydride. Although predicted to be stable in the probed pressure region we did not succeed in obtaining a pure WH_2 phase. Does it exist? What is the exact role of pressure and temperature in this case? Does the microstructure play a significant role in the formation of WH_2? It was reported in [Zaleski-Ejgierd 12], that laser heating leads to a sharpening of the Bragg peaks. Interpreting this as an annealing of the nanocrystalline structure, what are the effects on the hydride phase? Could this lead to the formation of pure WH_2 or could it be the nanocrystalline nature of the material that allows occupation of the tetrahedral sites in the first place? Thus, annealed tungsten hydride would be simply a monohydride.

Rhenium is widely used as a gasket material and the formation of rhenium hydride is widely known and accepted. It therefore came as a surprise when we found a new phase of rhenium hydride which forms at high temperatures but is stable at room temperature [Scheler 11a]. The observation of this phase happened during an experiment attempting the synthesis of gold hydride and demonstrates that even well-studied systems should not be neglected and might still hold surprises. Unfortunately, due to the nature of the experiments performed on the ϵ_2-phase of ReH, there was a very high risk of diamond failure and gasket collapse. Few questions therefore remain unanswered: What is the stability range of ϵ_2-ReH? Could it be recovered to ambient conditions? What are the exact conditions

required for its formation? ϵ_1-ReH decomposes at near ambient conditions but the new phase could be stable or metastable due to the presence of a large energy barrier which might prevent decomposition. It also remains to be experimentally proven whether stoichiometric ReH forms at high pressure or with time.

Iridium hydride proved to be completely different from all other hydrides in the investigated group of *d*-metals. It has a very high hydrogen content, the highest synthesis pressure of all known metal hydrides in this range and a crystalline structure different from all other metal hydrides. Due to the presence of hydrogen in non-interstitial positions, IrH_3 has a much higher compressibility compared to pure iridium. This of course leads to the question whether hydrogen is compressed in the metal matrix and whether IrH_3 might be a candidate for achieving the metallization of hydrogen in host matrices [Ashcroft 04]. The equation of state shows that the volume difference stabilizes at a value equivalent to hydrogen at ~250 GPa, far from metallization conditions. IrH_3 is stable to surprisingly low pressures and decomposes only slowly. Is it then (meta)stable when quenched to ambient conditions? The whole formation/decomposition process in iridium hydride happens very slowly, a phenomenon that has been observed in several systems throughout this work. The kinetic effects are difficult to address in theoretical calculations and thus such simulations might fail to predict certain phases or in contrast predict the existence of phases that are inaccessible due to kinetic barriers. For iridium hydride, we did not observe the predicted *Pnma* phase, but the reached pressures might just have been insufficient. Maybe the hydrides of osmium, silver and gold can be synthesized at accessible pressures but require higher thermal energy than provided in experiments thus far.

Most research projects on hydrogen systems nowadays focus on two aspects: The development of a suitable hydrogen storage material and the properties of free hydrogen at extreme pressures. However, as the results in this work show, there is a large margin for phenomena in between, such as hydrogen-mediated synthesis of nanomaterials or novel superconductors. The *d*-metal hydrides still hold various opportunities for researchers in the future, starting from measuring the electronic properties of these materials *in-situ* to the successful synthesis of the missing hydrides of osmium, silver and gold.

Appendix A

Data Tables

P[GPa]	V[Å^3]	c/a	a[Å]	c[Å]	(010)	(002)	(011)	(012)	(110)
7	24.516	1.628	2.591	4.218	2.244	2.109	1.981	1.537	1.295
10	21.862	1.626	2.495	4.056	2.161	2.028	1.907	1.479	1.247
15	19.112	1.622	2.387	3.872	2.068	1.936	1.824	1.413	1.194
20	17.339	1.619	2.313	3.743	2.003	1.872	1.766	1.368	1.156
25	16.04	1.615	2.255	3.642	1.953	1.821	1.721	1.332	1.128
30	14.921	1.613	2.203	3.552	1.908	1.776	1.68	1.3	1.101
35	14.234	1.61	2.169	3.492	1.879	1.746	1.655	1.279	1.085
40	13.566	1.608	2.136	3.434	1.85	1.717	1.629	1.259	1.068
45	12.975	1.606	2.105	3.381	1.823	1.69	1.605	1.24	1.053
50	12.464	1.604	2.078	3.333	1.8	1.667	1.584	1.223	1.039
55	12.012	1.602	2.053	3.29	1.778	1.645	1.564	1.208	1.027
60	11.624	1.601	2.031	3.253	1.759	1.626	1.547	1.194	1.016
65	11.265	1.6	2.011	3.217	1.741	1.609	1.531	1.182	1.005
70	10.933	1.599	1.991	3.183	1.725	1.592	1.516	1.17	0.996
75	10.627	1.598	1.973	3.152	1.709	1.576	1.502	1.159	0.987
80	10.355	1.596	1.957	3.123	1.695	1.562	1.489	1.148	0.978
85	10.122	1.595	1.942	3.098	1.682	1.549	1.478	1.14	0.971
90	9.867	1.594	1.926	3.071	1.668	1.535	1.466	1.13	0.963
95	9.648	1.593	1.912	3.046	1.656	1.523	1.455	1.121	0.956
100	9.468	1.592	1.901	3.026	1.646	1.513	1.446	1.114	0.95
105	9.276	1.59	1.889	3.003	1.636	1.502	1.436	1.106	0.944
110	9.096	1.589	1.877	2.982	1.625	1.491	1.427	1.099	0.938
115	8.917	1.588	1.865	2.961	1.615	1.48	1.418	1.091	0.932
120	8.784	1.586	1.856	2.944	1.608	1.472	1.411	1.086	0.928

Table A.1: Hydrogen EoS (see [Loubeyre 96]), c/a-ratio and observed d-spacings of Bragg reflections up to 120 GPa.

Table A.2: XRD experiments carried out in the course of this thesis. The used DAC's are DC (Symmetric D-type "doughnut"), B (Betsa), GG (Gregoryanz-Guillaume type) and P.C. (long Piston Cylinder). Inhouse beamtimes were conducted in collaboration with the team at the respective beamlines and are not assigned experiment numbers.

Metal	Experiment	Date	Source	DAC
Pt	HS4048	June 2010	ID09, ESRF	DC
	HS4039	July 2010	ID09, ESRF	DC
	inhouse	August 2010	ID09, ESRF	DC
W	EE6317	February 2011	I15, DLS	DC
	EE6833	May 2011	I15, DLS	DC
	EE7263	October 2011	I15, DLS	DC
	HS4458	November 2011	ID09, ESRF	DC
Au	EE6317	February 2011	I15, DLS	B
	EE7263	October 2011	I15, DLS	P.C.
	inhouse	May 2012	P02, PETRA-III	GG
Re	EE6317	February 2011	I15, DLS	B
	EE6833	May 2011	I15, DLS	B
Ir	inhouse	July 2011	P02, PETRA-III	DC
	EE7263	October 2011	I15, DLS	DC
	HS4609	July 2012	ID09, ESRF	DC
	scheduled	August 2012	P02, PETRA-III	DC
	inhouse	October 2012	P02, PETRA-III	DC
Cu	inhouse	July 2011	P02, PETRA-III	DC
	EE7263	October 2011	I15, DLS	DC
	HS4724	October 2012	ID09, ESRF	GG
Ag	inhouse	July 2011	P02, PETRA-III	DC
	HS4458	November 2011	ID09, ESRF	DC
	inhouse	May 2012	P02, PETRA-III	DC
Os	EE7263	October 2011	I15, DLS	DC
	HS4458	November 2011	ID09, ESRF	DC
	inhouse	May 2012	P02, PETRA-III	DC

P[GPa]	V[Å^3]	a[Å]	c[Å]	c/a	ΔV[Å^3]
27.5	15.906	2.783	4.742	1.704	1.986
31.3	15.844	2.782	4.728	1.699	2.044
34	15.87	2.784	4.73	1.699	2.16
37	15.796	2.779	4.723	1.699	2.176
42	15.67	2.772	4.708	1.698	2.2
45	15.594	2.77	4.694	1.695	2.209
48	15.501	2.763	4.69	1.697	2.201
50	15.491	2.765	4.679	1.692	2.241

Table A.3: Platinum hydride refined unit-cell parameters for phase II (*hcp*), loading 1.

P[GPa]	V[Å^3]	a[Å]	c[Å]	c/a	ΔV[Å^3]
27	15.815	2.779	4.731	1.703	1.875
29	15.883	2.783	4.736	1.702	2.013
30.8	15.88	2.784	4.73	1.699	2.07
31.9	15.846	2.782	4.727	1.699	2.076
33.2	15.838	2.782	4.726	1.699	2.088
35.5	15.741	2.777	4.715	1.698	2.081
38.5	15.657	2.772	4.704	1.697	2.087
40.4	15.614	2.77	4.699	1.696	2.094
41.4	15.581	2.768	4.697	1.697	2.096
43.6	15.465	2.761	4.684	1.696	2.045
44.1	15.453	2.761	4.681	1.695	2.043
45.2	15.434	2.761	4.677	1.694	2.054
47.3	15.382	2.758	4.672	1.694	2.062
50.4	15.199	2.746	4.654	1.695	1.959
51.8	15.132	2.742	4.646	1.694	1.932
54.5	15.048	2.738	4.637	1.694	1.908

Table A.4: Platinum hydride refined unit-cell parameters for phase II (*hcp*), loading 2.

P[GPa]	V[Å^3]	a[Å]	c[Å]	c/a
18	102.649	3.125	12.141	3.885
25	101.697	3.112	12.128	3.897
27.5	100.924	3.102	12.111	3.904
31	100.648	3.101	12.086	3.898
34	100.67	3.102	12.081	3.895
37	99.299	3.083	12.061	3.912

Table A.5: Platinum hydride refined unit-cell parameters for phase I (complex phase), loading 1.

P[GPa]	V[Å^3]	a[Å]	c[Å]	c/a
27	100.225	3.096	12.072	3.899
29	100.989	3.101	12.124	3.909
30.8	100.594	3.091	12.154	3.932
31.4	101.203	3.097	12.188	3.936
33.2	100.515	3.098	12.091	3.902

Table A.6: Platinum hydride refined unit-cell parameters for phase I (complex phase), loading 2.

P[GPa]	V[Å^3]	ΔV[Å^3]
50.8	14.98	1.75
75.88	14.32	1.67
113.27	13.78	1.8
161.23	13.36	2.04
189.4	13.12	2.115
113	13.893	1.913
112.78	13.55	1.57

Table A.7: P-V data extracted from [Eremets 08], there interpreted as silane.

P[GPa]	V[Å^3]	ΔV[Å^3]	a[Å]	c[Å]	c/a
16.2	15.625	1.51	2.843	4.463	1.57
19.9	15.24	1.244	2.819	4.429	1.571
23.7	14.84	0.962	2.792	4.397	1.575
26.5	14.64	0.845	2.775	4.39	1.582
28.5	14.515	0.779	2.765	4.382	1.585
30.2	14.4	0.712	2.752	4.391	1.595
30.8	15.19	1.519	2.814	4.431	1.575
33.3	15.205	1.603	2.819	4.42	1.568
35.9	14.655	1.124	2.791	4.344	1.556
42.1	14.605	1.234	2.774	4.382	1.579
45.2	15	1.706	2.794	4.438	1.588
46.4	14.91	1.646	2.796	4.405	1.576

Table A.8: Lattice parameters and volume differences measured for rhenium hydride, initial experiment, pressure increase. Before 16.2 GPa, the sample was heated to 150 °C for 19.5 hours. Waited for 16h between 30.2 and 30.8 GPa. Heated to 200 °C for 4.5h after 45.2 GPa and 300 °C for 8.5h after 46.4GPa.

P[GPa]	V[Å^3]	ΔV[Å^3]	a[Å]	c[Å]	c/a
46	27.92	0.686	2.732	4.321	1.582
37	28.4	0.698	2.744	4.357	1.588
31	28.47	0.57	2.753	4.338	1.576
25	28.88	0.601	2.762	4.372	1.583
17.5	29.23	0.542	2.771	4.395	1.586
11.5	30.04	0.745	2.798	4.43	1.583
4	30.62	0.759	2.818	4.453	1.58
0	31.21	0.896	2.84	4.467	1.573

Table A.9: Lattice parameters and volume differences measured for rhenium hydride, initial experiment, pressure decrease after heating to 300 °C.

P[GPa]	V[Å^3]	ΔV[Å^3]	a[Å]	c[Å]	c/a
17.3	30.13	1.971	2.803	4.429	1.58
14.6	30.25	1.913	2.807	4.434	1.58
18.2	30.08	1.98	2.801	4.427	1.581
23.2	30.25	2.463	2.811	4.421	1.573
23.2	29.62	1.833	2.799	4.367	1.56
26.9	30.06	2.494	2.805	4.411	1.573
28.9	30.04	2.59	2.803	4.412	1.574
32.6	29.98	2.738	2.802	4.41	1.574
35.2	29.96	2.86	2.801	4.41	1.574

Table A.10: Lattice parameters and volume differences measured for rhenium hydride, second experiment, pressure increase. Heated to 200 °C after 18.2 GPa

P[GPa]	V[Å^3]	ΔV[Å^3]	a[Å]	c[Å]	c/a
28.3	32.488	3.172	2.863	4.577	1.599
29.9	32.509	3.304	2.86	4.589	1.604
32.4	32.315	3.28	2.857	4.57	1.599
34.4	32.055	3.153	2.848	4.563	1.602
36.5	31.969	3.204	2.846	4.557	1.601
38.4	31.809	3.165	2.839	4.556	1.605
34.5	31.92	3.025	2.842	4.564	1.606
37.5	32.293	3.592	2.868	4.532	1.58
37.5	32.112	3.41	2.857	4.543	1.59
40.1	32.012	3.474	2.853	4.543	1.593
42.6	31.907	3.522	2.849	4.538	1.593
44	31.731	3.43	2.843	4.534	1.595
46.3	31.637	3.472	2.84	4.529	1.595
47.8	31.707	3.629	2.844	4.528	1.592
49.7	31.597	3.628	2.84	4.523	1.593
47	31.782	3.658	2.847	4.528	1.59
40.3	32.067	3.541	2.858	4.535	1.587
34.1	32.258	3.337	2.862	4.546	1.588
30.2	32.473	3.289	2.872	4.546	1.583
22.2	32.956	3.197	2.887	4.564	1.581
15.8	33.392	3.131	2.899	4.587	1.582
8.2	33.839	2.927	2.913	4.606	1.582

Table A.11: Lattice parameters and volume differences measured for tungsten hydride, Loading 1 (Feb. 2011).

P[GPa]	V[Å^3]	ΔV[Å^3]	a[Å]	c[Å]	c/a
37.9	32.569	3.893	2.865	4.583	1.6
35.8	32.723	3.912	2.873	4.579	1.594
30.9	32.851	3.715	2.875	4.589	1.596
21.6	33.191	3.386	2.885	4.604	1.595
17	33.724	3.56	2.895	4.646	1.605
12.4	34.151	3.607	2.908	4.663	1.604
11.2	34.119	3.472	2.909	4.654	1.6
9.9	34.288	3.528	2.913	4.666	1.602
9.3	34.281	3.467	2.915	4.657	1.597

Table A.12: Lattice parameters and volume differences measured for tungsten hydride, Loading 2 (May 2011).

P[GPa]	V[Å^3]	ΔV[Å^3]	a[Å]	c[Å]	c/a
47	31.675	3.551	2.841	4.53	1.595
52.1	31.547	3.712	2.841	4.515	1.589
56.8	31.664	4.084	2.848	4.509	1.583
60.6	31.313	3.932	2.834	4.503	1.589
65.7	30.828	3.703	2.82	4.476	1.587
69.9	31.102	4.181	2.828	4.49	1.588
73.7	30.971	4.23	2.826	4.479	1.585
78.7	30.846	4.331	2.822	4.472	1.585
83.5	30.295	3.991	2.806	4.441	1.583
87.3	30.402	4.259	2.808	4.451	1.585
91.3	29.99	4.012	2.796	4.429	1.584
97.2	29.672	3.931	2.788	4.408	1.581
101.4	29.625	4.046	2.785	4.41	1.584
105.1	29.224	3.785	2.773	4.387	1.582
110.9	29.098	3.871	2.768	4.385	1.584
115.2	28.841	3.767	2.76	4.372	1.584
115.9	28.494	3.444	2.748	4.356	1.585

Table A.13: Lattice parameters and volume differences measured for tungsten hydride, Loading 4 (Nov. 2011).

P[GPa]	V[Å^3]	ΔV[Å^3]	a[Å]	c[Å]	c/a
30.1	32.981	3.79	2.881	4.589	1.593
35.8	32.83	4.019	2.878	4.578	1.591
39.4	32.741	4.159	2.876	4.571	1.589
44.2	32.439	4.151	2.867	4.557	1.59
48.5	32.318	4.281	2.864	4.549	1.588
46.4	32.251	4.092	2.862	4.548	1.589
44.9	32.428	4.181	2.867	4.556	1.589
42.7	32.409	4.031	2.869	4.548	1.585
40.4	32.468	3.949	2.868	4.557	1.589
38.4	32.551	3.907	2.871	4.561	1.589
35.1	32.915	4.06	2.882	4.575	1.587
29.4	33.125	3.886	2.884	4.599	1.595
29.1	33.13	3.869	2.884	4.601	1.596
16.6	33.764	3.568	2.899	4.639	1.6
14.8	33.958	3.615	2.906	4.643	1.598
17.1	33.823	3.668	2.902	4.636	1.597
19	33.669	3.664	2.898	4.629	1.597
21.2	33.492	3.657	2.891	4.626	1.6
23.4	33.338	3.668	2.888	4.614	1.597
26.1	33.153	3.68	2.882	4.608	1.599
28.2	33.087	3.764	2.882	4.599	1.596
30.2	33.013	3.829	2.881	4.594	1.595
32.3	32.948	3.906	2.88	4.588	1.593
30.3	32.985	3.808	2.881	4.588	1.592
28.1	33.085	3.754	2.884	4.594	1.593
25.5	33.201	3.685	2.886	4.604	1.595
22.6	33.318	3.589	2.888	4.612	1.597
17.9	33.672	3.58	2.897	4.634	1.6
18.5	33.63	3.586	2.896	4.63	1.599
16.8	33.79	3.611	2.901	4.637	1.599
12.1	34.158	3.588	2.91	4.657	1.6
15.6	33.862	3.586	2.902	4.642	1.599
15.2	33.866	3.556	2.903	4.64	1.598
12	34.247	3.669	2.913	4.66	1.6
10.7	34.348	3.658	2.916	4.664	1.599

Table A.14: Lattice parameters and volume differences measured for tungsten hydride, Loading 3 (Oct. 2011).

Time[h]	P[GPa]	$Ir_{(111)}$	$IrH_{(001)}$	rel. Int.
0.13	64	144.6	1.29	$8.89 \cdot 10^{-3}$
1.2	64	129.2	2.1	$1.63 \cdot 10^{-2}$
1.38	64	127.1	2.89	$2.28 \cdot 10^{-2}$
1.67	64	99.22	2.7	$2.72 \cdot 10^{-2}$
3.03	65.5	138.44	5.03	$3.63 \cdot 10^{-2}$
3.8	67.4	140.24	7.38	$5.26 \cdot 10^{-2}$
4.17	71.3	138.5	9.52	$6.87 \cdot 10^{-2}$
4.47	74	159.44	13.85	$8.69 \cdot 10^{-2}$
4.8	77	125.04	12.23	$9.78 \cdot 10^{-2}$
5.73	77	154.9	24.54	0.16
7.92	77	127.18	29.62	0.23
15.33	78.5	126.04	47.04	0.37
15.78	80.9	123.32	51.24	0.42
16.33	83.8	110.92	45.18	0.41
16.75	86	111.48	58.24	0.52
17.48	89.2	105.76	52.68	0.5
18.18	92.7	108.7	67.96	0.63
18.87	94.8	76.6	45.5	0.59
22.37	94.8	84.66	79.24	0.94
25.25	94.8	67.06	83.88	1.25
28.05	96.9	59	88.18	1.49
28.88	102.3	54.66	99.7	1.82
29.65	105.4	55.52	103.02	1.86
39.35	105.4	26.26	102.54	3.9
40.12	105.4	31.88	135.92	4.26
40.87	107.7	25.58	113.14	4.42
45.1	107.7	16.62	90.58	5.45
45.58	107.7	13.46	75.18	5.58
46.22	107.7	17.88	111.44	6.23
46.53	107.7	19.76	135.1	6.84
47	107.7	15.16	109.28	7.21
47.38	107.7	17.77	128.76	7.25
48.03	107.7	16.9	120.56	7.13
48.58	107.7	12.76	116.08	9.1
49.02	107.7	16.83	132.82	7.89
49.62	107.7	16.51	132.6	8.03
50.03	107.7	15.37	128	8.33
51.55	107.7	13.11	123.32	9.41
52.7	107.7	15.66	155.56	9.93
62.12	107.7	10.23	110.6	10.81
64.08	107.7	9.9	109.5	11.06
64.17	107.7	10.92	132.5	12.13
65.15	107.5	12.97	153.18	11.81

Table A.15: Synthesis process of iridium hydride. Table shows development of scattering intensities with time and pressure of the (111) peak of *fcc* iridium and the (001) peak if simple cubic iridium hydride.

Time[min]	Laser[W]	Int.
0	0	10.33
4.38	0.2	10.76
5.18	0.5	10.03
5.68	1	9.73
6.37	1.2	10.35
6.75	1.5	9.79
7.08	1.8	9.48
7.7	2	9.37
8.03	2.4	8.7
8.62	3	7.84
9.23	3.5	6.26
9.93	4.2	5.32
10.38	4.8	3.92
11.38	5.3	1.35
12.12	5.3	0.57

Table A.16: Integrated scattering intensity (arbitrary units) of the (111) peak of iridium during laser heating at 115 GPa.

Time[min]	Laser[W]	(001)	(011)	(111)	(002)	(012)
0	0	1	1	1	1	1
4.38	0.2	1	0.99	1.02	1	1.01
5.18	0.5	1	0.99	1.01	0.98	1.01
5.68	1	0.99	0.98	1	0.97	1
6.37	1.2	0.98	0.99	1.01	0.97	1.01
6.75	1.5	0.98	0.99	1.01	0.96	0.99
7.08	1.8	0.98	0.99	1	0.95	1.04
7.7	2	0.98	0.98	1	0.95	1.01
8.03	2.4	0.97	0.98	1.01	0.95	1.02
8.62	3	0.97	0.96	0.99	0.93	1.03
9.23	3.5	0.96	0.95	0.98	0.93	0.98
9.93	4.2	0.95	0.92	0.94	0.89	0.94
10.38	4.8	0.91	0.85	0.87	0.83	0.87
11.38	5.3	0.87	0.75	0.77	0.76	0.74
12.12	5.3	0.83	0.66	0.67	0.71	0.65
13.22	5.3	0.82	0.61	0.6	0.65	0.58
14.32	6	0.79	0.47	0.45	0.59	0.44
15.13	6	0.77	0.4	0.39	0.55	0.37

Table A.17: Widths (FWHM) of the five strongest diffraction peaks of iridium hydride during laser heating at 115 GPa

Time[h]	$Ir_{(111)}$	$IrH_{(001)}$	rel. Int.	a[Å]	FWHM[deg]
0.133	27.733	$5.797 \cdot 10^{-2}$	$2.09 \cdot 10^{-3}$	2.687	0.122
0.483	25.75	0.175	$6.803 \cdot 10^{-3}$	2.688	0.102
0.617	30.433	0.289	$9.48 \cdot 10^{-3}$	2.688	$9.382 \cdot 10^{-2}$
0.767	34.267	0.581	$1.696 \cdot 10^{-2}$	2.688	$8.763 \cdot 10^{-2}$
0.85	41.567	0.731	$1.758 \cdot 10^{-2}$	2.687	$9.28 \cdot 10^{-2}$
1.017	43.017	1.018	$2.367 \cdot 10^{-2}$	2.687	$9.117 \cdot 10^{-2}$
1.25	44.717	1.174	$2.626 \cdot 10^{-2}$	2.687	$9.231 \cdot 10^{-2}$
1.567	39.35	0.608	$1.545 \cdot 10^{-2}$	2.688	$9.584 \cdot 10^{-2}$
1.783	43.167	1.231	$2.851 \cdot 10^{-2}$	2.69	$8.455 \cdot 10^{-2}$
1.867	44.033	1.321	$2.999 \cdot 10^{-2}$	2.69	$8.38 \cdot 10^{-2}$
1.983	43.35	1.745	$4.025 \cdot 10^{-2}$	2.69	$8.004 \cdot 10^{-2}$
2.033	43.517	1.897	$4.358 \cdot 10^{-2}$	2.69	$8.105 \cdot 10^{-2}$
2.15	41.8	2.528	$6.049 \cdot 10^{-2}$	2.69	$8.182 \cdot 10^{-2}$
2.25	45.783	3.027	$6.611 \cdot 10^{-2}$	2.69	$8.384 \cdot 10^{-2}$
2.333	40.567	3.68	$9.071 \cdot 10^{-2}$	2.69	$8.267 \cdot 10^{-2}$
2.45	37.167	3.958	0.107	2.69	$8.273 \cdot 10^{-2}$
2.583	32.417	4.033	0.124	2.689	$8.367 \cdot 10^{-2}$
2.65	28.183	3.878	0.138	2.689	$8.413 \cdot 10^{-2}$
2.783	27.483	3.607	0.131	2.689	$8.371 \cdot 10^{-2}$
2.967	25.767	4.097	0.159	2.689	$8.275 \cdot 10^{-2}$
3.3	19.5	3.647	0.187	2.689	$8.23 \cdot 10^{-2}$
3.45	18.85	3.683	0.195	2.689	$8.173 \cdot 10^{-2}$
3.517	17.65	3.868	0.219	2.689	$8.155 \cdot 10^{-2}$
3.767	11.24	2.802	0.249	2.689	$8.084 \cdot 10^{-2}$
4.167	32.767	6.565	0.2	2.689	$8.252 \cdot 10^{-2}$
4.383	34.167	9.97	0.292	2.69	$8.193 \cdot 10^{-2}$
4.767	38.567	5.997	0.155	2.688	$8.238 \cdot 10^{-2}$
5.033	33.42	6.065	0.181	2.688	$8.161 \cdot 10^{-2}$
5.383	33.417	10.627	0.318	2.69	$7.987 \cdot 10^{-2}$
5.583	27.917	12.24	0.438	2.69	$7.883 \cdot 10^{-2}$
5.8	23.2	12.175	0.525	2.691	$7.897 \cdot 10^{-2}$
6.033	14.403	9.992	0.694	2.691	$7.787 \cdot 10^{-2}$
6.2	11.6	24.233	2.089	2.693	$7.447 \cdot 10^{-2}$
6.267	6.943	28.733	4.138	2.694	$7.339 \cdot 10^{-2}$
6.3	5.3	29.333	5.535	2.694	$7.294 \cdot 10^{-2}$
6.35	4.178	30.2	7.228	2.694	$7.205 \cdot 10^{-2}$
6.417	3.28	31.067	9.472	2.694	$7.217 \cdot 10^{-2}$
6.467	3.185	31.35	9.843	2.694	$7.152 \cdot 10^{-2}$
6.517	3.14	32.4	10.318	2.692	$7.525 \cdot 10^{-2}$
6.633	4.435	32.4	7.306	2.691	$7.616 \cdot 10^{-2}$
6.683	3.818	32.3	8.459	2.692	$7.495 \cdot 10^{-2}$

Table A.18: Laser heating during run-3 of iridium hydride. In addition to the relative scattering intensity, the d-spacing of the (001)-peak (equivalent to lattice parameter a) and the FWHM of this reflection are given.

P[GPa]	Time[min]	$Ir_{(111)}$	$IrH_{(001)}$	rel. Int.
55.8	0	130.5	1,926	14.76
53.7	0.4	139	1,875	13.49
52	0.68	135.1	1,921	14.22
50	0.93	214.5	2,110	9.84
48	1.25	181.4	1,909	10.52
46.2	1.5	255.1	2,073	8.13
44.2	1.7	206.3	1,923	9.32
41.4	1.9	215.5	1,988	9.23
38.8	2.1	134.3	1,715	12.77
36.5	2.28	236.5	1,950	8.25
29.8	2.45	287.5	1,489	5.18
28.1	2.63	244.7	1,390	5.68
27	2.78	261.6	1,211	4.63
26.3	3.25	266.7	1,426	5.35
25.1	3.42	227.4	1,529	6.72
24.4	3.58	259.2	1,783	6.88
23.9	3.73	266.8	1,344	5.04
22.9	4.17	209.3	829.6	3.96
22.4	4.35	246.3	1,824	7.41
21.8	4.55	207.6	1,572	7.57
21.1	4.75	226.6	1,645	7.26
20.5	4.98	220.3	1,585	7.19
19.4	5.25	231.6	1,569	6.77
18.7	5.75	291.4	1,548	5.31
17.5	6.03	182.5	967.2	5.3
16.4	6.32	306.5	1,606	5.24
15.8	6.97	438.4	1,381	3.15
14.9	7.17	424	1,085	2.56
13.9	7.52	677.9	971.7	1.43
13.1	7.68	1,272	977.2	0.77
11.9	8.1	1,126	572.3	0.51
10.4	8.27	1,444	542.6	0.38
9.5	8.55	232.6	17.12	$7.36 \cdot 10^{-2}$
7.7	8.75	1,944	169.3	$8.71 \cdot 10^{-2}$
6.4	9.05	1,320	27.78	$2.1 \cdot 10^{-2}$

Table A.19: Decompression process of run-3 for iridium hydride. Shown is the relative intensity of iridium hydride compared to iridium.

P[GPa]	a_{Ir}[Å]	V_{Ir}[Å^3]	a_{IrH}[Å]	V_{IrH}[Å^3]	ΔV[Å^3]
47.3	3.723	51.6	2.711	19.915	7.015
45.7	3.724	51.67	2.715	20.022	7.105
43.8	3.728	51.82	2.716	20.043	7.088
41.7	3.728	51.82	2.72	20.12	7.165
39.6	3.738	52.21	2.726	20.248	7.196
37.1	3.746	52.58	2.734	20.426	7.281
35	3.749	52.69	2.743	20.641	7.468
32.8	3.755	52.93	2.747	20.732	7.499
30.4	3.758	53.06	2.751	20.811	7.546
27.4	3.768	53.52	2.764	21.12	7.74
26.6	3.771	53.63	2.761	21.054	7.646
24.9	3.775	53.81	2.771	21.267	7.814
23.2	3.776	53.85	2.77	21.264	7.802

Table A.20: Lattice parameters and volume differences measured for iridium hydride, run-1.

P[GPa]	a_{Ir}[Å]	V_{Ir}[Å^3]	a_{IrH}[Å]	V_{IrH}[Å^3]	ΔV[Å^3]
64	3.676	49.657	2.672	19.074	6.66
64	3.674	49.61	2.671	19.056	6.654
64	3.674	49.596	2.67	19.033	6.634
64	3.674	49.589	2.67	19.031	6.634
65.5	3.674	49.573	2.67	19.038	6.645
67.4	3.669	49.387	2.666	18.945	6.598
71.3	3.663	49.159	2.663	18.893	6.604
74	3.658	48.961	2.66	18.814	6.573
77	3.653	48.744	2.655	18.719	6.533
77	3.652	48.702	2.655	18.707	6.532
77	3.651	48.662	2.653	18.667	6.502
78.5	3.65	48.645	2.652	18.653	6.492
80.9	3.647	48.49	2.649	18.59	6.467
83.8	3.643	48.356	2.646	18.52	6.431
86	3.639	48.179	2.643	18.46	6.416
89.2	3.633	47.936	2.637	18.346	6.362
92.7	3.626	47.681	2.632	18.236	6.315
94.8	3.621	47.467	2.627	18.132	6.265
94.8	3.619	47.394	2.625	18.091	6.243
94.8	3.618	47.355	2.623	18.056	6.217
96.9	3.618	47.34	2.624	18.068	6.233
102.3	3.609	47.017	2.618	17.936	6.181
105.4	3.602	46.742	2.611	17.806	6.12
105.4	3.599	46.629	2.611	17.798	6.14
105.4	3.599	46.635	2.61	17.787	6.128
107.7	3.599	46.615	2.611	17.795	6.141
107.7	3.599	46.604	2.613	17.841	6.19
107.7	3.598	46.587	2.613	17.837	6.19
107.7	3.598	46.592	2.612	17.822	6.174
107.7	3.598	46.584	2.612	17.817	6.171
107.7	3.598	46.583	2.612	17.815	6.169
107.7	3.598	46.578	2.612	17.822	6.178
107.7	3.598	46.584	2.612	17.818	6.172
107.7	3.598	46.569	2.612	17.814	6.171
107.7	3.598	46.568	2.612	17.825	6.183
107.7	3.598	46.565	2.612	17.824	6.183
107.7	3.597	46.556	2.612	17.823	6.184
107.7	3.597	46.549	2.612	17.823	6.185
107.7	3.597	46.556	2.612	17.825	6.186
107.7	3.597	46.527	2.612	17.829	6.197
107.7	3.597	46.522	2.612	17.828	6.198
107.7	3.597	46.535	2.612	17.817	6.183
107.5	3.597	46.527	2.612	17.821	6.189
107	3.596	46.485	2.612	17.83	6.209
107	3.594	46.441	2.611	17.802	6.191
114	3.588	46.195	2.606	17.701	6.153
120	3.578	45.814	2.595	17.477	6.024
120	3.577	45.76	2.594	17.448	6.008
126	0	0	2.586	17.286	0

Table A.21: Lattice parameters and volume differences measured for iridium hydride, run-2. "0" entries denote values not measured.

P[GPa]	a_{Ir}[Å]	V_{Ir}[Å^3]	a_{IrH}[Å]	V_{IrH}[Å^3]	ΔV[Å^3]
55.8	3.684	50.016	2.691	19.48	6.976
53.7	3.687	50.132	2.692	19.515	6.982
52	3.69	50.223	2.691	19.49	6.934
50	3.696	50.472	2.696	19.592	6.975
48	3.7	50.65	2.7	19.683	7.02
46.2	3.706	50.89	2.706	19.815	7.092
44.2	3.712	51.152	2.712	19.952	7.164
41.4	3.721	51.534	2.723	20.188	7.305
38.8	3.731	51.931	2.733	20.405	7.422
36.5	3.737	52.186	2.739	20.544	7.497
29.8	3.748	52.67	2.75	20.788	7.621
28.1	3.753	52.872	2.754	20.896	7.678
27	3.756	52.976	2.757	20.954	7.71
26.3	3.762	53.256	2.765	21.129	7.815
25.1	3.765	53.381	2.767	21.187	7.841
24.4	3.767	53.46	2.771	21.268	7.903
23.9	3.769	53.52	2.769	21.241	7.861
22.9	3.771	53.645	2.774	21.345	7.934
22.4	3.773	53.729	2.778	21.44	8.008
21.8	3.776	53.82	2.78	21.494	8.038
21.1	3.776	53.849	2.779	21.459	7.996
20.5	3.778	53.92	2.781	21.501	8.021
19.4	3.782	54.075	2.784	21.586	8.067
18.7	3.786	54.274	2.79	21.706	8.137
17.5	3.788	54.357	2.792	21.762	8.173
16.4	3.793	54.549	2.795	21.845	8.208
15.8	3.796	54.716	2.799	21.919	8.24
14.9	3.799	54.834	2.798	21.905	8.196
13.9	3.802	54.941	2.803	22.029	8.294
13.1	3.805	55.087	2.806	22.084	8.312
11.9	3.816	55.578	2.816	22.332	8.438
10.4	3.817	55.62	2.816	22.335	8.429
9.5	3.821	55.787	2.817	22.351	8.404
7.7	0	0	2.824	22.51	0
6.4	0	0	2.828	22.616	0

Table A.22: Lattice parameters and volume differences measured for iridium hydride, run-3. "0" entries denote values not measured.

Bibliography

[Adams 03] D.P. Adams, M.J. Vasile, T.M. Mayer & V.C. Hodges. *Focused ion beam milling of diamond : Effects of H2O on yield , surface morphology and microstructure.* Journal of Vacuum Science & Technology B, vol. 21, pages 2334–2343, 2003.

[Akahama 04a] Y. Akahama. *A comparison of volume compressions of silver and gold up to 150 GPa.* Journal of Applied Physics, vol. 95, no. 9, page 4767, 2004.

[Akahama 04b] Y. Akahama & H. Kawamura. *High-pressure Raman spectroscopy of diamond anvils to 250GPa - Method for pressure determination in the multimegabar pressure range.* Journal of Applied Physics, vol. 96, no. 7, page 3748, 2004.

[Akahama 07] Y. Akahama & H. Kawamura. *Diamond anvil Raman gauge in multimegabar pressure range.* High Pressure Research, vol. 27, page 473, 2007.

[Antonov 82] V.E. Antonov. *Synthesis of gold hydride under high pressures of hydrogen.* Doklady Akademii Nauk SSSR, vol. 266, no. 2, page 376, 1982.

[Antonov 83] V.E. Antonov, I.T. Belash, V.I. Malyshev, E.G. Ponyatovsky & N.A. Tulina. *Hydrogen Solubility in Rhenium at Pressures up to 90 kbar.* Doklady Akademii Nauk SSSR, vol. 269, no. 3, pages 617–619, 1983.

[Antonov 84] V.E. Antonov, I.T. Belash, V.Y. Malyshev & E.G. Ponyatovsky. *The Solubility of Hydrogen in the Platinum Metals under High Pressure.* Platinum Metals Review, no. 28, pages 158–163, 1984.

[Antonov 87] V.E. Antonov, I.T. Belash, O.V. Zharikov & A.V. Palnichenko. *A Study on Superconductivity of High-Pressure Phases in the Re-H, Ru-H, Rh-H and Ni-H Systems.* Physica Status Solidi (b), vol. 142, page 156, 1987.

[Antonov 02] V.E. Antonov. *Phase transformations, crystal and magnetic structures of high-pressure hydrides of d-metals.* Journal of Alloys and Compounds, vol. 330, pages 110–116, 2002.

[Antonov 04] V.E. Antonov, A.I. Latynin & M. Tkacz. *TP phase diagrams and isotope effects in the MoH/D systems.* Journal of Physics: Condensed Matter, vol. 16, no. 46, pages 8387–8398, 2004.

[Antonov 07] V.E. Antonov, A. Beskrovnyy, V. Fedotov, A. Ivanov, S. Khasanov, A. Kolesnikov, M. Sakharov, I. Sashin & M. Tkacz. *Crystal structure and lattice dynamics of chromium hydrides.* Journal of Alloys and Compounds, vol. 430, no. 1-2, pages 22–28, 2007.

[Ares 09] J.R. Ares, F. Leardini, P. Díaz-Chao, J. Bodega, J.F. Fernández, I.J. Ferrer & C. Sánchez. *Ultrasonic irradiation as a tool to modify the H-desorption from hydrides: MgH(2) suspended in decane.* Ultrasonics Sonochemistry, vol. 16, no. 6, pages 810–816, 2009.

[Armentrout 10] M.M. Armentrout & A. Kavner. *Incompressibility of osmium metal at ultrahigh pressures and temperatures.* Journal of Applied Physics, vol. 107, page 093528, 2010.

[Ashcroft 68] N.W. Ashcroft. *Metallic Hydrogen: A High-Temperature Superconductor?* Physical Review Letters, vol. 21, page 1748, 1968.

[Ashcroft 04] N.W. Ashcroft. *Hydrogen Dominant Metallic Alloys: High Temperature Superconductors?* Physical Review Letters, vol. 92, no. 18, page 187002, 2004.

[Atou 95] T. Atou & J.V. Badding. *In Situ Diffraction Study of the Formation of Rhenium Hydride at High Pressure.* Journal of Solid State Chemistry, vol. 118, pages 299–302, 1995.

[Babaev 04] E. Babaev, A. Sudbø& N.W. Ashcroft. *A superconductor to superfluid phase transition in liquid metallic hydrogen.* Nature, vol. 431, page 666, 2004.

[Babaev 05] E. Babaev, A. Sudbø& N.W. Ashcroft. *Observability of a Projected New State of Matter : A Metallic Superfluid.* Physical Review Letters, vol. 95, page 105301, 2005.

[Badding 91] J.V. Badding, R.J. Hemley & H.-K. Mao. *High-pressure chemistry of hydrogen in metals: in situ study of iron hydride.* Science, vol. 253, no. 5018, pages 421–424, 1991.

[Baer 08] B.J. Baer, M.E. Chang & W.J. Evans. *Raman Shift of stressed diamond anvils: pressure calibration and culet geometry dependence.* Journal of Applied Physics, vol. 104, page 034504, 2008.

[Baranowski 71] B. Baranowski, S. Majchrzak & T.B. Flanagan. *The volume increase of fcc metals and alloys due to interstitial hydrogen over a wide range of hydrogen contents.* Journal of Physics F: Metal Physics, vol. 1, no. 3, pages 258–261, 1971.

[Baranowski 72] B. Baranowski & K. Bojarski. *Formation of Chromium Hydride From metallic Chromium and High Pressure Gaseous Hydrogen.* Roczniki Chemii. Ann. Soc. Chim. Polonorum, vol. 46, pages 525–527, 1972.

[Baranowski 90] B. Baranowski, S.M. Filipek, M. Szustakowski, J. Farny & W. Woryna. *Search for Cold Fusion in Some Me-D Systems at High Pressures of Gaseous Deuterium.* Journal of the Less-Common Metals, vol. 158, pages 347 – 357, 1990.

[Baranowski 05] B. Baranowski & S.M. Filipek. *45 Years of nickel hydride, History and perspectives.* Journal of Alloys and Compounds, vol. 404, pages 2–6, 2005.

[Baranowski 07] B. Baranowski & L. Debowska. *Remarks on superconductivity in PdH.* Journal of Alloys and Compounds, vol. 437, no. 1-2, pages L4–L5, 2007.

[Baruchel 93] J. Baruchel, J.L. Hodeau, M.S. Lehmann, J.R. Regnard & C. Schlenker, editeurs. Neutron and Synchrotron Radiation for Condensed Matter Studies, volume 1. Springer Verlag, Berlin - Heidelberg, 1 edition, 1993.

[Bashkin 03] I.O. Bashkin, V.E. Antonov & E.G. Ponyatovsky. *Superconductivities of high-pressure phases in the metal-hydrogen systems.* In A. Narlikar, editeur, Studies of High Temperature Superconductors, Vol .45: Cuprates and Some Unconventional Systems, volume 1, pages 171–241. Nova Science Publishers, New York, 2003.

[Bassett 09] W.A. Bassett. *Diamond anvil cell, 50th birthday.* High Pressure Research, vol. 29, page 163, 2009.

[Berube 07] V. Berube, G. Radtke, M. Dresselhaus & G. Chen. *Size effects on the hydrogen storage properties of nanostructured metal hydrides : A review.* International Journal of Energy Research, vol. 31, pages 637–663, 2007.

[Besedin 98] S.P. Besedin & A.P. Jephcoat. *High-Pressure Studies of the Ni-H, Re-H and Al-H Systems.* Review of High Pressure Science and Technology, vol. 7, pages 301–303, 1998.

[Besedin 00] S. Besedin, A.P. Jephcoat & M. Hanfland. *Compressibility of hydrogen in Ni and Re hosts at pressures to 123 GPa.* High Pressure Research, vol. 17, no. 3, pages 225–234, 2000.

[Bosak 09] A. Bosak, M. Hoesch, M. Krisch, D. Chernyshov, P. Pattison, C. Schulze-Briese, B. Winkler, V. Milman, K. Refson, D. Antonangeli & D. Farber. *3D Imaging of the Fermi Surface by Thermal Diffuse Scattering.* Physical Review Letters, vol. 103, page 076403, 2009.

[Bovman 72a] E.G. Bovman, Y. Kagan & A. Kholas. *Properties of Metallic Hydrogen Under Pressure.* Journal of Experimental and Theoretical Physics USSR, vol. 35, page 783, 1972.

[Bovman 72b] E.G. Bovman, Y. Kagan & A. Kholas. *Structure of Metallic Hydrogen at Zero Pressure.* Journal of Experimental and Theoretical Physics USSR, vol. 34, page 1300, 1972.

[Bowman Jr. 02] R.C. Bowman Jr. & B. Fultz. *Metallic Hydrides I: Hydrogen Storage and Other Gas-Phase Applications.* MRS Bulletin, vol. 27, pages 688–693, 2002.

[Brazhkin 07] V.V. Brazhkin. *High-pressure synthesized materials: treasures and hints.* High Pressure Research, vol. 27, no. 3, pages 333–351, 2007.

[Brown 92] D.M. Brown & W.B. Daniels. *Vibrational Raman spectra of hydrogen and deuterium mixtures at high pressures.* Physical Review A, vol. 45, page 6430, 1992.

[Burtovyy 04] R. Burtovyy & M. Tkacz. *High-pressure synthesis of a new copper hydride from elements.* Solid State Communications, vol. 131, no. 3-4, pages 169–173, July 2004.

[Buzea 05] C. Buzea & K. Robbie. *Assembling the puzzle of superconducting elements: A review.* Superconductor Science and Technology, vol. 18, no. 1, pages R1–R8, 2005.

[Chellappa 06] R.S. Chellappa, D. Chandra, S.A. Gramsch, R.J. Hemley, J.-F. Lin & Y. Song. *Pressure-induced phase transformations in LiAlH4.* The Journal of Physical Chemistry B, vol. 110, page 11088, 2006.

[Chen 02] J. Chen, T. Sakai, N. Kitamura, H. Tanaka, T. Kiyobayashi, H.T. Takeshita & N. Kuriyama. *High pressure experiments*

on the Mg2Ni and Mg2NiH4 systems. Journal of Alloys and Compounds, vol. 332, pages 162–165, 2002.

[Cullity 83] B.D. Cullity & S.R. Stock. Elements of X-ray Diffraction. Prentice Hall, 3 edition, 1983.

[Cynn 02] H. Cynn, J.E. Klepeis, C.-S. Yoo & D.A. Young. *Osmium has the Lowest Experimentally Determined Compressibility.* Physical Review Letters, vol. 88, page 135701, 2002.

[Datchi 07] F. Datchi, A. Dewaele, P. Loubeyre, R. Letoullec, Y. Le Godec & B. Canny. *Optical pressure sensors for high-pressure-high-temperature studies in a diamond anvil cell.* High Pressure Research, vol. 27, page 447, 2007.

[Debessai 09] M. Debessai, T. Matsuoka, J. Hamlin, J. Schilling & K. Shimizu. *Pressure-Induced Superconducting State of Europium Metal at Low Temperatures.* Physical Review Letters, vol. 102, no. 19, pages 13–16, 2009.

[Degtyareva 03] V.F. Degtyareva. *Correlations between volume and content in metal hydrides*, 2003.

[Degtyareva 09] O. Degtyareva, J.E. Proctor, C. Guillaume, E. Gregoryanz & M. Hanfland. *Formation of transition metal hydrides at high pressure.* Solid State Communications, vol. 149, pages 1583–1586, 2009.

[Dewaele 04] A. Dewaele, P. Loubeyre & M. Mezouar. *Equations of state of six metals above 94GPa.* Physical Review B, vol. 70, no. 9, page 094112, 2004.

[Dewaele 08] A. Dewaele, M. Torrent, P. Loubeyre & M. Mezouar. *Compression curves of transition metals in the Mbar range: Experiments and projector augmented-wave calculations.* Physical Review B, vol. 78, no. 10, page 104102, 2008.

[Donnerer 13] C. Donnerer, T. Scheler & E. Gregoryanz. *High-Pressure Synthesis of Noble Metal Hydrides.* accepted for publication in Journal of Chemical Physics, 2013.

[Dorogokupets 07a] P.I. Dorogokupets & A. Dewaele. *Equations of state of MgO, Au, Pt, NaCl-B1, and NaCl-B2: Internally consistent high-temperature pressure scales.* High Pressure Research, vol. 27, no. 4, pages 431–446, 2007.

[Dorogokupets 07b] P.I. Dorogokupets & A.R. Oganov. *Ruby, metals, and MgO as alternative pressure scales: A semiempirical description of shock-wave, ultrasonic, x-ray, and thermochemical data at*

high temperatures and pressures. Physical Review B, vol. 75, page 024115, 2007.

[Dubrovinsky 07] L. Dubrovinsky, N. Dubrovinskaia, W. Crichton, A. Mikhaylushkin, S. Simak, I. Abrikosov, J. de Almeida, R. Ahuja, W. Luo & B. Johansson. *Noblest of All Metals Is Structurally Unstable at High Pressure.* Physical Review Letters, vol. 98, no. 4, page 045503, 2007.

[Dubrovinsky 12] L. Dubrovinsky, N. Dubrovinskaia, V.B. Prakapenka & A.M. Abakumov. *Implementation of micro-ball nanodiamond anvils for high-pressure studies above 6 Mbar.* Nature Communications, vol. 3, page 1163, 2012.

[Elias 09] D.C. Elias, R.R. Nair & T.M.G. Mohiuddin. *Control of Graphene's Properties by Reversible Hydrogenation.* Science, vol. 323, page 610, 2009.

[Eremets 08] M.I. Eremets, I.A. Trojan, S.A. Medvedev, J.S. Tse & Y. Yao. *Superconductivity in hydrogen dominant materials: silane.* Science, vol. 319, pages 1506–1509, 2008.

[Feng 10] Y. Feng, R. Jaramillo, J. Wang, Y. Ren & T.F. Rosenbaum. *High-pressure techniques for condensed matter physics at low temperature.* The Review of Scientific Instruments, vol. 81, no. 4, page 041301, 2010.

[Fichtner 09] M. Fichtner. *Properties of nanoscale metal hydrides.* Nanotechnology, vol. 20, no. 20, page 204009, 2009.

[Filipek 07] S.M. Filipek. *Metal Hydrides under High Hydrostatic Pressure.* Journal of Advanced Science, vol. 19, no. 1-2, pages 1–10, 2007.

[Fitzsimons 92] N.P. Fitzsimons, W. Jones & P.J. Herley. *Aspects of the synthesis of copper hydride and supported copper hydride.* Catalysis Letters, vol. 15, pages 83–94, 1992.

[Fukai 05] Y. Fukai. The Metal-Hydrogen System. Springer Verlag, Berlin, 2nd edition, 2005.

[Fukizawa 83] A. Fukizawa & Y. Fukai. *Effects of High pressure on the Structure of VH0.5 and NbH0.75.* Journal of the Physical Society of Japan, vol. 52, no. 6, pages 2102–2107, 1983.

[Gao 05] C. Gao & Y. Han. *Accurate measurements of high pressure resistivity in a diamond anvil cell.* Review of Scientific Instruments, vol. 76, page 083912, 2005.

[Gao 12] G. Gao, H. Wang, L. Zhu & Y. Ma. *Pressure-Induced Formation of Noble Metal Hydrides.* Journal of Physical Chemistry, vol. 116, pages 1995–2000, 2012.

[Gavriliuk 09] A.G. Gavriliuk, A.A. Mironovich & V.V. Struzhkin. *Miniature diamond anvil cell for broad range of high pressure measurements.* Review of Scientific Instruments, vol. 80, page 043906, 2009.

[George 10] L. George & S.K. Saxena. *Structural stability of metal hydrides, alanates and borohydrides of alkali and alkali-earth elements: A review.* International Journal of Hydrogen Energy, vol. 35, no. 11, pages 5454–5470, 2010.

[Gierak 09] J. Gierak. *Focused ion beam technology and ultimate applications.* Semiconductor Science and Technology, vol. 24, page 043001, 2009.

[Goedkoop 55] J.A. Goedkoop & A.F. Andresen. *The crystal structure of copper hydride.* Acta Crystallographica, vol. 8, no. 2, pages 118–119, 1955.

[Gregoryanz 03] E. Gregoryanz, A.F. Goncharov, K. Matsuishi, H.-K. Mao & Hemley R.J. *Raman Spectroscopy of Hot Dense Hydrogen.* Physical Review Letters, vol. 90, page 175701, 2003.

[Gregoryanz 04] E. Gregoryanz, C. Sanloup, M. Somayazulu, J. Badro, G. Fiquet, H.-K. Mao & R.J. Hemley. *Synthesis and characterization of a binary noble metal nitride.* Nature Materials, vol. 3, pages 294–297, 2004.

[Hammersley 96] A.P. Hammersley, S.O. Svensson, M. Hanfland, A.N. Fitch & D. Hausermann. *Two-dimensional detector software: From real detector to idealised image or two-theta scan.* High Pressure Research, vol. 14, pages 235–248, 1996.

[Hanfland 85] M. Hanfland, K. Syassen, S. Fahy, S.G. Louie & M.L. Cohe. *Pressure dependence of the first-order Raman mode in diamond.* Physical Review B, vol. 31, page 6896, 1985.

[Hazen 87] R.M. Hazen, H.-K. Mao, L.W. Finger & R.J. Hemley. *Single-crystal x-ray diffracion of* n-H_2 *at high pressures.* Physical Review B, vol. 36, pages 3944–3947, 1987.

[Hemley 05] R.J. Hemley, H.-K. Mao & V.V. Struzhkin. *Synchrotron radiation and high pressure: new light on materials under extreme conditions.* Journal of Synchrotron Radiation, vol. 12, pages 135–154, 2005.

[Hemmes 89] H. Hemmes, A. Driessen, R. Griessen & M. Gupta. *Isotope effects and pressure dependence of the T_c of superconducting stoichiometric PdH and PdD synthesized and measured in a diamond anvil cell.* Physical Review, vol. 39, no. 7, page 4110, 1989.

[Herranz 10] T. Herranz, K.F. McCarty, B. Santos, M. Monti & J. de La Figuera. *Real Space Observations of Magnesium Hydride Formation and Decomposition.* Chemistry of Materials, vol. 22, no. 4, pages 1291–1293, 2010.

[Hippert 05] F. Hippert, E. Geissler, J.L. Hodeau, E. Lelievre-Berna & J.-R. Regnard, editeurs. Neutron and X-ray Spectroscopy. Springer Verlag, Dordrecht, The Netherlands, 1 edition, 2005.

[Hirao 08] N. Hirao, F. Hiroshi, O. Yasuo, T. Kenichi & K. Takumi. *Synthesis and structure of new platinum hydrides at high pressure.* Acta Crystallographica, vol. A64, page C609, 2008.

[Holmes 89] N.C. Holmes, J.A. Moriarty, G.R. Gathers & W.J. Nellis. *The equation of state of platinum to 660 GPa (6.6 Mbar).* Journal of Applied Physics, vol. 66, pages 2962–2967, 1989.

[Holzapfel 05] W.B. Holzapfel. *Progress in the realization of a practical pressure scale for the range 1-300 GPa.* High Pressure Research, vol. 25, pages 87–99, 2005.

[Howie 12] R.T. Howie, C.L. Guillaume, T. Scheler, A.F. Goncharov & E. Gregoryanz. *Mixed Molecular and Atomic Phase of Dense Hydrogen.* Physical Review Letters, vol. 108, page 125501, 2012.

[Irifune 03] T. Irifune, A. Kurio, S. Sakamoto, T. Inoue & H. Sumiya. *Ultrahard polycrystalline diamond from graphite.* Nature, vol. 421, pages 599–601, 2003.

[Irifune 05] T. Irifune, M. Isshiki & S. Sakamoto. *Transmission electron microscope observation of the high-pressure form of magnesite retrieved from laser heated diamond anvil cell.* Earth and Planetary Science Letters, vol. 239, no. 1-2, pages 98–105, 2005.

[Jain 10] I.P. Jain, C. Lal & A. Jain. *Hydrogen storage in Mg: A most promising material.* International Journal of Hydrogen Energy, vol. 35, no. 10, pages 5133–5144, 2010.

[Janssen 07] G.C.A.M. Janssen & B.R. Pujada. *Stress in tungsten carbide-diamond like carbon multilayer coatings.* Applied Physics Letters, vol. 91, page 021913, 2007.

[Kalita 08] P. Kalita, A. Cornelius, K. Lipinskakalita, C. Gobin & H.P. Liermann. *In situ observations of temperature- and pressure-induced phase transitions in TiH2: Angle-dispersive and synchrotron energy-dispersive X-ray diffraction studies.* Journal of Physics and Chemistry of Solids, vol. 69, no. 9, pages 2240–2244, 2008.

[Kamenev 07] K.V. Kamenev, J. Sanchez-Benitez & S. Tancharakorn. *Miniature diamond anvil cell for 3He insert into quantum design physical property measurement system.* High Pressure Research, vol. 27, pages 189–192, 2007.

[Kawamura 04] H. Kawamura, M. Harada, Y. Akahama & K. Takemura. *Hydrogen ordering in rhenium hydride: anti-CdI2 type structure of ReH0.36.* Solid State Communications, vol. 130, no. 1-2, pages 59–62, 2004.

[Kawamura 05] H. Kawamura, T. Moriwaki, Y. Akahama & K. Takemura. *Formation of tungsten hydride at high pressures.* Proceedings of Joint 20th AIRAPT - 43rd EHPRG International Conference on High Pressure Science and Technology, Karlsruhe, vol. 2, 2005.

[Kim 11] D.Y. Kim, R.H. Scheicher, C.J. Pickard, R.J Needs & R. Ahuja. *Predicted Formation of Superconducting Platinum-Hydride Crystals under Pressure in the Presence of Molecular Hydrogen.* Physical Review Letters, vol. 107, page 117002, 2011.

[Klotz 09] S. Klotz, J.-C. Chervin, P. Munsch & G. Le Marchand. *Hydrostatic limits of 11 pressure transmitting media.* Journal of Physics D: Applied Physics, vol. 42, page 075413, 2009.

[König 99] R. König, A. Schindler & T. Herrmannsdörfer. *Superconductivity of Compacted Platinum Powder at Very Low Temperatures.* Physical Review Letters, vol. 82, no. 22, pages 4528–4531, 1999.

[Langfischer 02] H. Langfischer & B. Basnar. *Evolution of tungsten film deposition induced by focused ion beam.* Journal of Vacuum Science and Technology A, vol. 20, pages 1408–1415, 2002.

[Li 11] B. Li, Y. Ding, D.Y. Kim, R. Ahuja, G. Zou & H.-K. Mao. *Rhodium dihydride (RhH2) with high volumetric hydrogen density.* Proceedings of the National Academy of Sciences, pages 4–7, 2011.

[Liermann 10] H.-P. Liermann, W. Morgenroth, A. Ehnes, A. Berghäuser, B. Winkler, H. Franz & E. Weckert. *The Extreme Conditions*

Beamline at PETRA III, DESY: Possibilities to conduct time resolved monochromatic diffraction experiments in dynamic and laser heated DAC. Journal of Physics: Conference Series, vol. 215, page 012029, 2010.

[Loferski 10] P.J. Loferski. *2010 Minerals Yearbook; Platinum-group metals.* USGS Mineral Resources Program, pages 57.1–12, 2010.

[Loubeyre 96] P. Loubeyre, R. Letoullec, D. Hausermann, M. Hanfland, R.J. Hemley, H.-K. Mao & L.W. Finger. *XRD and equation of state of Hydrogen at megabar pressures.* Nature, vol. 383, page 702, 1996.

[Loubeyre 02] P. Loubeyre, F. Occelli & R. LeToullec. *Optical studies of solid hydrogen to 320 GPa and evidence for black hydrogen.* Nature, vol. 416, pages 613–617, 2002.

[Machida 10] S.-I. Machida, H. Hirai, H. Gotou, T. Sakakibara & T. Yagi. *Development of loading system for liquid hydrogen into diamond-anvil cells under low temperature.* Review of Scientific Instruments, vol. 81, no. 3, page 033901, 2010.

[McMillan 02] P.F. McMillan. *New materials from high-pressure experiments.* Nature Materials, vol. 1, no. 1, pages 19–25, 2002.

[Miyahara 08] M. Miyahara, T. Sakai, E. Ohtani, Y. Kobayashi, S. Kamada, T. Kondo, T. Nagase, J.H. Yoo, M. Nishijima & Z. Vashaei. *Application of FIB system to ultra-high-pressure Earth science.* Journal of Mineralogical and Petrological Sciences, vol. 103, page 88, 2008.

[Moser 09] D. Moser, D.J. Bull, T. Sato, D. Noréus, D. Kyoi, T. Sakai, N. Kitamura, H. Yusa, T. Taniguchi, W.P. Kalisvaart & P. Notten. *Structure and stability of high pressure synthesized MgTM hydrides (TM = Ti, Zr, Hf, V, Nb and Ta) as possible new hydrogen rich hydrides for hydrogen storage.* Journal of Materials Chemistry, vol. 19, no. 43, page 8150, 2009.

[Okuchi 09] T. Okuchi, H. Ohfuji, S. Odake, H. Kagi, S. Nagatomo & M. Sugata. *Micromachining and surface processing of the super-hard nano-polycrystalline diamond by three types of pulsed lasers.* Applied Physics A, vol. 96, pages 833–842, 2009.

[Olijnyk 02] H. Olijnyk & A.P. Jephcoat. *High-Pressure Vibrational Studies of HCP Metals by Raman Spectroscopy.* High Pressure Research, vol. 22, pages 43–45, 2002.

[Ono 05] S. Ono, T. Kikegawa & Y. Ohishi. *A high-pressure and high-temperature synthesis of platinum carbide.* Solid State Communications, vol. 133, no. 1, pages 55–59, 2005.

[Orimo 01] S.-I. Orimo & F.G. Majer. *Hydrogen in nanostructured vanadium-hydrogen systems.* Physical Review B, vol. 63, no. 9, page 094307, 2001.

[Orloff 00] J. Orloff. *Use of focused ion beams for making tiny sample holes in gaskets for diamond anvil cells.* Review of Scientific Instruments, vol. 71, no. 1, page 216, 2000.

[Papaconstantopoulos 80] D.A. Papaconstantopoulos. *Platinum Hydride: A Possible High Temperature Superconductor.* Journal of the Less Common Metals1, vol. 73, pages 305–309, 1980.

[Petch 53] N.J. Petch. *The Cleavage Strength of Polycrystals.* Journal of the Iron and Steel Institute, vol. 174, page 8, 1953.

[Phaneuf 99] M. Phaneuf. *Applications of focused ion beam microscopy to materials science specimens.* Micron, vol. 30, no. 3, pages 277–288, 1999.

[Ponyatovsky 84] E.G. Ponyatovsky, V.E. Antonov & I.T. Belash. *High Hydrogen Pressures. Synthesis of New Hydrides.* In Problems in Solid-State Physics, pages 109–172. Mir Publishers, Moscow, 1984.

[Reyntjens 01] S. Reyntjens & R. Puers. *A review of focused ion beam technology and its applications in microsystem technology.* Journal of Micromechanics and Microengineering, vol. 11, page 287, 2001.

[Sadki 04] E.S. Sadki, S. Ooi & K. Hirata. *Focused-ion-beam-induced deposition of superconducting nanowires.* Applied Physics Letters, vol. 85, no. 25, pages 6206–6208, 2004.

[Saitoh 08] H. Saitoh, A. Machida, Y. Katayama & K. Aoki. *Formation and decomposition of AlH 3 in the aluminum-hydrogen system.* Applied Physics Letters, vol. 93, page 151918, 2008.

[Sakintuna 07] B. Sakintuna, F. Lamaridarkrim & M. Hirscher. *Metal hydride materials for solid hydrogen storage: A review.* International Journal of Hydrogen Energy, vol. 32, no. 9, pages 1121–1140, 2007.

[Scheler 09] T. Scheler, M. Rodrigues, T. W. Cornelius, C. Mocuta, A. Malachias, R. Magalhaes-Paniago, F. Comin, J. Chevrier & T. H. Metzger. *Probing the elastic properties of individual nanostructures by combining in situ atomic force microscopy*

and micro-x-ray diffraction. Applied Physics Letters, vol. 94, page 023109, 2009.

[Scheler 11a] T. Scheler, O. Degtyareva & E. Gregoryanz. *On the effects of high temperature and high pressure on the hydrogen solubility in rhenium.* Journal of Chemical Physics, vol. 135, page 214501, 2011.

[Scheler 11b] T. Scheler, O. Degtyareva, M. Marqués, C. Guillaume, J. Proctor, S. Evans & E. Gregoryanz. *Synthesis and properties of platinum hydride.* Physical Review B, vol. 83, no. 21, page 214106, 2011.

[Schirber 75] J.E. Schirber & B. Morosin. *Lattice Constants of beta-PdHx and beta-PdDx with x near 1.0.* Physical Review B, no. 12, pages 117–118, 1975.

[Shilstein 85] S.S. Shilstein, V.P. Glazkov, A.V. Irodova, V.A. Somenkov, V.E. Antonov & E.G. Ponyatovsky. *The Crystal Structure of High-Pressure Hydrides.* Zeitschrift für Physikalische Chemie, vol. 146, pages 129–135, 1985.

[Solozhenko 05] V.L. Solozhenko & E. Gregoryanz. *Synthesis of superhard materials.* Materials Today, pages 44–51, November 2005.

[Somenkov 87] V. Somenkov, V. Glazkov, A. Irodova & S. Shilstein. *Crystal structure and volume effects in the hydrides of d metals.* Journal of the Less Common Metals, vol. 129, pages 171–180, 1987.

[Strobel 09] T. Strobel, M. Somayazulu & R.J. Hemley. *Novel Pressure-Induced Interactions in Silane-Hydrogen.* Physical Review Letters, vol. 103, no. 6, page 065701, 2009.

[Sudheer 08] S.K. Sudheer, B. Kakadia, V.P. Mahadevan Pillai, G.A. Shafeev & A.V. Simakin. *Processing of natural diamonds using nanosecond and picosecond lasers - relative merits and demerits.* Proceedings of SPIE, vol. 6881, pages 68811G1–13, 2008.

[Syassen 08] K. Syassen. *Ruby under Pressure.* High Pressure Research, vol. 28, page 75, 2008.

[Tkacz 90] M. Tkacz, S. Majchrzak & B. Baranowski. *High Pressure X-ray Studies of Palladium Hydride and Deuteride.* High Pressure Research, vol. 4, pages 387–389, 1990.

[Tripodi 04] P. Tripodi, D. Di Gioacchino & J.D. Vinko. *Superconductivity in PdH: Phenomenological explanation.* Physica C: Superconductivity, vol. 408-410, no. 81, pages 350–352, 2004.

[Tripodi 06] P. Tripodi. *High-T_c Palladium Hydride Superconductor.* United States Patent No. US 7,033,568 B2, 2006.

[Tripodi 09] P. Tripodi, D. Di Gioacchino & J.D. Vinko. *Answer to the remarks on superconductivity in PdH.* Journal of Alloys and Compounds, vol. 470, no. 1-2, pages L6–L8, 2009.

[Uchic 04] M.D. Uchic, D.M. Dimiduk, J.N. Florando & W.D. Nix. *Sample Dimensions Influence Strength and Crystal Plasticity.* Science, vol. 305, pages 986–989, 2004.

[Veprek 10] S. Veprek, A.S. Argon & R.F. Zhang. *Design of ultrahard materials: Go nano!* Philosophical Magazine, vol. 90, no. 31, pages 4101–4115, 2010.

[Verbetsky 00] V.N. Verbetsky & S.V. Mitrokhin. *Cobalt-, Rhodium- and Iridium-Hydrogen.* In Hydrogen in Metal Systems II, pages 116–135. Scitec Publications, 2000.

[Vinet 87] P. Vinet, J. Ferrante, J.H. Rose & J.R. Smith. *Compressibility of Solids.* Journal of Geophysical Research, vol. 92, page 9319, 1987.

[Volkert 07] C.A. Volkert & A.M. Minor. *Focused Ion Beam Microscopy and Micromachining.* MRS Bulletin, vol. 32, page 389, 2007.

[Wang 00] C.Z. Wang, K.M. Ho, M.D. Shirk & P.A. Molian. *Laser-Induced Graphitization on a Diamond (111) Surface.* Physical Review Letters, vol. 85, page 4092, 2000.

[Wang 09] Y. Wang, J. Zhang, H. Xu, Z. Lin, L.L. Daemen, Y. Zhao & L. Wang. *Thermal equation of state of copper studied by high PT synchrotron x-ray diffraction.* Applied Physics Letters, vol. 94, page 071904, 2009.

[Weir 96] S.T. Weir, A.C. Mitchell & W.J. Nellis. *Metallization of Fluid Molecular Hydrogen at 140 GPa (1.4 Mbar).* Physical Review Letters, vol. 76, pages 1860–1863, 1996.

[Wigner 35] E. Wigner & H.B. Huntington. *On the possibility of a Metallic Modification of Hydrogen.* Journal of Chemical Physics, vol. 3, pages 764–770, 1935.

[Wolf 93] R.J. Wolf, M.W. Lee, R.C. Davis, P.J. Fay & J.R. Ray. *Pressure-composition isotherms for palladium hydride.* Physical Review B, vol. 48, page 12415, 1993.

[Xu 05] R. Xu & T.C. Chiang. *Determination of Phonon Dispersion Relations by X-ray Thermal Diffuse Scattering.* Zeitschrift für Kristallographie, vol. 220, pages 1009–1016, 2005.

[Young 06] Andrea Young, Chrystele Sanloup, Eugene Gregoryanz, Sandro Scandolo, Russell Hemley & Ho-kwang Mao. *Synthesis of Novel Transition Metal Nitrides IrN2 and OsN2.* Physical Review Letters, vol. 96, no. 15, page 155501, April 2006.

[Zaleski-Ejgierd 12] P. Zaleski-Ejgierd, V. Labet, T.A. Strobel, R. Hoffmann & N.W. Ashcroft. *WH_n under pressure.* Journal of Physics: Condensed Matter, vol. 24, page 155701, 2012.

[Zhang 07] G.F Zhang, B. Zhang, Z.H Deng & J.F. Chen. *An Experimental Study on Laser Cutting Mechanisms of Polycrystalline Diamond Compacts.* Annals of the CIRP, vol. 56, page 201, 2007.

[Zhou 11] X.-F. Zhou, A. Oganov, X. Dong, L. Zhang, Y. Tian & H.-T. Wang. *Superconducting high-pressure phase of platinum hydride from first principles.* Physical Review B, vol. 84, no. 5, page 054543, 2011.

[Zurek 09] E. Zurek, R. Hoffmann, N.W. Ashcroft, A.R. Oganov & A.O. Lyakhov. *A little bit of lithium does a lot for hydrogen.* Proceedings of the National Academy of Science, vol. 106, page 17640, 2009.

[Züttel 04] A. Züttel. *Hydrogen storage methods.* Die Naturwissenschaften, vol. 91, no. 4, pages 157–72, 2004.

Publications

Publications in peer-reviewed journals:

"Synthesis and properties of platinum hydride", Phys. Rev. B **83**, 214106 (2011)
Thomas Scheler, Olga Degtyareva, Miriam Marqués, Christophe L. Guillaume, John E. Proctor, Shaun Evans, and Eugene Gregoryanz

"On the effects of high temperature and high pressure on the hydrogen solubility in rhenium", J. Chem. Phys. **135**, 214501 (2011)
Thomas Scheler, Olga Degtyareva, and Eugene Gregoryanz

"Mixed Molecular and Atomic Phase of Dense Hydrogen", Phys. Rev. Lett. **108**, 125501 (2012)
Ross T. Howie, Christophe L. Guillaume, Thomas Scheler, Alexander F. Goncharov, and Eugene Gregoryanz

"Proton tunneling in phase IV of hydrogen and deuterium", Phys. Rev. B **86**, 214104 (2012)
Ross T. Howie, Thomas Scheler, Christophe L. Guillaume, and Eugene Gregoryanz

Manuscripts in preparation (as of 20st March 2013):

"High-Pressure Synthesis of Noble Metal Hydrides", accepted for publication in J. Chem. Phys.
Christian Donnerer, Thomas Scheler and Eugene Gregoryanz

"Nanocrystalline Tungsten Hydrides at High Pressures", submitted
Thomas Scheler, Feng Peng, Christophe L. Guillaume, Ross T. Howie, Yanming Ma, Eugene Gregoryanz

"High-pressure synthesis and characterization of iridium-trihydride", submitted
Thomas Scheler, Miriam Marqués, Zuzana Konôpková, Christophe L. Guillaume, Ross T. Howie and Eugene Gregoryanz

Synthesis and properties of platinum hydride

Thomas Scheler,[1] Olga Degtyareva,[1] Miriam Marqués,[1] Christophe L. Guillaume,[1] John E. Proctor,[1] Shaun Evans,[2] and Eugene Gregoryanz[1]

[1]*School of Physics and Astronomy and Centre for Science at Extreme Conditions, The University of Edinburgh, Edinburgh, EH9 3JZ, United Kingdom*

[2]*European Synchrotron Radiation Facility, BP 220, Grenoble, France*

(Received 4 April 2011; published 9 June 2011)

Synchrotron x-ray diffraction experiments on compressed platinum-hydrogen mixtures reveal the formation of platinum hydride at a pressure of 27(1) GPa at room temperature. This compound exhibits two phases, PtH-I and PtH-II, coexisting up to the pressure of 42 GPa, above which the single phase of PtH-II is observed. Pt atoms in the PtH-II phase are shown to form a hexagonal closed-packed structure. This phase exhibits a high bulk modulus of 310 (10) GPa and is stable up to at least 53 GPa. *Ab initio* calculations show that PtH-II is superconducting with $T_c = 12$ K at 90 GPa, the highest temperature of superconducting transition among any known metal hydride.

DOI: 10.1103/PhysRevB.83.214106 PACS number(s): 64.60.−i, 62.50.−p, 74.62.Fj

Hydrogen is known to form compounds with many elements in the periodic table.[1] Among those, the metal hydrides are of particular interest due to their application in hydrogen storage for fuel cells[2,3] or heat storage for the solar-energy industry.[4] Also, in fundamental science, metal hydrides become increasingly important due to their relevance to the study of the behavior of pure hydrogen at extreme conditions[5,6] and as materials with potentially interesting properties.[1] Because of the very low solubility of hydrogen at ambient conditions in platinum, as well as most other transition metals, these elements do not form hydrides.

High pressure can provide a different route to the synthesis of new compounds, initiating chemical processes that would not happen otherwise. By bringing atoms closer together, high pressure forces short bonds to participate in novel chemical reactions. This can result in the formation of new materials with advanced properties such as extreme hardness (e.g. the formation of diamond from graphite). However, high temperatures are usually required in addition to high pressures to initiate the synthesis or a phase transition. A number of transition metals that do not react with hydrogen at normal conditions have been shown to form hydrides at high temperatures and moderate pressures.[1,7,8] The formation of platinum hydride has been suggested from thermodynamic calculations to happen at pressures below 10 GPa,[9,10] but this has not been observed in the experiments at the predicted pressure range (<10 GPa).[1,8] Pressures as high as 50 GPa and temperatures of 2000 K are needed to make platinum react with nitrogen, an inert gas at ambient conditions, forming platinum nitride.[11,12]

The apparent inertness of Pt has been playing a very important role in the development and use of the diamond-anvil cell technique for high-pressure experiments. Pt is commonly used as an internal standard for pressure calibration based on x-ray diffraction, electrodes for electrical conductivity measurements, as well as a heat absorber in laser-heating experiments of transparent materials. The validity of the high-pressure experiments depends upon the assumption that Pt is nonreactive and any observed change is due to the studied material. Recently, the direct synthesis of platinum hydride under pressure (>25 GPa) was reported.[13] Its formation was also suggested as a result of a chemical reaction involving decomposition of silane.[14] The details of structural, mechanical, and electronic properties of this novel material, however, remain unknown. In this paper, we report the formation of platinum hydride above 27(1) GPa at 300 K, crystallizing into two hexagonal phases, PtH-I and PtH-II. Our experimental data allowed us to characterize the crystal structure of PtH-II, demonstrating low compressibility, while our *ab initio* calculations reveal that this compound is a superconductor with $T_c = 12$ K at 90 GPa.

We have conducted four independent high-pressure experiments in symmetrical diamond anvil cells. Pure (>99.95%) platinum foil or powder was loaded in a 100–125-μm-diameter hole of a rhenium gasket together with hydrogen precompressed to 1800 bar. The solidified hydrogen also acted as the pressure-transmitting medium. To determine the pressure, we used *in-situ* fluorescence measurements of ruby chips loaded in the sample chamber. We have used Raman spectroscopy to verify the presence and purity of hydrogen. X-ray powder diffraction measurements were performed at beamline ID09 of the European Synchrotron Radiation Facility using monochromatic x-rays at a wavelength of 0.415 Å. The diffraction patterns were recorded with a MAR CCD and integrated using the Fit2D software.[15] Total energy calculations for hcp-PtH were performed under the framework of the density-functional theory using the VASP code[16] in connection with the projector-augmented wave (PAW) method.[17] The exchange and correlation energies were treated via the LDA and the GGA approximations using the Ceperley-Alder[18] and Perdew-Burke-Ernzerhof[19] parametrizations. In both cases, the Brillouin zone integrals were converged with respect to the plane-wave cutoff (600 eV) and k-point density (36^3 meshes). The calculated energy-volume (per formula unit) points were converted into static and finite-temperature pressure-volume isotherms using numerical procedures coded in the GIBBS program.[20] Thermal contributions are included by means of a nonempirical quasi-harmonic Debye-like model. Electron-phonon coupling (EPC) calculations were performed within the density-functional perturbation theory with the Quantum-Espresso code.[21] We used the Perdew-Zunger local density exchange-correlation functional.[22] The electronic-wave

 ©2011 American Physical Society

functions were represented in a plane-wave basis set with a kinetic energy cutoff of 44 Ry. The augmentation charges were expanded up to 880 Ry due to the use of ultrasoft pseudopotentials. A $6 \times 6 \times 6$ q-point mesh was used for both phonon and EPC calculations. At each q-point the phonon and EPC matrices were calculated with a $36 \times 36 \times 36$ k-point mesh. The superconducting T_c has been estimated from the Allen-Dynes modified McMillan equation[23] using a typical value of $\mu^* = 0.13$.

Up to 27(1) GPa, the observed x-ray diffraction pattern from the Pt sample corresponded to its face-centered cubic (fcc) phase (Fig. 1, lower panel), which is known to be stable to very high pressures.[24,25]. In one of the runs, the platinum sample was embedded in solid hydrogen for the duration of several days at 25 GPa, but we have not observed any indication of a reaction. When pressure was increased above 27 GPa, the diffraction pattern changed instantaneously, i.e., within the time needed to collect the x-ray pattern. Therefore we conclude that the reaction is a purely pressure (volume) driven process. The new complex pattern (Fig. 1, middle panel) contained signatures belonging to three distinct phases: fcc platinum and two different hexagonal phases with lattice parameters (I) $a = 3.096(1)$ Å, $c = 12.072(7)$ Å and (II) $a = 2.779(1)$ Å, $c = 4.731(1)$ Å, respectively ($P = 30.5$ GPa). From volume considerations (see below), we infer that these new phases belong to platinum hydride, which we call here PtH-I and PtH-II. Above 42 GPa, only the PtH-II phase is visible (Fig. 1, upper panel), up to at least 53 GPa, the maximum pressure reached in this study. The transformations are reversible upon pressure decrease. At room temperature, the PtH-II phase existed down to at least 26 GPa and PtH-I to 18 GPa, nearly 10 GPa below its synthesis pressure. At lower pressure, PtH-I decomposed into pure platinum and hydrogen. Such large hysteresis in pressure at 300 K suggests the possibility of recovering the synthesized material to ambient pressure at low temperatures.

The structure of PtH-II can be easily identified as the hexagonal-closed-packed (hcp) structure ($P6_3/mmc$ space group) occupied by Pt atoms. Taking into account the volume difference between Pt and PtH-II [$\Delta V = 2.09(4)$ Å^3] and using the analogy with other hcp metal hydrides,[1,8,27] we conclude that a nearly stoichiometric compound PtH (1:1 ratio of Pt:H) is formed with H atoms occupying the octahedral interstitial sites in the Pt host lattice (Fig. 2). While several metallic hydrides are known to exist in this hcp structure,[1,8,27] PtH-II is the first known case where an fcc metal transforms to an hcp phase upon hydrogenation.

PtH-II can be clearly distinguished from ReH_x, which is formed from Re metal used as a gasket material at the inner rim of the gasket hole as a product of reaction with hydrogen.[14] Although both materials crystallize in the hcp structure, their c/a ratios are distinctly different and hence produce different diffraction patterns. Additionally, in this study we avoided signal overlap between PtH and ReH_x by using a large gasket hole as a sample chamber combined with a tightly focused x-ray beam confining the probed region to the center of the sample.

The structure of PtH-I is complex and is not known for any other metal hydride. We assume that the stoichiometry does not change from the PtH-I to PtH-II (and reverse) and assign the 1:1 ratio of Pt:H to the PtH-I phase. The volume of the unit

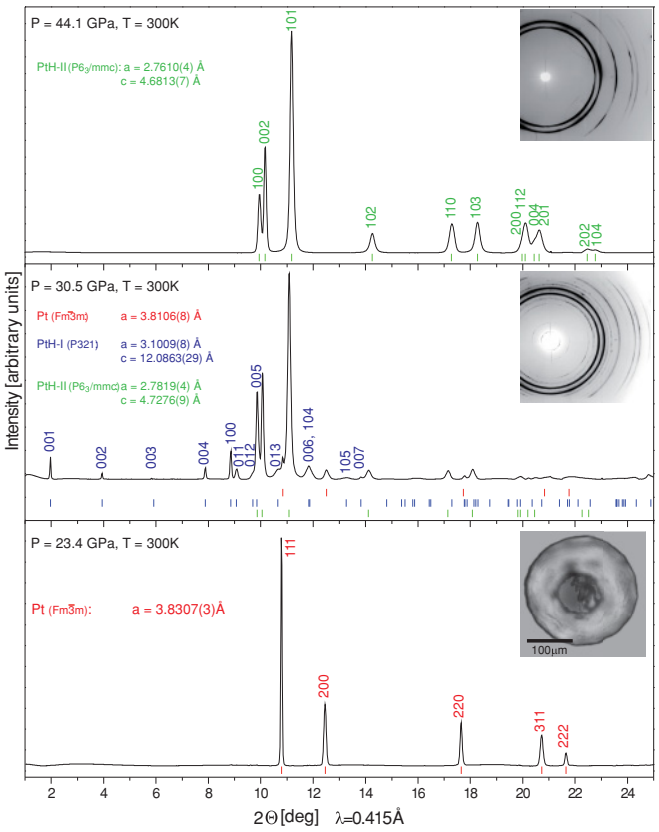


FIG. 1. (Color online) Representative x-ray diffraction patterns of pure platinum at 23.4 GPa before the formation of PtH (bottom), platinum hydride phases PtH-I and PtH-II, with the remaining phase of fcc Pt at 30.5 GPa (middle) and pure platinum hydride phase PtH-II ($P6_3/mmc$) at 44.1 GPa (upper panel). Tick marks below the spectra show the peak positions calculated from the refined lattice parameters that are given next to the spectra: In the middle panel, the tick marks correspond to Pt-fcc (top row, red on-line), PtH-I (middle row, blue online) and PtH-II (bottom row, green online). The hkl indices are shown for the Pt fcc (bottom panel), P321 phase of PtH-I (middle panel) and $P6_3/mmc$ phase of PtH-II (top panel). The inset in the bottom panel shows a micro-photograph of the sample chamber filled with solidified transparent H_2 and a piece of Pt before the reaction took place. The insets in the middle and top panels show the 2D diffraction images that correspond to the spectra shown.

cell obtained for the PtH-I phase implies 6 platinum atoms in the unit cell, and the volume difference between Pt and PtH-I [$\Delta V = 2.91(5)$ Å^3] suggests a tetrahedral occupation of hydrogen in the Pt lattice. This assumption would explain the volume difference between the I and II phases of PtH, in a close analogy to the volume reduction upon phase transformation between different Nb hydrides on pressure increase when H atoms move from tetrahedral to octahedral sites.[28]

Figure 3 shows the evolution of the volumes of both PtH phases, pure platinum and Pt + $\frac{1}{2}H_2$ with pressure. It appears that the volume of PtH becomes comparable with the one of Pt + $\frac{1}{2}H_2$ between 160 and 200 GPa and will be larger than the sum of its constituent elements above that pressure. That indicates that the PtH-II phase is likely to become unstable at pressures above 200 GPa. The analysis of the PtH equation of state reveals that the platinum hydride has a lower

compressibility compared to Pt. The evolution of volume was fitted with a Vinet equation of state and extrapolated to ambient conditions yielding the zero-pressure bulk modulus of PtH: $K_0 = 310(10)$ GPa (K_0' fixed to 5.08) and $V_0 = 17.33(1)$ Å^3. The bulk modulus of platinum hydride is noticeably higher than that of pure platinum (277 GPa).

The high-bulk modulus and the high-pressure conditions needed for the synthesis of this novel material are reminiscent of the recent discoveries of PtN_2, IrN_2, and OsN_2.[11,12,31] Indeed, the diatomic solidified gas (N_2) and the chemically inactive transition metals Pt, Ir, and Os readily formed nitrides with bulk moduli ranging from 358 GPa for metallic OsN_2 to 428 GPa for semiconducting IrN_2. Nevertheless, there are several interesting differences worth mentioning here. The nitrides were all formed at 50 GPa and high temperatures of 2000 K while PtH easily forms on "cold" compression. Another interesting point in the studies on nitrides, is that even though the metals were significantly heated, only a thin surface layer reacted to form nitrides.[31] From the relative intensity of the x-ray diffraction peaks of the nitrides with respect to their parent metal, it was estimated that although nitrides were synthesized in different quantities, the amount of nitride was always less than the remaining parent metal.[31] In the present study, in different runs the Pt samples occupied from 15% to 50% of the chamber volume above 5.5 GPa, the pressure at which hydrogen solidifies at 300 K (inset to Fig. 1, bottom panel). Even in the latter case, the whole platinum sample *completely* transformed into PtH and no detectable platinum diffraction signal was visible above 42 GPa (Fig. 1, upper panel). We have also monitored the diffraction pattern at a given pressure as function of time to determine if the prolonged exposure of platinum in dense hydrogen can modify the stoichiometry of the compound. On the time scale of several days we have not observed any deviations from the 1:1 ratio.

It was recently suggested that in the dense group IVa hydrides, where hydrogen is a dominant constituent, metallic states and superconductivity could be reached by subjecting the hydrides to high compressions.[6] The experimental confirmation quickly followed with the claim of the pressure-induced metallization and superconductivity in silane (SiH_4) at above 50 GPa.[29] We have argued[14] that at pressures above 50 GPa, silane partially decomposes, releasing hydrogen, which readily reacted with platinum electrodes used for the conductivity measurements in Ref. 29. We have also suggested[14] that the superconductivity and very low compressibility observed in Ref. 29 are much more likely to be due to the formation of the metallic platinum hydride rather than pressure induced metallization of the relatively soft molecular crystal of SiH_4. Most recent careful studies on silane revealed amorphisation, partial decomposition and recrystallisation into a polymeric phase[32] which remains insulating to at least 150 GPa.[33]

Here, we have performed *ab initio* calculations on the thermodynamic stability of the PtH-II phase and investigated the possibility of superconductivity. At lower pressure, e.g., 40 GPa, the hcp structure proved to be dynamically unstable, giving soft phonon modes with associated imaginary frequencies. However, due to a pressure-induced phonon stabilization, the imaginary frequencies at the Γ point of the Brillouin zone become real at 80 GPa and this structure emerges as dynamically stable at around 90 GPa, with the disappearance

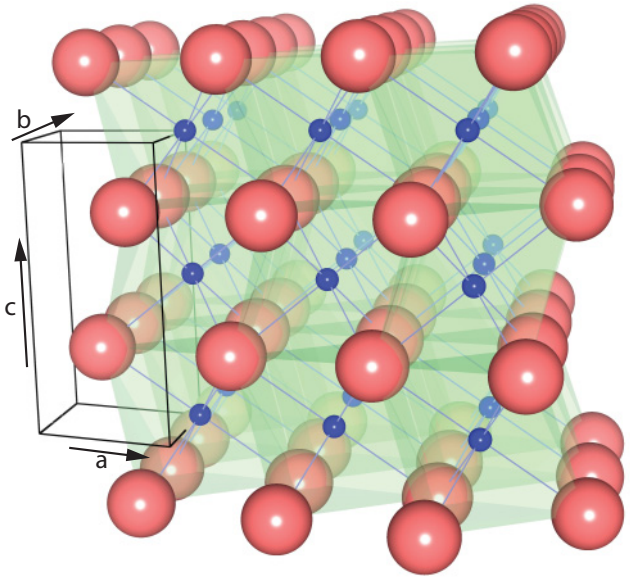


FIG. 2. (Color online) The atomic arrangement for the PtH-II structure (visualised using VESTA[26]). Two Pt atoms occupy the 2c position (1/3 2/3 1/4) of the space group $P6_3/mmc$ (large spheres, red online), as determined by x-ray diffraction in the present work. The octahedral interstitials (shaded) are occupied by the hydrogen atoms at the positions 2a (0 0 0) (small spheres, blue online), in analogy with other known hcp metal hydrides[8]. The bond length between Pt and H as shown here is 1.994 Å (at 30.5 GPa).

of a soft mode along the Γ-M line. Despite the instability at lower pressures, the proposed structure and stoichiometry turned out to be the most stable in our calculations. More interestingly, superconductivity appears with an estimated T_c value of 12 K at the pressure of 90 GPa. The inset to Fig. 3 shows the calculated T_c that are comparable to the experimentally observed superconducting temperatures in the claimed "metallic silane,"[29] which we interpret here as superconductivity in PtH.

At ambient pressure, platinum is known to have a superconducting transition at millikelvin temperature range.[34] Therefore, the solubility of hydrogen at high pressures enhances the temperature of the superconducting transition by several orders of magnitude. In most superconducting *d*-metals, the presence of hydrogen in the metal lattice either decreases the critical temperature (e.g., TcH, ReH_x, VH, NbH) or does not affect it at all (e.g., RuH, MoH).[35] Paladium in which no superconductivity has been detected down to $2x10^{-4}$ K shows a similarly high T_c in paladium hydride of about 9–11 K.[35] The observed superconductivity in silane that is here attributed to platinum hydride and the high calculated values of T_c for hcp PtH is a remarkable finding for such a simple system.

Our combined diamond-anvil-cell experiments and theoretical calculations have demonstrated the possibility of the room temperature ("cold") high-pressure synthesis of superconducting platinum hydride with a low compressibility. Most syntheses of metal hydrides are reported at high temperatures and pressures below 10 GPa, with such limit in pressure imposed by the large volume press techniques

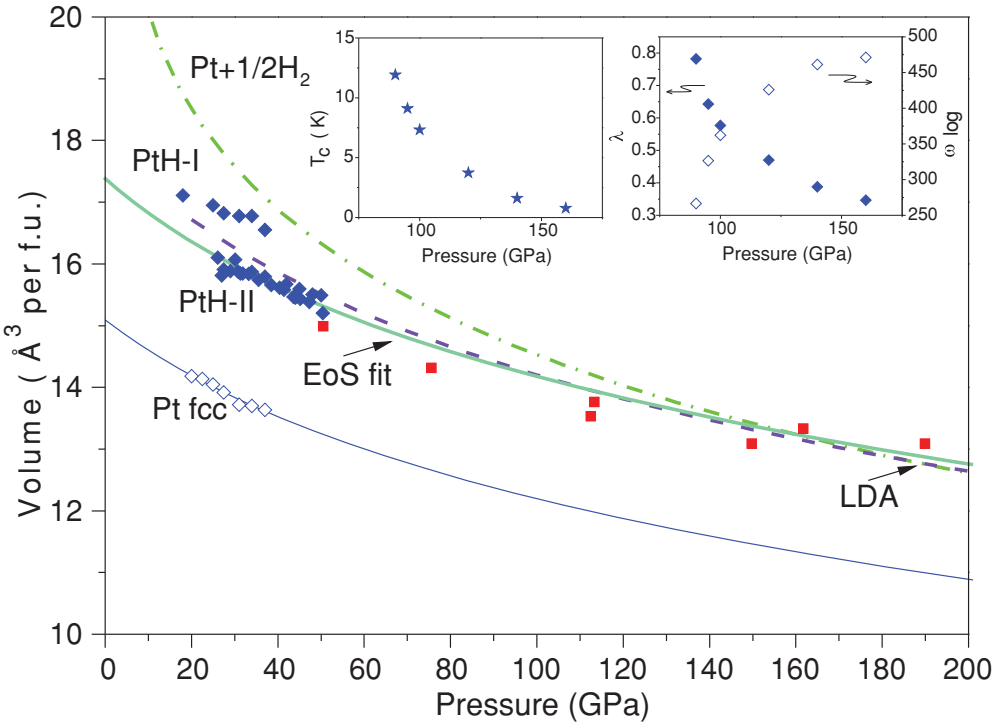


FIG. 3. (Color online) Equations of state of platinum hydride. The solid diamond symbols show the *P*-*V* data for PtH-I and PtH-II phases, and open diamond symbols show the *P*-*V* data for the fcc phase of Pt, all measured in the present work. Solid squares show the data from Ref. 29 for comparison. The solid curve shows a Vinet-type fit for the equation of state of the PtH-II phase, with the dashed line showing the equation of state calculated from first principles at 300 K using LDA (while the EoS resulting from GGA lies slightly higher). For comparison, the equations of state are shown for pure Pt from the Refs. 24 and 25 (thin solid curve) and H_2 in Pt + $\frac{1}{2}H_2$ from Ref. 30 (dash-dotted line). Left inset shows the calculated superconducting transition temperature T_c in the hcp PtH-II phase as a function of pressure. Right inset gives values of the electron–phonon coupling parameter, λ (solid symbols), and the asymptotic phonon momentum $\omega_{\log}$ (open symbols).

used.[1,7,8] It is only recently that the diamond anvil cell technique has been applied for the direct synthesis of hydrides from pure elements at higher pressures enabling the formation of copper hydride at 14 GPa[36] and platinum hydride at 26 GPa.[13] Our results demonstrate the power of this experimental technique, reporting interesting properties of the platinum hydride synthesised at pressures above 27 GPa.

Finally, our results are of importance to the field of high-pressure science from the point of view of experimental techniques. For many years, platinum has been used in high-pressure experiments as a pressure calibrant, heat absorber, or electrical probe material without the formation of platinum hydride being considered. Our results show that the possibility of platinum hydride formation must be taken into account in experiments involving hydrogen. Due to the high T_c and low compressibility of platinum hydride, the results presented in this study will undoubtedly stimulate theoretical and experimental studies of the properties and synthesis of hydrogen-rich metallic compounds.

ACKNOWLEDGMENTS

This work is supported by a research grant from the UK Engineering and Physical Sciences Research Council and experimental facilities made available by the European Synchrotron Radiation Facility. Computer resources were provided by MALTA (CSD2007-0045 and CTQ2009-14596-C02-02 projects). T.S. gratefully acknowledges the support of the EPSRC Scottish Doctoral Training Centre in Condensed Matter Physics. O.D. acknowledges V. Degtyareva for stimulating discussions and the Royal Society for their support.

[1] Y. Fukai, *The Metal-Hydrogen System* (Springer Verlag, Berlin, 2005).
[2] N. L. Rosi *et al.*, Science **300**, 1127 (2003).
[3] I. P. Jain, C. Lal, and A. Jain, Int. J. Hydrogen Energy **35**, 5133 (2010).
[4] M. Felderhoff, B. Bogdanovic, Int. J. Mol. Sci. **10**, 325 (2009).
[5] N. W. Ashcroft, Phys. Rev. Lett. **21**, 1748–1749 (1968).
[6] N. W. Ashcroft, Phys. Rev. Lett. **92**, 187002 (2004).
[7] V. E. Antonov, T.E.Antonova, I.T.Belash, A.E.Gorodetskii, and E.G.Ponyatovskii, Dokl.Akad.Nauk SSSR **266**, 376 (1982) [Dokl.Phys.Chem. (Proc.Acad.Sci.USSR) **266**, 722 (1982)].
[8] V. E. Antonov, J. Alloys Compd. **330**, 110 (2002).

[9]A. Driessen *et al.*, J. Phys. Condens. Matter **2**, 9797 (1990).
[10]H. Sugimoto and Y. Fukai, Acta Metall. Mater. **40**, 2327 (1992).
[11]E. Gregoryanz *et al.*, Nat. Mater. **3**, 294 (2004).
[12]J. C. Crowhurst *et al.*, Science **311**, 1275 (2006).
[13]N. Hirao *et al.*, International Symposium on Metal-Hydrogen Systems, Reykjavik, Iceland, 2008; see also Acta Crystallogr. Sect. A **64**, C609 (2008).
[14]O. Degtyareva, Solid State Commun. **149**, 1583 (2009).
[15]A. P. Hammersley, S. O. Svensson, M. Hanfland, A. N. Fitch, and D. Hausermann, High Press. Res. **14**, 235 (1996).
[16]G. Kresse and J. Furthmuller, Phys. Rev. B **54**, 11169 (1996)
[17]G. Kresse, D. Joubert, Phys. Rev. B **59**, 1758 (1999).
[18]D. M. Ceperley and B. J. Alder, Phys. Rev. Lett. **45**, 566 (1980).
[19]J. P. Perdew, K. Burke, and M. Ernzerhof, Phys. Rev. Lett. **77**, 3865 (1996).
[20]M. A. Blanco, E. Francisco, and V. Luaña, Comput. Phys. Commun. **158**, 57 (2004).
[21]P. Giannozzi *et al.*, J. Phys. Condens. Matter **21**, 395502 (2009); see also [http://www.quantum-espresso.org].
[22]J. P. Perdew and A. Zunger, Phys. Rev. B **23**, 5048 (1981).
[23]P. B. Allen and R. C. Dynes, Phys. Rev. B **12**, 905 (1975).
[24]N. C. Holmes *et al.*, J. Appl. Phys. **66**, 2962 (1989).
[25]A. Dewaele, P. Loubeyre, and M. Mezouar, Phys. Rev. B **70**, 1 (2004).
[26]K. Momma and F. Izumi, J. Appl. Crystallogr. **41**, 653 (2008).
[27]V. Somenkov, V. Glazkov, A. Irodova, and S. Shilstein, J. Less Common Met. **129**, 171 (1987).
[28]A. Fukizawa and Y. Fukai, J. Phys. Soc. Jpn. **52**, 2102 (1983).
[29]M. I. Eremets *et al.*, Science **319**, 1506 (2008).
[30]P. Loubeyre *et al.*, Nature (London) **282**, 702 (1996).
[31]A. Young, C. Sanloup, E. Gregoryanz, S. Scandolo, R. Hemley, and H. K. Mao, Phys. Rev. Lett. **96**, 155501 (2006).
[32]M. Hanfland, J. E. Proctor, C. L. Guillaume, O. Degtyareva, and E. Gregoryanz, Phys. Rev. Lett. **106**, 095503 (2011).
[33]T. A. Strobel, A. F. Goncharov, C. T. Seagle, Z. Liu, M. Somayazulu, V. V. Struzhkin, and R. J. Hemley, Phys. Rev. B **83** 144102 (2011).
[34]R. Konig, A. Schindler, and T. Herrmannsdorfer, Phys. Rev. Lett. **82**, 4528 (1999).
[35]I. O. Bashkin, V. E. Antonov, and E. G. Ponyatovsky, in *Studies of High Temperature Superconductors* (Nova Science Publishers, New York, 2003), Vol 45, pp. 171–241.
[36]R. Burtovyy and M. Tkacz, Solid State Commun. **131**, 169 (2004)

On the effects of high temperature and high pressure on the hydrogen solubility in rhenium

Thomas Scheler, Olga Degtyareva, and Eugene Gregoryanz[a)]
SUPA, School of Physics and Astronomy and Centre for Science at Extreme Conditions, The University of Edinburgh, Edinburgh EH9 3JZ, United Kingdom

(Received 19 August 2011; accepted 27 September 2011; published online 1 December 2011)

In situ x-ray diffraction experiments on rhenium hydride compressed up to 46 GPa reveal a hydrogen solubility (x) significantly larger than the previously assumed saturation limit of $x \sim 0.38(4)$. In the layered anti-CdI_2-type structure of rhenium hydride, the hydrogen solubility was found to increase to $x \sim 0.5$ at 15 GPa over time. When heated to temperatures above 420 K at pressures above 23 GPa, rhenium hydride undergoes an isomorphous phase transition into the NiAs-type structure accompanied by an increase in hydrogen solubility to $x \sim 0.85$. The formation of fully stoichiometric rhenium hydride is discussed. © *2011 American Institute of Physics*. [doi:10.1063/1.3652863]

I. INTRODUCTION

The metal hydrides have attracted increased attention in the recent past, owing to their applications in industry and their importance for fundamental science.[1–4] While many metals readily react with hydrogen to form hydrides at ambient conditions, most transition metals between the chromium group (group 6) and copper group (group 11) do not.[3] With the exception of palladium, high pressures, and high temperatures are necessary for the synthesis of binary hydrides. At pressures above 1 GPa, the solubility of hydrogen in these metals rises steeply and most of them form hydrides under thermodynamic equilibrium conditions.[4] The exact synthesis conditions vary widely, ranging from just 0.6 GPa in the case of nickel hydride[5] to 27 GPa for platinum hydride.[6] At even higher pressures, the synthesis of silicon tetrahydride at 124 GPa from the constituent elements was reported recently.[7] Most of these compounds show ideal or at least near stoichiometric composition, i.e., usually a H/M atomic ratio of 1:1, where M denotes the metal. Only the hydrides of ruthenium, copper, and rhenium have never been found to exhibit a hydrogen solubility $x > 0.5$. While for ruthenium hydride, the hydrogen solubility was found to be extremely small (only $x = 0.035$),[8] the only study on a high-pressure synthesis of copper hydride finds a hydrogen solubility of up to $x = 0.4$.[9] However, the data reveal no signs of saturation and higher solubilities might be possible.

While reports on the high-pressure syntheses of the binary hydrides of copper and ruthenium are scarce, rhenium hydride is a well-studied material.[10–16] Owing to its very high bulk modulus (370 GPa), but at the same time low brittleness, rhenium is widely used in high-pressure science as a gasket material. The formation of rhenium hydride in the gasket at high pressure is a well-known fact (see, *e.g.*, Ref. 14). The hydride was first synthesized almost 30 years ago in a large volume press at pressures around 9 GPa and temperatures of 440 K.[10] Measuring the amount of hydrogen released by quenched samples, a maximum hydrogen solubility of $x \sim 0.22$ was found. This value was later confirmed by neutron diffraction experiments.[11] In the mid 1990s, diamond anvil cell (DAC) experiments revealed an increase in solubility to $x \sim 0.38(4)$ when rhenium is compressed under a pure hydrogen atmosphere to above 9 GPa at room temperature.[13] To date, this is the commonly accepted stoichiometry of rhenium hydride and even at much higher pressures (above 100 GPa), no increase in solubility was detected.[14] Here, we present results from x-ray diffraction experiments on the rhenium hydrogen system compressed to pressures of up to 46 GPa using the diamond anvil cell technique and simultaneous heating to temperatures up to 570 K. We found a drastically increased hydrogen solubility and suggest that $ReH_{1.0}$ forms at sufficiently high pressures.

II. EXPERIMENTAL DETAILS

In the first of two independent experiments, the formation of rhenium hydride from the gasket material in a DAC was observed which is a common situation in high-pressure experiments involving hydrogen. In the second run, pristine Re powder was loaded into a DAC. In both runs, symmetric DACs were used and hydrogen was gas-loaded to a pressure of 1500 bar. The solid hydrogen also acted as the pressure transmitting medium. The revised hydrostatic ruby pressure scale was used to measure the pressure inside the sample volume.[17] The ruby fluorescence signal indicated that the conditions remained quasi-hydrostatic up to 46 GPa, the highest pressures reached in this study. In the second run, the Re-gasket was sputter coated with gold to prevent the formation of rhenium hydride in the gasket. In order to allow full hydrogenation, the sample was loaded and compressed to 15 GPa more than one month prior to carrying out the x-ray measurements. The cells were heated in an oven to temperatures between 420 K and 570 K for durations between 8 h and 20 h. X-ray diffraction experiments were conducted at the high-pressure beam line I15 at the Diamond Light Source, UK. Synchrotron radiation at a wavelength of 0.4133 Å (30 keV) was collimated by a stack of tungsten pinholes

[a)]Electronic mail: e.gregoryanz@ed.ac.uk.

 © 2011 American Institute of Physics

Author complimentary copy. Redistribution subject to AIP license or copyright, see http://jcp.aip.org/jcp/copyright.jsp

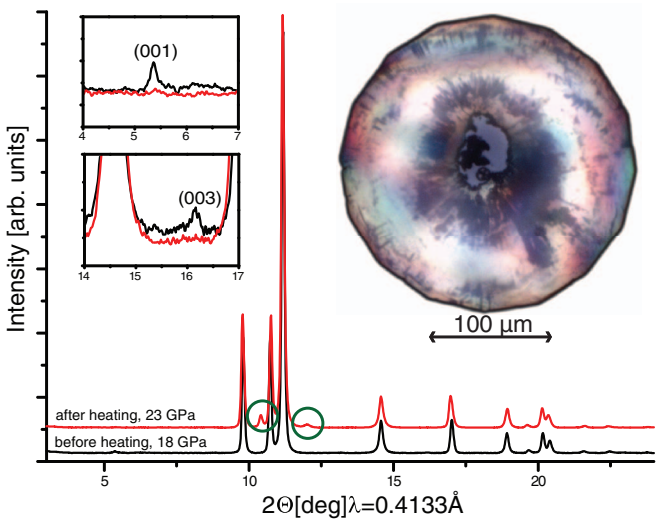


FIG. 1. Diffraction patterns of Re-H before (lower, black) and after (upper, red) heating. The diffraction pattern before heating was taken at 18 GPa, the pattern after heating at 23 GPa. The insets show the disappearance of the (001) and (003) superstructure reflections. In circles (green): Reflections of fcc-Au from the sputter-coated gasket. The optical microscopy picture shows the gasket, gasket hole, Re-piece, and ruby sphere. The dark shaded area shows the extension of the original gasket hole before partial collapse during compression and heating. The culet diameter is 250 μm.

to obtain a beam diameter of ~20 μm. Angular dispersive powder diffraction patterns were recorded using a MAR345 image plate detector. All data after heating were taken after the cells cooled down to room temperature. The diffraction patterns were integrated using the FIT2D software.[18]

III. RESULTS AND DISCUSSION

In both runs, before and after heating, the integrated diffraction patterns clearly show the hcp-like structure of rhenium hydride up to 46 GPa (see Fig. 1), which can be indexed in the $P6_3/mmc$ space group. Also in both runs, a difference in unit-cell volume between pure rhenium and our sample was found, indicating the formation of rhenium hydride (see Table I). Before the first heating cycle, we were able to observe weak reflections at $2\Theta \sim 5.4^\circ$ and $2\Theta \sim 16.2^\circ$. These can be identified as the Re-H superstructure peaks of the (001) and (003) forbidden reflections, first reported by Kawamura *et al.*[15] After heating the samples for several hours (8 h at 470 K and 23 GPa), the superstructure peaks disappeared and an increase in unit-cell volume was measured (see Table I at 23.2 GPa). Upon further pressure increase, the volume difference to pure Re increased monotonously. The highest pressure reached in the second run was 35 GPa due to diamond failure at this point. In the first run, the volume increase was found to continue up to 46 GPa, at which pressure, the cell was heated to 570 K for 8 h. During the heating, the gasket hole collapsed completely. The non-hydrostatic ruby signal did not indicate a significant pressure drop and we were able to detect the rhenium hydride signal from the gasket in which we measured a drop in unit-cell volume (see Table I at 46.0 GPa). At this point, the superstructure reflections also appeared again. On pressure decrease, the volume difference remained constant.

TABLE I. Lattice parameters and unit-cell volumes per rhenium atom of rhenium hydride at various pressures. The data at 18.2 GPa was taken before heating, at 23.2, 35.2, and 45.2 after heating. Data at 46.0 GPa was taken after heating to 570 K. The volume of pure Re at the same pressures and the volume difference are added for comparison. The hydrogen solubility is found by dividing the volume difference by the volume expansion per hydrogen atom (i.e., 2.0 Å^3 – see text).

P (GPa)	a (Å)	c (Å)	V_{at} (Å^3)	V_{Re} (Å^3)	ΔV (Å^3)
18.2	2.801(1)	4.427(1)	15.04(1)	14.05	0.99
23.2	2.811(1)	4.421(1)	15.13(1)	13.90	1.23
35.2	2.801(1)	4.410(1)	14.98(1)	13.55	1.34
45.2	2.794(1)	4.438(1)	15.00(1)	13.29	1.71
46.0	2.732(1)	4.321(1)	13.96(1)	13.28	0.68

It is generally accepted that in a hydride with a metal host lattice of hexagonally closed packed structure, the hydrogen atoms occupy the octahedral equilibrium interstitial sites,[3] resulting in a NiAs-type structure. This has been confirmed experimentally by neutron diffraction for rhenium hydride.[11] The presence of the hydrogen atoms leads to an expansion of the host lattice, which, for $ReH_{0.23}$, was measured by neutron diffraction to be 2.0 Å^3 per hydrogen atom.[11] The exact reason for this volume expansion is yet unclear but it was suggested that it might be due to electron donation of the absorbed hydrogen atom to the *s*- and *d*-bands of the host metal.[19] Furthermore, a linear dependency of the hydrogen solubility on the lattice expansion was found.[3,10] Together with measuring the unit-cell volume, this allows for the *in situ* determination of the hydrogen content in x-ray studies. Other methods of determining the hydrogen content are (i) measuring the amount of released hydrogen from quenched samples[10] and (ii) determining the hydrogen to metal atomic ratio by neutron diffraction.[11] However, because of the extremely small sample quantities produced in a DAC and the common inaccessibility of pressures above 20 GPa by neutron diffraction, the comparison of unit cell volumes remains the only viable method to determine the hydrogen solubility in metal hydrides synthesized in the DAC. This method was used to determine the hydrogen solubility in $ReH_{\sim 0.4}$.[13–15]

As mentioned above, Kawamura *et al.*[15] reported that $ReH_{0.36}$ exhibits a layered superstructure where hydrogen atoms occupy only every second layer in the hcp lattice. In accordance with the notation for other metal hydrides (see below and Ref. 4), this anti-CdI_2-type structure of rhenium hydride will be referred to as the the ϵ_1-phase here. This phase has been found to be stable up to very high pressures above 100 GPa.[14,20] The presence of the (001) and (003) superstructure reflections in our data confirm that before heating our sample was indeed in the ϵ_1-phase (residing at pressure for more than one month). At this point, we measured a volume difference of 1.98 Å^3 per unit-cell or ~0.99 Å^3 per metal atom (see Table I at 18.2 GPa), indicating a hydrogen solubility of $x \sim 0.5$. This is already larger than the previously reported maximum solubility of hydrogen in rhenium of $x < 0.4$. The increased hydrogen solubility in our sample can be explained by the long hydrogenation time. Most previous experiments were presumably performed on a time scale of a few hours between initial hydrogenation and reaching

Author complimentary copy. Redistribution subject to AIP license or copyright, see http://jcp.aip.org/jcp/copyright.jsp

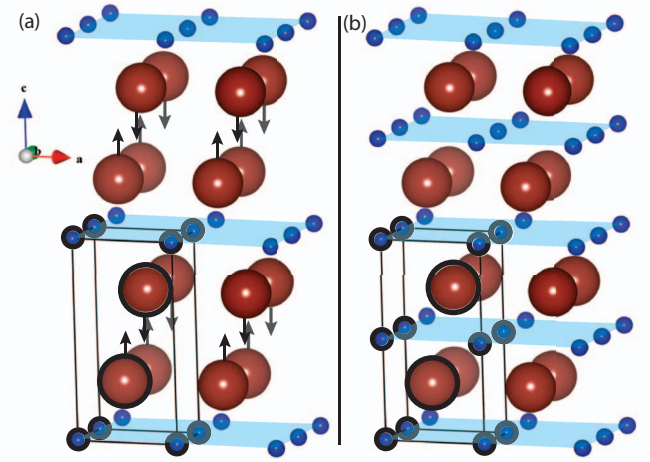


FIG. 2. (a) Layered anti-CdI_2-type structure of ϵ_1-Re_2H. The arrows indicate the displacement of the Re-atoms from their equilibrium positions in the hcp lattice (not to scale). This displacement gives rise to the superstructure reflections in ϵ_1-Re_2H. (b) NiAs-type structure of ϵ_2-ReH. The transparent blue sheets depict hydrogen layers with available interstitial sites. In both figures, the unit cell is indicated by the wire frame and circles around atoms belonging to the unit cell.

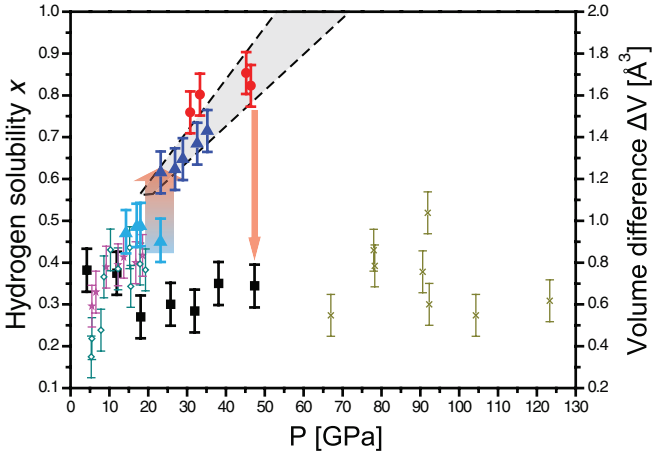


FIG. 3. Evolution of volume differences (right vertical axis, volume per metal atom, see Table I) and derived hydrogen solubility (left vertical axis) assuming 2.0(1) Å^3 per hydrogen atom (Ref. 11). The uncertainty in the volume (error bars) is estimated from the extrapolation to higher hydrogen solubilities and represents the methodological error. Larger filled symbols denote results from this study. Light blue triangles: Data from second run before heating (below 23 GPa). Dark blue triangles: Data from second run after heating (above 23 GPa). The upward arrow indicates the changes upon heating. Red circles: Data from the first run after heating. Black squares: ϵ_1-Re-H transformed back from ϵ_2-Re-H after heating to 570 K (indicated by the downward arrow). Data from other publications (diamonds (Ref. 13), stars (Ref. 15), crosses (Ref. 14)) are included for comparison. The shaded area is a guide to the eye for a linear extrapolation of the present data to full stoichiometry which would be achieved at pressures between 50 and 70 GPa.

the highest pressure. If slow kinetics hinder the immediate hydrogen saturation, this would not be seen in those experiments. A hydrogen solubility of $x \sim 0.5$ would also be the stoichiometric composition of ϵ_1-Re_2H.

After heating the sample to 420 K at a pressure of 23 GPa, an increase in unit cell volume difference to $\Delta V = 2.46$ Å^3 (atomic volume difference $\Delta V_{at} = 1.23$ Å^3) was measured, which we interpret as an increase in hydrogen solubility to $x \sim 0.6$. At this point, we were not able to observe any superstructure reflections anymore, indicating an isomorphous phase-transition into a structure where the hydrogen atoms randomly occupy the vacant interstitial sites. This corresponds to a deficient NiAs-type structure and will be denoted as the ϵ_2 phase here. For a comparison of the two structures, see Fig. 2. The $\epsilon_1 \rightarrow \epsilon_2$ phase transition is also evident in a change of the c/a ratio of the hydride lattice parameters. Pure rhenium has a $c/a = 1.613$, while ϵ_1-$ReH_{\sim 0.4}$ has a pressure independent $c/a = 1.583$.[13] We measured $c/a = 1.582(2)$ for the ϵ_1-phase and a lower $c/a = 1.573(2)$ for the ϵ_2-phase, both constant with pressure.

Upon pressure increase, the difference in unit-cell volumes between pure rhenium and rhenium hydride and thus the hydrogen solubility increased further to reach a level of $x \sim 0.7$ at 35 GPa in the second run. Data from the first run up to 46 GPa showed a further increase to $x \sim 0.85$, the highest value reached in this study and more than twice as high than the previously found saturation limit (see Fig. 3). Linear extrapolation of x leads to the estimate of full stoichiometry at pressures between 50 and 70 GPa (shaded area in Fig. 3). A continuous increase in hydrogen solubility with pressure is not uncommon and can also be observed in rhenium upon initial hydrogenation in the ϵ_1-phase. At ambient temperature, the hydrogenation process in rhenium starts at 5 GPa and leads to an early saturation at 10 GPa with $x \sim 0.4$.[13] Further increase of the hydrogen solubility to 0.5 might be hindered by slow kinetics and is only observable with time. Interestingly, both technetium hydride and cobalt hydride also exhibit a structure similar to layered ϵ_1-Re_2H.[4] The ϵ_1-phase in Co-H emerges at a hydrogen solubility of $x \sim 0.38$, coincidentally also the highest hydrogen content previously reported for Re-H synthesized at room temperature and the composition at which its layered structure was first described by Kawamura *et al.*[15] At slightly higher values ($x \sim 0.45$), technetium hydride also exists in the layered ϵ_1-phase. With increasing pressure, both hydrides show an increase in hydrogen solubility. At ~7 GPa, Co-H undergoes a structural phase transition to the face centered cubic γ-phase which quickly approaches ideal stoichiometry (i.e., $x \sim 1$). Tc-H undergoes an isomorphous transition to the NiAs-type ϵ_2 phase at just over 1 GPa and reaches $x \sim 0.8$ at 2 GPa.[21] In particular, the $\epsilon_1 \rightarrow \epsilon_2$ transition in Tc-H is similar to our findings in Re-H although at much lower pressures.

The observation that the ϵ_2 phase in Re-H is stable after cooling down to room temperature suggests the presence of a large energy barrier preventing the phase transition at lower temperatures. Interestingly, heating to 570 K for 8.5 h at 46 GPa decreased the hydrogen solubility to $x < 0.4$. At the same point the (001) and (003) superstructure peaks appeared again, i.e., rhenium hydride transformed back into the ϵ_1-structure (see Fig. 3). Upon pressure decrease, x remained constant within the error of the experiment (non-hydrostatic conditions). One explanation for the transformation from the ϵ_2-back into the ϵ_1-phase could be pressure and temperature driven hydrogen diffusion further into the gasket. At the point, where the gasket hole collapsed completely due to hydrogen loss, the central hydrogen supply was depleted and the hydrogen solubility would drop. Below a certain limit

Author complimentary copy. Redistribution subject to AIP license or copyright, see http://jcp.aip.org/jcp/copyright.jsp

(presumably $x \sim 0.5$), the hydride would then transform back into the ϵ_1-phase.

IV. CONCLUSION

We have shown that under pressure and with time, rhenium hydride in its ϵ_1-anti-CdI_2-phase approaches its stoichiometric composition of Re_2H and that the application of high temperature at elevated pressures induces an isomorphous $\epsilon_1 \rightarrow \epsilon_2$ transition to the NiAs-type structure. This transition is not observed in rhenium hydride at room temperature and pressures up to 120 GPa. The ϵ_2-phase has a significantly higher hydrogen solubility of up to $x \sim 0.85$. Our data indicate that fully stoichiometric rhenium hydride might form at pressures above 50 GPa. We further suggest that the presence of an energy barrier prevents the formation of the ϵ_2-phase at room temperature. Most *d*-metal hydrides have so far only been studied in the large volume press, i.e., at pressures below 10 GPa. The results presented in this study are a sign that also other metal hydrides might exhibit interesting properties at higher pressures that have not been discovered yet.

ACKNOWLEDGMENTS

This work is supported by a research grant from the UK Engineering and Physical Sciences Research Council. T.S. gratefully acknowledges the support of the EPSRC Scottish Doctoral Training Centre in Condensed Matter Physics. O.D. acknowledges V. Degtyareva for stimulating discussions and the Royal Society for their support. We thank A. Kleppe from beam line I15 at Diamond Light Source for technical support.

[1] A. Züttel, Die Naturwiss. **91**, 157 (2004).
[2] L. George and S. K. Saxena, Int. J. Hydrogen Energy **35**, 5454 (2010).
[3] Y. Fukai, *The Metal-Hydrogen System* (Springer-Verlag, Berlin, 2005).
[4] V. E. Antonov, J. Alloys Compd. **330**, 110 (2002).
[5] B. Baranowski, S. Majchrzak, and T. B. Flanagan, J. Phys. F **1**, 258 (1971).
[6] T. Scheler, O. Degtyareva, M. Marqués, C. L. Guillaume, J. E. Proctor, S. Evans, and E. Gregoryanz, Phys. Rev. B **83**, 214106 (2011).
[7] M. Hanfland, J. E. Proctor, C. L. Guillaume, O. Degtyareva, and E. Gregoryanz, Phys. Rev. Lett. **106**, 095503 (2011).
[8] V. E. Antonov, I. T. Belash, O. V. Zharikov, and A. V. Palnichenko, Phys. Status Solidi B **142**, K155 (1987).
[9] R. Burtovyy and M. Tkacz, Solid State Commun. **131**, 169 (2004).
[10] V. E. Antonov, I. T. Belash, V. Yu. Malyshev, E. G. Ponyatovskii, and N. A. Tulina, Dokl. Akad. Nauk SSSR **269**, 617 (1983).
[11] S. S. Shilstein, V. P. Glazkov, A. V. Irodova, V. A. Somenkov, V. E. Antonov, and E. G. Ponyatovskii, Z. Phys. Chem. Neue Folge **146**, 129 (1985).
[12] V. A. Somenkov, V. P. Glazkov, A. V. Irodova, and S. S. Shilstein, J. Less–Common Met. **129**, 171 (1987).
[13] T. Atou and J. Badding, J. Solid State Chem. **118**, 299 (1995).
[14] S. P. Besedin and A. P. Jephcoat, Rev. High Pressure Sci. Technol. **7**, 301 (1998).
[15] H. Kawamura, A. Harada, Y. Akahama, and K. Takemura, Solid State Commun. **130**, 59 (2004).
[16] V. E. Antonov, V. K. Fedotov, A. I. Harkunov, A. I. Kolesnikov, N. I. Novokhatskaya, G. Grosse, F. E. Wagner, T. Hansen, and A. S. Ivanov, Phys. Rev. B **64**, 184302 (2001).
[17] K. Syassen, High Press. Res. **28**, 75 (2008).
[18] A. P. Hammersley, S. O. Svensson, M. Hanfland, A. N. Fitch, and D. Häusermann, High Press. Res. **14**, 235 (1996).
[19] V. F. Degtyareva, in *Proceedings International Conference – Hydrogen Material Science and Chemistry of Carbonic Nanomaterials*, Sudak, Ukraine, 2003, edited by D. V. Schur, S. Yu. Zaginaichenko, and T. N. Verziroglu (IHSE, Kiev, 2003), pp. 242–243.
[20] O. Degtyareva, J. E. Proctor, C. L. Guillaume, E. Gregoryanz, and M. A. Hanfland, Solid State Commun. **149**, 1583 (2009).
[21] V. I. Spitsyn, V. E. Antonov, O. A. Balakhovskii, I. T. Belash, E. G. Poniatovskii, V. I. Raschupkin, and V. S. Shekhtman, Dokl. Akad. Nauk SSSR **260**, 132 (1981).

Author complimentary copy. Redistribution subject to AIP license or copyright, see http://jcp.aip.org/jcp/copyright.jsp

Mixed Molecular and Atomic Phase of Dense Hydrogen

Ross T. Howie,[1] Christophe L. Guillaume,[1] Thomas Scheler,[1] Alexander F. Goncharov,[2] and Eugene Gregoryanz[1,*]

[1]*Centre for Science at Extreme Conditions and School of Physic and Astronomy, University of Edinburgh, Edinburgh, EH9 3JZ, United Kingdom*

[2]*Geophysical Laboratory, CIW, 5251 Broad Branch Road, Washington, D.C. 20015, USA*

(Received 1 November 2011; published 19 March 2012)

We used Raman and visible transmission spectroscopy to investigate dense hydrogen (deuterium) up to 315 (275) GPa at 300 K. At around 200 GPa, we observe the phase transformation, which we attribute to phase III, previously observed only at low temperatures. This is succeeded at 220 GPa by a reversible transformation to a new phase, IV, characterized by the simultaneous appearance of the second vibrational fundamental and new low-frequency phonon excitations and a dramatic softening and broadening of the first vibrational fundamental mode. The optical transmission spectra of phase IV show an overall increase of absorption and a closing band gap which reaches 1.8 eV at 315 GPa. Analysis of the Raman spectra suggests that phase IV is a mixture of graphenelike layers, consisting of elongated H_2 dimers experiencing large pairing fluctuations, and unbound H_2 molecules.

DOI: 10.1103/PhysRevLett.108.125501 PACS numbers: 62.50.−p, 61.50.Ks, 78.30.Na, 78.40.Ri

The behavior of hydrogen at very high pressures is still poorly understood due to the limitations imposed on conventional experimental techniques. Currently, three solid phases of hydrogen and deuterium (labeled I, II, and III) are known (see Fig. 1) [1,2]. Phase I has a hexagonal closed-packed structure with freely rotating molecules. Phase II (the broken symmetry phase), which possesses some degree of orientational order and may differ from the lattice symmetry of phase I, exists at temperatures below 135 K and up to ~160 GPa [3,4]. Phase III is separated from phase II by an almost vertical phase line from 0 to 125 K at ~155 (165 for D_2) GPa [5,6], and the transition between the two is characterized by a large discontinuity (~ 100 cm^{-1}) in the vibron frequency. Phases I, II, and III coexist at a triple point at 125 K and 155 GPa (135 K and 165 GPa for D_2), above which a phase line with positive slope separates phases I and III. The I-III transition exhibits a similar discontinuity in vibron frequency which rapidly decreases with increasing temperature, disappearing at 250 K [7]. At 77 K and pressures in excess of 275 GPa, a change of color [8,9] and band gap of the order of 2 eV has been reported with an estimation that the band gap would close at pressures of 420–450 GPa [8–10]. Because of the difficulties associated with the containment of hydrogen at high pressures and elevated temperatures (> 250 K), the highest pressure reached at 300 K prior to this study is approximately 180 GPa [11]. Therefore, experimental high-pressure 300 K studies of hydrogen are of fundamental interest, as they may reveal new facts relevant to the I-III and other possible phase transformations or even shed light on the behavior of the melting curve at high pressures [12–14] and predicted unusual liquid state [15]. Vibrational spectroscopy is crucial for making direct measurements on the state of bonding of the material at high pressures and temperatures. In addition to information on bonding, these spectroscopic techniques have been the sole means for identifying phase transitions in H_2 at above 150 GPa, because vibrational excitations are extremely sensitive to changes in crystal structure, including melting [5,6,12]. The combined experimental evidence, from the shock-wave study on hot dense liquid hydrogen [16] and from static studies [12,14] on solid and liquid hydrogen states, indicates that the application of "*high*"

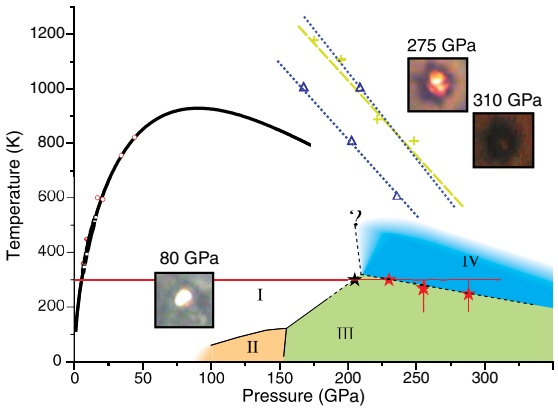


FIG. 1 (color online). Proposed phase diagram of H_2. The melting curve (thick solid line) is a Ketchin fit from Ref. [12], and the symbols along it are from Refs. [12,27]. The solid lines separating the phases I, II, and III are from Ref. [28]. The thin solid lines show the *P-T* paths taken in this study, and the stars along them show phase I to III and III to IV transformations. The dashed lines are proposed boundaries between I–III, III–IV, and I–IV phases. The calculated transition lines between molecular and atomic liquid are shown with dashed lines and crosses [24] and triangles [25]. The microphotographs show the appearance of deuterium in phase I and hydrogen in phase IV.

 © 2012 American Physical Society

temperatures might facilitate the dissociation of the hydrogen molecule and therefore promote transformation to an atomic and metallic state at lower pressures. In this Letter, using high-pressure Raman and visible transmission spectroscopy, we show that at high temperatures ($T = 300$ K) and above 220 GPa hydrogen adopts an unusual structure containing 6-atom rings corresponding to a ''predissociated'' semimetallic state separated by a layer of free-like (unbound) molecules.

We have conducted several experiments at room and low temperatures on H_2 (and D_2) with the highest pressures reached 315 (275) GPa (see Ref. [17] for the details). With increasing pressure, the low energy (< 1000 cm^{-1}) bands of H_2 (D_2) broaden and decrease in intensity [Figs. 2(a) and 2(b)]. However, when pressures above ~190 GPa were reached, we observed the appearance of a new, relatively intense broad Raman band at 500 cm^{-1} (Fig. 2). The emergence of this band is accompanied by the drastic change of the slope of the main vibrational mode ν_1 from -5 to -12.7 cm^{-1}/GPa (Fig. 3). The full width at half maximum (FWHM) of the ν_1 mode also reflects changes at the transition; from the solidification point at 5.5 GPa, the FWHM increases linearly, reaching 100 cm^{-1} by 210 GPa. At this point, the broadening abruptly changes rate, and within an interval of 50–60 GPa (at 260–270 GPa) the FWHM reaches ~460 cm^{-1} (Fig. 3). Our observations of the low energy broad band are similar to a band at 450 cm^{-1} observed in H_2-III at 178 GPa and 18 K [6]). The change in slope of the ν_1 and the increase of FWHM are in good agreement with similar observations made in phase III at low temperatures (18 K for librons and 250 K for vibrons) [6,9]. The 190 GPa–300 K P-T point, where we observe an apparent phase transition, could fit on the phase I-III boundary of existing low temperature data if extrapolated to 300 K and above 190 GPa (Fig. 1).

As pressure is increased above 220 GPa and the ν_1 mode reaches a frequency of ~3800 cm^{-1}, the transition to a new phase (referred here as IV) starts. The transformation is evidenced by the profound changes in vibrational and low (< 1200 cm^{-1}) energy spectra. At above 220 GPa, the low-frequency broad band is superseded by three new sharp Raman modes. A new vibrational mode ($\nu_2 \sim 4150$ cm^{-1}) appears at 235 GPa (Fig. 2). At the same pressure, the ν_1 frequency reduces below the values expected for the vibron of phase III at 77 K (Fig. 3). This observation suggests that phase IV has a modified bonding character compared to phase III (see below). The ν_1 mode frequency softens very rapidly with pressure at a much higher rate than the vibron of phase III. At 315 GPa, the frequency of the ν_1 mode is 2750 cm^{-1} (35% reduction of frequency compared to ~4260 cm^{-1} at 40 GPa where the

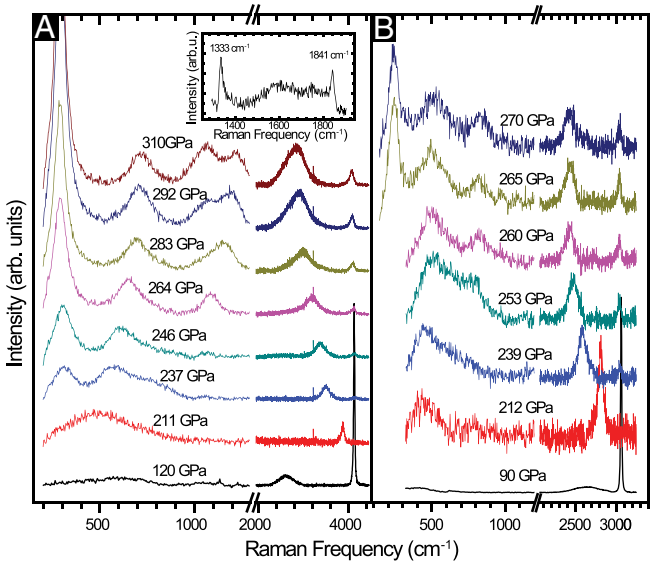


FIG. 2 (color online). Representative Raman spectra of H_2 (a) and D_2 (b) at different pressures (shifted vertically for clarity). The weak broad peaks at ~2400 cm^{-1} on spectra at 120 GPa for H_2 and 90 GPa for D_2 are due to the 2nd-order Raman from diamond. The inset in (a) shows the stressed diamond peak at 315 GPa.

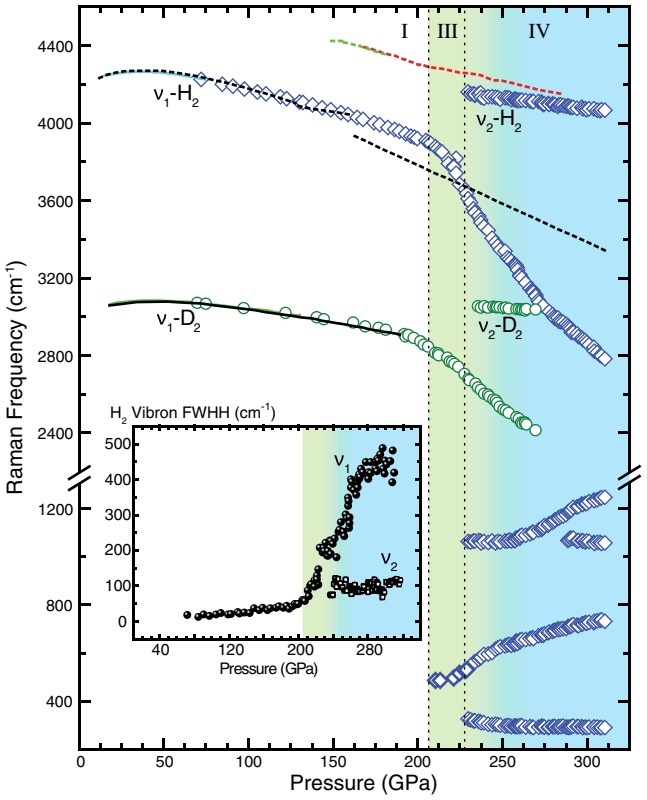


FIG. 3 (color online). H_2 and D_2 phonons frequency shifts as a function of pressure. Open squares are the ν_1, ν_2, and low energy modes of hydrogen; open circles are ν_1 and ν_2 modes of deuterium. The dashed lines are infrared and Raman measurements at low temperatures from Refs. [6,8,20]. The solid line is the ν_1 mode of deuterium at 300 K from Ref. [11]. Inset: Hydrogen ν_1 (solid circles) and ν_2 (open squares) modes FWHM as a function of pressure.

ν_1 mode goes through the maximum of its frequency), which is much lower than that in phase III at 77 K and 320 GPa ($\nu_1 \sim 3400$ cm^{-1} [8]). The FWHM of the ν_2 mode lies on the linear extrapolation of the vibron mode of phase I (Fig. 3) and is clearly driven by the normal pressure-induced broadening unlike the ν_1 mode, indicating two very different local atomic environments involved in these modes (see below). In the high-pressure regime, the frequency of the ν_1 versus pressure shows a slope change (slope changes from -12.7 to -7 cm^{-1}/GPa), and a 1050 cm^{-1} band branches off to give rise to another weakly softening band above 280 GPa (Figs. 2 and 3), which rapidly increases in intensity. The relative intensity of the lowest-frequency band at 295 cm^{-1} significantly increases, while the mode shows small softening with pressure (Fig. 2). This complex behavior suggests that the ν_1 mode couples to other modes of the same symmetry (e.g., Ref. [18]) with the gain of intensity for the 295 and 1050 cm^{-1} modes. The strong coupling between the modes also forces a small upturn of the ν_1 vibron frequency with pressure above 275 GPa (Fig. 3).

The structures of high-pressure phases of hydrogen are unknown, which makes the definitive interpretation of the observed phenomena difficult. We use the structure(s) recently proposed by the *ab initio* theoretical calculations for phase III of hydrogen [19] to analyze our findings. With the inclusion of the zero-point energy, the calculations suggest 3 structures ($C2/c$, $Cmca$-12, and $Pbcn$) as the most plausible candidates for phase III. In $C2/c$ and $Cmca$-12 structures, all H_2 molecules have approximately the same bond length (within 1%) but would have the second Raman vibrational mode due to the Brillouin zone *doubling* with respect to phase I. This is in some agreement with the experimentally observed infrared [10,20] and ν_2 Raman [6] modes. The extremely weak Raman ν_2 vibron was observed in phase III and was assigned to a folded mode from the Brillouin zone boundary; the frequency of this mode is quite close to that of the strong IR mode (Fig. 3), as they both correspond to the vibrational states near the top of the vibrational band [21]. Both IR and Raman (at $\sim$175 GPa) are relatively close in frequency (~ 4400 cm^{-1}) to the unbound state [21]. On the other hand, the proposed for H_2-III $Pbcn$ structure could explain all features of the Raman spectra of phase IV reported here. This structure is highly unusual; it consists of unbound molecules sandwiched between the honeycomb graphenelike layers made of 6-atom rings, which have different size lengths (from 0.85 to 1.04 Å; see Fig. S2 in [17] and Ref. [19]), yielding both molecular and atomic hydrogen at the same time. The density-functional theory calculations give the positions of Raman active modes [19] for the $Pbcn$ structure; we observe 6 out of 16 predicted fully symmetric modes (A_g) which are expected to be the most intense. The spectral positions of all observed modes agree well with the theoretical calculations (see Fig. S3 in [17]). Using empirical formula relating the frequencies (ν) and the bond lengths (r), $\nu r^3 = \text{const}$ [22], we *qualitatively* assign the observed vibron frequencies in the $Pbcn$ structure. The 0.72 Å length, which is very close to the bond length of an unbound molecule, could be easily assigned to the ν_2 mode ($\nu_2 \sim 4150$ cm^{-1}), and the ν_1 2800 cm^{-1} mode could be assigned to the 0.82 Å bond length. At this point we note that 1.04 and 1.03 Å bond lengths *could* correspond to a calculated (see Fig. S3) and observed doublet at 1050 and 1200 cm^{-1}. We have not observed the band at $\sim$1800 cm^{-1}, corresponding to the 0.95 Å length, but this band most probably is hidden behind the stressed diamond signal, covering the area from 1333 to 1850 cm^{-1} at 315 GPa (inset in Fig. 2). Two other modes observed here below 700 cm^{-1} (Fig. 3) correspond to the out-of-plane translational and librational modes.

The increased vibron mode softening, its broadening, and the presence of the intense ν_2 mode in phase IV can be understood by the difference in local molecular association. Phase IV provides a unique continuous route for molecular dissociation (retaining unbound molecules), similar to that which has been previously observed in ice VII through the hydrogen bond symmetrization [18]. In the vicinity of the symmetrization transition, the lattice becomes highly anharmonic, causing a pronounced softening and broadening of the O-H stretch mode [18] very similar to the observations in this study. We speculate that the pressure-dependent changes of the soft mode, mode coupling, and optical absorption are related to the predicted continuous structural transformation of the $Pbcn$ structure into the higher symmetry $Ibam$ [19] configuration with formation of the perfect graphenelike hydrogen layers with *equal* distances between atoms in a 6-member ring. Because of the larger zero-point energy, the higher mobility of the proton compared to the deuteron is expected, leading to the enhanced proton tunneling in the regime approaching symmetrization as was observed in water [23]. In this case, the hydrogen vibron would show larger softening of the ν_1 mode relative to deuterium as demonstrated in the divergence from the $\sqrt{2}$ ratio between H_2 and D_2 ν_1 modes (see Fig. S2 in Ref. [17]) as the lighter hydrogen tunnels more easily. This also could explain the presence of the regime of an increased optical absorption above $\sim$280 GPa (see Fig. 4). Above 268 GPa, a strong band-gap feature appears in the spectra and shifts in red with pressure. The overall absorption increases with pressure in this regime; the sample becomes dark in appearance (Fig. 1 and Ref. [17]). Although the band-gap shift with pressure is comparable to that for phase III (Fig. 4), the overall significant increase in absorption suggests that above 278 GPa hydrogen may become semimetallic. This is in excellent agreement with the theoretical prediction that $Pbcn$ structure will metallize at above 300 GPa [19].

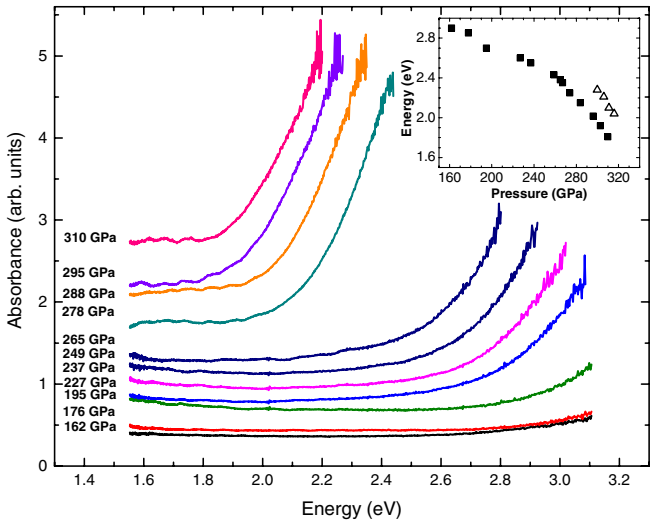


FIG. 4 (color online). Optical absorption spectra of H_2 in a visible spectral range at 300 K and different pressures. The reference transmission spectrum was measured at 75 GPa. Inset: Estimated band gap as a function of pressure at 300 K (solid squares) and at 77 K from Ref. [8] (open triangles).

We have observed reversible phase IV to III transformations between 230 and 285 GPa upon cooling or warming (see Fig. S5 in [17]). These results allow us to constrain the phase diagram of hydrogen at very high pressures. Our observations suggest that phase IV supersedes phase III at high temperatures and will most likely become metallic. The transition line between phases III and IV has a negative slope, and it is relatively shallow in P-T coordinates. This substantiates that the transition is entropy driven, which is supported by the described above difference in structure and related to it proton tunneling in phase IV. Theory [19], together with this experimental study, confirms that a unique mixed molecular and atomic state provides a route to solid metallic hydrogen at high temperatures. In order to better understand the connection between the described here phase IV, the melting curve, and predicted atomic liquid states [24,25], further investigations are clearly needed. We tentatively place the second triple point at 210 GPa and 320 K, but the slope of the I–IV boundary needs to be established. This boundary is of particular interest, because it has important consequences for the behavior of the melting curve. Independently of the I–IV slope boundary, it is very likely that the melting curve will change its slope at some P-T condition, because the phases I and IV are very dissimilar. Depending on the sign of this slope, one could expect that the predicted ground liquid state [15] could be realized at higher pressures or may be not realized at all as in case with Li [26]. Since phase IV could have strong quantum tunneling of protons within two-dimensional layers, it could possess some features of quantum proton fluid. It is interesting to note that the intersection of the molecular to atomic liquid states boundary predicted theoretically [24,25] and the extrapolation of the melting curve is in close proximity to the stability field of phase IV discovered in this work (Fig. 1). This is a clear indication of the connection between changes in both liquid and solid states in this interesting and unusual material.

The authors are grateful to Chris Pickard for providing unpublished data, very useful discussions, and remarks. This work is supported by research grants from the U.K. Engineering and Physical Sciences Research Council and Institute of the Shock Physics, Imperial College. T. S. acknowledges financial support by the EPSRC CM-DTC. A. F. G. acknowledges support from the NSF, Army Research Office, NAI, and EFRee.

*Corresponding author.
e.gregoryanz@ed.ac.uk

[1] H. Mao and R. Hemley, Rev. Mod. Phys. **66**, 671 (1994).
[2] N. Ashcroft, in *Proceedings of the International School of Physics "Enrico Fermi,"* edited by R. Hemley *et al.* (IOS, Amsterdam, 2002), Vol. CXLVII, pp. 151–194, and references therein.
[3] H. Lorenzana, I. Silvera, and K. Goettel, Phys. Rev. Lett. **64**, 1939 (1990).
[4] I. Goncharenko and P. Loubeyre, Nature (London) **435**, 1206 (2005).
[5] R. J. Hemley and H. Mao, Phys. Rev. Lett. **61**, 857 (1988).
[6] A. F. Goncharov, R. J. Hemley, H. K. Mao, and J. Shu, Phys. Rev. Lett. **80**, 101 (1998).
[7] A. Goncharov, I. Mazin, J. Eggert, R. J. Hemley, and H. K. Mao, Phys. Rev. Lett. **75**, 2514 (1995).
[8] P. Loubeyre, F. Occelli, and R. LeToullec, Nature (London) **416**, 613 (2002).
[9] Y. Akahama, H. Kawamura, N. Hirao, Y. Ohishi, and K. Takemura, J. Phys. Conf. Ser. **215**, 012056 (2010).
[10] A. Goncharov, E. Gregoryanz, R. Hemley, and H. Mao, Proc. Natl. Acad. Sci. U.S.A. **98**, 14 234 (2001).
[11] B. Baer, W. Evans, and C. Yoo, Phys. Rev. Lett. **98**, 235503 (2007).
[12] E. Gregoryanz, A. F. Goncharov, K. Matsuishi, H. K. Mao, and R. J. Hemley, Phys. Rev. Lett. **90**, 175701 (2003).
[13] S. Bonev, E. Schwegler, T. Ogitsu, and G. Galli, Nature (London) **431**, 669 (2004).
[14] N. Subramanian, A. F. Goncharov, V. V. Struzhkin, M. Somayazulu, and R. J. Hemley, Proc. Natl. Acad. Sci. U.S.A. **108**, 6014 (2011).
[15] E. Babaev, A. Sudbo, and N. Ashcroft, Nature (London) **431**, 666 (2004).
[16] W. Nellis, S. Weir, and A. Mitchell, Phys. Rev. Lett. **76**, 1860 (1996).
[17] See Supplemental Material at http://link.aps.org/supplemental/10.1103/PhysRevLett.108.125501 for the additional details.
[18] A. Goncharov, V. V. Struzhkin, H. K. Mao, and R. J. Hemley, Phys. Rev. Lett. **83**, 1998 (1999).
[19] C. J. Pickard and R. J. Needs, Nature Phys. 3, 473 (2007); C. Pickard (private communications).

[20] M. Hanfland, R. Hemley, and H. Mao, Phys. Rev. Lett. **70**, 3760 (1993).
[21] J. van Kranendonk and G. Karl, Rev. Mod. Phys. **40**, 531 (1968).
[22] G. Herzberg, in *Molecular Spectra and Molecular Structure I: Diatomic Molecules* (Krieger, Malabar, FL, 1989), p. 457; see also W. Sherman, J. Phys. C **13**, 4601 (1980).
[23] J. Pruzan, E. Wolanin, M. Gauthier, J. C. Chervin, B. Canny, D. Hausermann, and M. Hanfland, J. Phys. Chem. B **101**, 6230 (1997).
[24] I. Tamblyn and S. Bonev, Phys. Rev. Lett. **104**, 065702 (2010).
[25] M. Morales, C. Pierleonib, E. Schweglerd, and D. M. Ceperley, Proc. Natl. Acad. Sci. U.S.A. **107**, 12 799 (2010).
[26] C. L. Guillaume, E. Gregoryanz, O. Degtyareva, M. I. McMahon, M. Hanfland, S. Evans, M. Guthrie, S. V. Sinogeikin, and H-K. Mao, Nature Phys. **7**, 211 (2011).
[27] F. Datchi, P. Loubeyre, and R. LeToullec, Phys. Rev. B **61**, 6535 (2000).
[28] A. F. Goncharov, R. J. Hemley, and H. Mao, J. Chem. Phys. **134**, 174501 (2011).

Auxiliary information for "Mixed Molecular and Atomic Phase of Dense Hydrogen"

Ross T. Howie, Christophe L. Guillaume, Thomas Scheler, Alexander F. Goncharov and E. Gregoryanz

Experimental Details

We have generated high pressures in the long piston-cylinder diamond anvil cells of our own design with diamonds having culet sizes from 50 to 20 microns. We have used rhenium foils of 200-250 microns thick as gasket material. The hydrogen (deuterium) gas was clamped at ∼1750-2000 bar and pressurised to 1 GPa while in the gas loader. The primary experimental concern is the containment of such a light, reactive element as hydrogen at temperatures above 250 K (Refs. [12] and [14] in the main text of the paper). H_2 can diffuse into diamond, causing anvil embrittlement and contributing to anvil failure. In addition, the large stress-induced increase of fluorescence and optical absorption in diamond anvils are amongst the many complications associated with high pressure optical studies. In this study, we prevented the premature diamond failure by several improvements to previous experimental techniques. We have used a focussed ion beam to drill a sample chamber in the rhenium gasket which avoided infra-red damage caused by laser drilling (Fig. S1A, 1B). As in our recent study on Li (Ref. [26] of the main text of the paper), where the identical problem of the diamond failure at room temperature also exists, we drilled the smallest possible sample chamber therefore minimising the area of contact between the sample and diamond. The recent improvements of the throughput and spatial resolution to our Raman set-up [S1] allowed us to collect signal from samples of 2 to 5 microns in diameter (Fig. 1 in the main text of the paper and Fig. S1 below), while reducing the collection time to 2 s. We have used 514 and 647 nm laser excitation wavelengths to measure the Raman spectra. We find that minimising the time of diamond exposure to the laser light significantly decreases diamond failure. Nevertheless, in all our experiments the front diamond through which the laser light was introduced to the sample chamber failed first. The increased spatial resolution also allowed us to reduce the amount of pressure induced luminescence, resulting in high quality spectra (see Fig. 2 in the main text of the paper). Below 150-160 GPa, pressure was measured using ruby chips and correlated to the frequency of the stressed diamond edge. Above 170-180 GPa the stressed diamond edge was used to estimate the pressure (see inset to Fig. 2 in the main part of the paper) using the Akahama *et al.* scale [S2].

[S1] M. Marques *et al.*, Phys. Rev. B, **83**, 184106 (2011).
[S2] Y. Akahama, and H. Kawamura, J. Appl. Phys. **96**, 3748 (2004).

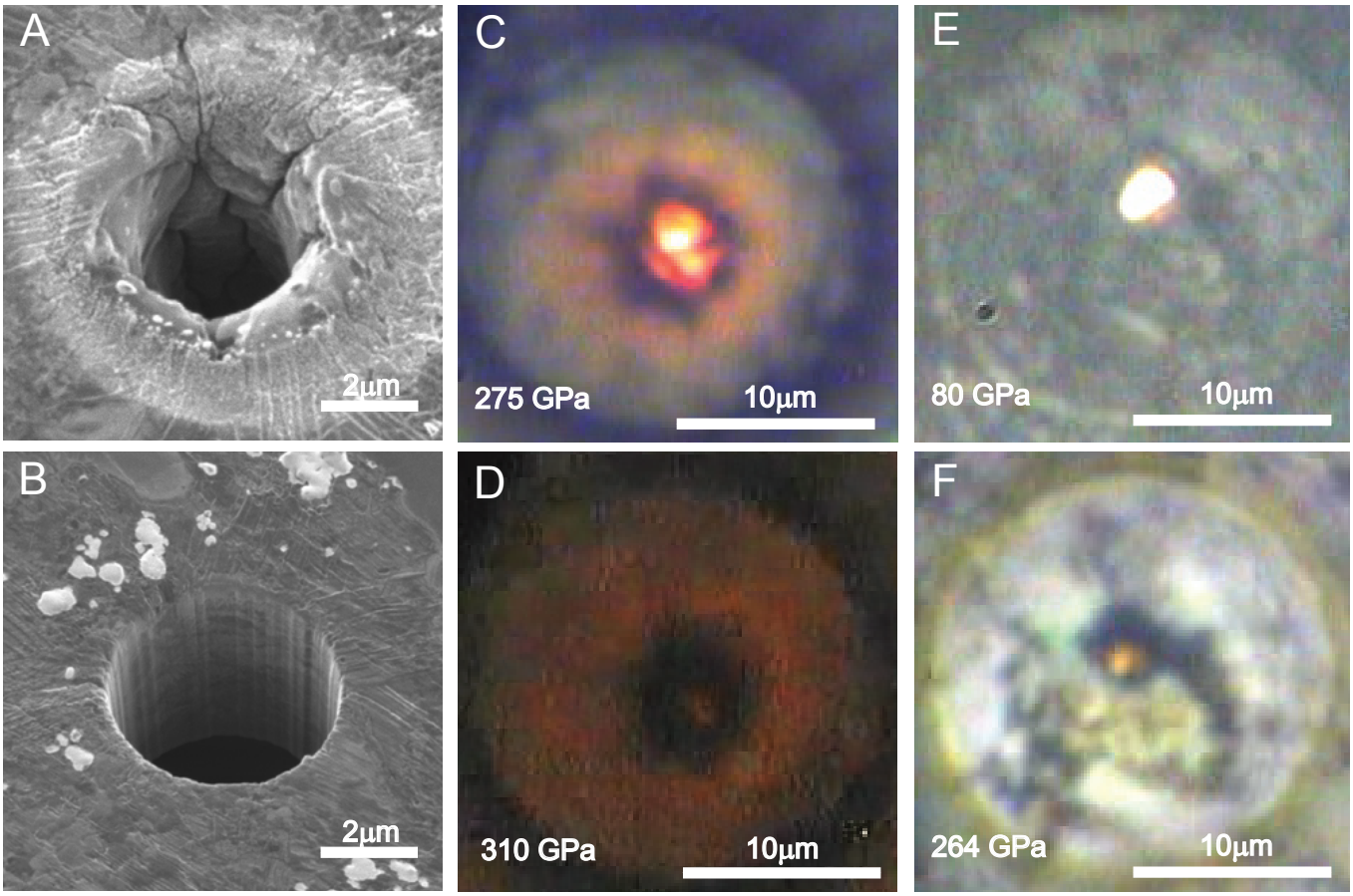


FIG. S1: Scanning ion micrograph of a laser-drilled (A) and ion-milled (B) gasket hole. Optical microscopy images of hydrogen sample in transmitted and reflected white light at 275 GPa (C) and 310 GPa (D). Optical microscopy images of deuterium sample in transmitted and reflected white light at 80 GPa (E) and 264 GPa (F)

Bonds lengths in the *Pbcn* structure at 300 GPa

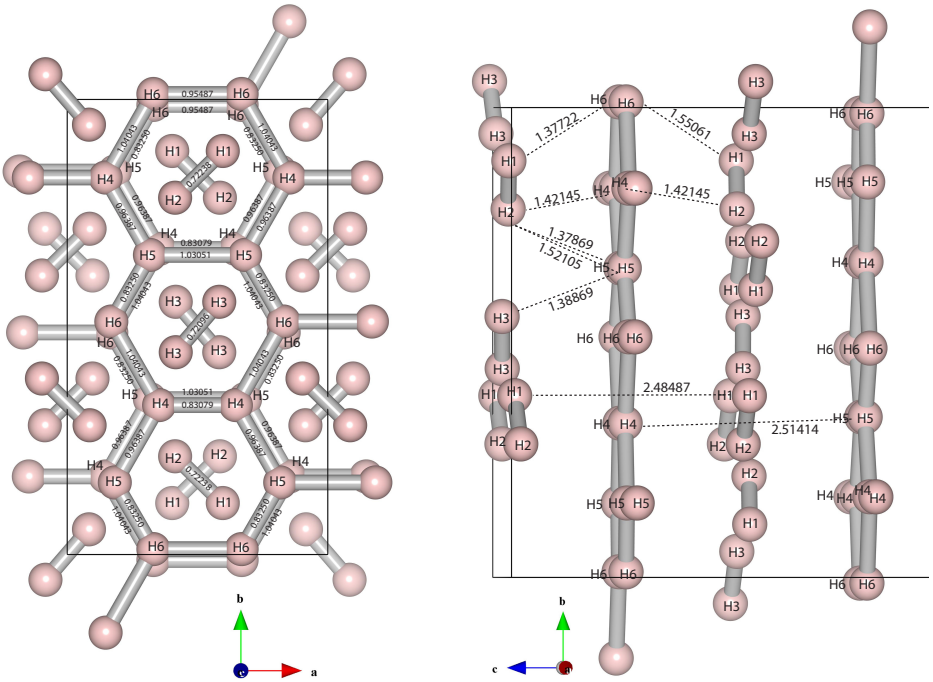


FIG. S2: The structure and the bonds lengths of the *Pbcn* phase at 300 GPa with the atomic positions from Ref. [19] of the main text of the paper.

Calculated and measured frequencies of the *Pbcn* structure.

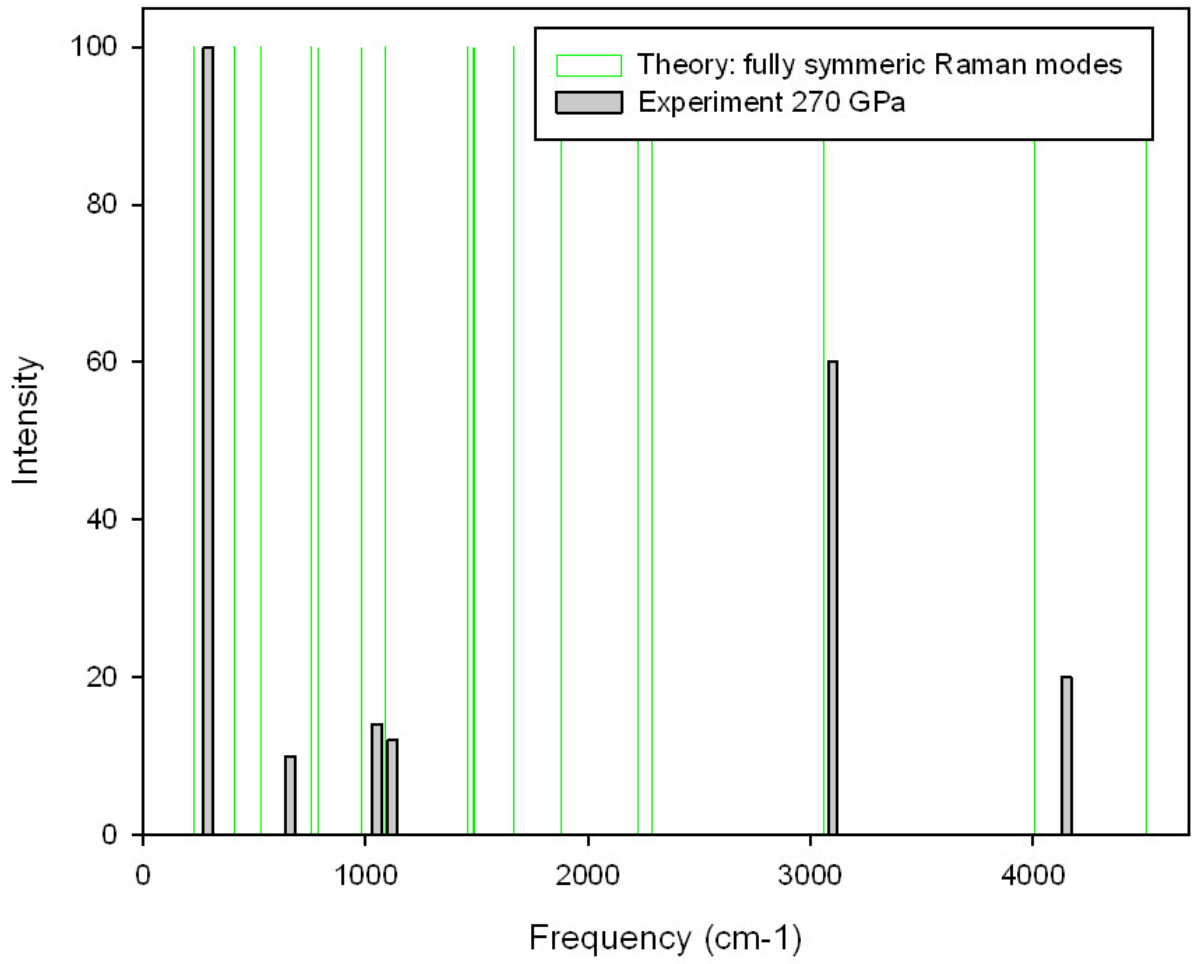


FIG. S3: The calculated (see Ref. [19] in the main text of the paper) fully symmetric (A_g) and measured Raman modes at 270 GPa. The energy range between 1333 and 1850 cm^{-1} is covered by the Raman signal from diamond and no reliable experimental observations could be made. The 3^{rd} high frequency vibron predicted at ∼4500 cm−1 was not observed probably due to the reduced quantum efficiency of the CCD in this energy range.

Raman frequencies of deuterium versus frequencies of hydrogen at different pressures

In order to distinguish between rotational modes and phonons and to see if the hydrogen and deuterium vibrons behave identically under pressure we have plotted the values of the observed frequencies of deuterium versus those of hydrogen (Fig. S4). The frequencies of the phonons scale down as $\sqrt{2}$ while the frequencies of rotons scale down as 2. At higher pressure the measured ν_1 vibrons frequencies ratio deviates from $\sqrt{2}$ due to higher rates of tunneling in hydrogen.

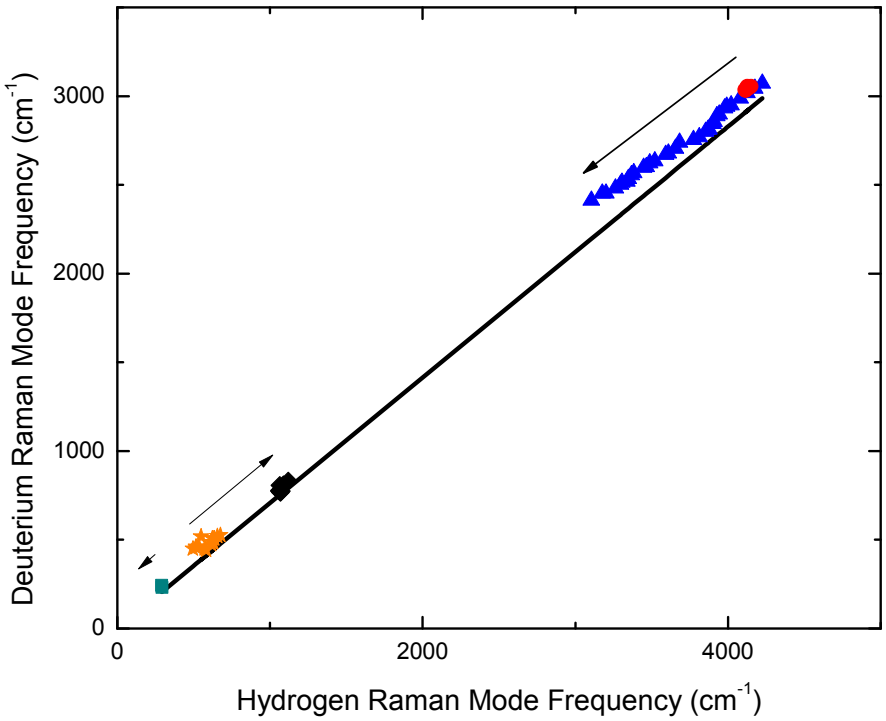


FIG. S4: The values of the observed frequencies in hydrogen and deuterium from 70 to 275 GPa. The blue filled triangles are ν_1 mode, the red filled circles are ν_2 mode. The filled squares and stars are the low energy phonon modes. The arrows indicate the change in frequency of the given excitation when pressure is increased. The straight solid line has slope of $1/\sqrt{2}$.

Phase IV to III transformation as function of temperature at different pressures.

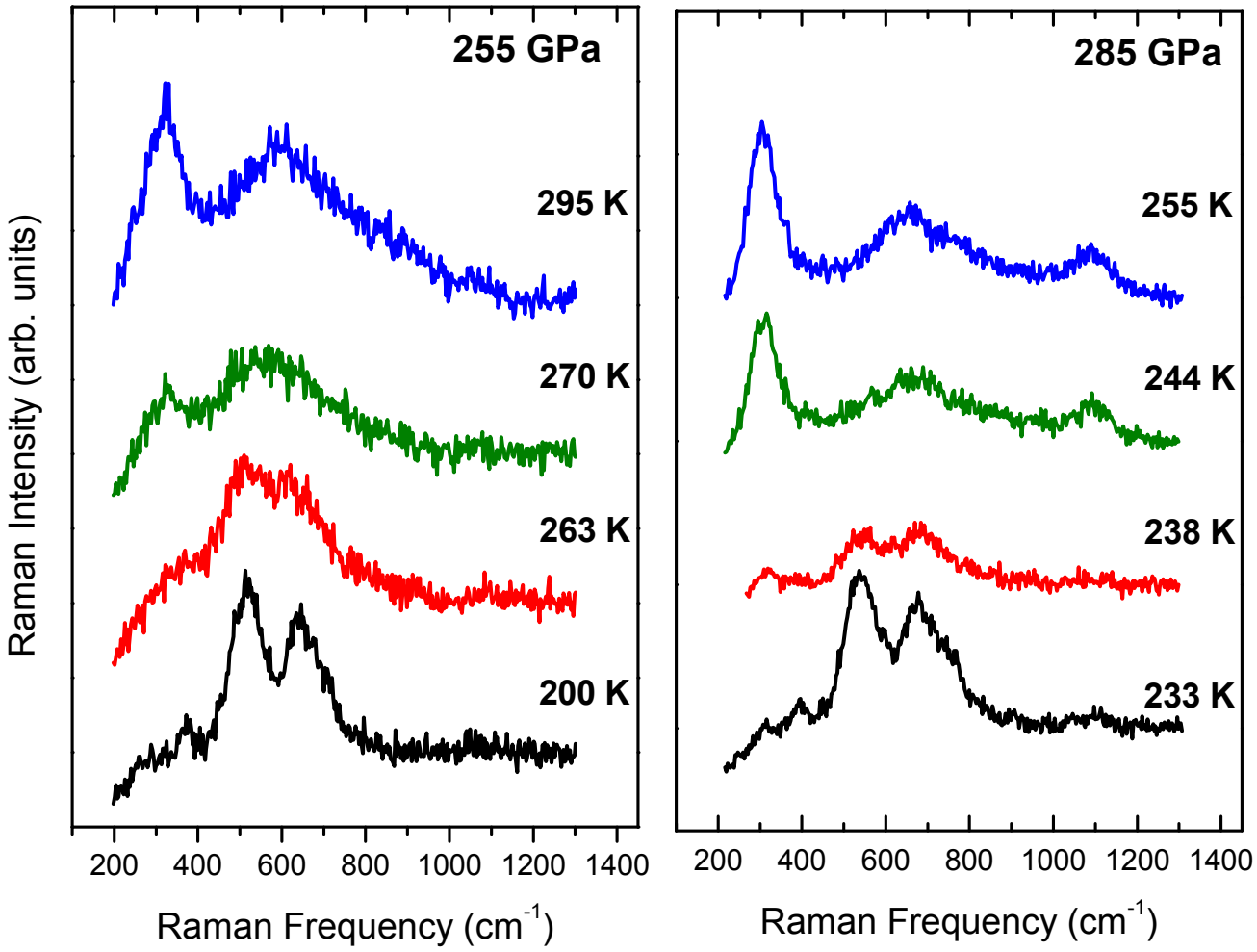


FIG. S5: Representative Raman spectra of hydrogen at 250-285 GPa upon cooling (left panel) and heating (right panel) showing the IV $\Longleftrightarrow$ III phase transformation and its reproducibility. The transformation between the phase is clearly attested by the change of low energy ($<$1000 cm^{-1}) phonons and vibrons (not shown) within narrow temperature range. The low temperature doublet of phase III is identical to the one reported in the Ref. 10 of the main body of the paper.

PHYSICAL REVIEW B **86**, 214104 (2012)

Proton tunneling in phase IV of hydrogen and deuterium

Ross T. Howie, Thomas Scheler, Christophe L. Guillaume, and Eugene Gregoryanz*
Centre for Science at Extreme Conditions and School of Physics and Astronomy, University of Edinburgh, Edinburgh EH9 3JZ, United Kingdom
(Received 6 August 2012; published 10 December 2012)

Using *in situ* optical spectroscopy we have investigated the temperature stability of the mixed atomic and molecular phases IV of dense deuterium and hydrogen. Through a series of low-temperature experiments at high pressures, we observe phase III-to-IV transformation, imposing constraints on the *P-T* phase diagrams. The spectral features of the phase IV-III transition and differences in appearances of the isotopes Raman spectra strongly indicate the presence of proton tunneling in phase IV. No differences between isotopes were observed in absorption spectroscopic studies, resulting in identical values for the band gap. The extrapolation of the combined band gap yields 375 GPa as the minimum transition pressure to the metallic state of hydrogen (deuterium). The minute changes in optical spectra above 275 GPa *might* suggest the presence of a new solid modification of hydrogen (deuterium), closely related structurally to phase IV.

DOI: 10.1103/PhysRevB.86.214104 PACS number(s): 62.50.−p, 61.50.Ks, 78.40.Ri

The recent experimental discovery of phase IV of hydrogen and deuterium is exemplary of how studies of hydrogen at multimegabar pressures is constitutive to the understanding of the pressure-induced complexity in simple systems at extreme compressions.[1] Raman studies have shown that, at 300 K, hydrogen transforms to a new phase (phase IV) at pressures above 220 GPa. Quite unique and unusual features of the Raman spectra, e.g., the appearance of the second fundamental vibrational mode, were interpreted as phase IV, consisting of graphene-like six-member rings made up of elongated H_2 dimers, which experience large pairing fluctuations, and unbound H_2 molecules. This unusual structure, having *Pbcn* symmetry and 48 atoms per unit cell, was earlier proposed by density functional theory (DFT) as a possible candidate for phase III at 0 K.[2] The newly found experimental ability to compress hydrogen at room temperature above 180 GPa in the diamond anvil cell has resulted in major revision of the hydrogen phase diagram.[1] However, the new findings did not answer many questions and both experimental[3] and theoretical[4,5] studies produced somewhat contradictory results, posing many more uncertainties about the possible states of dense hydrogen. For example, in one experimental study at 300 K, H_2 phase IV was probably observed (which is not supported by the data presented on deuterium) however the authors did not suggest a mixed atomic-molecular state, instead claiming pressure-induced molecular dissociation and metallization above 260 GPa.[3] On the other hand, theoretical studies[4,5] predict the transformation of phases III and IV into molecular phase V at pressures above 250 GPa, which is at variance with many experimental observations.[1,6–8]

Our previous study focused on the behavior of hydrogen and deuterium at 300 K and[1] reported some preliminary results on H_2 phase IV at low temperatures. Compared to the three other molecular phases (I, II and III),[9] little is known about the low-temperature stability field of H_2 phase IV[1] and nothing is known about the stability field of deuterium phase IV. As hydrogen and deuterium have the highest relative isotopic mass difference among elements, the effects of zero point energy (ZPE) might play an important role. Based on the fact that phase IV exists at relatively "high" temperatures and the transition line separating it from phase III has a negative slope with respect to the pressure axis, we surmised[1] that the transition to the mixed state (phase IV) is entropy driven. This suggestion is supported by the significant differences in the Raman spectra of phase III vs phase IV, which is indicative of very dissimilar structures of these phases. Since the structure of phase III is not known and the proposed structural model for phase IV needs confirmation, it is impossible to make a quantitative comparison of entropies and ZPEs of both phases. Therefore, experiments aimed at determining the stability fields of hydrogen (deuterium) are highly desirable and of fundamental interest, because they are expected to provide a clear picture of the hydrogen (deuterium) phase diagram and therefore reveal new aspects relevant to the theoretical modeling and interpretation.

In this study, we mapped out phases III and IV of deuterium (hydrogen) up to 300 GPa and between 200 and 300 K. We investigate the low-temperature stability of deuterium (hydrogen) phase IV, revealing the differences in the stability fields of the isotopes and similarities in the electronic structures. We show that the phase III-to-IV transformation is accompanied by a large discontinuity of the fundamental vibrational mode frequency, the largest discontinuity observed between different phases of hydrogen (deuterium). We also demonstrate that the full width at half-maximum (FWHM) of the vibrational fundamental reaches ∼450 cm^{-1} for H_2 and ∼250 cm^{-1} for D_2 in phase IV while staying below ∼150 cm^{-1} for both isotopes at pressures above 250 GPa in phase III. The large difference between the peak widths of the main vibrational modes of the two isotopes in phase IV indicates substantial proton tunneling in hydrogen, probably due to the higher ZPE of the lighter species.

High-purity normal D_2 (H_2) was loaded at 0.2 GPa into a long piston-cylinder diamond anvil cell and compressed at room temperature. At the desired pressure, the cell was mounted in a custom-built continuous-flow cryostat and Raman measurements were performed on cooling/warming scans between 200 and 300 K. We have used both 514-nm Ar^+ ion and 647-nm Kr^+ ion laser excitation wavelengths for optical measurements. Pressure was determined from the shift of the T_2g Raman band of the stressed diamond using

 ©2012 American Physical Society

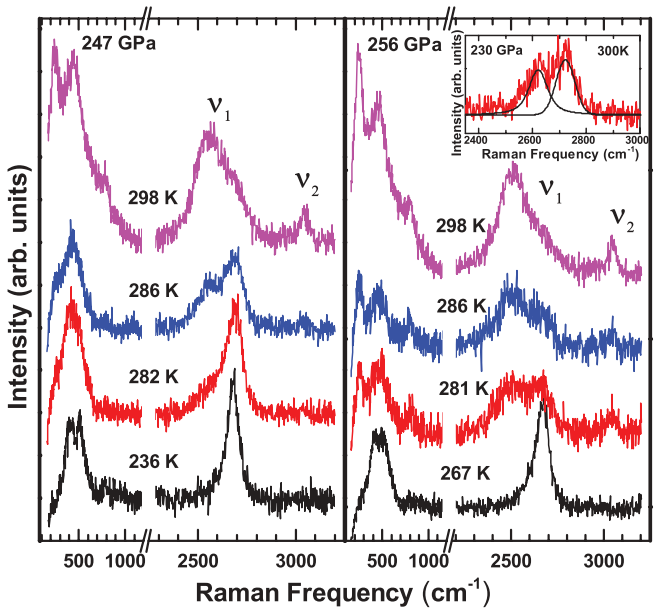


FIG. 1. (Color online) Representative Raman spectra of deuterium upon cooling (left) and warming (right) showing phase IV-III transformations at 247 and 256 GPa. Inset: Coexistence of the ν_1 modes at 300 K and 230 GPa in phases III (higher frequency mode) and IV (lower frequency mode)

the relation proposed in Ref. 10. For a full description of the experimental procedures see Refs. 1 and 11–14.

Selected Raman spectra of deuterium at 247 and 256 GPa and at various temperatures are shown in Fig. 1. At room temperature (phase IV) both ν_1 and ν_2 vibrational modes are clearly visible, having very different widths. Upon cooling at 247 GPa the ν_1 mode of D_2 shows splitting, with a higher frequency band emerging from phase III and the lower band from the remaining phase IV (Fig. 1). Upon cooling the intensities of all Raman modes associated with phase IV decrease, while new peaks appear and grow (Fig. 1). By 285 K, the transition to phase III is complete, the ν_2 mode disappears, and the ν_1 hardens significantly. To our knowledge, there are no published Raman spectra of low-frequency modes in phase III of deuterium to compare our data with. However, the overall spectrum appearances[1,15] and $\sqrt{2}$ scaling of the corresponding modes frequencies between hydrogen and deuterium[1,16] unequivocally demonstrate that the phase at low temperatures is phase III. The temperature scans at higher pressures (e.g., the 256 GPa run in Fig. 1) show identical changes in the Raman spectra, although at different transition temperatures. We find that the III ↔ IV transformation in both isotopes is very well defined, happens within a 10 K range, and is reversible without any hysteresis in either pressure or temperature, which is expected from light materials with high ZPEs. The spectral positions of the fundamental vibrational modes of both isotopes shift considerably during the phase transition and the value of the shift increases with increasing pressure and decreasing temperature [Fig. 2(a)]. For example, when phase IV is reached for deuterium at 300 K and 230 GPa the discontinuity between the vibron modes in two phases is around 60 cm^{-1} (see inset in Fig. 1) but as the pressure is increased above 230 GPa and the temperature lowered, the vibron mode frequencies undergo more pronounced hardening upon entering phase III from phase IV, reaching discontinuity values of above 200 cm^{-1} [Fig. 2(a); see also below and Fig. 3].

The most interesting observation is the discontinuity of the FWHM of the ν_1 mode at the III ↔ IV transition, which reflects fundamental changes during the phase transformation

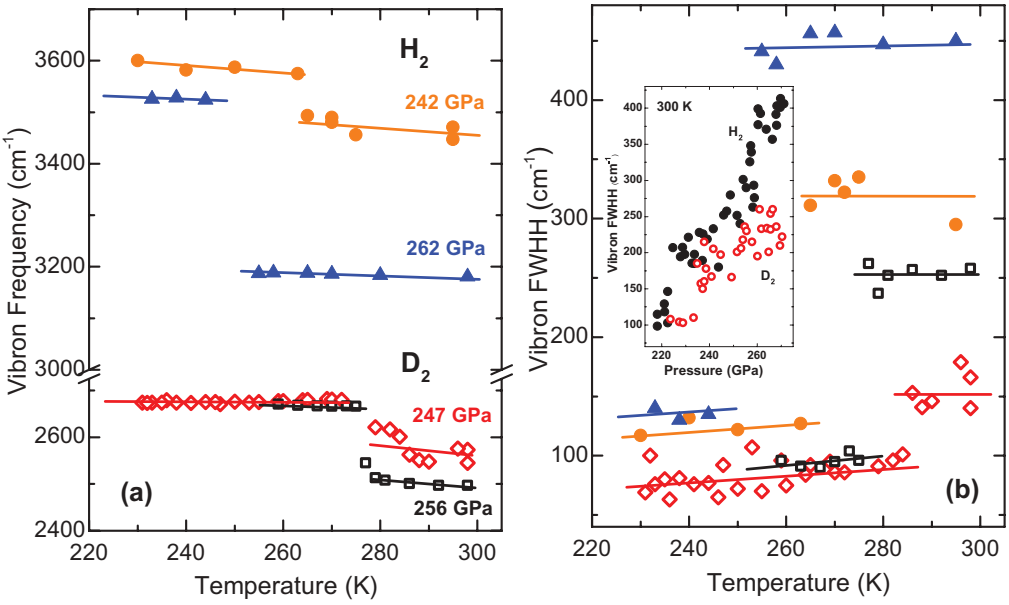


FIG. 2. (Color online) (a) Frequency discontinuities of the ν_1 modes of H_2 (filled triangles, 262 GPa; filled circles, 242 GPa) and D_2 (open squares, 256 GPa; open diamonds, 247 GPa) across the III-to-IV transformations. (b) FWHM of the ν_1 vibrons of H_2 (filled triangles, 262 GPa; filled circles, 242 GPa) and D_2 (open squares, 256 GPa; open diamonds, 247 GPa) plotted versus temperature. Note the quite similar values of FWHM for both isotopes in phase III. Lines in (a) and (b) are guides for the eye only. Inset: FWHM of the H_2 (filled circles) and D_2 (open circles) ν_1 vibron versus pressure at 300 K.

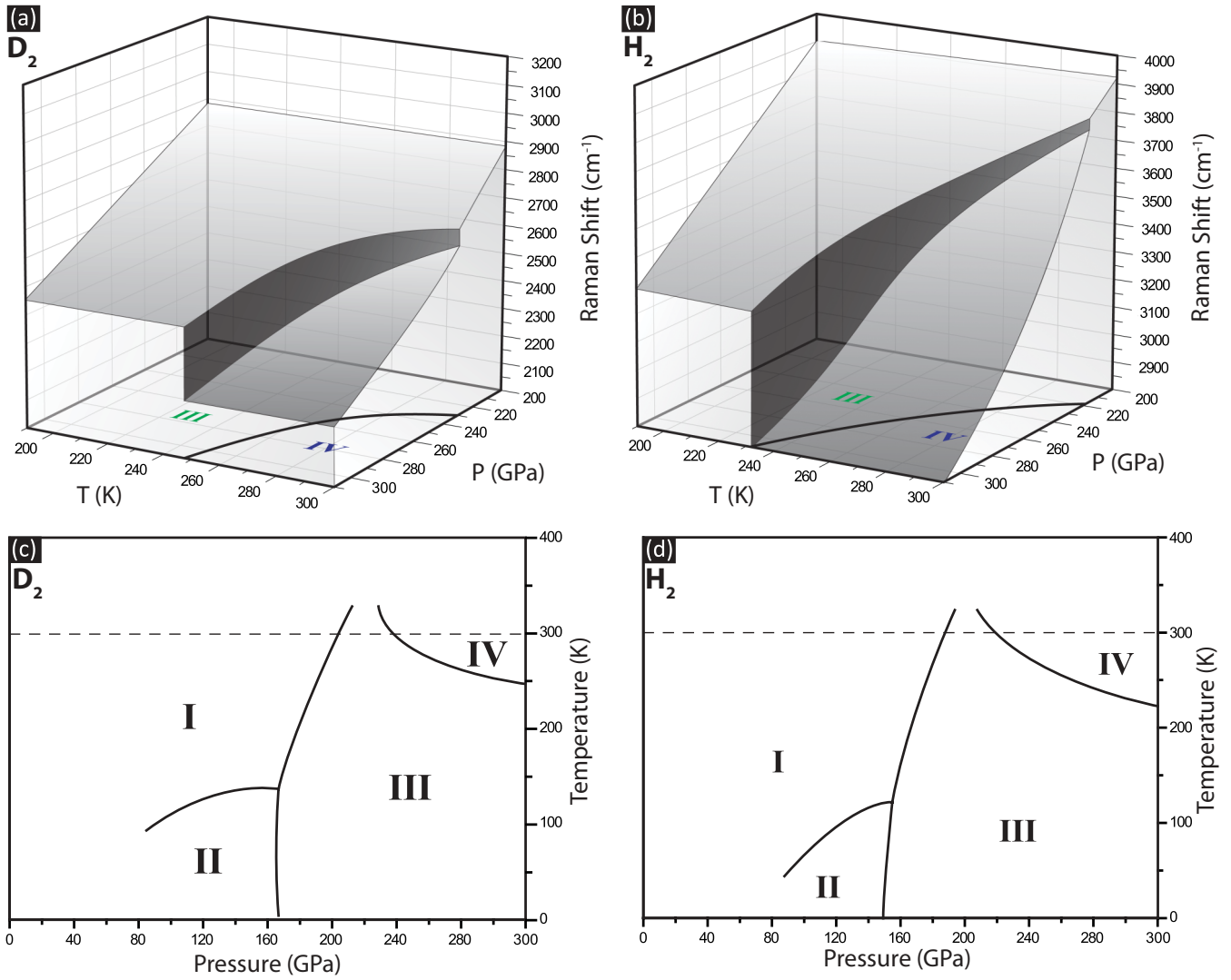


FIG. 3. (Color online) Generalized *P-T*- ν_1 diagrams for (a) D_2 and (b) H_2 showing the difference in the vibron frequency landscapes. *P-T* phase diagrams for (c) D_2 and (d) H_2. The lines separating the phases I, II and III at temperatures below 200 K are from Ref. 9.

and demonstrates the quite unusual character of phase IV. Figure 2(b) shows the FWHM of the ν_1 vibron of D_2 (H_2) versus temperature at different pressures. In phase III, the FWHM of ν_1 is marginally larger for hydrogen—between 290 and 250 GPa the width of ν_1 varies from 150 to 100 cm^{-1}—while for D_2 it is from 100 to 75 cm^{-1} [Fig. 2(b)]. However, in the same pressure range (290 to 250 GPa), the picture changes quite drastically upon warming by 10 K and entrance into phase IV: at 290 GPa ν_1 for H_2 broadens to ~450 cm^{-1} (350 cm^{-1} at 250 GPa), while ν_1 for D_2 reaches ~250 cm^{-1} at 290 GPa (150 cm^{-1} at 250 GPa). The most plausible explanation for the increased FWHM of ν_1 in phase IV is the intermolecular proton exchange and reduced lifetime of molecules. The expanded intramolecular bond length and association of these elongated molecules in six-member rings[1,2] would facilitate such intermolecular proton tunneling in one phase (IV) compared to another (III) under nearly identical *P-T* conditions; particularly, this effect will be enhanced in lighter hydrogen as reflected by its much larger FWHM. It is important to note that some other factors such as larger anharmonicity or enhanced electron-photon coupling could also be responsible for the observed mode broadening. The ultimate explanation of the described effects should come from theoretical studies. In fact, a very recent *ab initio* variable-cell molecular dynamics simulations[17] study observed "intralayer proton transfer" increasing with pressure and temperature in phase IV, in broad agreement with the present work.

The effect of the increased FWHM of the vibrational mode is already present in phase III,[1,7,18] but phase III has only one type of molecule with characteristic lifetime and bond length, with the FWHM being from 75 to 150 cm^{-1} for both isotopes in a wide *P-T* range [Fig. 2(b)]. In phase IV, the *Pbcn* structure was shown to be dynamically unstable,[4] but several *Pbcn*-like structural models with P_c-48 (which still has imaginary phonons),[4] P_c-96,[4] and C_c[5] (both dynamically stable) symmetries having six-member rings were proposed. X-ray diffraction studies are needed to unambiguously determine the structure of phase IV but such experiments are exceedingly difficult at the moment. Our observations of the

FWHM behavior across the III-IV transformation illustrate the importance of temperature effects and that phase IV is a thermally driven partially disordered phase, thus adding additional weight to the proposed mixed atomic and molecular state of dense hydrogen (deuterium).[1,2]

By combining the P-T scans of the ν_1 mode frequencies we constructed three-dimensional P-T-ν diagrams of both species [Figs. 3(a) and 3(b)]. The overall appearance of the phase diagrams is markedly similar but there are several subtle differences. The III-to-IV transition pressures are shifted to slightly higher values for D_2. As a result, the III-IV phase line of D_2 lies above the one for H_2 [Figs. 3(c) and 3(d)]. Our measurements for H_2 yield a III-IV line gradient of -1.6 K/;GPa, while the slope is twice as shallow for D_2 as shown in Fig. 3. Another difference between the isotopes during the III-IV transformation is the very different values of the vibron frequency discontinuities. With increasing pressure the discontinuity upon the III $\leftrightarrow$ IV transition increases (see Figs. 2 and 3), reaching much larger values for hydrogen, e.g., $\sim$500 cm^{-1} for H_2 at 315 GPa and 250 cm^{-1} for D_2 at 300 GPa. These are the largest discontinuities observed between the different phases; for comparison the largest value of the frequency softening of the ν_1 mode upon entering phase III from phase II is only around 100 cm^{-1} for *both* H_2 and D_2.[19,20]

ZPE and thermal effects must play a crucial role in the formation of phase IV under the P-T conditions described here. The competition between ZPE and entropy would shape the appearance of the phase diagrams [Figs. 3(c) and 3(d)] and create differences in the slopes. Recent DFT studies proposed more energetically stable then $Pbcn$ candidate structures for the phase IV with P_c[4] or C_c[5] symmetries. These calculations suggest that hydrogen would transform to phase IV above 220 GPa and $\sim$300 K and that this phase would be separated from the phase III by phase line having negative (with respect to pressure axis) slope, in good agreement with our current and previous results.[1] The calculated Raman spectral positions and intensities of the Pc structure[4] are in much better agreement with our experimental observations than $Pbcn$, although they are still not a perfect fit (Fig. 4). The DFT calculations also proposed a $C2/c$ structure as a possible candidate for phase III

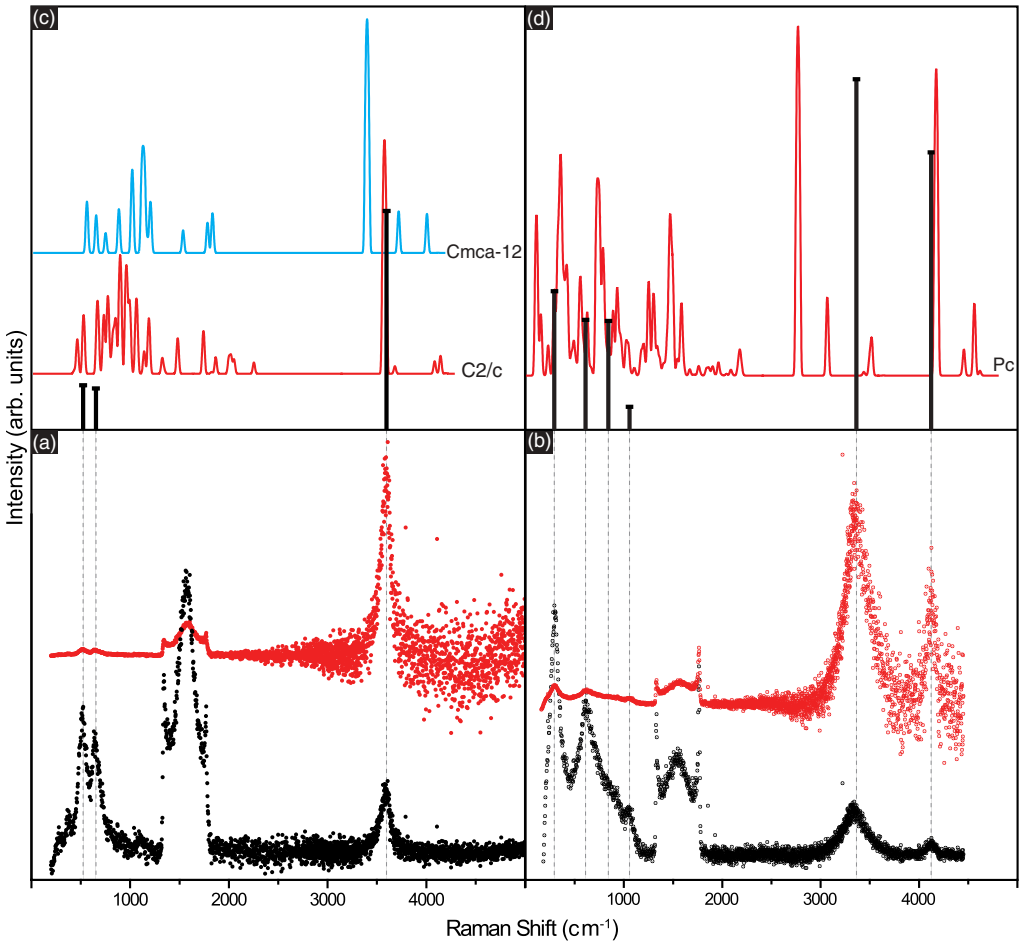


FIG. 4. (Color online) Comparison of experimentally observed and theoretically calculated[2] Raman intensities and spectral positions of the hydrogen bands at 250 GPa. (a, b) Experimental raw spectra observed in phases III (a) and IV (b) are shown below (in black); spectra corrected for decreasing sensitivity of the detector are shown above (in red). The broad peaks between 1333 and $\sim$1800 cm^{-1} are due to the first-order Raman from diamond. (c, d) Experimental renormalized spectra plotted as Gaussian distributions for phases III (c) and IV (d) [vertical (black) lines]; theoretically calculated spectra for (c) $C2/c$ (red) and $Cmca$-12 (blue) and (d) P_c (red). Note that the intensities for renormalized and theoretically calculated spectra are given on a logarithmic scale to show much weaker low-frequency modes and additional vibrational bands besides ν_1 and ν_2.

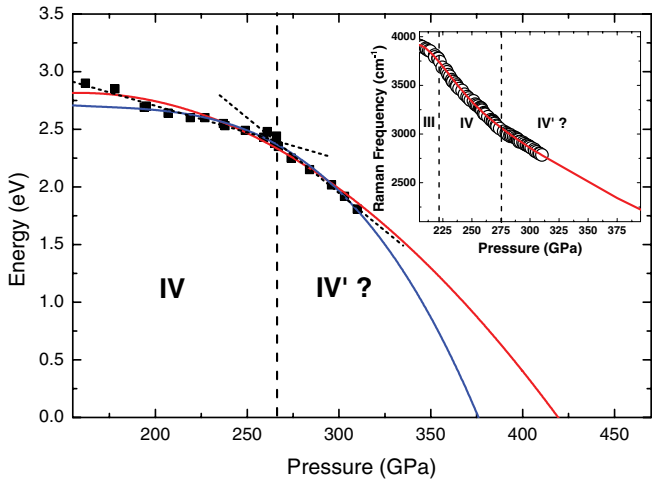


FIG. 5. (Color online) Hydrogen and deuterium combined band-gap points (filled squares) as a function of the pressure at 300 K. Dotted (black) straight lines are linear fits to the measured data points in phases IV and IV′. Quadratic [upper (red) curve] and cubic [lower (blue) curve] polynomial fits extrapolated to higher pressures are shown as solid lines. Inset: Frequency of the ν_1 mode of hydrogen as a function of pressure. Open circles are measured ν_1 vibron frequencies versus pressure. The solid (red) line shows the nearly linear (from 275 to 400 GPa) extrapolation of the ν_1 frequency up to above 375 GPa—the minimal pressure needed to close the optical band gap. Dashed vertical lines indicate the proposed phase transition between phase IV and phase IV′.

(a comparison between observed and calculated Raman spectra in phase III is shown in Fig. 4) and, more importantly, the re-entrance back into a molecular phase V (*Cmca*-12 above 280[4] or *Cmca*-4 above 250 GPa[5]) which appears to have metallic properties in both studies. These predictions of a new metallic phase seem to be in agreement with the recent claims of metallization of $H_2(D_2)$ at above 260 GPa.[3] However, our optical spectroscopy results above 260 GPa are in strong disagreement with Ref. 3, where the *total* disappearance of the Raman signal, increased reflectivity, and a closed band gap were reported. We observed an *increase* in Raman signal intensities with pressure (in our studies higher pressures than in Ref. 3 were reached for both isotopes, as evidenced by the lower vibron frequencies) and an optical band gap of ∼2 eV persisting above 300 GPa. This metallization claim contradicts several experiments conducted at identical compressions[6,7] including a quite recent infrared study of phase III of H_2 at low temperatures and up to 360 GPa.[8] The theoretically proposed molecular metallic phases (*Cmca*-12 and *Cmca*-4) are Raman active (see Fig. 4), which would also be at variance with the claimed disappearance of Raman modes in Ref. 3. Therefore we attribute the experimental findings in Ref. 3 to the changes in the sample chamber geometry and partial sample loss rather than to the claimed "metallic liquid atomic state."

However, the slight changes in optical properties at 275 GPa, such as the appearance of the fourth low-energy mode (see Fig. 2 in Ref. 1), the change in slopes of the ν_1 frequency, and the value of the D_2/H_2 band gaps with pressure (Fig. 5), *might* indicate the presence of a new solid structure (phase IV') of dense H_2 (D_2). The very similar Raman spectra suggest that if phase IV′ exists, it is structurally very closely related to phase IV. Phase IV′ appears to be semiconducting in our measurements but one can estimate the pressures needed to close the band gap and reach the metallic state. We have combined D_2 and H_2 band-gap points and used different polynomials to fit and extrapolate our data (Fig. 5). The pressures at which the band gap is fully closed vary widely depending on the power of the polynomial but the lowest value is approximately 375 GPa (Fig. 5). It is instructive to estimate the frequency of the Raman ν_1 mode at this pressure. Indeed, the frequency and increasing intensity of the ν_1 mode are very sensitive to compression (inset in Fig. 5). Therefore the frequency should be considered as an absolute pressure gauge in the experiments with H_2 (D_2) and could be used for direct result comparison in both experimental and theoretical studies. The extrapolation of hydrogen frequency versus pressure is almost linear (Fig. 5) and yields 2350 ± 50 cm^{-1} at 375 GPa. We note that this value is about 55% of the vibron frequency under ambient conditions and is much lower than any frequencies ever reported in experiments.

In summary, we have mapped out the transformation between phase III and phase IV of H_2 (D_2), demonstrating increased proton tunneling in phase IV. We estimate that the H_2 (D_2) will metallize above 375 GPa, a pressure which is in good agreement with several previous experimental measurements.[6,7]

The authors are grateful to Chris Pickard, Graeme Ackland, and Stanimir Bonev for very useful discussions and Yanming Ma for providing unpublished data. This work was supported by research grants from the U.K. Engineering and Physical Sciences Research Council and the Institute of Shock Physics, Imperial College.

*e.gregoryanz@ed.ac.uk

[1] R. T. Howie, C. L. Guillaume, T. Scheler, A. F. Goncharov, and E. Gregoryanz, Phys. Rev. Lett. **108**, 125501 (2012).
[2] C. Pickard and R. Needs, Nat. Phys. **3**, 473 (2007).
[3] M. Eremets and I. Troyan, Nat. Mater. **10**, 927 (2011).
[4] C. J. Pickard, M. Martinez-Canales, and R. J. Needs, Phys. Rev. B **85**, 214114 (2012); **86**, 059902(E) (2012).
[5] H. Liu, H. Wang, Y. Ma *et al.*, J. Chem. Phys. **137**, 074501 (2012).
[6] P. Loubeyre, F. Occelli, and R. LeToullec, Nature **416**, 613 (2002).
[7] Y. Akahama, H. Kawamura, N. Hirao, Y. Ohishi, and K. Takemura, J. Phys.: Conf. Ser. **215**, 012056 (2010).
[8] C. S. Zha, Z. Liu, and R. J. Hemley, Phys. Rev. Lett. **108**, 146402 (2012).
[9] A. Goncharov, R. Hemley, and H. K. Mao, J. Chem. Phys. **134**, 174501 (2011).
[10] Y. Akahamaa and H. Kawamura, J. Appl. Phys. **100**, 043516 (2006).
[11] J. E. Proctor, E. Gregoryanz, K. S. Novoselov, M. Lotya, J. N. Coleman, and M. P. Halsall, Phys. Rev. B **80**, 073408 (2009).

[12]M. Marquès, M. Santoro, C. L. Guillaume, F. A. Gorelli, J. Contreras-Garcia, R. T. Howie, A. F. Goncharov, and E. Gregoryanz, Phys. Rev. B **83**, 184106 (2011).
[13]C. L. Guillaume *et al.*, Nat. Phys. **7**, 207 (2011).
[14]F. A. Gorelli, S. F. Elatresh, C. L. Guillaume, M. Marques, G. J. Ackland, M. Santoro, S. A. Bonev, and E. Gregoryanz, Phys. Rev. Lett. **108**, 055501 (2012).
[15]A. Goncharov, E. Gregoryanz, R. Hemley, and H. Mao, Proc. Natl. Acad. Sci. USA **98**, 14234 (2001).
[16]I. Silvera, Rev. Mod. Phys. **52**, 393 (1980).
[17]H. Liu and Y. Ma, arXiv:1210.0280.
[18]A. Goncharov and J. Crowhurst, Phase Trans. **80**, 1051 (2007).
[19]R. J. Hemley and H. K. Mao, Phys. Rev. Lett. **61**, 857 (1988).
[20]A. F. Goncharov, I. I. Mazin, J. H. Eggert, R. J. Hemley, and H. K. Mao, Phys. Rev. Lett. **75**, 2514 (1995).

High-Pressure Synthesis of Noble Metal Hydrides

Christian Donnerer, Thomas Scheler and Eugene Gregoryanz*
Centre for Science at Extreme Conditions and School of Physics and Astronomy, The University of Edinburgh, Edinburgh, EH9 3JZ, UK

The formation of hydride phases in the noble metals copper, silver and gold was investigated by *in-situ* x-ray diffraction at high hydrogen pressures. In the case of copper, a novel hexagonal hydride phase, Cu_2H, was synthesised at pressures above 18.6 GPa. This compound exhibits an anti-CdI_2-type structure, where hydrogen atoms occupy every second layer of octahedral interstitial sites. In contrast to chemically produced CuH, this phase does not show a change in compressibility compared to pure copper. Furthermore, repeated compression (after decomposition of Cu_2H) led to the formation of cubic copper hydride at 12.5 GPa, a phenomenon attributed to an alteration of the microstructure during dehydrogenation. No hydrides of silver (up to 87 GPa) or gold (up to 113 GPa) were found at both room and high temperatures.

PACS numbers:

I. Introduction

Despite hydrogen being highly reactive, none of the group-6 to group-11 transition metals react with it at ambient conditions.[1–3] However, at elevated pressures, the chemical potential of hydrogen rises steeply and reactions, usually leading to the formation of a binary metal hydride, are induced.[3–5] The group-11 noble metals play an interesting role in this context. While the formation of gold hydride was reported more than 30 years ago[6], it has not been confirmed since. In fact, recent *ab-initio* calculations found no evidence for a reaction between gold and hydrogen, due to a large energy barrier preventing the dissociation of hydrogen molecules at the gold surface.[7] For silver, to the best of our knowledge, no bulk hydride phase has ever been found. Theoretical studies predict that *fcc*-silver hydride stabilises at pressures above 50 GPa.[8]

In contrast, copper hydride was one of the very first *d*-metal hydrides to be discovered. It was first synthesised in 1844 by reacting hypophosphorous acid with copper sulphate (known as Wurtz method).[9] Forming a stoichiometric monohydride[10], it adopts a hexagonal wurtzite-type structure ($P6_3mc$ space group).[11] This is unusual compared to other transition metal hydrides, many of which exist in NiAs-type or NaCl-type structure. Often, the metal atoms form a closed-packed host lattice in which hydrogen atoms occupy interstitial sites[4] and participate in metallic bonds. As a result, the presence of hydrogen atoms does not influence the mechanical properties of its host lattice, except for a measurable volume expansion. However, in wurtzite CuH, the bulk modulus was measured to be 72(2) GPa[12], significantly lower than the bulk modulus of pure copper (137.4 GPa).[13] This can be attributed to the hydrogen-copper bond which has been described as partly covalent and ionic.[14,15] Chemically produced CuH is unstable at ambient conditions, but at temperatures below -5°C, it can be stored permanently.[16] At room temperature it decomposes at pressures below 8.4(6) GPa.[17] Copper hydride is widely used as a reagent for reduction reactions in organic synthesis[18] and can also be used to obtain extremely reactive catalysts.[19] Most recently, a facile synthesis of CuH through sonochemistry was reported.[20]

However, the direct synthesis of hexagonal CuH from elements under thermodynamic equilibrium (*i.e.* at high pressures and temperatures) has never been reported. Through Gibbs free energy calculations, based on the decomposition pressure, a formation pressure of 30 GPa was predicted.[17] Interestingly, a different form of copper hydride has been synthesised at pressures above 14.4 GPa, the only high pressure study of copper hydride formation we are aware of.[21] This hydride retains the *fcc* lattice of copper, where hydrogen atoms occupy interstitial sites at a hydrogen-to-metal atomic ratio of $\sim$ 0.4. In accordance with the notation for other hydrides[4], this cubic phase will be referred to as the γ-phase of CuH here. It was suggested that this phase *could only be observed* in a reaction of hydrogen with *dehydrogenated* copper, obtained from decomposing hexagonal wurtzite-type CuH (*i.e.* copper mono hydride synthesised by the Wurtz method). Conversely, pristine copper foil remained inert and no other hydride phase was observed at pressures up to 20 GPa.[21]

In this study, we present results of synchrotron-based powder x-ray diffraction (XRD) experiments on copper, silver and gold in a dense hydrogen medium. In the copper-hydrogen system, we identified a novel hexagonal hydride phase, distinctly different from wurtzite-type CuH and γ-Cu-H. This phase formed at 18.6 GPa and remained stable up to 51 GPa in an anti-CdI_2 type structure, with a stoichiometric composition of Cu_2H. It decomposes at pressures below 10 GPa. On repeated compression a volume expansion in *fcc*-Cu was measured, indicating the formation of cubic copper hydride, although with a lower hydrogen content than previously reported.[21] No hydride phases were observed upon pressurization of silver and gold.

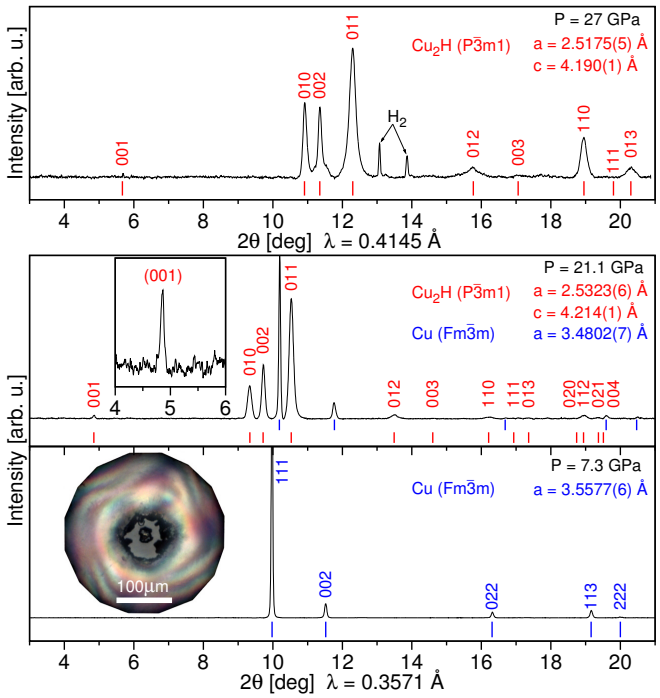


FIG. 1: (Colour online) Integrated XRD spectra of pure Cu at 7.3 GPa (bottom panel); Cu_2H along with remaining Cu at 21.1 GPa (middle panel); the fully converted Cu_2H along with reflections from excess H_2 at 27 GPa (upper panel). Tick marks indicate calculated peak positions of Cu (blue) in the bottom panel, Cu (top row, blue) and Cu_2H (bottom row, red) in the middle panel and Cu_2H (red) in the upper panel. The inset shows the (001) superstructure peak of the layered anti-CdI_2 structure of Cu_2H. The optical micrograph in the bottom panel shows the sample at 50 GPa.

II. Experimental Details

We conducted six independent high-pressure experiments, two each for copper, silver and gold. Metal samples from commercial thin foils (Alfa Aesar, 10 μm thickness, 99.8% purity) were loaded into symmetrical diamond anvil cells (DACs). Hydrogen was subsequently gas-loaded to pressures between 1600 and 2000 bar and thus also acted as the pressure transmitting medium. The samples were always surrounded by excess hydrogen (monitored visually and by Raman spectroscopy), even at the highest pressures. The gasket material was rhenium, with a hole drilled to a diameter of ~50% of the culet diameter. Pressure was measured *in-situ* using the revised ruby fluorescence pressure scale.[22] The diffraction patterns were recorded on MAR345 or MAR555 detectors and integrated using the Fit2D[23] software.

III. Results and Discussion

In the first experimental run on copper, the metal remained unchanged in its *fcc* phase ($Fm\bar{3}m$ spacegroup) up to 21.1 GPa. At this pressure, over time, new reflections started to emerge (see Fig. 1). Although the new reflections gained intensity at higher pressures, the *fcc* signature remained visible up to 51 GPa, the highest pressure achieved in this run. Initially, this new phase was indexed in the $P6_3/mmc$ spacegroup (*hcp* lattice), an increased volume per formula unit compared to *fcc*-Cu indicates the formation of a hydride. The new diffraction pattern is also easily distinguishable from rhenium hydride which forms at the inner gasket rim and also exhibits an *hcp*-like structure.[24] Apart from a smaller unit-cell volume compared to ReH, the c/a-ratio of the new hexagonal phase remained at a constant 1.661(3) throughout the experiment (see inset Fig. 2) whereas it is between 1.61 and 1.58 for rhenium hydride.[25] In the second run, the new phase appeared at 18.6 GPa. In contrast to the first run, the sample converted completely within 2 hours, leaving no signal from *fcc*-Cu. The only difference between the two experiments was the size of the loaded copper sample: The volume of the sample in the second run was an order of magnitude smaller than in the first run. While it is not impossible that with time a larger sample would fully convert, it can be concluded that, even at very high pressures, the penetration depth of hydrogen into bulk copper is limited. A similar behaviour is known from platinum nitride[26] where only a thin surface layer reacted even at pressures above 50 GPa and temperatures exceeding 2000 K.

We therefore assume a synthesis pressure of 18.6 GPa for the hexagonal phase. Decomposition occurred at pressures below 10.5 GPa, close to the decomposition pressure of wurtzite-type CuH (8.4(6) GPa[17]). However, the new hexagonal phase is distinctly different: Over the entire experimental pressure range, the volume difference compared to pure Cu remained between 1.23(1) and 1.05(1) Å^3 per atom, much lower than for wurtzite-type CuH (see Fig. 2). In fact, volume considerations allow to estimate the hydrogen content (see *e.g.* Refs. 3,24,27). It has been found empirically that hydrogen atoms occupying the octahedral interstitial sites of an *hcp* metal expand the lattice by ~2.1 Å^3 per hydrogen atom.[27] As the lattice expansion scales linearly with hydrogen content[27], it can be inferred that the new hexagonal phase exhibits a Cu_2H composition. After platinum[28], copper is the second *fcc* metal known to transform into an *hcp* hydride. Both possess significantly larger c/a ratios (1.66 to 1.7) than all other *hcp* *d*-metal hydrides[4], providing a signature for this transformation. The hexagonal Cu_2H phase will be referred to as the ϵ-phase of copper hydride.

A Vinet equation of state was fitted to the data, yielding a zero-pressure volume of $V_0 = 13.10(1)$ Å^3 and bulk modulus of $K_0 = 145(5)$ GPa ($K' = 4.8(3)$) for ϵ-

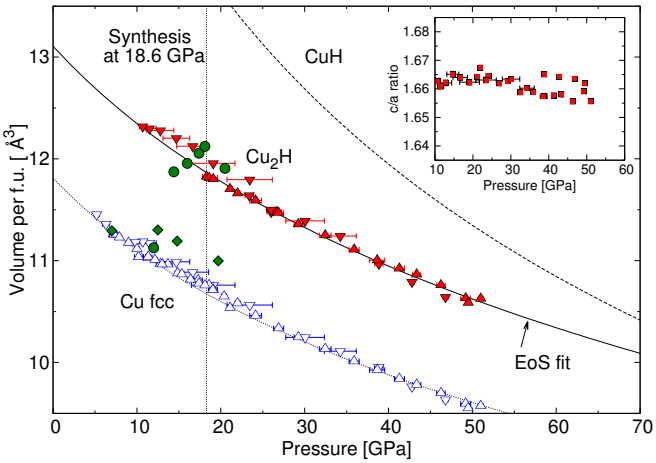


FIG. 2: (Colour online) Equation of state of copper and its hydrides. Blue open triangles denote *fcc*-Cu, red solid triangles ϵ-Cu_2H and green diamonds γ-$CuH_{\sim 0.15}$. Triangles pointing upwards are data points from compression, triangles pointing downwards are from decompression. For comparison, green circles are data points belonging to γ-$CuH_{\sim 0.4}$, taken from Ref. 21. Dotted and dashed lines are literature equations of state for *fcc*-Cu and wurtzite-type CuH, respectively (Refs. 13 and 12). The solid line is a Vinet-type fit to the observed equation of state of ϵ-Cu_2H. The inset shows the pressure variation of the c/a-ratio for ϵ-Cu_2H.

Cu_2H (compared to $K_0 = 137.4$ GPa for *fcc*-Cu).[13] This is in agreement with the widely accepted concept that interstitial hydrogen does not influence the mechanical properties of its host metal, but in stark contrast to the mechanical properties of wurtzite-type CuH (see Table I). This can be attributed to the different bonding of hydrogen atoms in the chemically synthesised hydride, which causes a significant increase in compressibility and volume ($V_0 = 16.75$Å^3, $K_0 = 72(2)$ GPa).[12] Optical observations of our samples during hydrogenation and at higher pressures did not show a change in appearance. In addition to the absence of changes in the compressibility and the typical volume expansion, this led to the conclusion that the interstitial hydrogen atom donates its electron partly to the *s*- and *d*-bands of the surrounding metal (as found for many other hydrides[3]), such that the hydride retains a metallic character.

It is often assumed that the hydrogen sublattice in metal hydrides with hydrogen:metal ratio below 1 would form a disordered solid.[3] With a hydrogen:metal ratio of 0.5 in ϵ-Cu_2H, hydrogen atoms would be randomly distributed over the available sites, leaving 50% vacant. However, in our data, an additional weak reflection can be seen, matching the forbidden (001) reflection of the *hcp* lattice. Such reflections (00l, with odd l) appear when the $c/2$ translational symmetry is absent in the hexagonal lattice, through atoms being displaced from their equilibrium hexagonal positions. This suggests an anti-CdI_2 type superstructure ($P\bar{3}m1$ space group) for

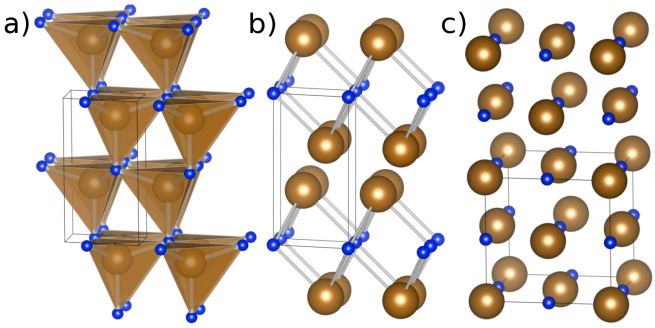


FIG. 3: (Colour online) Ordering of hydrogen (small, blue) and copper (large, copper) atoms showing A) wurtzite-type CuH ($P6_3/mc$ space group), B) anti-CdI_2 structure ϵ-Cu_2H ($P\bar{3}m1$ space group, the displacement of copper atoms is exaggerated) and C) cubic γ-Cu-H ($Fm\bar{3}m$ space group). (visualised via VESTA[30])

Cu_2H: In this structure, instead of occupying random sites, hydrogen atoms fill every second layer of octahedral interstices. This periodic vacancy and filling of sites along the c-axis causes the displacement of the metal atoms. The anti-CdI_2 type structure is also observed in the hydrides of other metals, such as technetium[29], cobalt[27] and rhenium.[24,25]

The new positions of the metal atoms in the unit-cell are thus given by $(\frac{2}{3}, \frac{1}{3}, \frac{1}{4} + \delta)$ and $(\frac{1}{3}, \frac{2}{3}, \frac{3}{4} - \delta)$. The displacement δ can be determined by comparing calculated with observed intensities. Throughout both experiments, the relative intensity of the (001) reflection, $I_{(001)}/I_{(110)}$, remained at a constant 2.3(3)%, corresponding to a fractional displacement of $\delta = 0.016(2)$, larger than for $CoD_{0.5}$ ($\delta = 0.012$) and $TcH_{0.5}$ ($\delta = 0.01$). This may be due to imperfect hydrogen ordering in the latter hydrides: For $CoD_{0.5}$, neutron diffraction showed that ∼4% of hydrogen atoms occupy 1b sites of the lattice, forming a second sublayer that should be vacant in an ideal anti-CdI_2 structure.[27] Generally, a lower hydrogen content seems to manifest in smaller displacements, as $\delta = 0.007$ for $CoD_{0.38}$ and 0.009 for $ReH_{0.36}$.[25] From the larger displacement in Cu_2H it can be inferred that the intermediate layers are indeed completely vacant and that the structure is of perfect or nearly perfect anti-CdI_2-type.

TABLE I: Equation of state parameters for Cu, wurtzite-type CuH and hexagonal Cu_2H. The bulk modulus of the chemically obtained CuH is significantly lower than for pure copper, in contrast to Cu_2H, where the mechanical properties are unchanged.

	Reference	EoS type	B_0 [GPa]	B_0'	V_0 [Å^3]
Cu	13	Birch-Murnaghan	137.4	5.52	11.81
CuH	12	Murnaghan	72(2)	2.7(3)	16.75
Cu_2H	This work	Vinet	145(5)	4.8(3)	13.10(1)

In order to test the hypothesis that γ-Cu-H only forms with dehydrogenated copper, we decompressed the sample in the ϵ-phase to below decomposition pressure. After the sample fully separated into Cu and H_2, pressure was increased in steps up to ∼20 GPa. At 12.5 GPa, an increase in unit-cell volume of *fcc*-Cu was measured, indicating the formation of γ-Cu-H. Multiple hydride phases have also been observed in other metal-hydrogen systems, such as manganese hydride, which forms both γ- and ϵ-phases, depending on the temperature during compression.[31]

In the case of γ-Cu-H, the volume difference per atom increased from 0.338(6) Å^3 at 12.5 GPa to 0.386(6) Å^3 at 19.7 GPa. For *fcc* metals, hydrogen atoms typically occupy octahedral interstices in the γ-phase, leading to a volume expansion of ∼2.9 Å^3 per hydrogen atom.[32] Assuming that this is the case for γ-Cu-H, a metal:hydrogen ratio of ∼ 0.15 is found. Compared to the the results reported by Burtovyy *et al.*[21], we find the same synthesis pressure of 12.5 GPa, but a smaller volume increase of the host lattice (3.45(5)% vs 8-11%) and thus hydrogen content (∼ 0.15 compared to ∼ 0.4 in Ref. 21). If the formation of γ-Cu-H does indeed depend on the history of the individual copper sample, the difference in hydrogen content in the γ-phase may be accounted for by different initial hydrogenation conditions: Burtovyy *et al.* used commercial wurtzite-type copper hydride to prepare their samples, whereas we used pristine copper foil which was hydrogenated under thermodynamic equilibrium. Furthermore, it was speculated[21] that small crystallites of copper, created through the decomposition of CuH, may show higher reactivity and could thus form the γ-phase more easily. An alteration of the microstructure during hydrogenation/dehydrogenation cycles is common in metals. This process could be more effective in the decomposition of wurtzite-type CuH than of ϵ-Cu_2H, leading to favourable conditions for hydrogen uptake in the γ-phase. A different explanation is that the lower hydrogen content seen in our data originates from slow kinetics, impeding the hydrogenation of the sample. It is not uncommon that kinetic effects play an important role in the formation of isomorphous metal hydrides (*i.e.* the incorporation of hydrogen into the metal matrix without it undergoing a structural phase transition, see *e.g.* rhenium hydride[24]). In the present case, the time difference between crossing synthesis conditions and reaching maximum pressure for the γ-phase was only 1 hour, in contrast to 20 hours between individual data points in the study by Burtovyy *et al.*. At room temperature, higher hydrogen concentrations in the γ-phase may only be achieved after a certain time.

It is interesting to note that wurtzite-type CuH could not be synthesised under thermodynamic equilibrium at pressures up to 51 GPa. Extrapolation of the equations of state of wurtzite-type CuH and ϵ-Cu_2H shows that both acquire the same volume at approximately 95 GPa, due to the larger compressibility of the first hydride. It can be argued that at this pressure the ϵ phase might undergo a transition to the wurtzite phase.

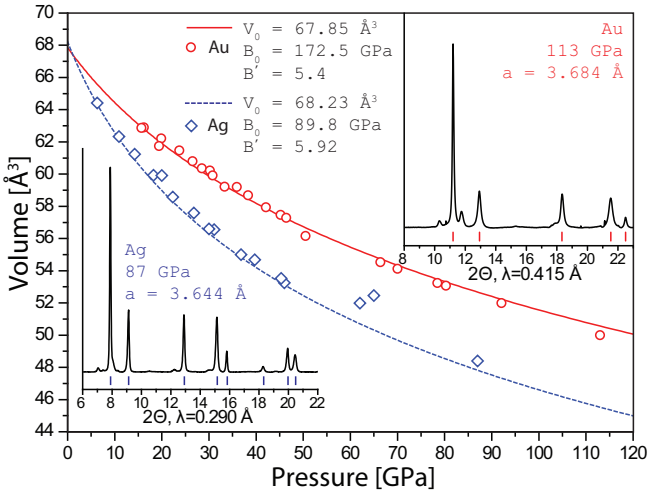


FIG. 4: (Colour online) Equation of state of silver (blue diamonds) and gold (red circles) measured in a hydrogen medium. The lines are literature EoS for *fcc*-silver[34] and *fcc*-gold.[35]

We compressed silver to 87 GPa and gold to 113 GPa at room temperature without observing any signs of hydrogenation (*i.e.* volume increase or phase transition). For silver, single-sided laser heating to well above 1000°C was applied at 40 GPa while the gold-hydrogen mixture was externally heated to ∼ 300°C at pressures up to 45 GPa, to no effect in both cases. Figure 4 shows the measured pressure-volume data for silver and gold. No significant deviation from the known equations of state for both metals can be seen. It was predicted that *fcc*-silver hydride stabilises at pressures above 50 GPa[8], which could not be confirmed. More recently, a theoretical study reported that pressures in excess of 180 GPa might be necessary.[7] In the same paper, the authors find that the formation of a gold hydride is impeded by a large energy barrier preventing the dissociation of hydrogen molecules at the metal surface. However, hydrogen undergoes a structural phase transition into a mixed atomic and molecular state at 220 GPa (phase IV, see Ref. 33). At this point, a direct reaction of gold (and also silver) with hydrogen is very likely.

IV. Conclusion

In conclusion, we synthesised a novel hexagonal copper hydride from elements at pressures above 18.6 GPa. This ϵ-Cu_2H phase is the third known copper hydride, along with wurtzite-type CuH and cubic γ-Cu-H. The presence of superstructure peaks allowed to identify the structure as anti-CdI_2-type, where the hydrogen atoms are

arranged in layers instead of being randomly oriented. Furthermore, we were able to reproduce the synthesis of γ-Cu-H, albeit with a lower hydrogen concentration. It remains uncertain whether the formation of γ-Cu-H is promoted by the hydrogenation history or the particular grain size and microstructure of the copper sample. However, it can be concluded that wurtzite-type copper hydride is in fact not the thermodynamically favourable structure of this hydride, despite having the highest hydrogen content and being the easiest to synthesise under non-equilibrium conditions.

Acknowledgments

This work is supported by a research grant from the UK Engineering and Physical Sciences Research Council. T.S. gratefully acknowledges the support of the CM-DTC. We thank A. Kleppe from I15, Diamond Light Source, M. Hanfland at ID09A, ESRF, and Z. Konopkova at P02, PETRA-III, for technical support.

* e-mail: e.gregoryanz@ed.ac.uk

[1] F. Lewis, Nature **242**, 45 (1973).
[2] B. Hammer and J. Norskov, Nature **376**, 238 (1995).
[3] Y. Fukai, *The metal-hydrogen system: basic bulk properties*, vol. 21 (Springer, 2005).
[4] V. Antonov, J. of Alloys and Compounds **330**, 110 (2002).
[5] O. Degtyareva, J. Proctor, C. Guillaume, E. Gregoryanz, and M. Hanfland, Solid State Communications **149**, 1583 (2009).
[6] V. Antonov, Dokl. Acad. Nauk. SSSR **266**, 376 (1982).
[7] G. Gao, H. Wang, L. Zhu, and Y. Ma, J. Phys. Chem. C **116**, 1995 (2012).
[8] D. Y. Kim, R. H. Scheicher, C. J. Pickard, R. J. Needs, and R. Ahuja, Phys. Rev. Lett. **107**, 117002 (2011).
[9] A. Wurtz, Cr Hebd Acad Sci **18**, 702 (1844).
[10] H. Müller and A. Bradley, Journal of the Chemical Society (Resumed) **129**, 1669 (1926).
[11] J. Goedkoop and A. Andresen, Acta Crystallographica **8**, 118 (1955).
[12] M. Tkacz, S. Majchrzak, and B. Baranowski, International Journal of High Pressure Research **6**, 85 (1990).
[13] L. Liu, M. Liu, H. Verbeek, C. Höffner, and G. Will, Journal of Physics and Chemistry of Solids **51**, 435 (1990).
[14] M. Tkacz and R. Burtovyy, Journal of alloys and compounds **404**, 368 (2005).
[15] S. M. Filipek, Journal of Advanced Science **19**, 1 (2007).
[16] N. Fitzsimons, W. Jones, and P. Herley, Catalysis letters **15**, 83 (1992).
[17] M. Tkacz and R. Burtovyy, Solid state communications **132**, 37 (2004).
[18] M. Semmelhack and R. Stauffer, The Journal of Organic Chemistry **40**, 3619 (1975).
[19] B. Lipshutz, K. Noson, W. Chrisman, and A. Lower, Journal of the American Chemical Society **125**, 8779 (2003).
[20] P. Hasin and Y. Wu, Chemical Communications **48**, 1302 (2012).
[21] R. Burtovyy and M. Tkacz, Solid state communications **131**, 169 (2004).
[22] W. Holzapfel, High Pressure Research **25**, 87 (2005).
[23] A. P. Hammersley, S. O. Svensson, M. Hanfland, A. N. Fitch, and D. Hausermann, High Pressure Research **14**, 235 (1996).
[24] T. Scheler, O. Degtyareva, and E. Gregoryanz, The Journal of chemical physics **135**, 214501 (2011).
[25] H. Kawamura, M. Harada, Y. Akahama, and K. Takemura, Solid state communications **130**, 59 (2004).
[26] E. Gregoryanz, C. Sanloup, M. Somayazulu, J. Badro, G. Fiquet, H.-k. Mao, and R. J. Hemley, Nature Materials **3**, 294 (2004).
[27] V. Fedotov, V. Antonov, T. Antonova, E. Bokhenkov, B. Dorner, G. Grosse, and F. Wagner, Journal of alloys and compounds **291**, 1 (1999).
[28] T. Scheler, O. Degtyareva, M. Marqués, C. Guillaume, J. Proctor, S. Evans, and E. Gregoryanz, Physical Review B **83**, 214106 (2011).
[29] V.P.Glazkov, A.V.Irodova, V.A.Somenkov, S.Sh.Shil'shtein, V.E.Antonov, and E.G.Ponyatovskii, Sov.Phys.Solid State **26**, 1961 (1984).
[30] K. Momma and F. Izumi, Journal of Applied Crystallography **41**, 653 (2008).
[31] Y. Fukai, T. Haraguchi, H. Shinomiya, and K. Mori, Scripta materialia **46**, 679 (2002).
[32] B. Baranowski, S. Majchrzak, and T. Flanagan, Journal of Physics F: Metal Physics **1**, 258 (2002).
[33] R. T. Howie, C. L. Guillaume, T. Scheler, A. F. Goncharov, and E. Gregoryanz, Phys. Rev. Lett. **108**, 125501 (2012).
[34] Y. Akahama, Journal of Applied Physics **95**, 4767 (2004).
[35] A. Dewaele, P. Loubeyre, and M. Mezouar, Physical Review B **70**, 094112 (2004).

Nanocrystalline Tungsten Hydrides at High Pressures

Thomas Scheler[1], Feng Peng[2], Christophe L. Guillaume[1], Ross T. Howie[1], Yanming Ma[2], Eugene Gregoryanz[1*]
[1] *SUPA, School of Physics and Astronomy and Centre for Science at Extreme Conditions, The University of Edinburgh, Edinburgh, EH9 3JZ, UK*
[2] *State Key Lab of Superhard Materials, Jilin University, 130012 Changchun, P.R. China*

A combined experimental and theoretical study has been carried out on the synthesis and characterization of tungsten hydride at high pressures. We confirm the synthesis of tungsten monohydride at above 25 GPa and 300 K. At higher pressures, hydrogen content is found to increase and *ab-initio* calculations reveal the formation of tungsten dihydride in a mixed composition of $(1-y)$WH + (y)WH$_2$ with $y \sim \frac{1}{3}$. Synchrotron x-ray diffraction and transmission electron microscopy (TEM) measurements demonstrate the formation of a nano-crystalline microstructure upon hydrogenation. TEM micrographs show elongated grains with diameters of ∼20 nm, a structure similar to nanocrystalline diamond.

PACS numbers:

The application of extreme conditions, namely high pressures and temperatures, offers a very general route for synthesizing novel materials and manipulating their physical properties. In the past this led to several important discoveries, including nanopolycrystalline diamond (NPD) [1], cubic boron nitride (c-BN) [2] and the highly incompressible nitrides of osmium, iridium and platinum [3, 4]. Most recently, nanotwinned c-BN was found to be ultrahard, even exceeding the hardness of diamond [5]. In the past few years, hydrogen compounds and alloys have attracted the renewed attention of researchers due to their potential applications in a hydrogen economy [6–8] and implications for the behaviour of free hydrogen, such as its elusive metallic state [9, 10]. Here, high-pressure synthesis has also been successfully applied to synthesize novel hydrides, *e.g.* platinum hydride [11, 12], ϵ_2-rhenium hydride [13], a polymeric phase of silicon tetrahydride at pressures exceeding 1 Mbar [14] and tungsten hydride [15, 16]. With the exemption of SiH_4, the aforementioned materials are interstitial metal hydrides in which the hydrogen atoms occupy octahedral or tetrahedral sites in the closed-packed metal host lattice. Most of the known hydride phases of the *d*-metals between the Cr-group and Cu-group elements are of this type [17]. Furthermore, none of the metals in this group readily reacts with hydrogen at ambient conditions and high pressures are necessary to form a hydride under equilibrium conditions [17]. The conditions for the formation of stoichiometric hydrides range from less than 1 GPa (*e.g.* NiH at 0.6 GPa, [18]) to 27 GPa in platinum [11], so far the highest synthesis pressure observed in this group.

In this paper, we present a combined x-ray diffraction, electron microscopy and computational study of tungsten hydride at high pressures. We studied the formation, decomposition and mechanical properties of tungsten hydride synthesized from the elements in a diamond anvil cell up to 115 GPa by x-ray diffraction as well as the microstructure of recovered dehydrogenated tungsten by transmission electron microscopy. The hydrogenation process was found to create a nanocrystalline microstructure. Theoretical *ab-initio* calculations in conjunction with measurement of the equation of state suggest that between 25 and ∼ 50 GPa, tungsten dihydride is formed and coexists with the monohydride at higher pressures in a mixed composition of $(1-y)$WH + (y)WH$_2$, saturating at $y \sim \frac{1}{3}$ above 50 GPa. Details on the experimental and computational methods are given in the supplementary material (Ref. [19]).

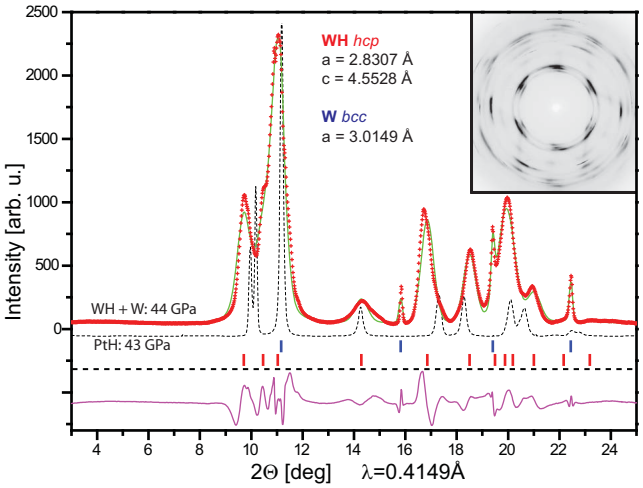


FIG. 1: (Color online) Powder x-ray diffraction spectrum of tungsten hydride at 44 GPa. The green line denotes the result from a LeBail fit. Tick marks indicate peak positions for cubic W (upper, blue) and hexagonal WH (lower, red). The diffraction spectrum of platinum hydride at 43 GPa is added for comparison [11] (grey dashed line). Note the difference in peak width. PtH forms under similar conditions as WH and also exhibits the *hcp*-structure.

Tungsten is a widely used material in both industry

and science. In high-pressure applications it is particularly valued as a pressure calibrant and gasket material [20]. In the past, it was widely accepted that tungsten does not react with hydrogen, even at very high pressures, and therefore was frequently used as a sealing material in high-pressure experiments. However, it was reported a few years ago that binary tungsten hydride is formed when compressing pure tungsten to above 25 GPa at room temperature in a dense hydrogen medium [15]. In a recent theoretical study of this material, several potentially metastable phases of varying hydrogen content were found [16], although only tungsten monohydride was observed experimentally. The monohydride is characterized by a hexagonally closed-packed arrangement of the tungsten atoms (spacegroup $P6_3/mmc$) with hydrogen atoms occupying the octahedral interstitial sites. This is equivalent to the NiAs-type structure, which is known for many other hydrides in the *d*-metals as well and is also the one adopted by the hydrides of the same group, MoH [21] and CrH [22].

In our experimental runs, we observe a reaction between tungsten and hydrogen at 25 GPa with the appearance of new diffraction peaks in addition to *bcc*-tungsten. The new phase can be indexed in the $P6_3/mmc$ spacegroup with an expanded volume per tungsten atom in the unit-cell. So far, our observations are identical with earlier reports on tungsten hydride. The synthesis conditions of WH are reminiscent of *hcp* platinum hydride [11] (PtH), which forms at pressures above 27 GPa and room temperature. However, in contrast to PtH, the hydride formation in tungsten progresses very slowly over time and the diffraction pattern of WH exhibits broadened Bragg peaks (see Figure 1). In one of our experimental runs, we reached pressures of ∼45 GPa within hours of surpassing synthesis conditions. At this time, the sample has not been completely converted to tungsten hydride and the sharp Bragg peaks of *bcc*-tungsten are still clearly visible (see Figure 1). For comparison we include the diffraction pattern of platinum hydride at similar pressures. It is evident that the diffraction peaks of tungsten hydride are considerably broadened compared to both its parent metal and another hydride synthesized under nearly identical conditions. While increasing pressure seems to accelerate the transformation process, with time the whole sample fully transforms into the hydride also at constant pressures. In one of the experimental runs the sample was left at a pressure of 38 GPa for one month. Afterwards, the whole sample was hydrogenated and no sign of *bcc*-tungsten was detected. Laser heating has also been shown to accelerate the transition into the hydride phase [16]. On decompression, tungsten hydride was found to be stable to pressures far below synthesis conditions. We observed the decomposition reproducibly at pressures between 8 and 9 GPa. The slow progression of the hydrogenation process, its acceleration upon heating and the large hysteresis effect in decomposition suggest the presence of a kinetic energy barrier hindering the formation at lower pressures and faster hydrogenation. We found that dehydrogenated tungsten still exhibits broadened Bragg peaks compared to its original state.

We recovered such dehydrogenated tungsten samples from the diamond anvil cells and used focused ion beam techniques to prepare transmission electron microscopy (TEM) samples. TEM brightfield and darkfield imaging revealed elongated crystallites with shortest dimensions of below 20 nm (see Figure 2(a-c)). The observed structure is similar to that of NPD which also exhibits elongated crystallites with diameters of 10-20 nm and lengths of up to a few 100 nm [1]. This new form of artificial diamond was reported to be harder than natural single crystalline diamond [1]. Electron diffraction measurements on dehydrogenated tungsten further show that the crystallites are not randomly oriented but follow a preferred orientation (Figure 2(d)) which explains the texture in the x-ray diffraction patterns. In a control experiment we prepared TEM samples from untreated tungsten. Both, TEM micrographs and electron diffraction patterns (Figure 2(e)) indicate perfect single crystallinity.

This microstructure can be related to the observed broadening of the diffraction peaks. Peak broadening in x-ray diffraction patterns during high-pressure experiments can be attributed to three different effects: i) instrument broadening, ii) strain broadening and iii) size broadening. While instrument broadening can be neglected when using modern third generation synchrotron radiation sources, both strain and size broadening contribute to the peak shape. The simple Scherrer formula $L = \frac{K\lambda}{\beta cos(\Theta)}$ (see *e.g.* Ref. [14]) connects the peak width to the crystallite size, ignoring however any strain contribution. Here, L is the grain size, λ the x-ray wavelength, β the peak width and Θ the scattering angle of the reflection. K is the empirical Scherrer constant and usually 1. When comparing the values in Table 1 for tungsten hydride with the results of the TEM measurements on recovered dehydrogenated tungsten, it is evident that strain plays a significant role at rising pressures (indicated by the decreasing calculated grain size). However, when extrapolating the data in Table 1 to zero pressure, a grain size comparable to what is found in the TEM images can be derived. It should be emphasized here, that the calculated values at high pressures do not correspond to actual grain sizes. From the emergence of the broad diffraction peaks upon synthesis we conclude that it is, in fact, the hydrogenation process that leads to the formation of a nanomaterial.

We offer the following explanation for the formation

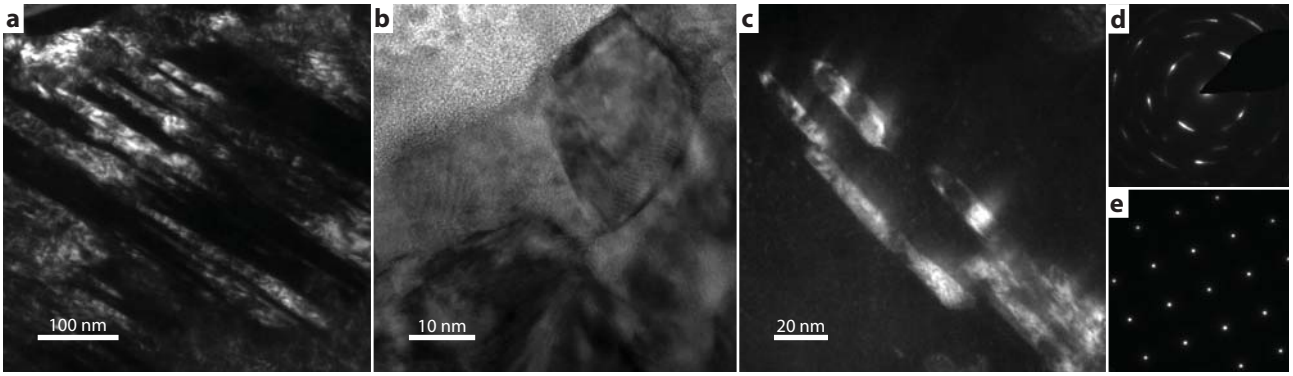


FIG. 2: Transmission electron micrographs of recovered nanocrystalline tungsten. a) Darkfield image showing an array of elongated crystallites. b) Brightfield image of crystallites near the surface with preferred orientation perpendicular to the TEM-section. c) Darkfield image of small grains inside the sample. d) Electron diffraction pattern of nanocrystalline tungsten. e) Electron diffraction pattern of a control sample.

TABLE I: Calculated grain size from the widths of the Bragg peaks in tungsten hydride at various pressures using the Scherrer approximation.

P [GPa]	HKL	Position [deg]	FWHM [deg]	est. grain size [nm]
9.7	(010)	9.368	0.21	11.5
9.7	(110)	16.251	0.229	11
15.8	(010)	9.439	0.344	7
15.8	(110)	16.301	0.276	9
37.5	(010)	9.512	0.398	6
37.5	(110)	16.432	0.26	9.5
49.7	(010)	9.57	0.41	6
49.7	(110)	16.52	0.304	8
73.7	(010)	9.715	0.428	5.5
73.7	(110)	16.785	0.377	6.5
115	(010)	9.998	0.476	5
115	(110)	17.198	0.454	5.5

mechanism of a nanostructured material during the hydrogenation process: The unusually slow progression of hydride formation (hindered by a large energy barrier), accompanied by a structural phase transition, and the volume expansion during hydrogenation, creates significant stress between the hydrogenated and non-hydrogenated parts of the tungsten sample. Starting from the sample surface, hydrogenation slowly progresses into the material with only a very small volume near the hydride boundary undergoing the transition at any given time. With the release of local boundary strain, this leads to the formation of nanometer sized crystallites. The long dimension of the crystal grains found in our TEM studies is probably oriented along the hydride boundary during synthesis. The decomposition pressure usually lies close to the thermodynamic equilibrium of the system while the formation pressure lies higher due to the dissociation barrier encountered by the hydrogen molecule at the metal surface. Thus, once pressure is lowered below the equilibrium conditions, rapid dehydrogenation occurs leaving the microstructure intact. As a consequence, the dehydrogenated tungsten exhibits the same microstructure as its binary hydride. It can be expected, that annealing at high temperatures would lead to a realignment of the nanometer sized grains and the formation of larger crystallites. Indeed, Zaleski-Ejgierd *et al.* seem to have observed this exact effect when laser heating tungsten hydride to above 1000 K [16]. Room temperature however does not appear to have immediate or short term effect on the crystallite size. One of the samples studied by transmission electron microscopy was residing at ambient conditions for several months before TEM-sample preparation, while a different sample was recovered from high pressure only a few days prior to TEM measurements. There were no detectable differences in the microstructure between the two specimens.

Decreasing the grain size in materials down to a few tens of nanometers often entails significantly altered material properties, and it is known that, as the grain size decreases, the influence of interface and confinement effects on the properties of a material increases [23, 24]. As a result, a nanostructured material might exhibit increased resistance to plastic deformation [25] or different chemical stabilities compared to macroscopic systems [26]. In the case of metal hydrides, the grain size has profound impact on (de)hydrogenation processes, the overall hydrogen content and the volume expansion of the metallic host lattice [26] due to interface stress between the grains. It was found for example in ball milled nanoparticles of vanadium hydride that the hydrogen content depends on the particle size [27]. These possible nanometric effects make it difficult to compare tungsten hydride to other transition metal hydrides, *e.g.* in terms of volume expansion as a measure for hydrogen content [17] or when comparing experimental with computational results.

We attempted to fit a Vinet-type equation of state to our x-ray diffraction data resulting in a zero-pressure bulk modulus of near 500 GPa (depending on parametrization). Such extremely low compressibility could be attributed to a size-effect of the nanocrystalline microstructure. However, the quality of fit was not convincing, showing deviations at lower and very high pressures. The construction of the equation of state obviously assumes constant stoichiometry throughout the probed pressure range, which unfortunately cannot be guaranteed for metal hydrides. In fact, the volume difference between hydride phase and parent metal is directly used to infer the hydrogen content, assuming no change in compressibility between hydride and metal (see *e.g.* Refs. [11, 13, 17]).

We therefore performed *ab-initio* calculations to understand hydrogen content and the experimental equation of states. Structure predictions through CALYPSO methodology [28–30] were performed by fixing the W atomic positions in the *hcp* lattice, taken from the known experimental XRD pattern. We performed structural searches within various stoichiometric compositions WH_n (n = 0.5, 1.0, 1.5, 2) with simulation cell sizes of 1-4 formula units (f.u.) at 30 and 60 GPa, respectively. We did not probe higher hydrogen contents since the resulting volumes are too large to fit our experimental data. Our calculations gave convex hulls on the formation enthalpy of various WH_n with respect to elemental W and solid H_2 as shown in Fig. 3 (Details can be found in Ref. [19]). As expected, at zero pressure all W-H systems exhibit positive formation enthalpy and cannot form. At 20 and 40 GPa, the monohydride WH is the most stable compound and also the only stoichiometry which can be synthesized, which agrees well with the observed appearance of the hexagonal hydride phase in this pressure range. Interestingly, at a pressure of 60 GPa and above, WH_2 becomes stable against decomposition into WH + $\frac{1}{2}H_2$. Our results are in good agreement with those presented in Ref. [16]. However, below 120 GPa, the proposed formation of $P4/nmm$-structured WH_4 or other phases with even higher hydrogen contents can be excluded based on our experimental observations. At pressures above ∼220 GPa, when hydrogen enters phase IV which is characterized by a mixed atomic and molecular state of hydrogen [31], the formation of higher stoichiometries is possible due the absence of the dissociation barrier.

From our calculations, WH stabilizes in the $P6_3/mmc$ spacegroup and WH_2 in the $Pnma$ spacegroup above 50 GPa. For WH, tungsten atoms form a hexagonal closed-packed host matrix with hydrogen atoms occupying the octahedral interstitial sites. In the $Pnma$ structure of WH_2, the metal atoms are arranged in a slightly distorted hexagonal lattice. In addition to the octahedral sites in the WH-phase, hydrogen atoms also occupy half of the available tetrahedral sites. A transition between these two phases therefore does not require a major rearrangement of the metal host lattice and thus, WH_2 can form in addition to WH at higher pressures. Figure 4 shows the calculated equation of state for WH, WH_2 and a mixed composition phase of $(1-y)$WH + $(y)WH_2$ ($y = \frac{1}{3}$), together with our experimental data for comparison. We found that below 25 GPa, the experimental EoS can be satisfactorily

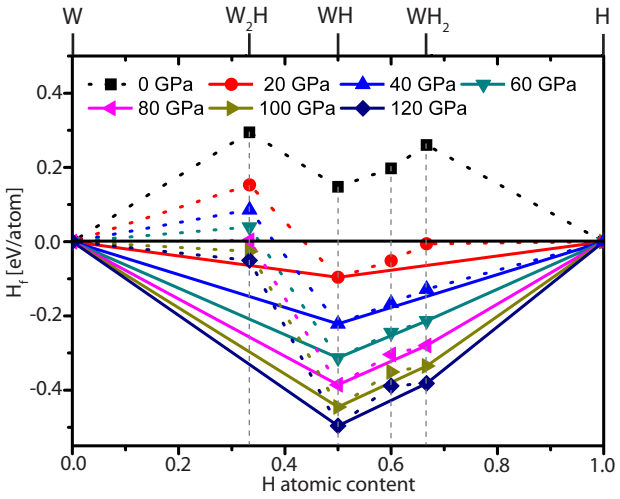


FIG. 3: (Color online) The relative enthalpies of formation per atom with respect to elemental W and molecular H_2 for different WH_n compositions. The convex hulls are shown by solid lines. Dotted lines through the neighboring points residing above the convex hull are guides for the eye.

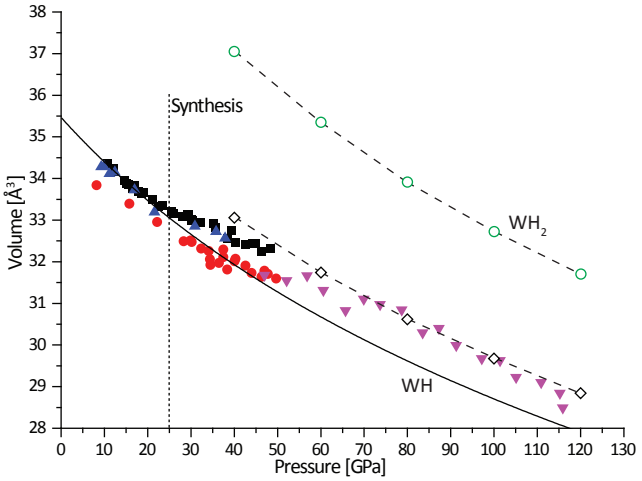


FIG. 4: (Color online) Pressure-Volume diagram of tungsten hydride. The solid line indicates the calculated equations of state for WH, the open circles the EoS for WH_2. Open diamonds denote calculated pV data for a fractional mixture of $\frac{2}{3}$ WH and $\frac{1}{3}$ WH_2. The dashed lines are guides to the eye. Solid symbols are experimental unit-cell volumes fitted with a hexagonal cell.

explained by pure tungsten monohydride. However, at pressures between 25 and 50 GPa, the experimental volume deviates from the EoS of pure WH, suggesting an additional uptake of hydrogen. Above 50 GPa, the observed pressure-volume data show a behaviour which is not explained by either pure WH or pure WH_2. Instead, a mixed-phase model of WH + WH_2 where all octahedral sites and a fraction of the available tetrahedral sites are occupied, can explain the observed behaviour. This leads to the conclusion that the reaction WH + $\frac{1}{2}H_2 \rightarrow WH_2$ is initiated and driven by pressure but appears to be halted at pressures above 50 GPa reaching a composition of $(1-y)$WH + $(y)WH_2$ ($y = \frac{1}{3}$). In other words, once all octahedral sites are filled and sufficient pressure is applied, hydrogen atoms start to occupy a fraction of the tetrahedral sites. Whether the metallic lattice transforms into the distorted *Pnma* structure or remains perfectly hexagonally oriented is experimentally difficult to address because of the very broad diffraction peaks which allow indexing in either configuration. At the highest pressures reached in this study (120 GPa), the reaction is still not complete and tetrahedral occupation seems to saturate at $\sim$17% ($= y/2$). Even with time (some of our samples resided in this pressure region for several weeks), no higher hydrogen content was reached. In samples that were not fully transformed into the monohydride phase, a slightly smaller volume is measured, indicating a lower hydrogen content, probably due to a deficient filling of the octahedral sites. The nanocrystalline nature of the hydride however might add to uncertainty in hydrogen content and atomic ordering. At the same lattice expansion, a larger hydrogen content might be possible due to surface-effects in the nanocrystalline grains.

The results presented here are of immediate interest to the field of high-pressure research. The change in microstructure as well as increased hydrogen uptake could have potentially significant consequences since tungsten is often employed as a sealing material in experiments involving pure hydrogen. Due to the higher synthesis pressure of the hydride phase and slower formation kinetics, tungsten gaskets show improved stability at pressures above 1 Mbar compared to rhenium. We hope that the findings presented here will encourage further experimental and theoretical studies on the influence of microstructure and also kinetic effects on the formation and properties of metal hydrides.

Acknowledgments

The authors would like to thank A. Kleppe from I15 at Diamond Light Source, M. Hanfland from ID09a at the European Synchrotron Radiation Facility and M. Ward from the Leeds Electron Microscopy and Spectroscopy Centre for technical support. The authors further thank O. Degtyareva for useful discussions and T. Strobel for providing unpublished data. This work is supported by a research grant from EPSRC. TS acknowledges financial support from CM-DTC. FP and YM are supported by the National Natural Science Foundation of China under Grant No. 11025418. The allocation of beamtime and access to instruments by ESRF, DLS and LEMAS/LENNF is greatly acknowledged.

Corresponding author: e.gregoryanz@ed.ac.uk

[1] T. Irifune, A. Kurio, S. Sakamoto, T. Inoue, H. Sumiya, *Nature* **421**, 599-601 (2003).
[2] R.H. Wentorf, *J. Chem. Phys.*, **34**, 809-812 (1961).
[3] E. Gregoryanz, C. Sanloup, M. Somayazulu, J. Badro, G. Fiquet, H.-K. Mao and R.J. Hemley, *Nature Mater.*, **3**, 294-297 (2004).
[4] A.F. Young, C. Sanloup, E. Gregoryanz, S. Scandolo, R.J. Hemley and H.-K. Mao, *Phys. Rev. Lett.*, **96**, 155501 (2006).
[5] Y. Tian, B. Xu, D. Yu, Y. Ma, Y. Wang, Y. Jiang, W. Hu, C. Tang, Y. Gao, K. Luo, Z. Zhao, L.-M. Wang, B. Wen, J. He and Z.Liu, *Nature* **493**, 385 (2013).
[6] A. Züttel, *Die Naturwissenschaften*, **91**, 157 (2004)
[7] B. Sakintuna *et al.*, *International Journal of Hydrogen Energy*, **32**, 1121 (2007)
[8] V. Yartys *et al.*, in T. Veziroglu, S. Zaginaichenko, D. Schur, B. Baranowski, A. Shpak, & V. Skorokhod (Eds.), Hydrogen Materials Science and Chemistry of carbon Nanomaterials (Vol. 172, pp. 75-104) (2004)
[9] N.W. Ashcroft, *Phys. Rev. Lett.*, **92**, 187002 (2004)
[10] E. Babaev *et al.*, *Phys. Rev. Lett.*, **95**, 105301 (2005)
[11] T. Scheler, O. Degtyareva, M. Marqués, C.L. Guillaume, J.E. Proctor, S. Evans and E. Gregoryanz, *Phys. Rev. B*, **83**, 214106 (2011).
[12] O. Degtyareva, J.E. Proctor, C.L. Guillaume, E. Gregoryanz, M. Hanfland, *Solid State Commun.* **149**, 1583-1586 (2009).
[13] T. Scheler, O. Degtyareva, E. Gregoryanz, *J. Chem. Phys.* **135**, 214501 (2011).
[14] M. Hanfland, J.E. Proctor, C.L. Guillaume, O. Degtyareva, E. Gregoryanz, *Phys. Rev. Lett.* **106**, 095503 (2011).
[15] H. Kawamura, T. Moriwaki, Y. Akahama, K. Takemura, *Proc. of Joint 20th AIRAPT - 43rd EHPRG International Conference on High Pressure Science and Technology* Karlsruhe (2005).
[16] P. Zaleski-Ejgierd, V. Labet, T.A. Strobel, R. Hoffmann, N.W. Ashcroft, *J.Phys.: Condens. Matter* **24**, 155701 (2012).
[17] Y. Fukai, *The Metal-Hydrogen System.* (Springer Verlag, Berlin 2005)
[18] S.P. Besedin and A.P. Jephcoat, *Rev. High Pressure Sci. Technol.* **7**, 301 (1998)
[19] See supplementary material at (...)
[20] A. Dewaele, P. Loubeyre, M. Mezouar, *Phys. Rev. B* **70**, 094112 (2004)
[21] B. Baranowski and K. Bojarski, *Roczniki Chemii Ann. Soc. Chim. Polonorum* **46**, 525 (1972).
[22] V. Antonov, A.I. Latynin and M. Tkacz, *J. Phys.: Con-*

dens. Matter **16**, 8387 (2004).
[23] M.D. Uchic, D.M. Dimiduk, J.N. Florando, W.D. Nix, *Science* **305**, 986-989 (2004).
[24] G.C.A.M. Janssen, B.R. Pujada, *Appl. Phys. Lett.* **91**, 121913 (2007).
[25] S. Veprek, A.S. Argon R.F. Zhang, *Philosophical Magazine*, **90**, 4101-4115 (2010).
[26] M. Fichtner, *Nanotechnology* **20**, 204009 (2009).
[27] S.-I. Orimo, F. Kimmerle and G. Majer, *Phys. Rev. B*, **63**, 094307 (2001).
[28] Y. Wang, J. Lv, L. Zhu, Y. Ma, *Phys. Rev. B*, **82**, 094116 (2010).
[29] Y. Wang, J. Lv, L. Zhu, Y. Ma, *Comput. Phys. Commun.*, **183**, 2063 (2012) - CALYPSO code is free for academic use, please register at http://www.calypso.cn
[30] J. Lv, Y. Wang, L. Zhu and Y. Ma, *J. Chem. Phys.*, **137**, 084104 (2012).
[31] R.T. Howie, C.L. Guillaume, T. Scheler, A.F. Goncharov and E. Gregoryanz, *Phys. Rev. Lett.* 108, 125501 (2012).

Supplementary Material for: Structural and Mechanical Study of Tungsten Hydride

Thomas Scheler[1], Feng Peng[2], Christophe L. Guillaume[1], Ross T. Howie[1], Yanming Ma[2], Eugene Gregoryanz[1]
[1] *SUPA, School of Physics and Astronomy and Centre for Science at Extreme Conditions, The University of Edinburgh, Edinburgh, EH9 3JZ, UK*
[2] *State Key Lab of Superhard Materials, Jilin University, 130012 Changchun, P.R. China*

Experimental Methods

In four independent runs, we loaded pristine tungsten powder consisting of single crystalline grains, several microns in size, together with hydrogen compressed to 2000 bar into symmetric diamond anvil cells. The hydrogen also acted as the pressure-transmitting medium. Even at the highest pressures reached in these experiments, the tungsten sample was always surrounded by excess hydrogen. In three out of four runs we used diamonds with 250 μm culets, in the fourth run we used 90 μm beveled diamonds to achieve pressures above 1 Mbar. Pressure was determined using the revised hydrostatic ruby scale up to 70 GPa and the calibrated hydrogen vibron shift above. Rhenium foil of 250μm was used as a gasket material. Gasket holes of around 50% of the culet diameter were drilled using a YAG infrared laser. The final thickness of the gasket was measured to be 25μm in the case of the larger culets and $\sim$ 15μm for the bevelled culets. Angle-dispersive x-ray diffraction patterns using microfocused monochromatic synchrotron radiation ($\lambda = 0.4149$Å) were collected at the beamlines I15 at Diamond Light Source, UK, and ID09a at European Synchrotron Radiation Facility, France. MAR345, MAR555 and Perkin Elmer flat panel detectors were used for data collection. X-ray diffraction patterns were analyzed using Fit2D [1], Jade MDI 9 and JANA 2006. TEM-samples were prepared by focused ion beam milling and subsequent lift-out and transfer to a copper TEM-grid. The finished samples had a thickness of 80-100 nm. TEM data was collected at the Leeds Electron Microscopy And Spectroscopy centre, UK.

Computational Details

The incorporation of hydrogen into *d*-band metals is a consequence of the hydrogen dissociation arising from the catalysis of the transition metals. Atomic hydrogen usually occupies the tetrahedral (T) or octahedral (O) interstices of the metal lattices[2, 3]. We therefore consider those structures generated by hydrogen occupancies at T or O interstitial sites[3]. The underlying *ab-initio* structural relaxations were performed using density functional theory (DFT) within the Perdew-Burke-Ernzerhof (PBE) parametrization of the generalized gradient approximation (GGA)[4] and the local-density approximation (LDA) Ceperley-Alders exchange-correlation potential parametrized by Perdew-Zunger scheme (CA-PZ)[5] were used with the PAW potentials as implemented in the Vienna *ab-initio* simulation package (VASP)[6]. The adopted all-electron projector-augmented wave (PAW)[7] pseudopotentials of W and H treat $5d$, $6s$ and $1s$ electrons as valence. The cutoff energy of 700 eV and appropriate Monkhorst-Pack k-meshes were chosen to ensure that all the enthalpy calculations were well converged to less than 1 meV/atom.

The experimental data indicates that the W atoms occupy the *hcp* lattice points. Furthermore, the W atoms have also been shown to occupy the *hcp* lattice points in the predicted structures of WH and WH_2 (see Ref. [8]). In order to obtain the different stoichiometries (including W_2H, WH, W_2H_3 and WH_2), W atoms were fixed on the *hcp* lattice points and H atoms occupy the T or O interstitial sites. Through structural relaxations with VASP, we chose the structure with competitive energies as the best one in different stoichiometries. To check the validity of these results, we performed structure predictions through a global minimization of free energy surfaces based on the CALYPSO (Crystal structure AnaLYsis by Particle Swarm Optimization) methodology as implemented in CALYPSO code [9–13]. We searched the structures of stoichiometric WH and WH_2 with simulation cell sizes of 1-4 formula units (f.u.) at 30 and 60 GPa and fixed the W atoms in the *hcp* lattices, then H atoms added in the system randomly. The predicted structure of WH is the anti-NiAs structure, of $P6_3/mmc$ symmetry (Z = 2) at 30 and 60 GPa. The predicted structures of WH_2 are hexagonal and orthorhombic phases with space group $P6_3/mc$ and $Pnma$ at 30 and 60 GPa, respectively. To obtain the most likely stoichiometry at different pressures, we investigated the phase stabilities of W-H systems by calculating the formation enthalpy of various WH_n ($n = 0.5$, 1.0, 1.5, 2) compounds in a pressure range of 0 to 120 GPa. The formation enthalpy of WH_n was calculated by using fractional representation $W_{1-y}H_y$ ($0 < y < 1$) with respect to the decomposition into W and H_2, as

$$h_f(\mathrm{W}_{1-y}\mathrm{H}_y) = h(\mathrm{W}_{1-y}\mathrm{H}y) - (1-y)h(\mathrm{W}) - yh(\mathrm{H}) \quad (1)$$

where the enthalpies h for $\mathrm{W}_{1-y}\mathrm{H}_y$ are obtained for the most stable structures at the desired pressures. We adopted the most stable structures for solid H_2 and elemental W in their corresponding stable pressure ranges, *i.e.* H_2 in the $P63/m$ (0-100 GPa), $C2/c$ (110-120 GPa) structures and W in the *bcc* (0-120 GPa) structure[14]. The convex hulls are depicted in Fig. 3 (main text) for pressures at 0, 20, 40, 60, 80, 100 and 120 GPa. The main results can be summarized as follows (see also main text): (i) At P = 0 GPa, all the WH_n systems which have positive h_f are not stable. This is consistent with the experimental observation that no WH_n compound forms at ambient pressure. (ii) At P = 20 and 40 GPa, among different compositions, WH is the most stable stoichiometry and the only one stoichiometry that can be synthesized. (iii) At P = 60, 80, 100 and 120 GPa, WH remains as the most stable composition, while WH_2 is metastable. In conclusion, the stoichiometry of W-H compounds varies under high pressure. The atomic fraction of H in W-H compounds rises with the increasing pressure. This is the reason for the differences between calculated and observed equation of state. Detailed information on the calculated structures is given in Tables 1-5.

For WH, analysis of the density of states (DOS) spectrum and electronic band structure indicates high accumulation of occupied states at the Fermi level, indicative of metallic character. For WH_2 ($Pnma$) as for WH, there is again no bandgap at the Fermi level, and still a substantial density of states (see Figs. 1 and 2). Interestingly, there is a bandgap at half occupation of the valence levels, *i.e.* four electrons per formula unit, which again probably separates hydridic and W $5d$ states. The calculated partial DOSs for WH and WH_2 (Figs. 1 and 2) show that they all contain the low-lying hybridization bands between W $5d$ and H $1s$ states, which are the results of the introduction of H into W. It is also found that W $5d$ states contribute most to the total DOS and dominate the DOS at the Fermi level. To check the dynamical stabilities of the currently predicted W-H compounds, we have also checked the full phonon dispersion curves for them. The absence of any imaginary phonons gives direct proof of their dynamical stabilities at the corresponding stable pressure ranges (Fig. 3).

TABLE I: Detailed structural information of $P\bar{3}m1$ for W_2H at 44 GPa

Parameter	Value	
a,b	2.746 Å	
c	4.7072 Å	
α,β	90°	
γ	120°	
Atom	Site	Fractional coordinates (x,y,z)
W	2d	0.3333, 0.6667, 0.2586
H	1a	0, 0, 0

TABLE II: Detailed structural information of $P6_3/mmc$ for WH at 44 GPa

Parameter	Value	
a,b	2.82641 Å	
c	4.57925 Å	
α,β	90°	
γ	120°	
Atom	Site	Fractional coordinates (x,y,z)
W	2c	0.3333, 0.6667, 0.25
H	2a	0, 0, 0

TABLE III: Detailed structural information of $P\bar{3}m1$ for W_2H_3 at 44 GPa

Parameter	Value	
a,b	2.90620 Å	
c	4.72150 Å	
α,β	90°	
γ	120°	
Atom	Site	Fractional coordinates (x,y,z)
W	2d	0.3333, 0.6667, 0.27078
H	2d	0.3333, 0.6667, 0.88470
H	1b	0, 0, 0

TABLE IV: Detailed structural information of $P6_3/mc$ for WH_2 at 40 GPa

Parameter	Value	
a,b	3.04256 Å	
c	4.62077 Å	
α,β	90°	
γ	120°	
Atom	Site	Fractional coordinates (x,y,z)
W	2b	0.3333, 0.6667, 0.24804
H	2b	0.3333, 0.6667, 0.62988
H	2a	0, 0, 0.37208

TABLE V: Detailed structural information of $Pnma$ for WH_2 at 100 GPa

Parameter	Value	
a	4.6119 Å	
b	2.8456 Å	
c	4.9460 Å	
α,β,γ	90°	
Atom	Site	Fractional coordinates (x,y,z)
W	4c	-0.2675, 0.75, 0.0883
H	4c	-0.1169, 0.25, -0.0701
H	4c	-0.0093, 0.25, 0.2907

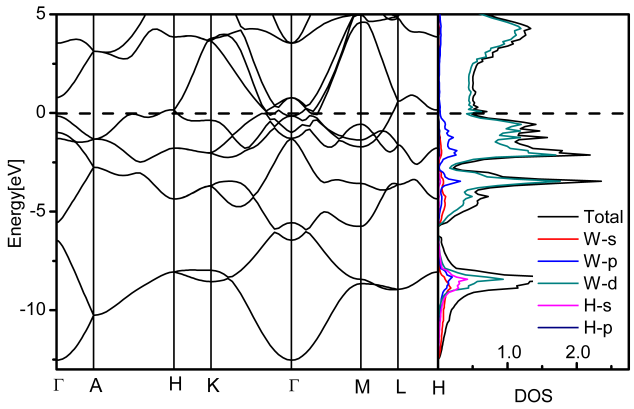


FIG. 1: Electronic band structure (left panel) and density of states (DOS) (right panel) of $P6_3/mmc$ for WH at 30 GPa.

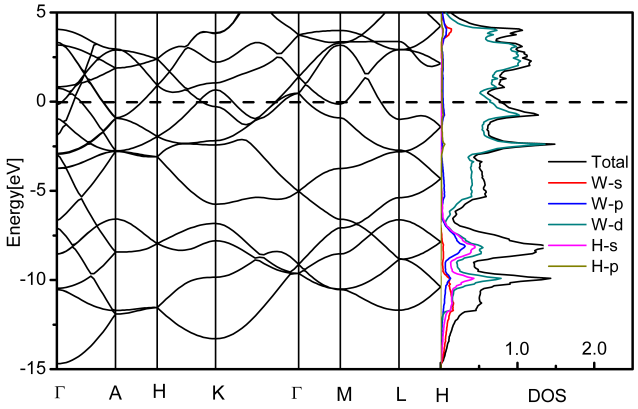


FIG. 2: Electronic band structure (left panel) and DOS (right panel) of $Pnma$ for WH_2 at 60 GPa.

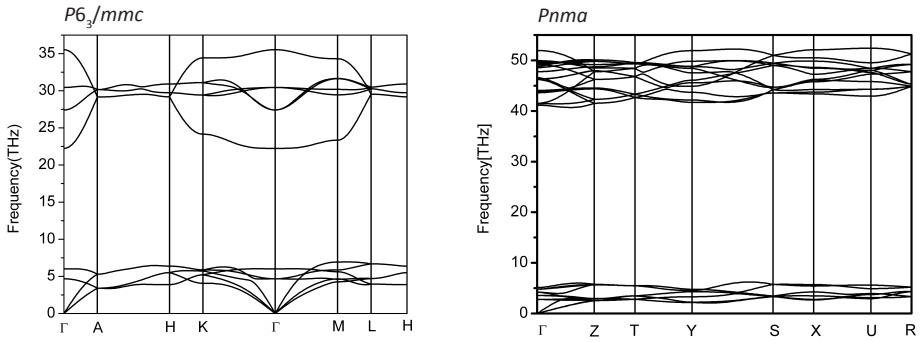


FIG. 3: Phonon dispersion curves of $P6_3/mmc$ (WH) at 30 GPa (left panel) and $Pnma$ (WH_2) at 60 GPa (right panel).

[1] A.P. Hammersley *et al.*, High Press. Res. **14**, 235 (1996)
[2] Besedin, S. P.; Jephcoat, A. P.; Hanfland, M. High Pressure Res. 2000, 17, 225-234.
[3] Fukai, Y. Metal-Hydrogen System; Springer: Berlin, 2005.
[4] Perdew, J. P.; Burke, K.; Ernzerhof, M. Phys. Rev. Lett. 1996, 77, 3865-3868.
[5] J.P. Perdew, A. Zunger, Phys. Rev. B 1981, 23, 5048-5079.
[6] Kresse, G.; Furthmler, J. Phys. Rev. B 1996, 54, 11169-11186.
[7] Blhl, P. E. Phys. Rev. B 1994, 50, 17953-17979.
[8] Zaleski-Ejgierd P., Labet V., Strobe T. A., Hoffmann R., Ashcroft N. W. J. Phys.: Condens. Matter 2012, 24, 155701.
[9] Y. Wang, J. Lv, L. Zhu, Y. Ma, Y., Phys. Rev. B, **82**, 094116 (2010).
[10] Y. Wang, J. Lv, L. Zhu, Y. Ma, Y., Comput. Phys. Commun., **183**, 2063 (2012) - CALYPSO code is free for academic use, please register at http://www.calypso.cn
[11] J. Lv, Y. Wang, L. Zhu and Y. Ma, J. Chem. Phys., **137**, 084104 (2012).
[12] Yanchao Wang, Maosheng Miao, Jian Lv, Li Zhu, Ketao Yin, Hanyu Liu, and Yanming Ma, J. Chem. Phys. 2012, 137, 224108 .
[13] CALYPSO code is free for academic use, please register at http://www.calypso.cn
[14] Pickard, C. J., Needs, R. J. Nat. Phys. 2007, 3, 473-476.

High-pressure synthesis and characterization of iridium-trihydride

Thomas Scheler[1], Miriam Marqués[2], Zuzana Konôpková[3],
Christophe L. Guillaume[1], Ross T. Howie[1] and Eugene Gregoryanz[1,*]
[1] *Centre for Science at Extreme Conditions, School of Physics and Astronomy, The University of Edinburgh, Edinburgh, EH9 3JZ, UK,*
[2] *MALTA Team and Dpto. Química Física y Analítica. Universidad de Oviedo, E-33006 Oviedo, Spain,*
[3] *DESY Photon Science, Notkestr. 85, 22 607 Hamburg, Germany*

We have performed *in-situ* synchrotron x-ray diffraction studies of the iridium-hydrogen system up to 125 GPa. At 55 GPa, a phase transition in the metal lattice from the *fcc*- to a distorted simple cubic phase is observed. The new phase is characterized by a drastically increased volume per metal atom, indicating the formation of a metal hydride, and substantially decreased bulk modulus of 190 GPa (383 GPa for pure Ir). *Ab-initio* calculations show, that the hydrogen atoms occupy the face-centered positions in the metal matrix, making this the first known *non-interstitial* noble metal hydride and, with a stoichiometry of IrH_3, the one with the highest volumetric hydrogen content. Computations also reveal that several energetically competing phases exist, which can all be seen as having distorted simple cubic lattices. Slow kinetics during decomposition at pressures as low as 6 GPa suggest that this material is metastable at ambient pressure and low temperatures.

PACS numbers:

High pressure as a general route to material synthesis [1–3] has been used in the past to obtain hydride phases of most transition metals under thermodynamic equilibrium conditions [4, 5]. However, in particular for the noble metals, the required pressures can be substantial (with the sole exception of palladium [6]). So far, the highest reported pressures for hydride synthesis are 25 GPa for tungsten [7, 8] and 27 GPa for platinum hydride [9]. Most known *d*-metal hydrides exhibit a closed-packed metal host lattice with hydrogen atoms occupying the octahedral or tetrahedral interstitial sites, the former being by far the most common modification [5]. Thus, these hydrides usually exhibit a hydrogen:metal (H:M) ratio close to 1, with few exceptions where higher ratios are achieved (*e.g.* rhodium-dihydride [10]). No hydride phases are known for the noble metals silver, gold [11], osmium and iridium. Interstitial hydrogen alloys are interesting due their potentially important physical properties, such as modified crystalline structures and mechanical properties [12], altered microstructure [8] (nanocrystallinity), hydrogen mediated superconductivity [13, 14] or potential hydrogen storage capabilities [10, 15, 16]. Furthermore, according to theoretical predictions, hydrogen confined in a host matrix might undergo the elusive transition to a metallic groundstate at considerably lower pressures than pure hydrogen [17, 18]. Recent studies [19] estimate the metallization pressure for pure hydrogen to be above 375 GPa, still out of reach of current static compression techniques. The formation of a hydride phase is readily observed in x-ray diffraction (XRD) measurements as an expansion of the unit-cell (see *e.g.* in rhenium [12]), or a structural phase transition with increased volume per metal atom compared to the parent metal (*e.g.* *bcc*-to-*hcp* in tungsten [7, 8, 20] or *fcc*-to-*hcp* in platinum [9]). It has been found that, due to contributing its electron to the valence band of the surrounding metal, the presence of one hydrogen atom expands the host lattice by 2-3 Å^3 (depending on the material, see Ref. [4, 5]). From the formation of the nitrides of iridium and osmium [21] at conditions identical to those at which platinum nitride forms [22], it could be argued that an equivalent behaviour might be observed for hydrogen. However, although platinum hydride readily forms at 27 GPa, no hydride phases of iridium or osmium are known.

We have performed x-ray diffraction (XRD) studies on iridium in a hydrogen medium at pressures up to 125 GPa in the diamond anvil cell (DAC) (see Ref. [23] for details). At 55 GPa an additional phase appears in XRD patterns of iridium. The new phase can easily be indexed in the $Pm\bar{3}m$ space group (simple cubic, see Figure 1) and exhibits a significantly larger volume per atom than pure iridium at the same pressure. This indicates the formation of a compound material, *i.e.* a metal hydride (as opposed to a phase transition in pure iridium). At 65 GPa, the volume difference amounts to $\sim$ 6.6 Å^3 per metal atom, substantially more than usually observed for interstitial metal hydrides (*e.g.* 2.1 Å^3 for platinum hydride [9]). Direct comparison with other metal hydrides suggests a H:M ratio of 3 (assuming full stoichiometry). However, such comparisons are not directly valid since estimating the hydrogen content by comparing unit-cell volumes is based on *empirical* findings in *interstitial* hydrides. The simple cubic lattice does not exhibit comparable interstitial sites. At room temperature, the formation of the new phase progresses very slowly at first and accelerates exponentially over time during the first 50 hours after crossing synthesis conditions (see inset Figure 1). The transition was

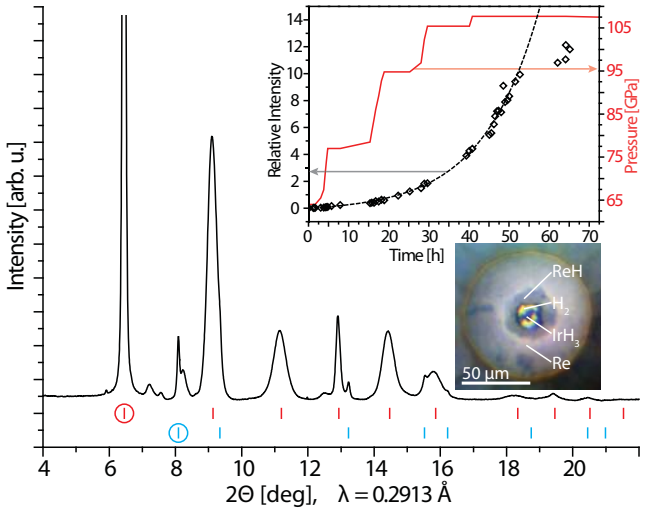


FIG. 1: Integrated x-ray diffraction pattern at 120 GPa, indexed with simple cubic iridium hydride ($a = 2.591$ Å, upper red tick marks) and *fcc* iridium ($a = 3.577$ Å, lower blue tick marks). Other visible reflections stem from rhenium hydride formed at the gasket rim. The inset shows the development over time of the relative scattering intensity (left scale) of the IrH_3 (001)-peak compared to the Ir (111)-peak (circled reflections in the diffraction pattern). The dashed line indicates an exponential guide to the eye to the data up to t=50h. The solid red line denotes the applied pressure (right scale). The optical micrograph shows the gasket and sample at 100 GPa. The extension of the rhenium hydride zone in the gasket is clearly visible.

measured through the relative scattering intensities between Bragg peaks belonging to the hydride phase and parent material measured in the same diffraction pattern. Interestingly, the progress is independent of pressure. During this period, pressure was increased to 110 GPa with no deviation from exponential growth detectable. However, after 50 h, the formation process slows down. Even after two weeks at 110 GPa, pure Ir is still present in the sample volume. We therefore employed low-power single-sided laser heating to accelerate the formation process. Indeed, within a few minutes, the parent material had completely vanished and only the hydride phase remained. Due to the low laser power applied (<6 W), temperature measurement was not possible but could only be estimated to be below 1000 K. In a subsequent experiment, we repeated the laser heating process at 55 GPa and achieved almost complete transformation of the sample within ca. 30 min.

On decompression we found the hydride phase of iridium to be visible to pressures as low as 6 GPa, with onset of decomposition visible between 15 and 20 GPa (indicated by a decrease in scattering intensity). Thus, we were able to establish the equation of state of this phase in the pressure range between 6 and 125 GPa. The data was fitted to a Vinet-type equation of state yielding a zero-pressure volume $V_0 = 23.33$Å^3 and a surprisingly low zero-pressure bulk modulus B_0 =190(3) GPa ($B_0' = 5.62(11)$) (see Fig. 2). A similar change in mechanical properties is only known for chemically produced hexagonal copper hydride where the bulk modulus drops from 142 GPa to 70 GPa, a phenomenon attributed to the hydrogen-metal bond which is partly covalent and ionic [24, 25]. However, copper hydride still exhibits a closed-packed structure. No other hydride is known to exhibit a simple cubic host lattice which makes it difficult to establish the correct crystal structure by comparison, *i.e.* determine the position of the hydrogen atoms which are almost invisible to x-rays. We therefore employed *ab-initio* computational methods to address crystal structure, thermodynamic properties and stability of this material. Assuming the $Pm\bar{3}m$ space group (Ir atoms located on the 1*a* sites), there are three potential stoichiometries IrH_n, $n = 1 - 3$. Taking the experimentally observed volume at 81 GPa (V = 18.59 Å^3), placing a single hydrogen atom on the 1*b* site yielded a calculated pressure of -0.5 GPa while three hydrogen atoms on the 3*d* sites lead to a pressure of 324.6 GPa. Therefore, these two configurations can be ruled out as possible candidates. A derived layered structure with only two of the three available 3*c* sites occupied (IrH_2, $P4/mmm$, Ir(1*a*), H(2*e*)) would correspond to a somewhat plausible pressure of 49.8 GPa. However, it is well known that calculations employing the PBE functional slightly overestimate the pressure and better agreement (98.5 GPa) is found for the IrH_3 structure with hydrogens occupying the 3*c* sites (for more details see Ref. [23]).

It can therefore be concluded that the hydrogen atoms most probably occupy the center of the faces in the simple cubic metal lattice, making this phase iridium trihydride. The calculated parameters for the equation of state are, V_0=23.739 Å^3, B_0=238.3 GPa, B_0'=4.36. The difference to the calculated volume of pure iridium at 65 GPa is 7 Å^3, in good agreement with experimental data. The calculated volume is 1.75 % larger than the experimental value, which is typical for GGA-based DFT calculations. However, the bulk modulus is unexpectedy larger than the one found in fitting an equation of state to our experimental data. The inclusion of the spin-orbit coupling (SOC) yields a slightly smaller bulk modulus (232.28 GPa), but associated to a bigger equilibrium volume (23.858 Å^3). This implies an almost negligible influence on the equation of state. Moreover, including Hubbard interaction to account for the correlated 5*d* states or going one step further on Jacob's ladder by using a rev-TPSS meta-GGA functional [28] leads to an even larger bulk modulus, 239.13 GPa and 249.90 GPa, respectively (see Figure 2). When constraining $B' = 4$ in fitting the equation of state to our experimental data, a bulk modulus of $B_0 = 231$ GPa is found. However,

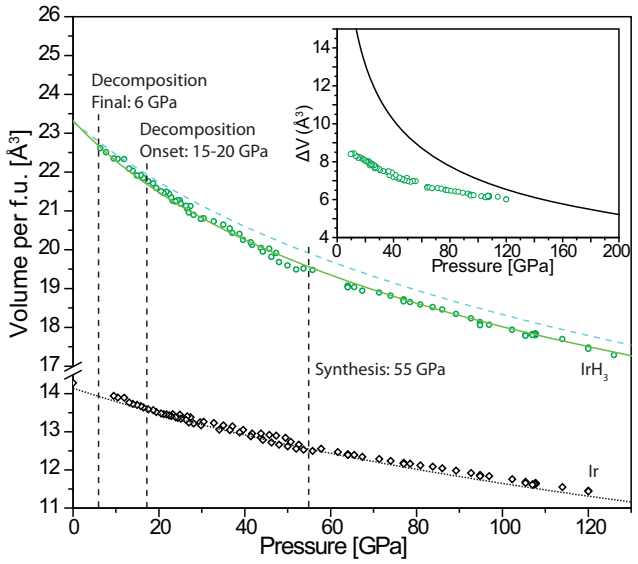


FIG. 2: (Colour online) Measured pressure-volume data of iridium (black diamonds) and iridium hydride (green circles). The dotted black line is a literature equation of state of iridium (V_0 = 14.145 Å^3, B_0 =383 GPa, B_0' = 3.1, see Refs. [21, 26]). The solid green line is a Vinet fit to our data (V_0 = 23.33 Å^3, B_0 =190(3) GPa, B_0' = 5.62(11)), the dashed blue line the calculated equation of state of IrH_3 using a rev-TPSS approach for the $Pm\bar{3}m$ structure (V_0=23.291 Å^3, B_0=249.9 GPa, B_0'=4.32). Inset shows the volume difference between IrH_3 and Ir in comparison to the equation of state for free hydrogen (solid line, showing volume for 3 hydrogen atoms, adapted from Ref. [27]).

the quality of fit deteriorates drastically, rendering this value significantly less plausible. Thus, to test if the lower experimental bulk modulus arises from a not-fully stoichiometric phase, we also calculated the equation of state of $IrH_{2.875}$, modelled by creating a single hydrogen vacancy on a 2x2x2 supercell of the simple cubic phase. However, its compressibility turned out to be very close to that of the fully stoichiometric IrH_3 phase (B_0=240 GPa). Although we can not exclude a deviation from ideal stoichiometry at higher pressures, it does not seem physically reasonable. Even if site vacancies exist in the synthesized material, taking into account the overestimation of the volume linked to the use of the PBE functional, the H:M ratio would still be very close to 3.

Interestingly, the $Pm\bar{3}m$ structure does not emerge as dynamically stable, with phonon softening in all the high-symmetry points at low pressures and in M and X at high pressures (see Figs. 1 and 2 in [23]). Freezing-in the atomic distortions involved in these soft modes leads to several structures with lower enthalphies (see Fig. 3a). For instance, the unstable M_3^- mode that consists of the closing and elongation of two of the C_2 axis of the Ir-Ir_6 octahedra yields to a $P4/nmm$ structure involving a doubling of the simple cubic unit-cell. It exhibits imaginary phonons at Γ (see Fig. 3 in [23]), related to a lowering of the symmetry to the $P\bar{4}2_1m$ space group, where two thirds of the hydrogen atoms deviate from the center of the cube faces. It corresponds, in fact, to the condensation of the M_3^- and M_2^+ modes. Moreover, the simultaneous condensation of the M_3^-,M_2^+ and X_5^- modes leads to a $P2_12_12_1$ structure without imaginary frequencies (see Fig. 4 in [23]).

From structural searches (see Ref. [23] for details), two competitive structures ($Pna2_1$ and C_c) appear as thermodynamically stable below 68 GPa at 0 K. These structures are also distortions of the simple cubic lattice with decreased distortion amplitude when increasing pressure. It can be noted that the observed diffraction peaks exhibit varying degrees of broadening which is not explained by a strain- or size-effect. However, the broadening can be explained by overlapping doublets or triplet peaks of these distorted-simple cubic structures, in which the positions of the iridium atoms deviate slightly from their ideal positions in a simple cubic cell (see Table 1 in Ref. [23]). In fact, the $Pna2_1$ structure is dynamically stable at 125 GPa and a Le Bail fit yields good agreement with experimental data (see Figs. 5 and 6 in Ref. [23]). However, this structure can not be confirmed as a unique solution given the variety of structures energetically competitive and very similar to the simple cubic structure at that pressure and susceptible to be stabilized by local stress, thermal and anharmonic effects. Particularly, entropic and anharmonic contributions might help to reduce the distortion amplitudes and, ultimately, stabilize less distorted structures than those computationally predicted at 0 K. It can be still concluded that the present structure is most probably no perfectly simple cubic but rather slightly distorted.

At pressures above 68 GPa, a different phase with $Pnma$ space group emerges as energetically favourable at 0 K and dynamically stable (see Fig. 7 in Ref. [23]). This structure, which still exhibits a H:M ratio of 3, is not a simple distortion of the simple cubic lattice (see Table 1 in Ref. [23]). Although the metallic atoms are hexaconnected as in the (distorted)-simple cubic structures, the motif of iridium octahedra with hydrogens located close to the center of the edges transforms to one of triangular prisms with interstitial hydrogens and short distances in between (At 125 GPa, the shortest H-H distance is 1.46 Å, being 1.85 Å for the simple cubic structure). We do not see any experimental evidence for this phase in our data up to 125 GPa. It can be assumed that, similarly to other hydride phases, the formation is hindered by an energy barrier, which also accounts for the large hysteresis between synthesis and decomposition in the cubic phase. It has been suggested

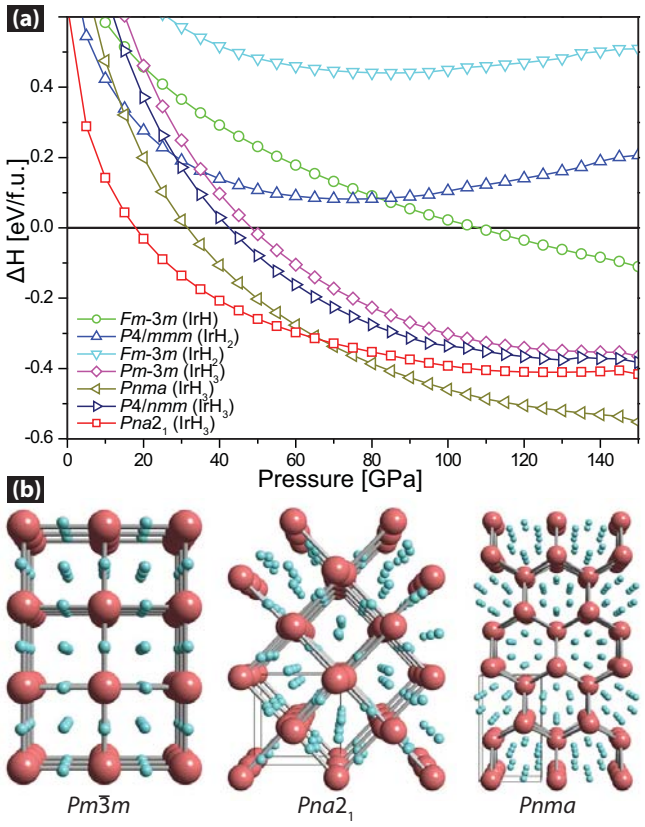


FIG. 3: (Colour online) (a) Calculated enthalpies of formation as a function of pressure for proposed iridium hydride structures. The enthalpy of the constituent elements at the corresponding pressure is taken as the reference enthalpy. $\Delta H = H(\mathrm{IrH}_n) - H(\mathrm{Ir}) - nH(0.5\mathrm{H}_2)$. (b) Atomic framework in the $Pm\bar{3}m$-structure (left), $Pna2_1$-structure (middle) and $Pnma$-structure (right). Details of the positioning for $Pna2_1$ and $Pnma$ can be found in Table 1 in [23]. Larger red spheres denote iridium atoms, smaller blue spheres hydrogen atoms.

that a higher observed synthesis pressure compared to the calculated equilibrium pressure is due to the additional energy required to dissociate the hydrogen molecule and macroscopically expand the metal sample (which requires energies comparable to the yield strength of the metal) [29]. Therefore, it could well be possible that the distorted cubic phase transforms into this phase at pressures above 125 GPa. Taking into account that experiments are performed at room temperature, it is also plausible that the observable structure remains trapped in any of the local minima of the flat energy surface in the vicinity of the simple cubic structure.

It is interesting to compare the differences between iridium hydride and other transition metal hydrides: In most known *d*-metal hydrides, synthesized at high pressures, the hydrogen atoms occupy the octahedral or tetrahedral interstitial sites in the closed-packed metal host lattices. On these sites, hydrogen appears to be mostly incompressible and the mechanical behaviour of the hydride is almost identical to that of the parent material. In iridium hydride however, the presence of the hydrogen atoms has profound impact on the material's mechanical properties, decreasing the bulk modulus significantly. It is sometimes observed that the formation process in other hydrides is slow but can usually be accelerated by increasing pressure (*e.g* in tungsten or rhenium), which is not observed here. Decomposition usually happens rapidly (instantaneously within the time scale of the experiment, *i.e.* usually <5 min.) as soon as pressure falls below equilibrium conditions. Again, this is not observed in IrH_3 where decomposition happens slowly. Since formation is accelerated at higher temperatures, it can be assumed that the material might be "frozen" at lower temperatures and decomposition prevented, rendering it (meta-)stable at ambient pressure (similar to copper hydride). The calculated elastic constants for the simple cubic structure ($Pm\bar{3}m$) at zero pressure (C_{11}= 460.63 GPa, C_{12}= 127.54 GPa, C_{44}= 24.31 GPa) of IrH_3 obey the Born stability criteria for the mechanical stability and inform on its metastability. It is also interesting to note the high Zener anisotropy ($2C_{44}/(C_{11}$-$C_{12})$=0.15) of this material and, especially, its low shear modulus (59.07 GPa, under the Voigt-Reuss-Hill approximation [30]), in contrast to the high value (210 GPa) for pure *fcc* iridium. Thus, one can conclude that the hydrogenation process turns a brittle into a ductile material. The observation of the high hydrogen content in conjunction with a severely increased compressibility lends itself to the debate whether the confined hydrogen might be compressed to densities surpassing the proposed metallization density. However, a direct comparison between the equations of state for iridium and iridium hydride shows that the volume difference approaches a constant value in the high-pressure limit corresponding to pure hydrogen at ∼250 GPa, well below predicted metallization pressures (see also inset Figure 2).

In conclusion, we have synthesized a novel metal hydride from the elements with very high hydrogen content and unusual crystalline structure (distorted simple cubic metal host lattice) that is seen up to the highest pressures reached in this study (125 GPa). The formation of the lowest-enthalpy phase above 68 GPa (*Pnma* spacegroup) is not observed and might be hindered by an energy barrier. The transition into the hydride phase as well as its decomposition are characterized by slow kinetics which suggests that the material might be metastable at ambient pressure and low temperatures. The results presented in this work have important implications for the synthesis of new materials at high pressures and the study of metal hydrides in general, and we hope that our findings will encourage further experimental and theoretical work.

Acknowledgments:

The authors would like to thank M. Hanfland (ID09a, ESRF) and A. Kleppe (I15, DLS) for technical support. This work is supported by a research grant from EPSRC. TS acknowledges financial support from CM-DTC. MM acknoledges the MALTA-Consolider program and MINECO for financial support. The allocation of beamtime by ESRF, Diamond Light Source and PETRA-III is greatly acknowledged.

*Corresponding author: e.gregoryanz@ed.ac.uk

[1] P.F. McMillan, Nature Materials, **1**, 19 (2002).
[2] V.L. Solozhenko & E. Gregoryanz, Materials Today **8**, issue 11, 44-51 (2005).
[3] V.V. Brazhkin, High Pressure Research, **27**, 333 (2007).
[4] V.E. Antonov, J. of Alloys and Compounds **330**, 110 (2002).
[5] Y. Fukai *The Metal-Hydrogen System.* (Springer Verlag, Berlin 2005).
[6] B.B. Baranowski, Platinum Metals Rev., **16**, 10 (1972).
[7] H. Kawamura, T. Moriwaki, Y. Akahama & K. Takemura, in *Proc. of Joint 20th AIRAPT - 43rd EHPRG International Conference on High Pressure Science and Technology*, Karlsruhe (2005)
[8] T. Scheler, F. Peng, C.L. Guillaume, R.T. Howie, Y. Ma, E. Gregoryanz, (to be published)
[9] T. Scheler, O. Degtyareva, M. Marqués, C.L. Guillaume, J.E. Proctor, S. Evans, & E. Gregoryanz, Phys. Rev. B, **83**, 214106 (2011)
[10] B. Li, Y. Ding, D.Y. Kim, R. Ahuja, G. Zou, H.-K. Mao, Proc. Natl. Acad. Sci. U.S.A., **108**, 18618 (2011)
[11] The synthesis of gold hydride was reported in 1982 (V.E. Antonov, Doklady Akademii Nauk SSSR, **266**, 376 (1982)), but has not been confirmed since then. We studied gold under hydrogen atmopshere at pressures up to 120 GPa and did not observe any signs of hydride formation (C. Donnerer, T. Scheler & E. Gregoryanz, accepted for publication in J. Chem. Phys.).
[12] T. Scheler, O. Degtyareva & E. Gregoryanz, J. Chem. Phys., **135**, 214501 (2011).
[13] H. Hemmes, A. Driessen, R. Griessen & M. Gupta, Phys. Rev. B, **39**, 4110 (1989)
[14] I.O. Bashkin, V.E. Antonov & E.G. Ponyatovsky in *Studies of High Temperature Superconductors, Vol. 45: Cuprates and Some Unconventional Systems*, Vol. 1, pp. 171-241 (Nova Science Publishers, New York 2003)
[15] B. Sakintuna, F. Lamari-Darkrim, F. & M. Hirscher, International Journal of Hydrogen Energy, **32**, 1121 (2007)
[16] I.P. Jain, C. Lal & A. Jain, International Journal of Hydrogen Energy, **35**, 5133 (2010)
[17] N.W. Ashcroft, Phys. Rev. Lett., **92**, 187002 (2004)
[18] E. Babaev, A. Sudbø, N.W. Ashcroft, Phys. Rev. Lett., **95**, 105301 (2005)
[19] R.T. Howie, C.L. Guillaume, T. Scheler, A.F. Goncharov & E. Gregoryanz, Phys. Rev. Lett., **108**, 125501 (2012); R.T. Howie, T. Scheler, C.L. Guillaume & E. Gregoryanz, Phys. Rev. B, **86**, 214104 (2012)
[20] P. Zaleski-Ejgierd, V. Labet, T.A. Strobel, R. Hoffmann & N.W. Ashcroft, J. Phys. Condens. Matter, **24**, 155701 (2012)
[21] A. Young, C. Sanloup, E. Gregoryanz, S. Scandolo, R. Hemley & H.-K. Mao, Phys. Rev. Lett., **96**, 155501 (2006)
[22] E. Gregoryanz, C. Sanloup, M. Somayazulu, J. Badro, G. Fiquet, H.-K. Mao & R.J. Hemley, Nature Materials, **3**, 294 (2004)
[23] See supplementary material at (...) for further details
[24] M. Tkacz & R. Burtovyy, J. alloys and compounds, **404**, 368 (2004)
[25] J. Filipek, Advanced Science, **19**, 1 (2007)
[26] H. Cynn, J.E. Klepsis, C.-S. Yoo & D.A. Young, Phys. Rev. Lett., **88**, 135701 (2002)
[27] P. Loubeyre, R. Letoullec, D. Hausermann, M. Hanfland, R.J. Hemley, H.-K. Mao & L.W. Finger, Nature, **383**, 702 (1996)
[28] J. Sun, M. Marsman, G.I. Csonka, A. Ruzsinsky, P. Hao, Y.-S. Kim, G. Kresse & J.P. Perdew, Phys. Rev. B **84**, 035117 (2011).
[29] V.E. Antonov, I. Latynin & M. Tkacz, Journal of Physics: Condensed Matter, **16**, 8387 (2004).
[30] R. Hill, Proc. Phys. Soc. Lond. **65**, 349 (1952).

Supplementary Material for: High-pressure synthesis and characterization of iridium-trihydride

Thomas Scheler[1], Miriam Marqués[2], Zuzana Konôpková[3],
Christophe L. Guillaume[1], Ross T. Howie[1] and Eugene Gregoryanz[1,*]
[1] *Centre for Science at Extreme Conditions, School of Physics and Astronomy, The University of Edinburgh, Edinburgh, EH9 3JZ, UK,*
[2] *MALTA Team and Dpto. Química Física y Analítica. Universidad de Oviedo, E-33006 Oviedo, Spain,*
[3] *DESY Photon Science, Notkestr. 85, 22 607 Hamburg, Germany*

Experimental methods:

In three experimental runs, we loaded symmetric diamond anvil cells with pristine iridium powder and hydrogen precompressed to 2000 bar. Beveled diamonds with a culet diameter of 90 μm were used to reach pressures above 1 Mbar. The gasket material was rhenium. Gasket holes were prepared using a combination of infrared laser drilling and focused ion beam (FIB) milling. The revised ruby fluorescence scale was used at pressures below 70 GPa. Above, the calibrated hydrogen vibron scale was used in conjunction with the diamond Raman edge scale. Single-sided laser heating was used to study the reaction kinetics. Angular dispersive synchrotron XRD-measurements were carried out at beamlines I15 (Diamond Light Source, UK), ID09a (European Synchrotron Radiation Facility, France) and P02.2 (Deutsches Elektronen Synchrotron, PETRA-III, Germany).

Computational methods:

Electronic structure calculations were performed within the density-functional theory (DFT) formalism with a plane-wave pseudopotential approach, as implemented in the Vienna *ab initio* simulation package [1]. We used the Perdew-Burke-Ernzerhof generalized gradient (GGA) exchange-correlation functional [2] and the projector augmented wave (PAW) all-electron description of the electron-ion-core interaction [3]. Due to the large pressures involved and to ensure a proper electronic treatment, we treat the $5s$, $5p$, $6s$ and $5d$ electrons as valence. Brillouin zone integrals were approximated using the method of Monkhorst and Pack [4], and the energies converged with respect to k-point density (k-point grid spacing of $2\pi\times$ 0.03 Å^{-1})) and to the plane wave kinetic energy cutoff (1000 eV). The equation of state parameters were determined through robust polynomial fittings of the calculated energy-volume points as coded in the GIBBS program [5]. Structure searches were performed through the *ab initio* evolutionary algorithm USPEX [6] in the pressure range of the experimentally detected phase. The initial structures were randomly generated containing up to 4 formula units. Each subsequent generation was created from 60% of the lowest-enthalpy structures of the preceeding generation through heredity, lattice mutation and permutation of the atoms. In addition, the lowest-enthalpy structure of a generation was carried over into the next generation. The underlying structural optimizations were performed with the VASP code. A plane-wave kinetic energy cutoff of 550 eV and a resolution of $2\pi\times$ 0.05 Å^{-1} for the sampling of the Brillouin zone were enough to assure energetic and structural convergence.
Phonon frequencies were calculated within density-functional perturbation theory as implemented in the Quantum-ESPRESSO package [7] The total energies required in the calculation of the phonons were obtained using the same Perdew-Burke-Ernzerhof parametrization of the exchange correlation potential [2]. The ion-electron interaction was described by an ultrasoft (Vanderbilt [8]) pseudopotential. Brillouin-zone integrations were performed using the same grids as in the VASP calculations.

[1] G. Kresse and J. Furthmuller, Phys. Rev. B **54**,11169 (1996).
[2] J. P. Perdew, K. Burke, and M. Ernzerhof, Phys. Rev. Lett. **77**, 3865 (1996)
[3] G. Kresse and D. Joubert, Phys. Rev. B **59**, 1758 (1999).
[4] H.J. Monkhorst and J. D. Pack, Phys. Rev. B **13**, 5188 (1976).
[5] A. Otero-de-la-Roza and V. Luaña, Comput. Phys. Comm. **182**, 1708 (2011).
[6] A.R. Oganov and C. W. Glass, J. Chem. Phys **124**, 244704 (2006).
[7] The QUANTUM-ESPRESSO code is available at http://www.quantum-espresso.org.
[8] D. Vanderbilt, Phys. Rev. B **41**, 7892 (1990).

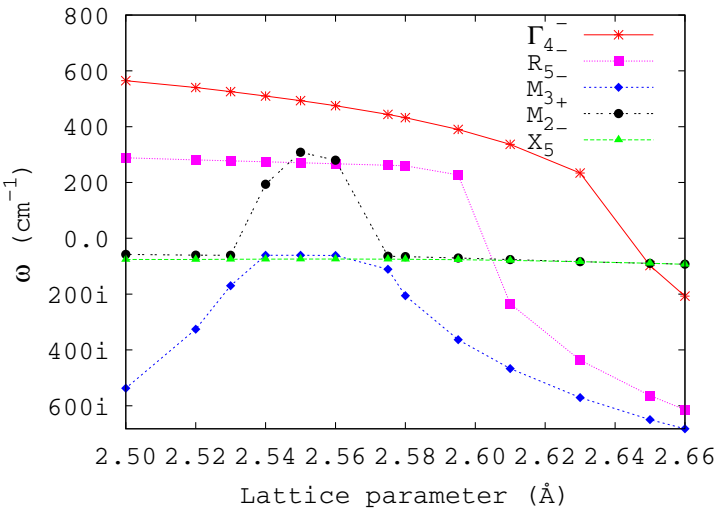


FIG. 1: Evolution of the soft modes in the $Pm\bar{3}m$ structure with the lattice parameter.

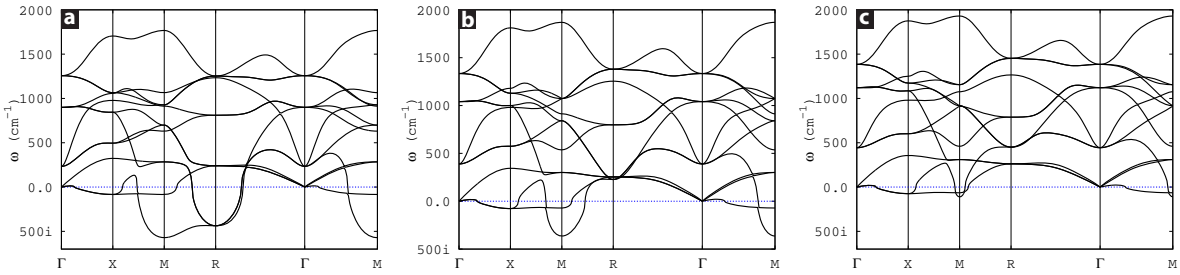


FIG. 2: Calculated phonon dispersion curves for the $Pm\bar{3}m$ structure at a) 116 GPa, b) 140 GPa and c) 160 GPa.

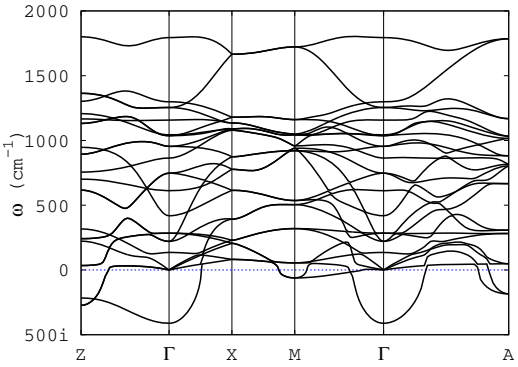


FIG. 3: Calculated phonon dispersions for the $P4/nmm$ structure (125 GPa).

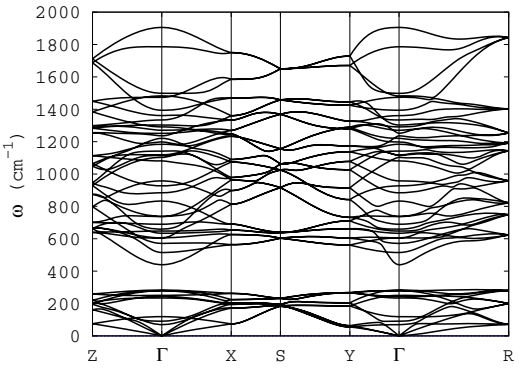


FIG. 4: Calculated phonon dispersions for the $P2_12_12_1$ structure (125 GPa). This structure is, in fact, the $Pnma(1)$ structure in Table I.

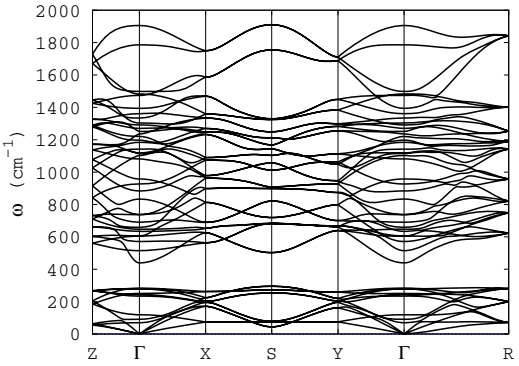


FIG. 5: Calculated Phonon dispersions for the $Pna2_1$ structure (125 GPa).

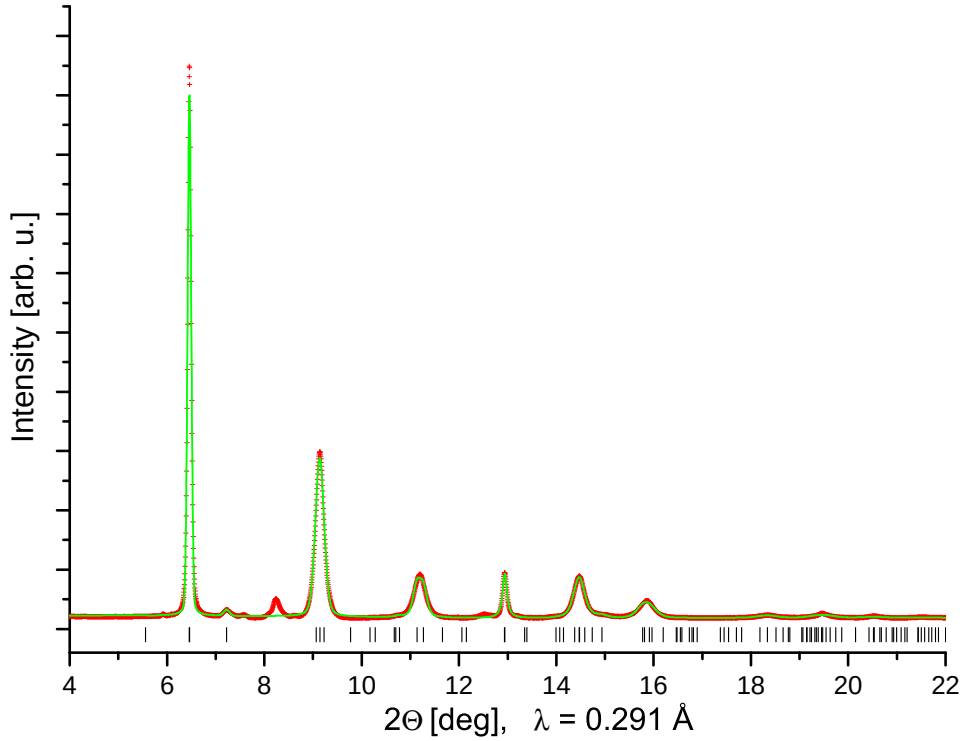


FIG. 6: Le Bail fit (green solid line) of the $Pna2_1$ structure to experimental data at 125 GPa (red crosses). The derived lattice parameters are $a = 3.6183$ Å, $b = 3.6834$ Å, $c = 5.1674$ Å, giving a volume of $V_{\rm at} = 17.2173$ Å^3. Tick marks indicate principal reflections of this space group. However, due to internal symmetry, some reflections have zero intensity. For comparison, a simple cubic lattice ($Pm\bar{3}m$) fitted to the same data yielded a lattice parameter of $a = 2.5823$ Å, giving a nearly identical volume of $V_{\rm at} = 17.2195$ Å^3.

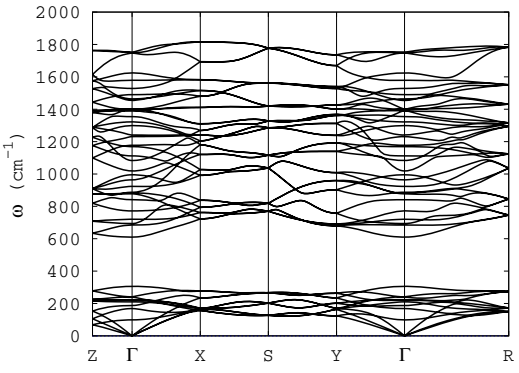


FIG. 7: Calculated Phonon dispersions for the $Pnma(2)$ structure (125 GPa).

Space group	Lattice parameters (Å)	Atomic coordinates (fractional)			
$P4/nmm$	a=3.692	Ir($2c$)	0.2500	0.2500	0.0455
(125 GPa)	b=3.692	H($4e$)	0.0000	0.0000	0.5000
	c=2.637	H($2a$)	0.7500	0.2500	0.0000
$P\bar{4}2_1m$	a=3.690	Ir($2c$)	0.0000	0.5000	0.9620
(125 GPa)	b=3.690	H($4e$)	0.2802	0.7802	0.5180
	c=2.639	H($2a$)	0.0000	0.0000	0.0000
$Pnma(1)$	a=3.703	Ir($4c$)	0.4453	0.2500	0.9971
(125 GPa)	b=5.229	H($8d$)	0.7238	0.4816	0.2274
	c=3.711	H($4c$)	0.9784	0.2500	0.9713
$Pna2_1$	a=3.698	Ir($4a$)	0.4457	0.5030	0.2492
(125 GPa)	b=3.718	H($4a$)	0.2773	0.7245	0.9801
	c=5.231	H($4a$)	0.7773	0.7755	0.5183
		H($4a$)	0.9786	0.5303	0.2492
$Pna2_1$	a=3.787	Ir($4a$)	0.4642	0.5027	0.2259
(60 GPa)	b=3.983	H($4a$)	0.3090	0.6972	0.9684
	c=5.474	H($4a$)	0.7578	0.7802	0.5418
		H($4a$)	0.0124	0.5725	0.2606
$Pnma(2)$	a=3.453	Ir($4c$)	0.2542	0.2500	0.9171
(125 GPa)	b=3.459	H($8d$)	0.1268	0.5384	0.6821
	c=5.948	H($4c$)	0.3767	0.2500	0.3972

TABLE I: Calculated parameters for some of the studied phases at 125 GPa. Data for the $Pna2_1$ structure at 60 GPa have been also included. The description of the simple cubic structure within the $P4/nmm$ and $P\bar{4}2_1m$ space groups leads to the following relations: $c_t = a_c$, $\frac{a_t}{c_t} = \sqrt{2}$ (t tetragonal and c cubic settings). The Ir atoms locate on $2c$ sites ($\frac{1}{4},\frac{1}{4},0$), and ($0,\frac{1}{2},0$) in the $P4/nmm$ and $P\bar{4}2_1m$ basis, respectively. The atomic coordinates for the $4e$ site in the $P\bar{4}2_1m$ structure are $\frac{1}{4},\frac{3}{4},\frac{1}{2}$. The relations that arise from the description within the $Pnma$ space group are, $a_o = c_o = \sqrt{2}a_c$, $b_o = 2a_c$ (o orthorhombic and c cubic settings). The Ir atoms locate on $4c$ sites ($\frac{1}{2},\frac{1}{4}$,0) and H atoms on $8d$ ($\frac{3}{4},\frac{1}{2},\frac{1}{4}$) and $4c$ ($0,\frac{1}{4}$,0) sites. The relations for the $Pna2_1$ space group are, $a_o = b_o = \sqrt{2}a_c$, $c_o = 2a_c$ (o orthorhombic and c cubic settings). The Ir atoms locate on $4a$ sites ($\frac{1}{2},\frac{1}{2},\frac{1}{4}$) and H atoms on 3 non-equivalent $4a$ sites ($\frac{1}{4},\frac{3}{4}$,0), ($\frac{3}{4},\frac{3}{4},\frac{1}{2}$) and ($0,\frac{1}{2},\frac{1}{4}$).